

# **Theoretical Analysis and Design for the Series-Resonator Buck Converter**

Cong Tu

Dissertation submitted to the faculty of the  
Virginia Polytechnic Institute and State University  
in partial fulfillment of the requirements for the degree of

Doctor of Philosophy  
in  
Electrical Engineering

Khai D. T. Ngo (Chair)  
Jaime De La Reelopez  
Majid Manteghi  
Steve C. Southward  
Yuhao Zhang

October 4, 2022  
Blacksburg, Virginia

Keywords: Resonant converter, multiphase converter, soft switching, series-capacitor buck converter, resonant inductor

© 2022, Cong Tu

# Theoretical Analysis and Design for the Series-Resonator Buck Converter

Cong Tu

## Abstract

High step-down dc/dc converters are widely adopted in a variety of areas such as industrial, automotive, and telecommunication. The 48 V power delivery system becomes increasingly popular for powering high-current and low-voltage chips. The Series-Capacitor Buck (SCB) converter doubles the duty ratio and equalizes the current between the two phases. Hard switching has hindered efforts to reduce volume via increased switching frequency, although a monolithically integrated SCB converter has boosted current density. A Series-Resonator Buck (SRB) converter is realized by adding a resonant tank in series with the series capacitor  $C_s$ . All switches turn on at zero-voltage (ZVOn), and the low-side switches turn off at zero-current (ZCOff). The design of the SRB converter includes characterizing the design variables' impacts on the converter performances and designing low-loss resonant components as the series resonator.

The Series-Resonator Buck converter belongs to the class of quasi-resonant converters. Its resonant frequency is higher than the switching frequency, and its waveforms are quasi-sinusoidal. This work develops a steady-state model of the SRB converter to calculate voltage gain, component peak voltages, and resonant inductor peak current. Each switching cycle is modeled based on the concept of generalized state-space averaging. The soft-switching condition of the high-side switches is derived. The ZVS condition depends on the normalized control variable and the load condition. The gain equation models the load-dependent characteristic and the peak gain boundary. The theoretical peak voltage gain of the SRB converter is smaller than the maximum

gain of the SCB converter. A smaller normalized load condition results in a larger peak voltage gain of the SRB converter.

The large-signal model of the SRB converter characterizes the low-frequency behavior of the low-pass filters with the series capacitor and the high-frequency behavior of the resonant elements. A design recommendation of  $t_{off}f_r < 0.5$  is suggested to avoid the oscillation between the series capacitor  $C_s$  and the output inductors  $L_o$ . In other words, the off-duration of the low-side switches is less than half of  $1/f_r$ , and therefore the negative damping effect from the parallel resonant tank to the  $v_{C_s}$  response is reduced. The transfer functions of the SRB converter are presented and compared with those of the SCB converter. The series resonator brings in an extra damping effect to the response of output capacitor voltage.

The understanding of the analytical relationships among the resonant tank energy, voltage gain, and component stresses was utilized to guide the converter design of the converter's parameters. A normalized load condition at  $\sqrt{2}$  minimizes the stresses of the series resonator by balancing the peak energy in the resonant elements  $L_r$  and  $C_r$ . The  $f_s$  variation with voltage gain  $M$  is less than 10%. The non-resonant components  $C_s$ ,  $L_{oa}$ , and  $L_{ob}$  are designed according to the specified switching ripples.

The ac winding loss complicates the winding design of a resonant inductor. This work replaces the rectangular window with a rhombic window to reduce the eddy current loss caused by the fringing effect. The window ratio  $k_y$  is added as a design variable. The impacts of the design variables on the inductance, core loss, and winding loss are discussed. The air-gap length  $l_g$  is designed to control the inductance. A larger  $k_y$  design results in a short inductor length  $l_c$  and a smaller winding loss. The disadvantages include a smaller energy density design and a larger core loss due to the smaller cross-sectional area. In the design example presented in the thesis, the

presence of the rhombic shape increases the gap-to-winding distance by two times, and also reduces the y-component of the magnetic field by a factor of two. The total inductor loss is reduced by 56% compared to a conventional design with a rectangular winding window while keeping the same inductance and the same inductor volume.

This dissertation implements a resonator, replacing the series capacitor, in an SCB converter. The resultant SRB converter shows a 30% reduction in loss and a 50% increase in power density. The root cause of the divergence issue is identified by modeling the negative damping effect caused by resonant elements. The presented transient design guideline clears the barriers to closed-loop regulation and commercialization of the SRB converter. This work also reshapes winding windows from rectangle to rhombus which is a low-cost change that reduces magnetic loss by half. The theoretical analysis and design procedures are demonstrated in a 200 W prototype with 7% peak efficiency increase compared to the commonly used 30 W commercial SCB product.

# Theoretical Analysis and Design for the Series-Resonator Buck Converter

Cong Tu

## General Audience Abstract

High step-down dc/dc converters are widely adopted in a variety of areas such as industrial, automotive, and telecommunication areas. The 48 V power delivery system becomes increasingly popular for powering high-current and low-voltage chips.

The Series-Capacitor Buck (SCB) converter doubles the duty ratio and equalizes the current between the two phases. Hard switching has hindered efforts to reduce volume via increased switching frequency although a monolithically integrated SCB converter has boosted current density.

A Series-Resonator Buck (SRB) converter is realized by adding a resonant tank in series with the series capacitor  $C_s$ . All switches turn on at zero-voltage (ZVOn), and the low-side switches turn off at zero-current (ZCOff). The challenges to designing the SRB converter include characterizing the design variables' impacts on the converter performances and designing low-loss resonant components as the series resonator.

The resultant SRB converter shows a 30% reduction in loss and a 50% increase in power density. The root cause of the divergence issue is identified by modeling the negative damping effect caused by the resonant elements. The presented transient design guideline clears the barriers of closed-loop regulation and commercialization of the SRB converter.

This work also reshapes winding windows from rectangle to rhombus, which is a low-cost change that reduces magnetic loss by half. The theoretical analysis and design procedures are

demonstrated in a 200 W prototype with 7% peak efficiency increase compared to the commonly used 30 W commercial SCB product.

# Acknowledgments

I would like to thank first and foremost my advisor, Dr. Khai D. T. Ngo for continually guiding and pushing me to excel in myself through his perpetual questioning and challenging. Dr. Ngo gives me the opportunity to work in the unique environment that is CPES, and makes time for his student every week no matter what his schedule is. His knowledge, mentorship, support, and kindness are unprecedented. I have learned and grown both personally and professionally.

I am grateful to my committee members, Dr. Jaime De La Reelopez, Dr. Majid Manteghi, Dr. Steve C. Southward, and Dr. Yuhao Zhang. Their helpful feedback and thought-provoking questions in the completion of this dissertation work are valued and appreciated.

I wish to acknowledge Texas Instruments for funding this research. Dr. Rengang Chen is generous with his time and his experience in industrial power management products furthers my understanding. This work was also supported in part by the CPES High-Density Integration (HDI) consortium members.

The excellent faculty and staff have facilitated my research, and provided the best resources available. I would like to thank the faculty members of CPES, Dr. Fred C. Lee, Dr. Dushan Boroyevich, Dr. Rolando Burgos, Dr. Guo-Quan Lu, Dr. Qiang Li, Dr. Christina DiMarino, Dr. Dong Dong, Dr. Richard Zhang, who I have interacted with in projects and classes. Thank Mr. David Gilham, Ms. Na Ren, Ms. Yan Sun, Mr. Dennis Grove, Ms. Ling Li, Mr. Matthew Scanland, Mr. Neil Croy, Ms. Audri Cunningham, Ms. Brandy Grim, Ms. Teresa Rose, Ms. Teresa Shaw, Ms. Marianne Hawthorne, Ms. Linda Long, and Ms. Lauren Shutt for their administrative support from day one.

I would also like to give my sincere thanks to all of the CPES students. This work would also not of been possible without the help of my fellow CPES colleagues.

Finally, I would like to thank my wife and my parents. Words cannot express how truly appreciative I am for their reassurance. They have provided me with the strength to continue through their love and support.

# Table of Contents

<b>Chapter 1</b>	<b>Introduction.....</b>	<b>1</b>
1.1	The 48 V Power Delivery System .....	2
1.2	Limitation of the Series-Capacitor Buck Converter .....	3
1.3	Introduction of Series-Resonator Cell .....	7
1.4	Four Parameters for the SRB Converter Design.....	9
1.5	Contributions of This Dissertation.....	10
1.5.1	Series-Resonator Buck Converter .....	10
1.5.2	Steady-State Analysis of the SRB Converter .....	12
1.5.3	Transient-State Analysis of the SRB Converter.....	13
1.5.4	Sequential Design Methodology of the SRB Converter .....	14
1.5.5	Rhombus-Window Inductor as Resonant Inductor with Significant AC Flux. 14	
1.6	Dissertation Outline .....	17
<b>Chapter 2</b>	<b>Steady-State Analysis of the SRB Converter.....</b>	<b>19</b>
2.1	Introduction.....	20
2.2	Series-Resonator Cell for Soft Switching .....	22
2.3	Gate-Driving Signal .....	23
2.4	Operating Principles with Series Resonator .....	24
2.4.1	Subinterval $[t_1, t_2]$ .....	24
2.4.2	Subinterval $[t_2, t_3]$ .....	26

2.4.3	Subinterval $[t_3, t_4]$ .....	27
2.4.4	Subinterval $[t_4, t_5]$ .....	27
2.4.5	Subinterval $[t_5, t_6]$ .....	28
2.4.6	Subinterval $[t_6, t_7]$ .....	29
2.4.7	Subinterval $[t_7, t_8]$ .....	29
2.4.8	Subinterval $[t_8, t_1]$ .....	30
2.5	Steady-State Model with Series Resonator.....	30
2.6	Soft-Switching Boundary.....	39
2.7	Gain Curve.....	41
2.8	Experimental Verification.....	46
2.9	Conclusion.....	48
<b>Chapter 3</b>	<b>Transient-State Analysis of the SRB Converter.....</b>	<b>50</b>
3.1	Introduction.....	53
3.2	Large-Signal Modeling with Generalized State-Space Averaging.....	54
3.3	Small-Signal Modeling of the SRB Converters.....	72
3.4	Conclusion.....	92
<b>Chapter 4</b>	<b>Design Methodology of the Series-Resonator Buck Converter.....</b>	<b>94</b>
4.1	Introduction.....	96
4.2	Impedance Design for Minimizing Circulating Energy.....	96
4.3	Control Variable Design for Specified Gain Range.....	98

4.4	Resonant Frequency Design for Minimum Switching Frequency.....	100
4.5	Capacitance Ratio Design for Specified Voltage Ripple.....	104
4.6	Inductance Ratio Design for Specified Current Ripple .....	105
4.7	Component Stresses .....	107
4.8	Design Flowchart and Experimental Verification .....	112
4.9	Conclusion .....	119
<b>Chapter 5 Rhombus-Window Resonant Inductor Design with Significant ac Flux ..</b>		<b>121</b>
5.1	Introduction.....	122
5.2	Selection of 2-MHz Magnetic Material .....	124
5.3	Structural Design of the Rhombus-Window Inductor .....	125
5.4	Inductance of the Rhombus-Window Inductor.....	126
5.5	Winding and Core Loss of the Rhombus-Window Inductor .....	128
5.6	Design Procedures with Given Inductor Current and Loss Budget.....	132
5.7	Experimental Verification of the Rhombus-Window Inductor .....	136
5.8	Conclusion .....	137
<b>Chapter 6 Conclusions and Future Work.....</b>		<b>139</b>
6.1	Summary .....	139
6.2	Future Work.....	140
6.3	List of Publications .....	141
6.3.1	Journal Papers.....	141

6.3.2	Conference Papers .....	142
6.3.3	Patents .....	142
<b>Appendix.....</b>		<b>143</b>
A.	Calculation of Switching Cycle .....	143
B.	Calculation of Output Voltage .....	156
C.	Calculation of Steady-State State Variables .....	158
D.	Calculation of ZVS Boundary .....	165
E.	Calculation of Gain Curve .....	170
F.	Calculation of Large Signal Equations .....	185
G.	Calculation of Small Signal Equations .....	202
H.	Calculation of Transfer Functions .....	222
I.	Calculation of Circulating Energy .....	248
J.	Calculation of Peak Circulating Energy .....	250
K.	Calculation of Switching Frequency Curve .....	254
L.	Calculation of Capacitor Voltage Ripple .....	257
M.	Calculation of Inductor Current Ripple .....	259
N.	Calculation of Component Stresses .....	261
O.	Schematic .....	265
<b>References .....</b>		<b>266</b>

# List of Figures

**Fig. 1-1. Power delivery architecture in a data center. The 48 V power delivery system is highlighted. ....2**

**Fig. 1-2. (a) Schematic of the two-Phase Buck converter and (b) schematic of the Series-Capacitor Buck converter. ....4**

**Fig. 1-3. The comparisons of (a) voltage change at switching transient normalized by the input voltage and (b) duty ratio in the 2-phase Buck converter in Fig. 1-2 and the Series-Capacitor Buck converter in Fig. 1-2. ....4**

**Fig. 1-4. The evaluation board of the TPS54A20 Series-Capacitor Buck converter [18]. ....5**

**Fig. 1-5. (a) Prototype of the SCB converter and (b) converter efficiency versus switching frequency in [6]. ....6**

**Fig. 1-6. Key voltage and current waveforms comparison between the (a) Series-Capacitor Buck converter and (b) Series-Resonator Buck converter. ....7**

**Fig. 1-7. Loss breakdown comparison between the Series-Capacitor Buck converter and Series-Resonator Buck converter shown in Fig. 1-6. The simulation utilized non-ideal switch models (EPC2049 for the SCB converter and EPC2045 for the SRB converter) from EPC, output inductors adding 2 mΩ ESR (representing the loss of the inductor VLM10555T-1R2M100-3 calculated by the manufacturer’s loss simulator), and resonant inductor adding 9 mΩ ESR (representing the loss simulated by the resonant inductor model described in [95]). Both converters operate at  $V_{in} = 48\text{ V}$ ,  $V_o = 7\text{ V}$ ,  $I_o = 20\text{ A}$ ,  $f_s = 2\text{ MHz}$  with  $L_{oa} = L_{ob} = 1.2\text{ }\mu\text{H}$ ,  $L_r = 150\text{ nH}$ ,  $C_r = 12\text{ nF}$ , and  $C_o = 20\text{ }\mu\text{F}$ . ....8**

**Fig. 1-8. Four design variables in (1-1), (1-2), (1-3), and (1-4) in the Series-Resonator Buck converter. ....10**

**Fig. 1-9. (a) The SRB converter is synthesized by replacing the series capacitor in the SCB converter in Fig. 1-6(a) with the series resonator highlighted in the schematic. (b) The SRB converter improves efficiency by 1.1% at the full-load condition benefiting from the soft switching introduced by the series resonator. The simulation utilized non-ideal switch models (EPC2049 for the SCB converter and EPC2045 for the SRB converter) from EPC and ideal passive components adding 2 mΩ inductor ESR. Both converters operate at  $V_{in} = 48\text{ V}$ ,  $V_o = 7\text{ V}$ ,  $I_o = 20\text{ A}$ ,  $f_s = 2\text{ MHz}$  with  $L_{oa} = L_{ob} = 1.2\text{ }\mu\text{H}$ ,  $L_r = 150\text{ nH}$ ,  $C_r = 12\text{ nF}$ , and  $C_o = 20\text{ }\mu\text{F}$ . ....11**

**Fig. 1-10. The modeled waveforms match the simulated ones in the steady-state in the SRB converter in Fig. 1-6.**

The waveforms were simulated using ideal components in LTspice with  $V_{in} = 48\text{ V}$ ,  $V_o = 7\text{ V}$ ,  $I_o = 20\text{ A}$ ,  $L_{oa} = L_{ob} = 1.2\text{ }\mu\text{H}$ ,  $L_r = 150\text{ nH}$ ,  $C_r = 12\text{ nF}$ , and  $C_o = 4\text{ }\mu\text{F}$ . The gate signals were illustrated in Fig. 2-3(b) with  $f_s = 2\text{ MHz}$  and  $t_{off} = 120\text{ ns}$ .....12

Fig. 1-11. The modeled waveforms match the simulated ones in the transient state in the SRB converter in Fig. 1-6. The waveforms were simulated in Simplis with  $V_{in} = 48\text{ V}$ ,  $\Delta V_{in} = 24\text{ V}$ ,  $V_o = 5\text{ V}$ ,  $L_r = 80\text{ nH}$ ,  $L_{oa} = L_{ob} = 1.5\text{ }\mu\text{H}$ ,  $C_r = 20\text{ nF}$ , and  $C_o = 47\text{ }\mu\text{F}$ . The control variable  $t_{off} = 120\text{ ns}$  is set by the dc source V3 with the conversion ratio  $t_{off}V_{ctoff} = 10^{-6}\text{ sV}$  in Fig. 3-4 on page 61. ....13

Fig. 1-12. Sequential design procedure of the SRB converter for the design variables listed in Fig. 1-8.....15

Fig. 1-13. Loss comparison between the conventional rectangular-window inductor and the rhombus-window inductor given the same component size. The inductor loss was simulated using eddy current mode in Ansys Maxwell 2D. The current and material specifications are in Table 5-1.....16

Fig. 2-1. (a) Series-Capacitor Buck converter and (b) Series-Resonator Buck converter.....22

Fig. 2-2. Switches' voltage and current of (a) the Series-Capacitor Buck converter and (b) the Series-Resonator Buck converter in Fig. 2-1. ....23

Fig. 2-3. Gate-driving signal of the (a) Series-Capacitor Buck converter and (b) Series-Resonator Buck converter in Fig. 2-1. ....23

Fig. 2-4. Eight switched intervals and waveforms for the SRB converter in Fig. 2-1 on page 22 using the gate-driving signals in Fig. 2-3 on page 23. The converter was simulated with non-ideal switch models from Efficient Power Conversion Corporation (EPC) and inductors with  $2\text{ m}\Omega$  equivalent series resistors. Other components were ideal. The component values were  $L_{oa} = L_{ob} = 1.2\text{ }\mu\text{H}$ ,  $L_r = 150\text{ nH}$ ,  $C_r = 12\text{ nF}$ , and  $C_o = 20\text{ }\mu\text{F}$ . All switches turn on with zero voltage, whereas  $S_{a2}$  and  $S_{b2}$  turn off from zero current. The equivalent circuits of eight intervals are listed in Fig. 2-5 to Fig. 2-12. ....25

Fig. 2-5. (a) Circuit during interval  $t_1 - t_2$  defined in Fig. 2-4 and (b) corresponding simplified schematic.....26

Fig. 2-6. (a) Circuit during interval  $t_2 - t_3$  defined in Fig. 2-4 and (b) corresponding simplified schematic.....26

Fig. 2-7. (a) Circuit during interval  $t_3 - t_4$  defined in Fig. 2-4 and (b) corresponding simplified schematic.....27

Fig. 2-8. (a) Circuit during interval  $t_4 - t_5$  defined in Fig. 2-4 and (b) corresponding simplified schematic.....28

Fig. 2-9. (a) Circuit during interval  $t_5 - t_6$  defined in Fig. 2-4 and (b) corresponding simplified schematic.....28

Fig. 2-10. (a) Circuit during interval  $t_6 - t_7$  defined in Fig. 2-4 and (b) corresponding simplified schematic....29

**Fig. 2-11. (a) Circuit during interval  $t_7 - t_8$  defined in Fig. 2-4 and (b) corresponding simplified schematic....30**

**Fig. 2-12. (a) Circuit during interval  $t_8 - t_1$  defined in Fig. 2-4 and (b) corresponding simplified schematic....31**

**Fig. 2-13. The equivalent circuits of the subintervals defined in Fig. 2-4 of the SRB converter in Fig. 2-1 on page 22.....32**

**Fig. 2-14. The modeled waveforms using the schematic in Fig. 2-1 on page 22 match the simulated ones in the steady state. The waveforms were simulated in LTspice using ideal components with  $V_{in} = 48\text{ V}$ ,  $f_s = 2.0\text{ MHz}$ ,  $V_o = 7\text{ V}$ ,  $I_o = 20\text{ A}$ ,  $L_{oa} = L_{ob} = 1.2\text{ }\mu\text{H}$ ,  $L_r = 150\text{ nH}$ ,  $C_r = 12\text{ nF}$ , and  $C_o = 4\text{ }\mu\text{F}$ . The fine tune of deadtime is not required because ideal components are used. ....38**

**Fig. 2-15. The modeled waveforms using the schematic in Fig. 2-1 on page 22 match the simulated ones in the steady state. The waveforms were simulated in LTspice using ideal components with  $V_{in} = 48\text{ V}$ ,  $f_s = 3.1\text{ MHz}$ ,  $V_o = 7\text{ V}$ ,  $I_o = 5\text{ A}$ ,  $L_{oa} = L_{ob} = 1.2\text{ }\mu\text{H}$ ,  $L_r = 150\text{ nH}$ ,  $C_r = 12\text{ nF}$ , and  $C_o = 4\text{ }\mu\text{F}$ . The fine tune of deadtime is not required because ideal components are used. ....39**

**Fig. 2-16. Minimum normalized load current  $J$  calculated by (2-26) for the high-side switch ( $S_{a1}$  and  $S_{b1}$  labeled in Fig. 2-1) soft switching versus normalized control variable  $t_{off}$  defined in Fig. 2-3 normalized by  $1/f_r$ .....41**

**Fig. 2-17. Voltage gain  $M$  calculated by (2-28) versus control variable  $t_{off}$  defined in Fig. 2-3 normalized by  $T_r$ . The boundary of peak gain for  $J \leq 2$  in dotted line is plotted using (2-41). The boundary of peak gain for  $J > 2$  in dashed line is plotted using (2-36). ....42**

**Fig. 2-18. Peak voltage gain calculated by (2-36) and (2-41) versus normalized load current  $J$ .....45**

**Fig. 2-19. The prototype of the Series-Resonator Buck (SRB) converter using the schematic in Fig. 2-1 on page 22 with  $L_{oa} = L_{ob} = 1.2\text{ }\mu\text{H}$ ,  $L_r = 150\text{ nH}$ ,  $C_r = 12\text{ nF}$ , and  $C_o = 20\text{ }\mu\text{F}$ . The maximum height of the prototype is 1 cm. ....47**

**Fig. 2-20. Experimental voltage waveforms for all the switches labeled in Fig. 2-1 were measured by the oscilloscope. The prototype is shown in Fig. 2-19 using the schematic in Fig. 2-1 on page 22 with  $L_{oa} = L_{ob} = 1.2\text{ }\mu\text{H}$ ,  $L_r = 150\text{ nH}$ ,  $C_r = 12\text{ nF}$ , and  $C_o = 20\text{ }\mu\text{F}$  and operated at the specifications in Table 2-1. ....48**

**Fig. 3-1. (a) Schematic and (b) state-variable waveforms of the SRB converter with  $V_{in} = 48\text{ V}$ ,  $V_o = 7\text{ V}$ ,  $I_o = 20\text{ A}$ ,  $f_s = 2\text{ MHz}$ ,  $L_{oa} = L_{ob} = 1.2\text{ }\mu\text{H}$ ,  $L_r = 150\text{ nH}$ ,  $C_s = 600\text{ nF}$ ,  $C_r = 12\text{ nF}$ , and  $C_o = 4\text{ }\mu\text{F}$ . The**

converter was simulated with ideal inductors with 2 mΩ equivalent series resistors. Other components were ideal. ....	55
<b>Fig. 3-2. Equivalent circuit of the large-signal model shown in (3-4) of the SRB converter in Fig. 3-1. ....</b>	<b>57</b>
<b>Fig. 3-3. Steady-state equivalent circuit of the large-signal model shown in (3-4) of the SRB converter in Fig. 3-1. The capacitors are open, and the inductors are shorted in Fig. 3-2.....</b>	<b>58</b>
<b>Fig. 3-4. Gate-driving circuits with soft-switching detectors and timer for the Simplis simulations in this chapter. The high-side switches <math>S_{a1}</math> and component currents are labeled in Fig. 3-1.....</b>	<b>61</b>
<b>Fig. 3-5. Modeled using (3-4) and simulated converter state variable waveforms when a <math>v_{in}</math> step change is applied to the SRB converter in Fig. 3-1 on page 55 using the gate driving circuit in Fig. 3-4 on page 61. The control variable <math>t_{off} = 120</math> ns is set by the dc source V3 with the conversion ratio <math>t_{off}V_{ctoff} = 10^{-6}</math> sV in Fig. 3-4 on page 61. The theoretical model using (3-4) matches the simulated results in Simplis with <math>V_{in} = 48</math> V, <math>\Delta V_{in} = 24</math> V, <math>R_{load} = 0.125</math> Ω, <math>R_{Lo} = 0.01</math> Ω, <math>L_{oa} = L_{ob} = 1.5</math> μH, <math>L_r = 80</math> nH, <math>C_s = 20</math> μF, <math>C_r = 1</math> nF, and <math>C_o = 47</math> μF.....</b>	<b>62</b>
<b>Fig. 3-6. Modeled using (3-4) and simulated resonant element waveforms when a <math>v_{in}</math> step change is applied to the SRB converter in Fig. 3-1 on page 55 using the gate driving circuit in Fig. 3-4 on page 61. The waveforms are zoomed in to show the switching ripples and their envelopes with <math>V_{in} = 48</math> V, <math>\Delta V_{in} = 24</math> V, <math>V_o = 5</math> V, <math>I_o = 40</math> A, <math>L_{oa} = L_{ob} = 1.5</math> μH, <math>L_r = 80</math> nH, <math>C_s = 20</math> μF, <math>C_r = 21</math> nF, and <math>C_o = 47</math> μF.....</b>	<b>64</b>
<b>Fig. 3-7. Modeled and simulated converter state variable waveforms when a <math>t_{off}</math> step change is applied to the SRB converter in Fig. 3-1 on page 55 using the gate driving circuit in Fig. 3-4 on page 61. The control variable <math>t_{off} = 120</math> ns is set by the dc source V3 with the conversion ratio <math>t_{off}V_{ctoff} = 10^{-6}</math> sV in Fig. 3-4 on page 61. The theoretical model using (3-4) matches the simulated results in Simplis with <math>V_{in} = 48</math> V, <math>t_{off} = 120</math> ns, <math>\Delta t_{off} = 100</math> ns, <math>R_{load} = 0.125</math> Ω, <math>R_{Lo} = 0.01</math> Ω, <math>L_{oa} = L_{ob} = 1.5</math> μH, <math>L_r = 80</math> nH, <math>C_s = 20</math> μF, <math>C_r = 21</math> nF, and <math>C_o = 47</math> μF.....</b>	<b>64</b>
<b>Fig. 3-8. Modeled and simulated converter state variable waveforms when a <math>i_o</math> step change is applied to the SRB converter in Fig. 3-1 on page 55 using the gate driving circuit in Fig. 3-4 on page 61. The control variable <math>t_{off} = 120</math> ns is set by the dc source V3 with the conversion ratio <math>t_{off}V_{ctoff} = 10^{-6}</math> sV in Fig. 3-4 on page 61. The theoretical model using (3-4) matches the simulated results in Simplis with</b>	

$V_{in} = 48\text{ V}$ ,  $t_{off} = 120\text{ ns}$ ,  $\Delta i_o = 20\text{ A}$ ,  $R_{load} = 0.125\ \Omega$ ,  $R_{Lo} = 0.05\ \Omega$ ,  $L_{oa} = L_{ob} = 1.5\ \mu\text{H}$ ,  $L_r = 80\text{ nH}$ ,  $C_s = 20\ \mu\text{F}$ ,  $C_r = 1\text{ nF}$ , and  $C_o = 47\ \mu\text{F}$ .....65

**Fig. 3-9.** The SRB converter in Fig. 3-1 on page 55 and the gate driving circuit in Fig. 3-4 on page 61 with (a) convergence using  $C_n = 500$  and with (b) divergence using  $C_n = 100$ . The waveforms were simulated in Simplis with  $V_{in} = 48\text{ V}$ ,  $t_{off} = 150\text{ ns}$ ,  $R_{load} = 0.125\ \Omega$ ,  $L_{oa} = L_{ob} = 1.5\ \mu\text{H}$ ,  $R_{Lo} = 0.02\ \Omega$ ,  $L_r = 80\text{ nH}$ ,  $C_r = 20\text{ nF}$ , and  $C_o = 47\ \mu\text{F}$ . A 1-V step change in the input voltage is applied at  $t = 1\text{ ms}$ . The control variable  $t_{off}$  is set by the dc source V3 with the conversion ratio  $t_{off}V_{ctoff} = 10^{-6}\text{ sV}$  in Fig. 3-4 on page 61.....68

**Fig. 3-10.** Minimum  $C_n$  defined in (1-3) on page 9 for convergence versus control variable  $t_{off}$  defined in Fig. 2-3 on page 23 normalized by  $1/f_r$  parametric with  $L_n$  defined in (1-4) on page 10 for the design of the SRB converter in Fig. 3-1 on page 55. The region with good convergence as shown in Fig. 3-8(a) is shaped in green. The graph was simulated using Simplis with  $V_{in} = 48\text{ V}$ ,  $R_{load} = 0.125\ \Omega$ ,  $L_r = 80\text{ nH}$ ,  $C_r = 20\text{ nF}$ , and  $C_o = 47\ \mu\text{F}$ . The control variable  $t_{off}$  is set by the dc source V3 with the conversion ratio  $t_{off}V_{ctoff} = 10^{-6}\text{ sV}$  in Fig. 3-4 on page 61. ....69

**Fig. 3-11.** The SRB converter in Fig. 3-1 on page 55 using the gate driving circuit in Fig. 3-4 on page 61 with (a) divergence using  $t_{off}f_r = 0.6$  and with (b) convergence using  $t_{off}f_r = 0.55$ . The waveforms were simulated in Simplis with  $V_{in} = 48\text{ V}$ ,  $R_{load} = 0.125\ \Omega$ ,  $L_{oa} = L_{ob} = 1.5\ \mu\text{H}$ ,  $C_n = 100$ ,  $R_{Loa} = R_{Lob} = 0$ ,  $L_r = 80\text{ nH}$ ,  $C_r = 20\text{ nF}$ , and  $C_o = 47\ \mu\text{F}$ . A 1 V step change in the input voltage is applied at  $t = 1\text{ ms}$ .....70

**Fig. 3-12.** Small-signal equivalent circuit of the SRB converter in Fig. 3-1 on page 55 is modeled using (3-4) on page 56 for the response of  $v_{Cs}$ . ....77

**Fig. 3-13.** The input-to- $v_{Cs}$  transfer function of the modeled and simulated converter in Fig. 3-1 on page 54 using the gate driving circuit in Fig. 3-4 on page 61. The theoretical result using (3-4) on page 56 matches the simulated one in Simplis with  $V_{in} = 48\text{ V}$ ,  $V_o = 5\text{ V}$ ,  $R_{load} = 0.125\ \Omega$ ,  $L_r = 80\text{ nH}$ ,  $L_{oa} = L_{ob} = 1.5\ \mu\text{H}$ ,  $C_s = 20\ \mu\text{F}$ ,  $C_r = 21\text{ nF}$ , and  $C_o = 47\ \mu\text{F}$ . The control variable  $t_{off} = 120\text{ ns}$  is set by the dc source V3 with the conversion ratio  $t_{off}V_{ctoff} = 10^{-6}\text{ sV}$  in Fig. 3-4 on page 61. ....80

**Fig. 3-14.** Small-signal equivalent circuit of the SRB converter in Fig. 3-1 on page 55 is modeled using (3-4) on page 56 for the response of  $v_{Co}$ . ....85

**Fig. 3-15. Small-signal equivalent circuit with the damping resistor  $R_e$  modeled in (3-32) of the SRB converter in Fig. 3-1 on page 55 modeled using (3-4) on page 56 for the response of  $v_{Co}$ . .....85**

**Fig. 3-16. The input-to-output transfer function of the modeled and simulated converter in Fig. 3-1 on page 55. The theoretical result using (3-4) on page 56 matches the simulated one in Simplis with  $V_{in} = 48\text{ V}$ ,  $V_o = 5\text{ V}$ ,  $R_{load} = 0.125\ \Omega$ ,  $L_r = 80\text{ nH}$ ,  $L_{oa} = L_{ob} = 1.5\ \mu\text{H}$ ,  $C_s = 20\ \mu\text{F}$ ,  $C_r = 21\text{ nF}$ , and  $C_o = 47\ \mu\text{F}$ . .....87**

**Fig. 3-17. (a) The input-to-output transfer functions of the SRB and SCB converters in Fig. 3-1 on page 55 with  $V_{in} = 48\text{ V}$ ,  $V_o = 5\text{ V}$ ,  $R_{load} = 0.125\ \Omega$ ,  $L_{oa} = L_{ob} = 1.5\ \mu\text{H}$ ,  $L_r = 80\text{ nH}$ ,  $C_s = 20\ \mu\text{F}$ ,  $C_r = 21\text{ nF}$ , and  $C_o = 47\ \mu\text{F}$ . (b) The ratio of the SRB pole frequency to the SCB pole frequency modeled by (3-35). (c) The ratio of the Q value of the SRB converter to that of the SCB converter parametric with  $R_{load}/Z_o$  modeled by (3-37). .....88**

**Fig. 3-18. The control-to-output transfer function of the modeled and simulated converter in Fig. 3-1 on page 55. The theoretical result using (3-4) on page 56 matches the simulated one in Simplis with  $V_{in} = 48\text{ V}$ ,  $V_o = 5\text{ V}$ ,  $R_{load} = 0.125\ \Omega$ ,  $L_r = 80\text{ nH}$ ,  $L_{oa} = L_{ob} = 1.5\ \mu\text{H}$ ,  $C_s = 20\ \mu\text{F}$ ,  $C_r = 21\text{ nF}$ , and  $C_o = 47\ \mu\text{F}$ . .....90**

**Fig. 3-19. The output impedance of the modeled and simulated converter in Fig. 3-1 on page 55. The theoretical result using (3-4) on page 56 matches the simulated one in Simplis with  $V_{in} = 48\text{ V}$ ,  $V_o = 5\text{ V}$ ,  $R_{load} = 0.125\ \Omega$ ,  $L_{oa} = L_{ob} = 1.5\ \mu\text{H}$ ,  $L_r = 80\text{ nH}$ ,  $C_s = 20\ \mu\text{F}$ ,  $C_r = 21\text{ nF}$ , and  $C_o = 47\ \mu\text{F}$ . .....91**

**Fig. 4-1. Normalized resonant tank energy  $E_{tank}$  calculated with (4-1) versus normalized load current  $J$ . .....97**

**Fig. 4-2. Voltage gain  $M$  calculated with (4-4) versus control variable  $t_{off}$  defined in Fig. 2-3 on page 23 normalized by  $T_r$ . .....98**

**Fig. 4-3. (a) Normalized switching frequency versus  $J$  calculated with (4-8). The curves shift higher as  $t_{offr}$  reduces from 0.5 to 0.2. The curves for  $t_{offr} < 0.2$  are not drawn as their maximum voltage gain is smaller than 0.05. (b) The ratio of switching frequency with  $t_{offr} = 0.5$  to switching frequency with  $t_{offr} = 0.2$  calculated with (4-8). The switching frequency curve can be approximated to the curve with  $t_{offr} = 0.5$  for simple calculation. ....102**

**Fig. 4-4. Normalized switching frequency versus  $J$  as design curve calculated with (4-9). .....103**

**Fig. 4-5. Capacitance ratio  $C_n$  calculated with (4-15) versus normalized load current  $J$  parametric with the**

series capacitor voltage ripple $\Delta V_{Cs}/V_{in}$ .....	105
<b>Fig. 4-6. Inductance ratio <math>L_n</math> calculated with (4-18) versus normalized load current <math>J</math> parametric with the output inductor current ripple <math>\Delta I_{Lo}/I_o</math> and the normalized control variable <math>t_{offr}</math>. .....</b>	<b>106</b>
<b>Fig. 4-7. Normalized RMS current stresses of the switches (a) <math>S_{a1}</math> (<math>S_{b1}</math>) calculated with (4-20), (b) <math>S_{a2}</math> calculated with (4-25), and (c) <math>S_{b2}</math> calculated with (4-26) in Fig. 3-1 on page 55. Large normalized control variable <math>t_{offr}</math> results in larger stress of <math>S_{a1}</math> because more power is delivered from the source to load. A large normalized load condition <math>J</math> leads to a larger voltage gain given the same <math>t_{offr}</math> and therefore higher current stress. The current stress variance of <math>S_{a2}</math> and <math>S_{b2}</math> are similar to the stress of <math>S_{a1}</math>. .....</b>	<b>109</b>
<b>Fig. 4-8. Peak current of resonant inductor normalized by the load current calculated with (4-27) versus the normalized load current. The resonant inductor current stress is load-dependent benefiting light-load efficiency. Larger characteristic impedance <math>Z_r</math> design helps reduce the peak resonant current. ....</b>	<b>110</b>
<b>Fig. 4-9. Sequential design procedure of the SRB converter in Fig. 4-10. A design example using this procedure is in Table 4-3 using specifications in Table 4-2.....</b>	<b>112</b>
<b>Fig. 4-10. Prototype of the Series-Resonator Buck (SRB) converter using the design procedure in Fig. 4-9, the specifications in Table 4-2, and the component values in Table 4-3. ....</b>	<b>115</b>
<b>Fig. 4-11. (a) Experimental voltage waveforms of all the switches from the prototype in Fig. 4-10 measured by the oscilloscope; measured and modeled normalized load current versus (b) normalized control signal using (2-26) and (c) normalized switching frequency using (4-9).....</b>	<b>116</b>
<b>Fig. 4-12. (a) Efficiency and (b) switching frequency modeled by (4-9) of the SRB prototype in Fig. 4-10 while keeping <math>V_{in} = 48</math> V and <math>V_o = 7</math> V (hollow circle: <math>f_s</math> in simulation, solid circle: <math>f_s</math> in experiment, and hollow square: <math>t_{off}</math> in simulation, solid square: <math>t_{off}</math> in experiment). The simulation utilized a non-ideal switch model from EPC and ideal passive components adding 2 m<math>\Omega</math> inductor ESR.....</b>	<b>118</b>
<b>Fig. 4-13. (a) Total loss and (b) converter size comparison between the SRB converter in Fig. 4-10 and the SCB converter with the same full load condition in Table I. The simulation utilized non-ideal switch models from EPC and ideal passive components adding 2 m<math>\Omega</math> inductor ESR. A heatsink (374024B60023 made by Aavid Thermalloy) is added for the SCB converter to keep the switch's average junction temperature the same. The SRB converter reduces switch loss by a factor of 2. Its resonant inductor size is less than one-third of the heatsink size in the SCB converter.....</b>	<b>119</b>

**Fig. 5-1. (a) Schematic of the SRB converter with the resonant inductor being highlighted; (b) simulated resonant inductor current and voltage waveforms.....123**

**Fig. 5-2. (a) Conventional rectangular-window inductor with significant current crowding; and (b) rhombus-window inductor with better current distribution. The inductor specifications are labeled in Fig. 5-13. The inductor current excitation is 36A peak current at 2MHz. The type is set as “Solid”. It was simulated using eddy current mode in Ansys Maxwell 2D. ....123**

**Fig. 5-3. Measured core loss density versus peak ac flux density at 2MHz. ....124**

**Fig. 5-4. Front view and 3-D view of the inductor with rhombus window. Key design parameters are listed above.....126**

**Fig. 5-5. (a) Magnetic circuit model of the rhombus-window inductor. (b) Simulated (dash line) and calculated (solid line) inductance versus the inductor air gap parametric with the window height ratio  $k_y$  with inductor specifications  $hw = 100 \mu\text{m}$ ,  $ww = 3 \text{ cm}$ ,  $lc = 9 \text{ cm}$ ,  $tc = 3 \text{ cm}$ ,  $\mu_r = 900$ ,  $dx = 1 \text{ mm}$ ,  $wc = 9 \text{ cm}$ , and  $hc = 6 \text{ cm}$  labeled in Fig. 5-4. The inductor current excitation is 36A peak current at 2MHz. The type is set as “Solid”. The inductance was simulated using eddy current mode in Ansys Maxwell 2D. ....126**

**Fig. 5-6. Inductor length  $lc$  versus design variables the core thickness  $tc$  labeled in Fig. 5-4. The inductor current excitation is 36A peak current at 2MHz. The type is set as “Solid”. The inductance was simulated using eddy current mode in Ansys Maxwell 2D. ....128**

**Fig. 5-7. The rhombus-window winding loss versus design variables the window height ratio  $k_y$  and the core thickness  $tc$  labeled in Fig. 5-4. The inductor current excitation is 36A peak current at 2MHz. The type is set as “Solid”. The copper loss was simulated using eddy current mode in Ansys Maxwell 2D and current specifications in Table 5-1.....129**

**Fig. 5-8. AC flux density in the cross-sectional area of the rhombus-window inductor with  $hw = 100 \mu\text{m}$ ,  $ww = 3 \text{ cm}$ ,  $lc = 9 \text{ cm}$ ,  $tc = 3 \text{ cm}$ ,  $k_y = 0.5$ ,  $\mu_r = 900$ ,  $dx = 1 \text{ mm}$ ,  $wc = 9 \text{ cm}$ , and  $hc = 6 \text{ cm}$  labeled in Fig. 5-4. The inductor current excitation is 36A peak current at 2MHz. The type is set as “Solid”. The flux was simulated using eddy current mode in Ansys Maxwell 2D using the current and material specifications in Table 5-1. ....130**

**Fig. 5-9. Inductor core loss versus design variables the window height ratio  $k_y$  and the core thickness  $tc$  labeled**

in Fig. 5-4. The inductor current excitation is 36A peak current at 2MHz. The type is set as “Solid”. The core loss was simulated using eddy current mode in Ansys Maxwell 2D and specifications in Table 5-1. ....131

Fig. 5-10. Design flowchart of the rhombus-window inductor labeled in Fig. 5-4 on page 126. A design example using specifications in Table 5-1 is shown in Fig. 5-11 and Fig. 5-12. ....133

Fig. 5-11. Design curves of inductor loss versus (a) footprint and (b) size meeting the inductor specifications in Table 5-1 as part of the design procedure in Fig. 5-10. The inductor loss was simulated using eddy current mode in Ansys Maxwell 2D. ....134

Fig. 5-12. (a) Small footprint design and (b) small volume design meeting the inductor specifications in Table 5-1 and following the design procedure in Fig. 5-10. ....135

Fig. 5-13. Loss comparison between the conventional rectangular-window inductor and the rhombus-window inductor given the same component size. The inductor loss was simulated using eddy current mode in Ansys Maxwell 2D. The current and material specifications are in Table 5-1. ....136

Fig. 5-14. (a) Prototype of the Series-Resonator Buck (SRB) converter using (b) the rhombus-window inductor using the inductor specifications in Fig. 5-12, Table 5-1 and following the design procedure in Fig. 5-10. The converter was with  $V_{in} = 48\text{ V}$ ,  $V_o = 5\text{ V}$ ,  $R_{load} = 0.125\ \Omega$ ,  $L_{oa} = L_{ob} = 0.3\ \mu\text{H}$ ,  $L_r = 80\text{ nH}$ ,  $C_s = 20\ \mu\text{F}$ ,  $C_r = 21\text{ nF}$ , and  $C_o = 4\ \mu\text{F}$ . ....137

Fig. 5-15. Measured voltage and inductor waveforms labeled in Fig. 5-1 on page 123 of the resonant inductor in Fig. 5-14 and specifications in the caption of Fig. 5-14 using oscilloscope MSO5104B. ....137

# List of Tables

**Table 2-1. Specifications of the SRB prototype.....46**

**Table 3-1. Numerical examples of variables in (3-22) using  $V_{in} = 48 V$ ,  $R_{load} = 0.125 \Omega$ ,  $R_{Lo} = 0.05 \Omega$ ,  $L_r = 80 nH$ ,  $L_{oa} = L_{ob} = 1.5 \mu H$ ,  $C_s = 20 \mu F$ ,  $C_r = 21 nF$ , and  $C_o = 47 \mu F$  .....78**

**Table 3-2. Numerical examples of variables from (3-22) to (3-30) using  $V_{in} = 48 V$ ,  $R_{load} = 0.125 \Omega$ ,  $R_{Lo} = 0.005 \Omega$ ,  $L_r = 80 nH$ ,  $L_{oa} = L_{ob} = 1.5 \mu H$ ,  $C_s = 20 \mu F$ ,  $C_r = 21 nF$ , and  $C_o = 47 \mu F$  .....82**

**Table 4-1. Component stresses in Fig. 3-1 on page 55 of the SRB prototype in Fig. 4-10 with components in Table 4-3.....111**

**Table 4-2. Specifications of the SRB prototype fed into the design procedure in Fig. 4-9 and resulting in the design in Table 4-3 and the prototype in Fig. 4-10 .....113**

**Table 4-3. Sequential design procedure of the SRB prototype in Fig. 4-10 using the design procedure in Fig. 4-9 and the specifications in Table 4-2.....114**

**Table 5-1. Specifications labeled in Fig. 5-4 on page 126 and fed into the inductor design procedure in Fig. 5-10 .....132**

# Chapter 1 Introduction

## Nomenclature

Symbol	Description
$C_n$	Capacitance ratio of the resonant capacitor to the series capacitor in (1-3)
$C_o$	Output capacitor in Fig. 1-2
$C_r$	Resonant capacitor in Fig. 1-8
$C_s$	Series capacitor in Fig. 1-8
$f_r$	Resonant frequency of the resonant tank in (1-1)
$J$	Normalized load current in (1-2)
$I_o$	Converter output current consumed by the load in Fig. 1-2
$L_r$	Resonant inductor in Fig. 1-8
$L_{oa}$	Output inductor of the upper phase in Fig. 1-2
$L_{ob}$	Output inductor of the lower phase in Fig. 1-2
$L_n$	Inductance ratio of the resonant inductor to the output inductor in (1-4)
$M$	Voltage gain in Fig. 1-12
$S_{a1}$	High-side switch of the upper phase in Fig. 1-2
$S_{b1}$	High-side switch of the lower phase in Fig. 1-2
$S_{a2}$	Low-side switch of the upper phase in Fig. 1-2
$S_{b2}$	Low-side switch of the lower phase in Fig. 1-2
$V_{in}$	Input voltage in Fig. 1-2
$V_{inMax}$	Minimum input voltage in Fig. 1-2
$V_{inMin}$	Maximum input voltage in Fig. 1-2
$V_o$	Output voltage in Fig. 1-2
$Z_r$	Characteristic impedance of the resonant tank in (1-2)

This chapter introduces the background of the 48 V power delivery system and its design challenges. Interleaved multiphase buck converters have been adopted for point-of-load

regulation. The Series-Capacitor Buck (SCB) converter shows superiority compared with the conventional two-phase buck converter but hard switching hindered efforts to reduce volume via increased switching frequency. This work suggests replacing the series capacitor with a series resonator cell. Major benefits with a series resonator cell are shown. A new topology, Series-Resonator Buck (SRB) converter, is presented. The dissertation outline follows.

### 1.1 The 48 V Power Delivery System

The 48 V power delivery system is increasingly popular. Take the data center as an example. Fig. 1-1 shows a typical power delivery architecture for a data center. Power comes from a transmission line, and then is sent into the server halls of a data center. A solid-state transformer steps the voltage down from 4.9 kV to 400 V. The 400 V dc voltage is delivered into the server rack level, and further stepped down to a 48 V dc voltage bus. This voltage bus is housed at the server rack level.

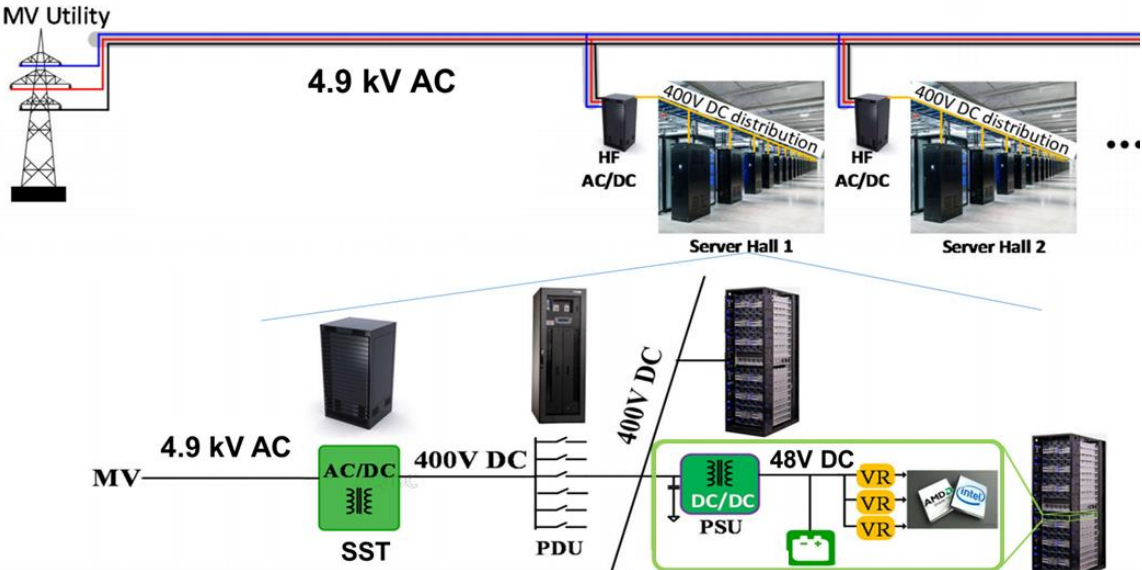


Fig. 1-1. Power delivery architecture in a data center. The 48 V power delivery system is highlighted.

As shown in Fig. 1-1, the 48 V bus is normally connected to a battery, which is a backup source in case of emergency. As a result, the bus voltage fluctuates around 48 V depending on the battery voltage. The 48V power system is housed at the board level. There are multiple voltage regulators to step down the voltage to power the CPU, GPU, and other loads. In a conventional power distribution system, a 12 V bus voltage is used rather than the 48 V shown here.

Compared with a conventional 12V system, the 48 V system has several benefits including:

- Smaller power distribution loss;
- Smaller conductor size requirement;
- Smaller conductor weight and cost.

Research projects designing the 48 V power delivery system are increasingly popular. Major challenges are in the development of high-performance 48 V point-of-load converters, such as high conversion ratio, high current, high power density, and wide variable gain for the regulation requirement.

## **1.2 Limitation of the Series-Capacitor Buck Converter**

High step-down dc/dc converters are widely adopted in a variety of areas such as industrial, automotive, and telecommunication [1]-[35].

Interleaved multiphase buck converters have been adopted for point-of-load regulation below 3.3 V and above 10 A from input voltage exceeding 12 V [1]-[17]. The conventional two-phase buck converter is shown in Fig. 1-2 (a). The Series-Capacitor Buck (SCB) converter was synthesized by adding a series capacitor in a two-phase buck converter, and it is shown in Fig. 1-2 (b) [1]-[4].

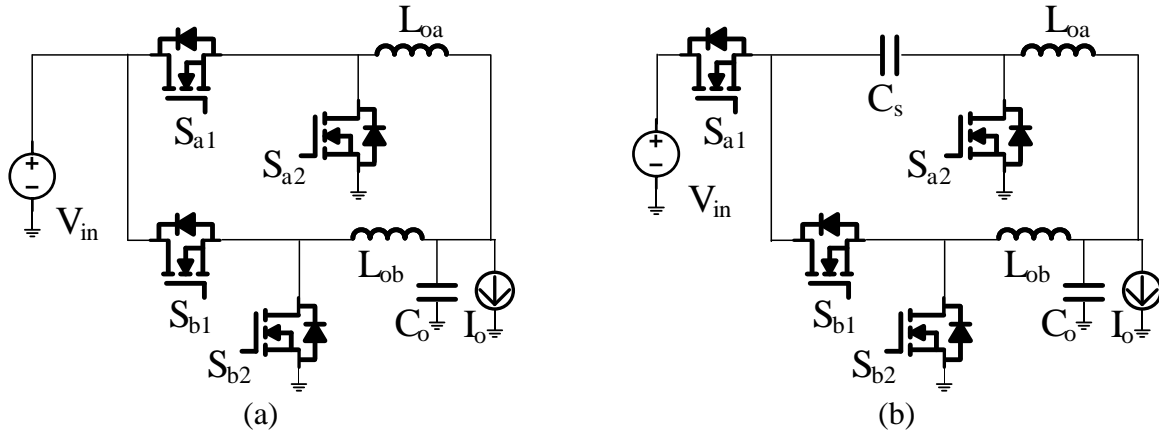


**Fig. 1-2. (a) Schematic of the two-Phase Buck converter and (b) schematic of the Series-Capacitor Buck converter.**

The series capacitor  $C_s$  is equivalent to a dc source with a voltage equal to half of the input voltage. This capacitor lowers the low-side switches' voltage stress in the steady state. The SCB is able to utilize a smaller-voltage-rating MOSFET with smaller on-resistance and smaller equivalent output capacitance.

The series capacitor  $C_s$  also reduce switches' voltage stress during the switching period shown in Fig. 1-3 (a). The switching loss is proportional to the square of  $\Delta V$ . The voltage change  $\Delta V$  represents the voltage difference of the switch between the beginning and the end of a turning-on

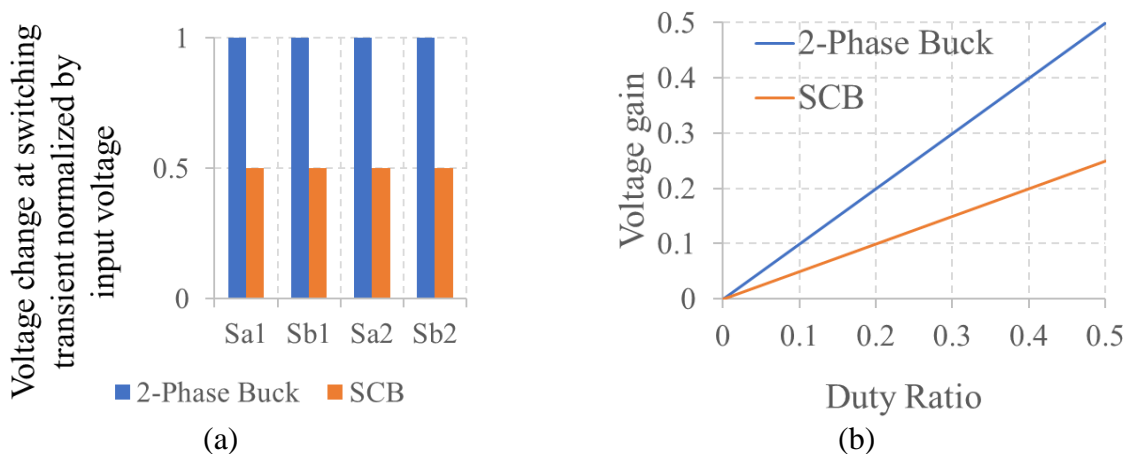


**Fig. 1-3. The comparisons of (a) voltage change at switching transient normalized by the input voltage and (b) duty ratio in the 2-phase Buck converter in Fig. 1-2 and the Series-Capacitor Buck converter in Fig. 1-2.**

or turning-off period. Compared with a conventional two-phase buck converter, the switching loss in the SCB is reduced due to the smaller  $\Delta V$ .

The SCB doubles the duty ratio, as compared with the conventional two-phase buck converter. A larger duty ratio in a high step-down converter is preferred, as it facilitates control of the switches' on time.

The extra side benefit of the series capacitor is that it equalizes the phase currents. In a two-phase buck converter, the inductor currents are typically unbalanced due to the component tolerance issue.

The SCB has been commercialized, and is becoming increasingly popular in recent years. Fig. 1-4 shows an evaluation board of the SCB developed by Texas Instruments. It carries an SCB-based module with integrated switch and gate-driving circuits. It is designed for small-size, low-voltage applications from a 12-V input rail. Typical applications include telecom, base station, storage, hub routers, and other networking equipment.

Hard switching has hindered efforts to reduce volume via increased switching frequency although a monolithically integrated SCB converter has boosted current density exceeding 60

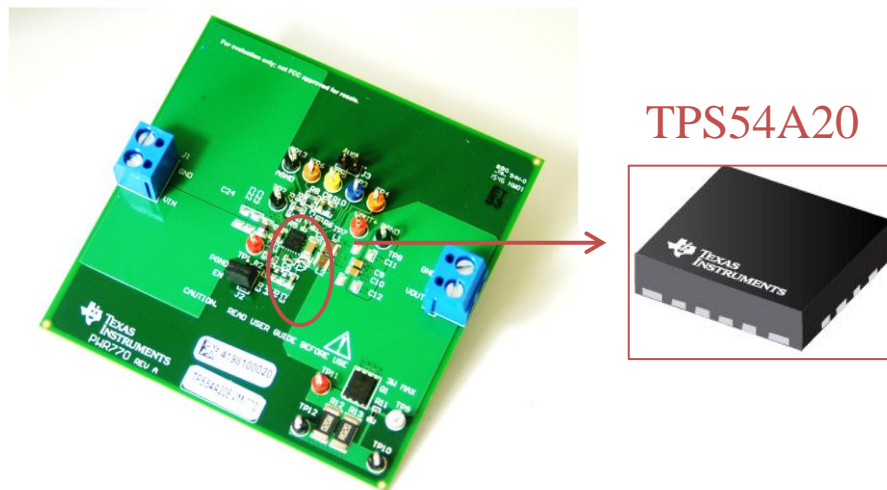
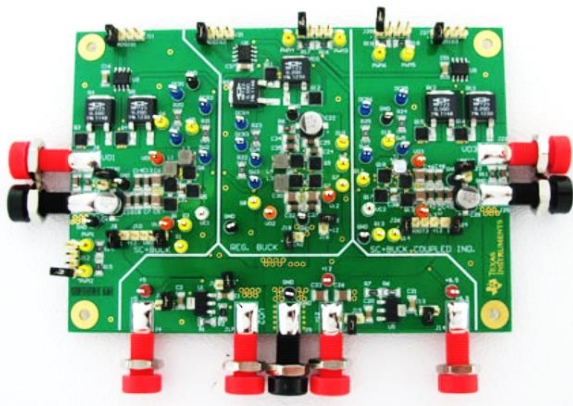


Fig. 1-4. The evaluation board of the TPS54A20 Series-Capacitor Buck converter [18].

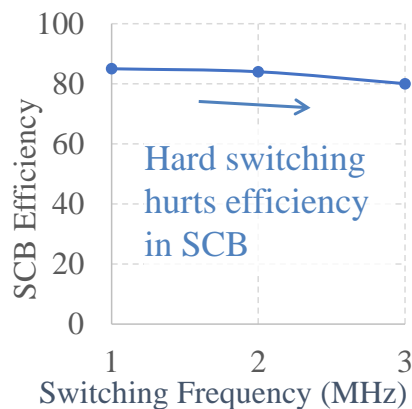
A/cm<sup>3</sup> [5]. The authors in [6] designed the prototype shown in Fig. 1-5 (a) to measure the efficiency at MHz-level switching frequencies. The switching loss caused the efficiency to drop by 5% as the frequency increased from 1 MHz to 3 MHz as shown in Fig. 1-5 (b).

Coupled inductors, tapped inductors, and resonant tanks were suggested in [5]-[11], [22]-[29] to enable soft switching, but switch voltage stresses exceeded 1.6 times the input unless snubbers or extra switches were added.

Some other works suggest that transformers can be utilized to achieve soft switching and a high step-down ratio [30] – [35], such as the LLC converter in [32] – [33] and the sigma converter in [34]. Those designs normally enable a wide voltage gain with soft-switching capability. However, the transformer requires lots of design effort. The cost is high. GaNFET features small on-resistance and small switch equivalent output capacitance, and therefore has been widely adopted for high-frequency converters [34] – [39]. Switched-capacitor converters are growing popular in recent years because of the high energy density of ceramic capacitors [40] – [71], [79] – [81], as compared to inductor-based converters [72] – [78]. Recent works on 48 V switched-capacitor converters hit a power density larger than 1000 W/in<sup>3</sup> for a gain ratio of 48:6 [80] – [81],



(a)



(b)

**Fig. 1-5. (a) Prototype of the SCB converter and (b) converter efficiency versus switching frequency in [6].**

and  $300 \text{ W/in}^3$  for a gain ratio of 48:1 [82] – [83]. The latest transformer-based solutions focus on the size reduction of the magnetic components [84] – [87]. Some new architectures for 48 V power delivery include a virtual intermediate bus [88], a multi-stack configuration [89], differential power processing [90], and a three-phase configuration [91].

### 1.3 Introduction of Series-Resonator Cell

The major barrier to efficiency improvement in the SCB converter is hard switching. A series resonator is therefore suggested to replace the series capacitor in the SCB converter shown in Fig. 1-6 (a).

A Series-Resonator Buck (SRB) converter [92] – [95] is synthesized by adding a resonant

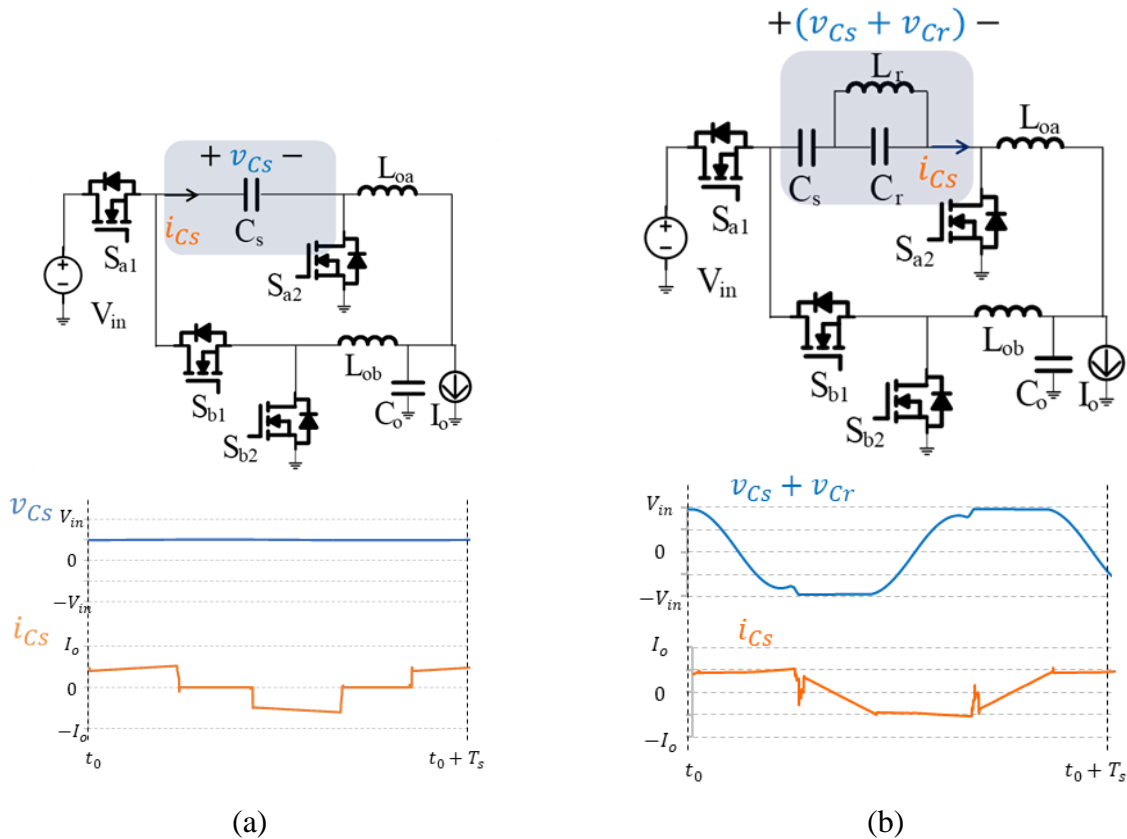


**Fig. 1-6. Key voltage and current waveforms comparison between the (a) Series-Capacitor Buck converter and (b) Series-Resonator Buck converter.**

tank in series with series capacitor  $C_s$  in Fig. 1-6 (b). The series-resonator cell includes the series capacitor  $C_s$  and the parallel resonant tank ( $L_r$  and  $C_r$ ). In a series-resonator cell, the resonant tank order could be any integer equal to or larger than 2.

The resonant tank formed by  $L_r$  and  $C_r$  in Fig. 1-6 (b) generates the resonant voltage  $v_{Cr}$  that opens up the opportunity for drain-to-source voltages  $v_{dsa1}$  and  $v_{dsb1}$  to reach zero for ZVOn of switches  $S_{a1}$  and  $S_{b1}$ . This also creates the resonant current  $i_{Lr}$  that opens up the opportunities for the current  $i_{a2}$  and  $i_{b2}$  to reach zero for ZCOff of switches  $S_{a2}$  and  $S_{b2}$ .

The soft switching enabled by the series-resonator cell minimizes the switching loss in the SRB converter. The switching loss reduction is highlighted in Fig. 1-7. The blue color represents the switching loss in both SCB and SRB converters at the same operating point. The switching loss in a conventional SCB converter accounts for about 50% of the overall converter loss. The

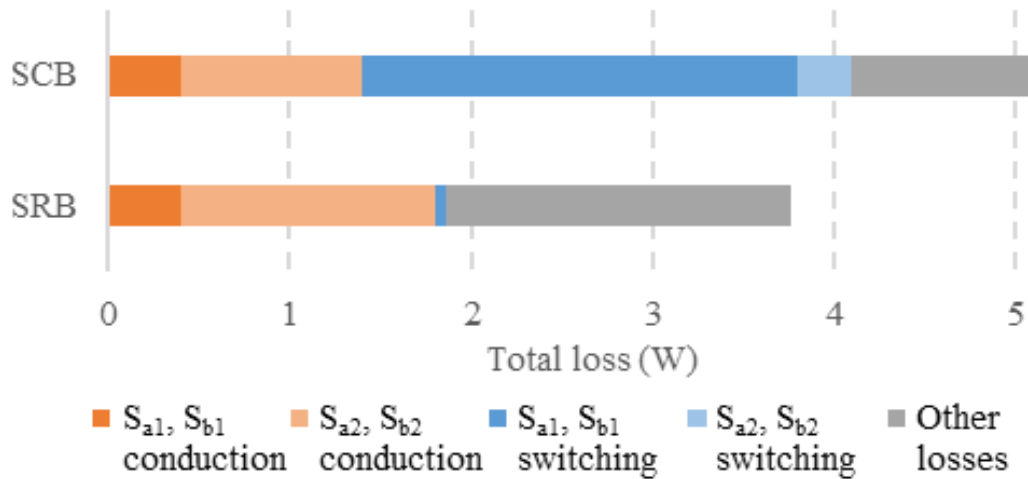


**Fig. 1-7. Loss breakdown comparison between the Series-Capacitor Buck converter and Series-Resonator Buck converter shown in Fig. 1-6. The simulation utilized non-ideal switch models (EPC2049 for the SCB converter and EPC2045 for the SRB converter) from EPC, output inductors adding 2 mΩ ESR (representing the loss of the inductor VLM10555T-1R2M100-3 calculated by the manufacturer’s loss simulator), and resonant inductor adding 9 mΩ ESR (representing the loss simulated by the resonant inductor model described in [95]). Both converters operate at  $V_{in} = 48 V$ ,  $V_o = 7 V$ ,  $I_o = 20 A$ ,  $f_s = 2 MHz$  with  $L_{oa} = L_{ob} = 1.2 \mu H$ ,  $L_r = 150 nH$ ,  $C_r = 12 nF$ , and  $C_o = 20 \mu F$ .**

switching loss in the SRB converter is much smaller, thanks to the soft switching enabled by the series-resonator cell -- it accounts for only 3% of the overall converter loss.

The series-resonator cell enables ZVOn of the high-side switches and both ZVOn and ZCOff of the low-side switches. The soft-switching feature reduces switching loss from 50% overall loss in the SCB to less than 3% overall loss in the SRB.

## 1.4 Four Parameters for the SRB Converter Design

Overall, there are six energy storage components in the SRB converter as highlighted in Fig. 1-8. Output capacitor  $C_o$  is designed to meet the steady-state output ripple requirement. Output inductors  $L_{oa}$  and  $L_{ob}$  have the same inductance for equalized current sharing. As a result, there are four energy storage component values to be designed. There are four degrees of freedom.

The first two design variables are the resonant frequency of resonant tank  $f_r$  and the characteristic impedance of resonant tank  $Z_r$  or the normalized load current:

$$f_r = 1/(2\pi\sqrt{L_r C_r}) \quad (1-1)$$

$$Z_r = \sqrt{L_r/C_r}, \quad J = \frac{I_o}{V_{in}/Z_r} \quad (1-2)$$

The design of resonant tank  $L_r$  and  $C_r$  can be calculated by (1-1) and (1-2).

The third design variable is capacitance ratio  $C_n$  defined by

$$C_n = C_s/C_r \quad (1-3)$$

Normally, resonant capacitor  $C_r$  resonates with resonant inductor  $L_r$ . The resonant capacitor is smaller than the series capacitor  $C_s$  which typically functions as a dc voltage source. As a result, the capacitance ratio is normally larger than 100. Modeling the transient response of this family of quasi-resonant converters is challenging due to significant current ripples [96] – [113], and the capacitance ratio influences the transient performance of the SRB converter.

The fourth design variable is the inductance ratio  $L_n$ , which is designed by:

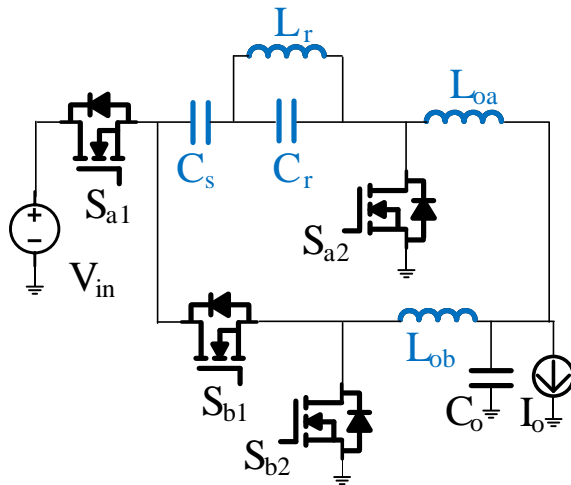
$$L_n = L_{oa}/L_r = L_{ob}/L_r \quad (1-4)$$

This inductance ratio impacts the cutoff frequency of the output filters. It determines the current ripple of the output inductor. The high-frequency design has been a challenge due to significant core loss and ac winding loss [114] – [149]. The magnetic components account for more than 50% of the volume of the converter in the Series-Resonator Buck converter. Proper inductor design is crucial for the converter's power density and efficiency. The design variables impact the converter in terms of both steady-state performance and transient-state performance. Multiple design tradeoffs are involved.

## 1.5 Contributions of This Dissertation

### 1.5.1 Series-Resonator Buck Converter

A Series-Resonator Buck (SRB) converter [92] – [95] with soft turn-on, as shown in



$$f_r = \frac{1}{2\pi\sqrt{L_r C_r}}$$

$$Z_r = \sqrt{\frac{L_r}{C_r}}$$

$$C_n = \frac{C_s}{C_r}$$

$$L_n = \frac{L_{oa}}{L_r} = \frac{L_{ob}}{L_r}$$

Fig. 1-8. Four design variables in (1-1), (1-2), (1-3), and (1-4) in the Series-Resonator Buck converter.

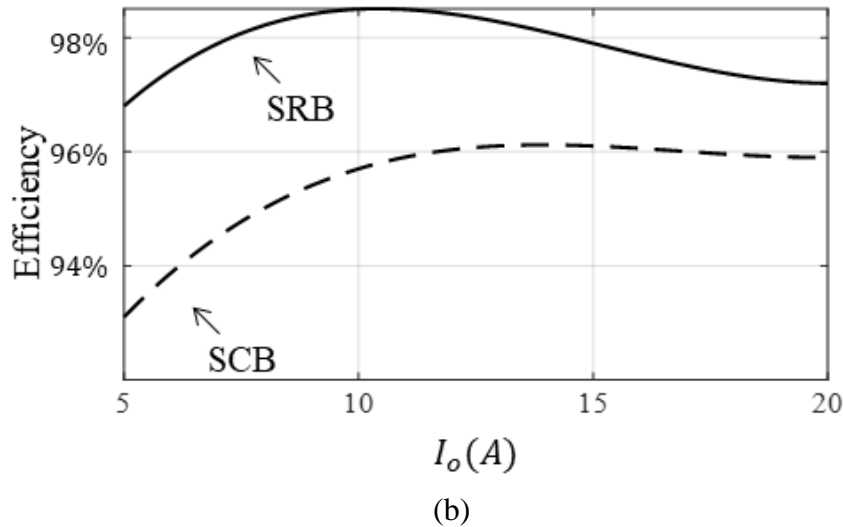
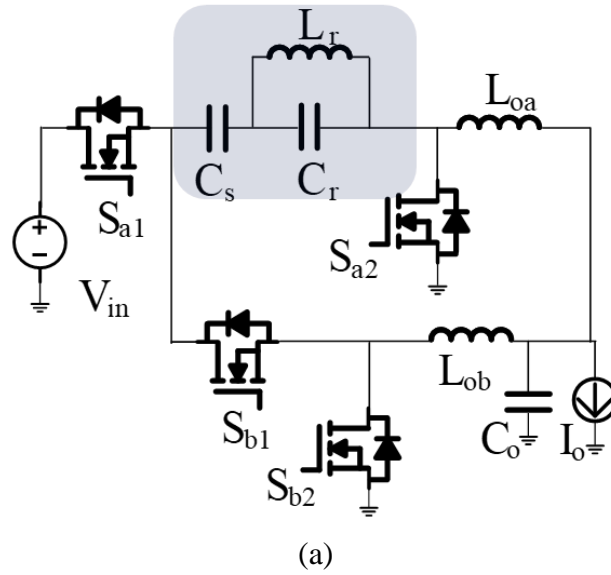
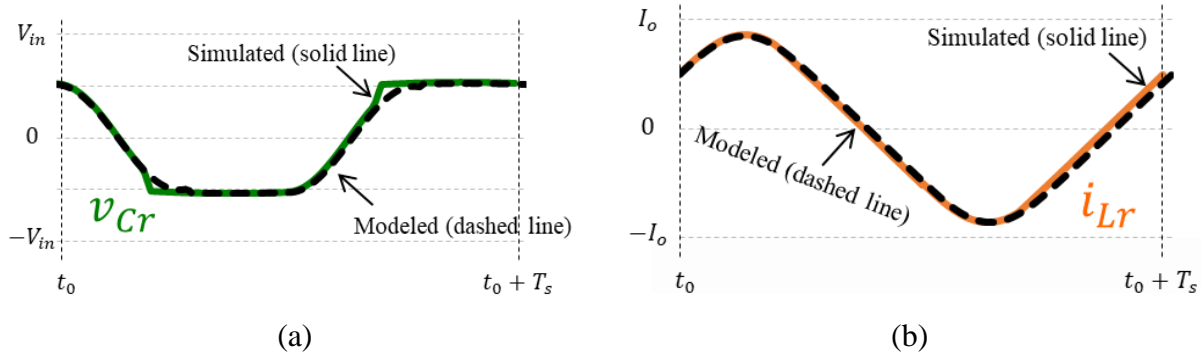


Fig. 1-9. (a) The SRB converter is synthesized by replacing the series capacitor in the SCB converter in Fig. 1-6(a) with the series resonator highlighted in the schematic. (b) The SRB converter improves efficiency by 1.1% at the full-load condition benefiting from the soft switching introduced by the series resonator. The simulation utilized non-ideal switch models (EPC2049 for the SCB converter and EPC2045 for the SRB converter) from EPC and ideal passive components adding 2 m $\Omega$  inductor ESR. Both converters operate at  $V_{in} = 48\text{ V}$ ,  $V_o = 7\text{ V}$ ,  $I_o = 20\text{ A}$ ,  $f_s = 2\text{ MHz}$  with  $L_{oa} = L_{ob} = 1.2\text{ }\mu\text{H}$ ,  $L_r = 150\text{ nH}$ ,  $C_r = 12\text{ nF}$ , and  $C_o = 20\text{ }\mu\text{F}$ .

Fig. 1-9(a), is synthesized by adding a resonant tank in series with series capacitor  $C_s$ . The presence of the resonant tank in the SRB converter reduces all switches' voltages to zero at turn-



**Fig. 1-10. The modeled waveforms match the simulated ones in the steady-state in the SRB converter in Fig. 1-6. The waveforms were simulated using ideal components in LTspice with  $V_{in} = 48\text{ V}$ ,  $V_o = 7\text{ V}$ ,  $I_o = 20\text{ A}$ ,  $L_{oa} = L_{ob} = 1.2\ \mu\text{H}$ ,  $L_r = 150\text{ nH}$ ,  $C_r = 12\text{ nF}$ , and  $C_o = 4\ \mu\text{F}$ . The gate signals were illustrated in Fig. 2-3(b) with  $f_s = 2\text{ MHz}$  and  $t_{off} = 120\text{ ns}$ .**

on, and all low-side switches' currents to zero before turn-off.

A 2-MHz prototype with a peak efficiency of 98.5%, 48 V at the input and 7 V, 20 A at the output was built. The efficiency curve in Fig. 1-9(a) compares the measured SRB converter efficiency and the benchmark SCB efficiency. The full-load efficiency is improved by 1.1%, and the light-load efficiency increases by 3.7%.

### 1.5.2 Steady-State Analysis of the SRB Converter

The existing steady-state model of the SCB converter cannot be applied to the SRB converter, as the switching ripples are reshaped by the series resonator. A steady-state model of the SRB converter is built to calculate the voltage gain, component peak voltages, and resonant inductor peak current. Fig. 1-10 compares the modeled waveforms and simulated waveforms from LTspice. The error is less than 1% at the nominal operating point, and is less than 3% at the worst case (minimal-load condition). The steady-state model assumes the inductor peak-to-peak current ripples and the capacitor peak-to-peak voltage ripples are less than 20% of their dc values.

The expectations were validated by a 2-MHz converter with a peak efficiency of 98.5%, 48 V

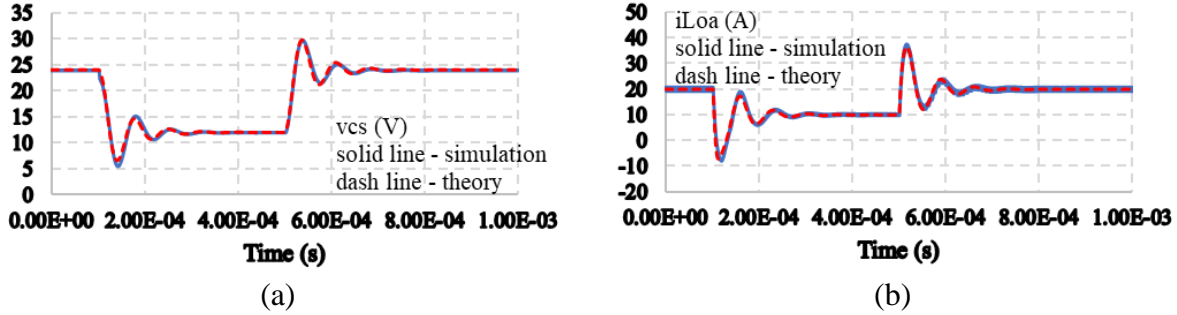


Fig. 1-11. The modeled waveforms match the simulated ones in the transient state in the SRB converter in Fig. 1-6. The waveforms were simulated in Simplis with  $V_{in} = 48\text{ V}$ ,  $\Delta V_{in} = 24\text{ V}$ ,  $V_o = 5\text{ V}$ ,  $L_r = 80\text{ nH}$ ,  $L_{oa} = L_{ob} = 1.5\text{ }\mu\text{H}$ ,  $C_r = 20\text{ nF}$ , and  $C_o = 47\text{ }\mu\text{F}$ . The control variable  $t_{off} = 120\text{ ns}$  is set by the dc source V3 with the conversion ratio  $\frac{t_{off}}{V_{ctoff}} = 10^{-6} \frac{\text{s}}{\text{V}}$  in Fig. 3-4 on page 61.

at the input and 7 V, 20 A at the output. The measured voltage waveforms, efficiency, switching frequency, and regulating variable ( $t_{off}$  of the low-side switches) were within 0.5% of the expectations.

### 1.5.3 Transient-State Analysis of the SRB Converter

Modeling the SRB converter is challenging because the resonant frequency of the resonant elements is in the same order as the switching frequency, and conventional state-space modeling is not applicable. The large-signal and small-signal models are built to model the transient response of the SRB converter based on the concept of generalized state-space averaging. Fig. 1-11 compares the modeled waveforms and simulated waveforms from Simplis. The transient-state model assumes the inductor peak-to-peak current ripples are less than 20% of their dc value.

The large-signal model of the SRB converter characterizes the low-frequency behavior of the low-pass filters with the series capacitor and the high-frequency behavior of the resonant elements. The large-signal model reveals the divergence response that occurs due to the oscillation between the series-capacitor  $C_s$  and the output inductors  $L_o$ . A design recommendation of  $C_n$  is suggested to avoid non-convergence.

The major transfer functions are derived from the small-signal model of the SRB converter, and are compared with those in the SCB converter. The small-signal model reveals a damping effect caused by the resonant elements in the input-to-output transfer function. The double poles from the output filter move to high frequency, and the Q value drops in the SRB converter.

The resonant tank in the SRB converter also adds a negative damping effect to the series resonance between series capacitor  $C_s$  and output inductors  $L_o$ . The oscillation is reinforced and may lead to instability.

#### **1.5.4 Sequential Design Methodology of the SRB Converter**

The converter specifications such as voltage gain, switching frequency, and component stresses couple with multiple design variables in the SRB converter. The existing design methodology relies on extensive iterations to find the optimum design point. A sequential design procedure helps reduce the time spent on simulations and design iterations.

Fig. 1-12 shows the sequential design procedure of the SRB converter suggested by this work. The design  $J_{max} = \sqrt{2}$  minimizes the normalized resonant tank energy by balancing the peak energy in resonant elements  $L_r$  and  $C_r$ . The gain equation models the load-dependent characteristics and the peak gain boundary. The switching frequency can be calculated using the steady-state model. The  $f_s$  variations with voltage gain  $M$  are small because the resonant element switching ripples change little with different values of  $M$ . Equations are provided to design the non-resonant passive components  $C_s$ ,  $L_{oa}$ , and  $L_{ob}$ , according to the size of switching ripples.

#### **1.5.5 Rhombus-Window Inductor as Resonant Inductor with Significant AC Flux**

One example of an application using inductors with significant ac flux is the Series-Resonator

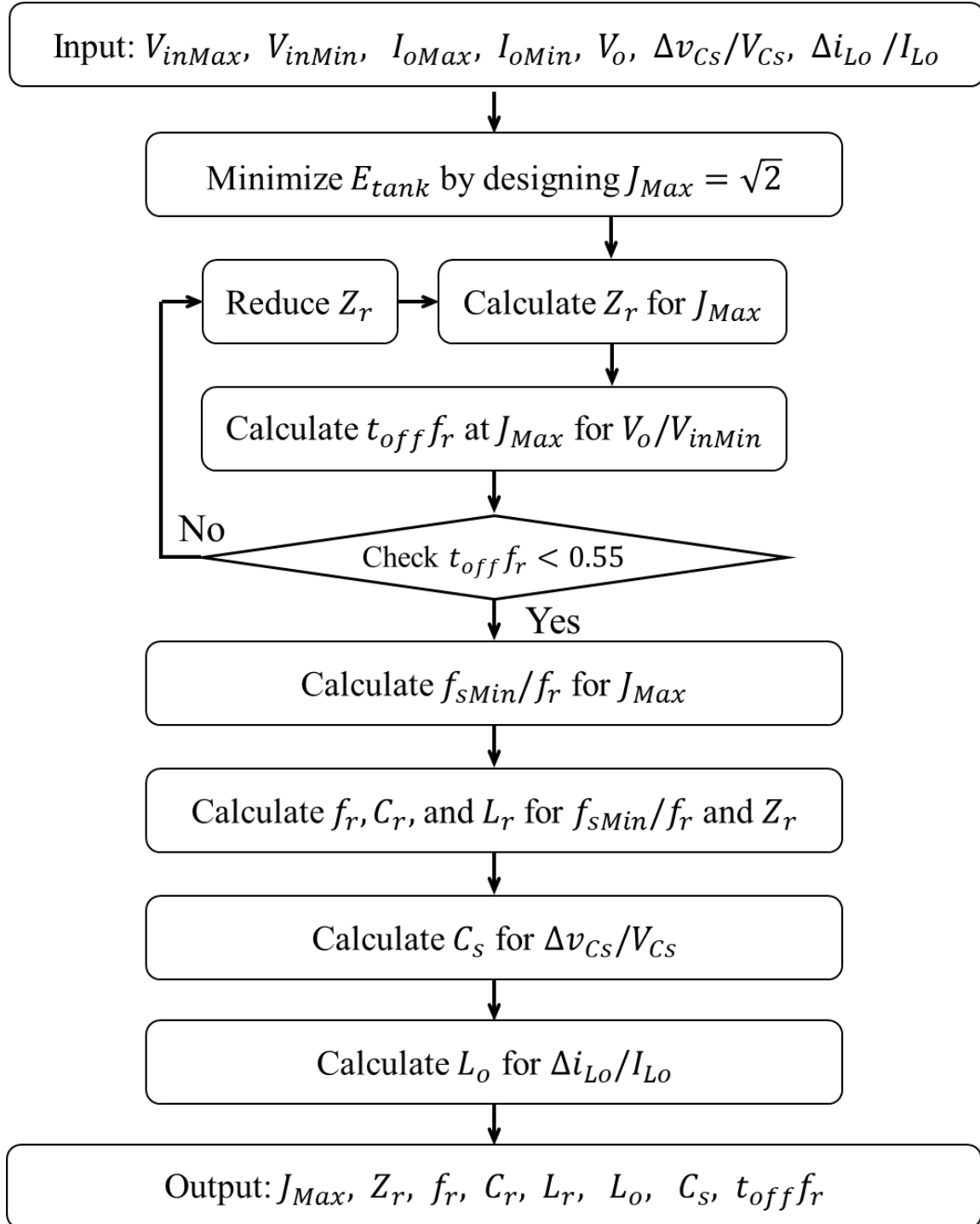
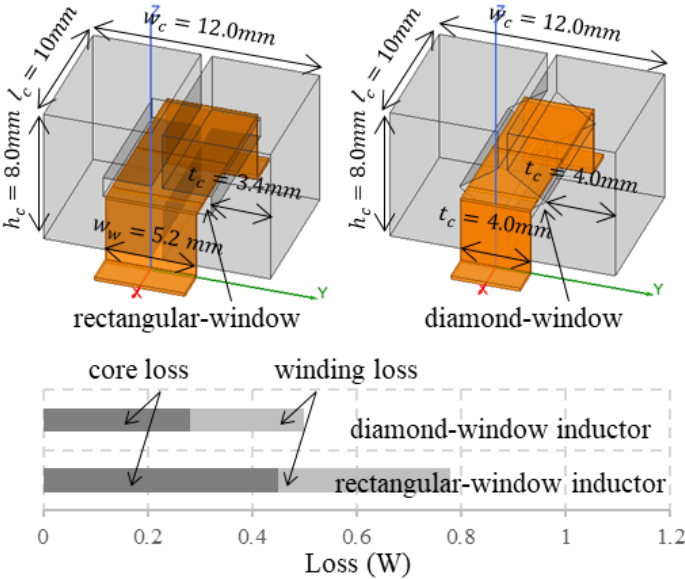


Fig. 1-12. Sequential design procedure of the SRB converter for the design variables listed in Fig. 1-8.

Buck (SRB) converter. The conventional rectangular-window core is replaced by a rhombus-window core to reduce the fringing flux on the winding; this results in a smaller winding loss. A detailed discussion of the inductance, core loss, and winding loss for the rhombus-window inductor is presented. The step-by-step design procedures meeting the given exemplary specifications are given. Experimental results are discussed to verify the theoretical analysis.

Fig. 1-13 compares the losses between the conventional rectangular-window inductor and the rhombus-window inductor given the same component size. The winding width of the rectangular-window design is larger, but the winding loss is 60% larger due to the fringing-effect loss. The rhombus-window design reduces loss by 40%. This work focuses on evaluating the rhombus-shaped window, and the analysis of different geometric shapes will be part of future work.



**Fig. 1-13. Loss comparison between the conventional rectangular-window inductor and the rhombus-window inductor given the same component size. The inductor loss was simulated using eddy current mode in Ansys Maxwell 2D. The current and material specifications are in Table 5-1.**

## 1.6 Dissertation Outline

Interleaved multiphase buck converters have been adopted for point-of-load regulation. The Series-Capacitor Buck (SCB) converter shows superiority compared with the conventional two-phase buck converter, but hard switching hindered efforts to reduce volume via increased switching frequency. This work replaces the series capacitor with the series resonator cell, and therefore synthesizes the Series-Resonator Buck (SRB) converter. This dissertation introduces the topologies, operations, steady-state modeling, transient-state modeling, design methodology, and magnetic designs.

Chapter 1 introduces the background, motivations, and objectives of this research. A review of traditional multiphase buck converters is presented. The challenges and the scope of this work are followed.

Chapter 2 introduces the series-resonator cell for soft switching, gate-driving signals, and operating principles. A steady-state model is built to characterize the soft-switching boundary and the voltage-gain curve. The soft-switching waveforms and theoretical analysis are verified experimentally.

Chapter 3 focuses on the large-signal model of the SRB converter. A transient-state model is built with the concept of generalized state-space averaging. A small-signal model is derived after the large-signal model is linearized and perturbed. The transfer functions of the SRB converter are presented and compared with those of the SCB converter.

Chapter 4 presents a design methodology for the SRB converter. The analytical relations between converter specifications, and component values are discussed. The design parameters are calculated sequentially given the converter specifications. The SRB prototype is compared to the conventional SCB converter in terms of efficiency and volume.

Chapter 5 shows the work on the magnetic designs of the SRB converter. A rhombic window inductor is introduced to reduce high-frequency ac loss while keeping the same size and cost. The inductor prototype is compared to the conventional rectangular-shaped window inductor.

Conclusions and future work are given in the last chapter.

## Chapter 2 Steady-State Analysis of the SRB Converter

### Nomenclature

Symbol	Description
$A_i$	State matrix in (2-19) for the i-th interval defined in Fig. 2-3
$B_i$	Input matrix in (2-19) for the i-th interval defined in Fig. 2-3
$C_n$	Capacitance ratio of the resonant capacitor to the series capacitor in (1-3)
$C_o$	Output capacitor in Fig. 2-1
$C_{OSS}$	Equivalent output capacitance of the switch in Fig. 2-5
$C_r$	Resonant capacitor in Fig. 2-1
$C_s$	Series capacitor in Fig. 2-1
$d_i$	Subinterval length $(t_{i+1} - t_i)/T_s$ in Fig. 2-3
$f_r$	Resonant frequency of the resonant tank in (1-1)
$J$	Normalized load current in (1-2)
$i_{a1}$	Current of switch $S_{a1}$ in Fig. 2-1
$i_{a2}$	Current of switch $S_{a2}$ in Fig. 2-1
$i_{b1}$	Current of switch $S_{b1}$ in Fig. 2-1
$i_{b2}$	Current of switch $S_{b2}$ in Fig. 2-1
$i_{Lr}$	Current of resonant inductor $L_r$ in Fig. 2-1
$i_{Loa}$	Current of output inductor $L_{oa}$ in Fig. 2-1
$i_{Lob}$	Current of output inductor $L_{ob}$ in Fig. 2-1
$I_o$	Converter output current consumed by the load in Fig. 2-1
$K$	Matrix containing the values of capacitance and inductance in (2-19)
$I_{oMax}$	Maximum output current Table 2-1
$I_{oMin}$	Minimum output current Table 2-1
$L_r$	Resonant inductor in Fig. 2-1
$L_{oa}$	Output inductor of the upper phase in Fig. 2-1
$L_{ob}$	Output inductor of the lower phase in Fig. 2-1
$L_n$	Inductance ratio of the resonant inductor to the output inductor in (1-4)

$M$	Voltage gain in Fig. 2-17
$R_{Loa}$	Inductor ESR in Fig. 2-13
$R_{Lob}$	Inductor ESR in Fig. 2-13
$S_{a1}$	High-side switch of the upper phase in Fig. 2-1
$S_{b1}$	High-side switch of the lower phase in Fig. 2-1
$S_{a2}$	Low-side switch of the upper phase in Fig. 2-1
$S_{b2}$	Low-side switch of the lower phase in Fig. 2-1
$t_i$	Switching timing in Fig. 2-3
$t_{off}$	Off-time of the low-side switches in Fig. 2-3
$T_s$	Switching period in Fig. 2-3
$x$	State variables in (2-19)
$\dot{x}$	State derivatives in (2-19)
$v_{Co}$	Voltage of capacitor $C_o$ in Fig. 2-1
$v_{Cr}$	Voltage of capacitor $C_r$ in Fig. 2-1
$v_{Cs}$	Voltage of capacitor $C_s$ in Fig. 2-1
$v_{dsa1}$	Drain-source voltage of switch $S_{a1}$ in Fig. 2-1
$v_{dsa2}$	Drain-source voltage of switch $S_{a2}$ in Fig. 2-1
$v_{dsb1}$	Drain-source voltage of switch $S_{b1}$ in Fig. 2-1
$v_{dsb2}$	Drain-source voltage of switch $S_{b2}$ in Fig. 2-1
$V_{in}$	Input voltage in Fig. 2-1
$V_o$	Output voltage in Fig. 2-1
$Z_r$	Characteristic impedance of the resonant tank in (1-2)
$\tau_i$	Subinterval length $t_{i+1} - t_i$ in Fig. 2-3

---

## 2.1 Introduction

The steady-state operation of the SRB converter belongs to the class of quasi-resonant converters [96] – [113]. The PWM switch network is replaced by a resonant switch network with resonant elements. The resonant frequency of those elements is typically higher than the switching frequency, and the switch network waveforms are quasi-sinusoidal pulses.

The operation with the series resonator highlighted in Fig. 2-1 cannot be solved using standard ac analysis because the switching devices are non-linear components, and introduce non-linear effects into the circuit. The low-side switches cannot be replaced with an ideal voltage source with rectangular waveforms as the switching node voltage varies with voltage gain and load conditions. The linear network theory for filter design therefore cannot be applied solely to the analysis of the SRB schematic.

A steady-state analysis of this class of quasi-resonant converters has been reported [97] – [106]. Ref. [97] – [99] analyzed the converter steady-state operation based on each switched stage over one switching cycle, and listed the complete responses of all energy-storage components. State-plane analysis [100] was used to present the state trajectories of the state variables, and to differentiate multiple discontinuous modes of operations. Ref. [101] – [102] modeled the average terminal voltages and currents of the resonant switch networks. The switch model is easy to use for analyzing this class of converters using the same resonant switches.

State-space averaging [103] is widely used to model PWM switch converters, whose switching frequency is much higher than the highest natural frequency in each switching interval. The state-space averaging method was extended by linear network theory to resonant switch network converters, the resonant frequency of whose resonant elements is in the same order as the switching frequency in other work [104]. Ref. [105] generalized the state-space averaging to quasi-resonant converters by separating low-frequency and high-frequency behaviors. Ref. [106] provided more mathematical analysis, and yielded more physical insights. Recent works suggest combining state-space modeling with state-plane analysis [107] and using the describing function method [108].

This chapter introduces the concept of the series-resonator cell for soft switching. The voltages

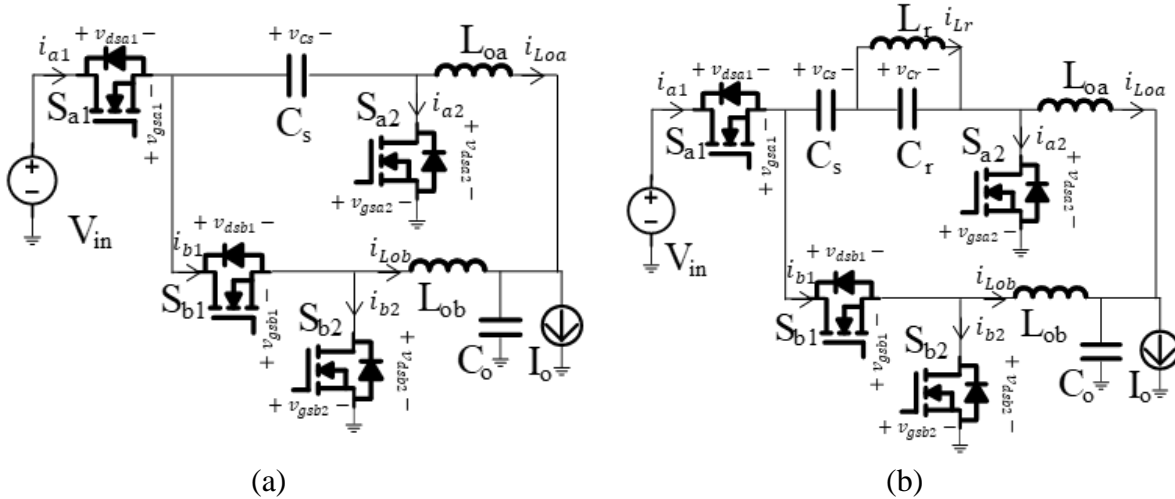


Fig. 2-1. (a) Series-Capacitor Buck converter and (b) Series-Resonator Buck converter.

and currents of the active switches in the SCB and SRB converters are compared to illustrate their soft-switching waveforms. The SRB gate-driving signals are shown, and the off-time is recommended as the control variable. The switching cycle in the steady state is broken down into eight subintervals, and their equivalent circuits are analyzed and modeled. The soft-switching boundary is characterized by an analytical equation with the help of theoretical analysis of the steady-state operation, and its impacts on the gain-curve boundary are discussed. The equations for the load-dependent gain curves are derived. The soft-switching capability of the SRB converter is verified by a 2-MHz converter with 48V input and 7V at 20A output.

## 2.2 Series-Resonator Cell for Soft Switching

An SRB converter is synthesized by adding a resonant tank in series with series capacitor  $C_s$ , as shown in Fig. 2-1 (b). The SRB is compared with the conventional SCB converter in Fig. 2-1 (a). The series-resonator cell includes series capacitor  $C_s$  and a parallel resonant tank. In a series-resonator cell, the resonant tank order could be any integer equal to or larger than 2.

Soft switching with the series-resonator cell is illustrated in Fig. 2-2 (b), and is then compared

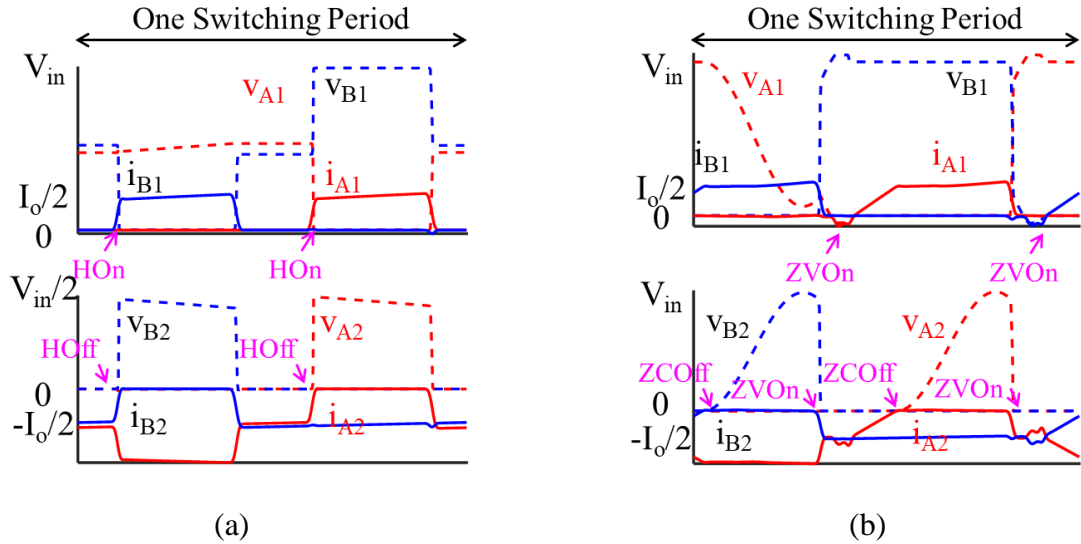


Fig. 2-2. Switches' voltage and current of (a) the Series-Capacitor Buck converter and (b) the Series-Resonator Buck converter in Fig. 2-1.

with the waveforms of the conventional SCB converter in Fig. 2-2 (a). Resonant tank components  $L_r$  and  $C_r$  generate resonant voltage  $v_{Cr}$  that opens up the opportunity for drain-to-source voltage  $v_{dsa1}$  and  $v_{dsb1}$  to reach zero for ZVOn of switches  $S_{a1}$  and  $S_{b1}$ . It also creates resonant current  $i_{Lr}$  that allows currents  $i_{a2}$  and  $i_{b2}$  to reach zero for ZCOff of switches  $S_{a2}$  and  $S_{b2}$ . No snubber is needed to limit the voltage stresses to the input voltage in the SRB's switches.

### 2.3 Gate-Driving Signal

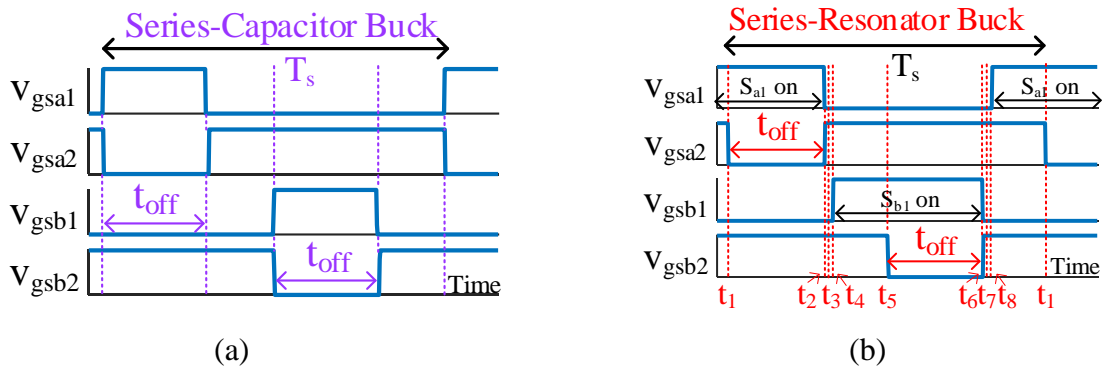


Fig. 2-3. Gate-driving signal of the (a) Series-Capacitor Buck converter and (b) Series-Resonator Buck converter in Fig. 2-1.

The gate signals for the SCB in Fig. 2-3(a) and SRB converters in Fig. 2-3(b) are compared

to identify a unified variable for output regulation. The waveforms for gate-to-source voltage  $V_{gsa2}$  and  $V_{gsb2}$  of the low-side switches are identical, whereas those of the high-side switches are not. Their off-time ( $t_{off}$ ) is thus recommended as the unified regulating variable. Simulation suggests that  $t_{off}$  is linearly proportional to the SRB's voltage gain. In both converters, there is a 180-degree phase shift between the gate signals for phases A and B.

## 2.4 Operating Principles with Series Resonator

The parallel resonant tank in Fig. 2-1 stores energy for soft switching, as illustrated by the simulated waveforms in Fig. 2-4. In this design, there are  $C_s \gg C_r$ ,  $L_{oa} \gg L_r$ , and  $L_{ob} \gg L_r$ . The resonant phenomenon only shows between  $L_r$  and  $C_r$ . Let [1, 0, 0, 1] represent the switching states with  $S_{a1}$  (an active switch) ON,  $S_{b1}$  (an active switch) OFF,  $S_{a2}$  (a synchronous switch) OFF, and  $S_{b2}$  (a synchronous switch) ON, respectively. The SRB converter cycles from [1, 0, 0, 1] to [0, 0, 0, 1] to [0, 0, 1, 1] to [0, 1, 1, 1] to [0, 1, 1, 0] to [0, 0, 1, 0] to [0, 0, 1, 1] to [1, 0, 1, 1] to [1, 0, 0, 1] in each switching period. The switching function  $d_n$  represents those  $n=8$  cycles one by one. The eight intervals within a switching period are delineated along with the switched topologies.

### 2.4.1 Subinterval [ $t_1, t_2$ ]

The switch  $S_{a2}$  turns off with ZCOFF at  $t_1$ . The switches  $S_{a1}$  and  $S_{b2}$  are on; the switches  $S_{b1}$  and  $S_{a2}$  are off as shown in Fig. 2-5.

Voltage  $v_{dsb1}$  is  $V_{in}$ . Voltage  $v_{dsa2}$  is dependent on  $V_{in}$ ,  $v_{Cs}$ , and  $v_{Cr}$ . The currents  $i_{a1}$  and  $i_{b2}$  are dependent on the output inductor current. Inductor  $L_{ob}$  is linearly discharged by  $V_o$ . The equivalent switch output capacitor  $C_{ossa2}$  is charged by the current of  $i_{a1}$  and  $i_{Loa}$ .

The duration of  $t_{off} = t_2 - t_1$  will be employed to control the voltage gain. The input current  $i_{A1}$  is equal to  $i_{Loa}$ . The converter input power  $V_{in} * i_{A1} * t_{off}$  in this interval is linearly controlled by  $t_{off}$ .

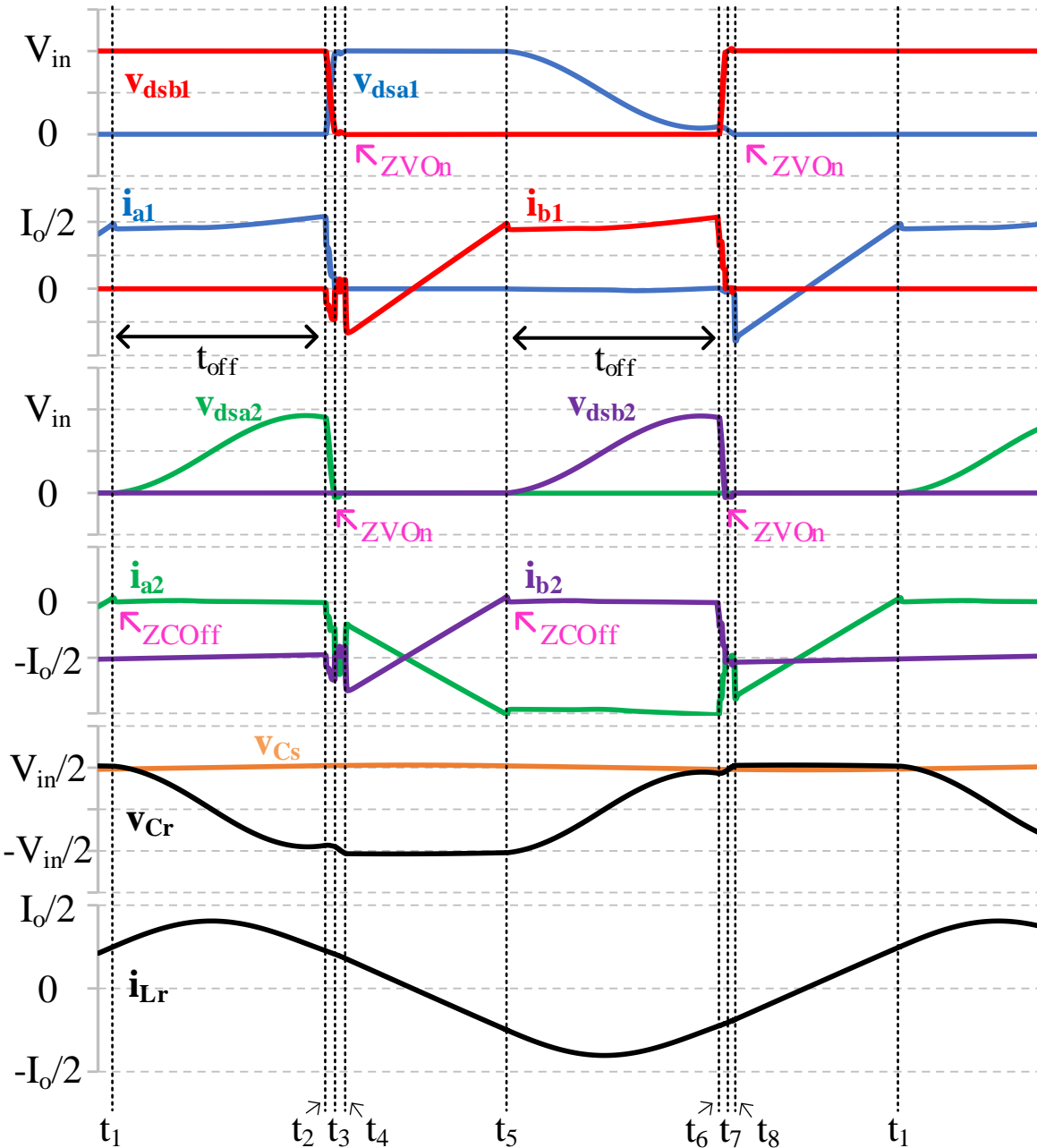


Fig. 2-4. Eight switched intervals and waveforms for the SRB converter in Fig. 2-1 on page 22 using the gate-driving signals in Fig. 2-3 on page 23. The converter was simulated with non-ideal switch models from Efficient Power Conversion Corporation (EPC) and inductors with  $2\text{ m}\Omega$  equivalent series resistors. Other components were ideal. The component values were  $L_{oa} = L_{ob} = 1.2\ \mu\text{H}$ ,  $L_r = 150\ \text{nH}$ ,  $C_r = 12\ \text{nF}$ , and  $C_o = 20\ \mu\text{F}$ . All switches turn on with zero voltage, whereas  $S_{a2}$  and  $S_{b2}$  turn off from zero current. The equivalent circuits of eight intervals are listed in Fig. 2-5 to Fig. 2-12.

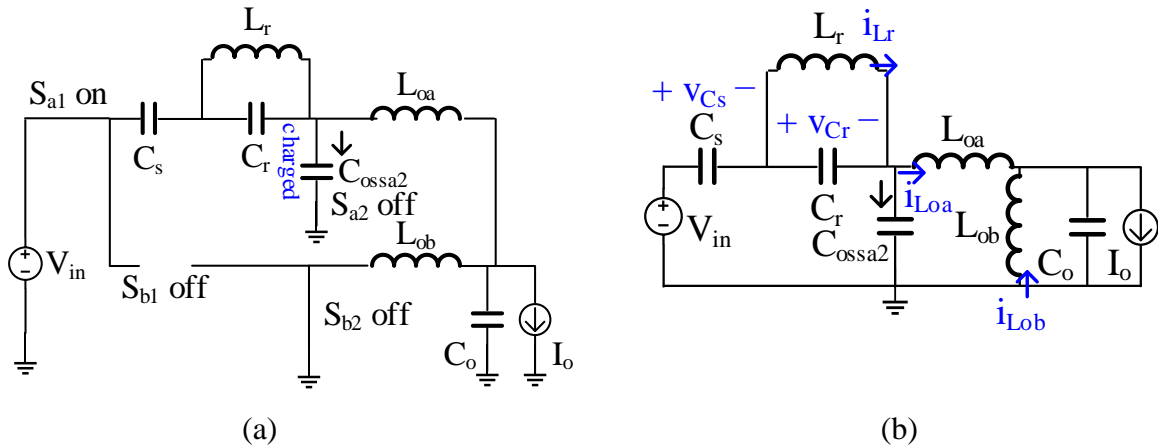


Fig. 2-5. (a) Circuit during interval  $t_1 - t_2$  defined in Fig. 2-4 and (b) corresponding simplified schematic.

This subinterval ends when switch  $S_{a1}$  receives the turn-off signal at  $t_2$ .

#### 2.4.2 Subinterval $[t_2, t_3]$

The switch  $S_{a1}$  receives the turn-off signal at  $t_2$ . The switch  $S_{b2}$  is on; the switches  $S_{a1}$ ,  $S_{b1}$ , and  $S_{a2}$  are off as shown in Fig. 2-6. The inductor  $L_{ob}$  is linearly discharged by  $V_o$ . The current  $i_{Loa}$  charges  $C_{oss a1}$  and discharges  $C_{oss b1}$  and  $C_{oss a2}$ .

This interval ends when  $v_{a2}$  reaches zero. The switch  $S_{a2}$  turns on into zero-voltage (ZVOn) at  $t_3$ .

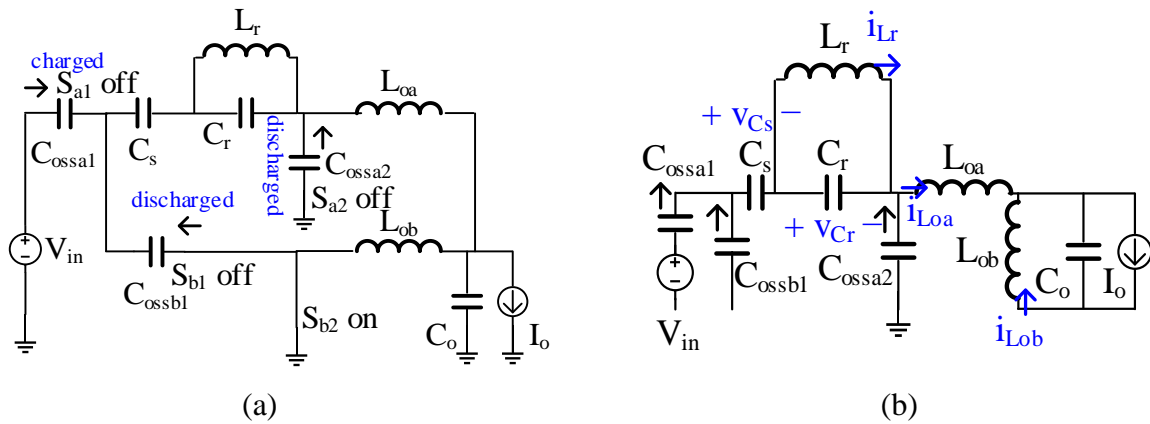


Fig. 2-6. (a) Circuit during interval  $t_2 - t_3$  defined in Fig. 2-4 and (b) corresponding simplified schematic.

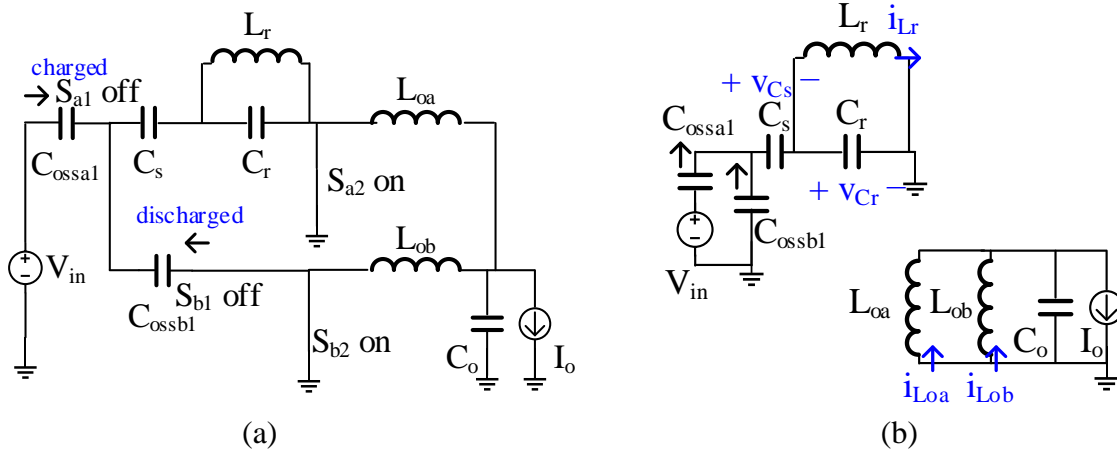


Fig. 2-7. (a) Circuit during interval  $t_3 - t_4$  defined in Fig. 2-4 and (b) corresponding simplified schematic.

### 2.4.3 Subinterval $[t_3, t_4]$

The switch  $S_{a2}$  turns on into zero-voltage (ZVOn) at  $t_3$ . The switches  $S_{a2}$  and  $S_{b2}$  are on; switches  $S_{a1}$  and  $S_{b1}$  are off as shown in Fig. 2-7.

The inductors  $L_{oa}$  and  $L_{ob}$  are linearly discharged by  $V_o$ . The capacitors  $C_r$ ,  $C_{ossal}$ , and  $C_{ossbl}$  are in parallel effectively if  $C_s \gg C_r$ . The current  $i_{Lr}$  charges  $C_{ossal}$  and  $C_r$ , and discharges  $C_{ossbl}$ . The time taken depends on the current  $i_{Lr}$  and the resonant tank design.

This interval ends when  $v_{a1}$  and  $v_{b1}$  resonate to zero. The switch  $S_{b1}$  turns on into zero-voltage (ZVOn) at  $t_4$ .

### 2.4.4 Subinterval $[t_4, t_5]$

The switch  $S_{b1}$  turns on into zero-voltage (ZVOn) at  $t_4$ . The switches  $S_{a2}$ ,  $S_{b1}$ , and  $S_{b2}$  are on; the switch  $S_{a1}$  is off as shown in Fig. 2-8.

The voltage  $v_{dsal}$  is  $V_{in}$ . The current  $i_{b1}$  is dependent on the resonant inductor current. The currents  $i_{a2}$  and  $i_{b2}$  are dependent on the output inductor current and the resonant inductor current. The inductors  $L_{ob}$  and  $L_{ob}$  are linearly discharged by  $V_o$ .

This subinterval ends when the switch current  $i_{b2}$  resonates to zero at  $t_5$ .

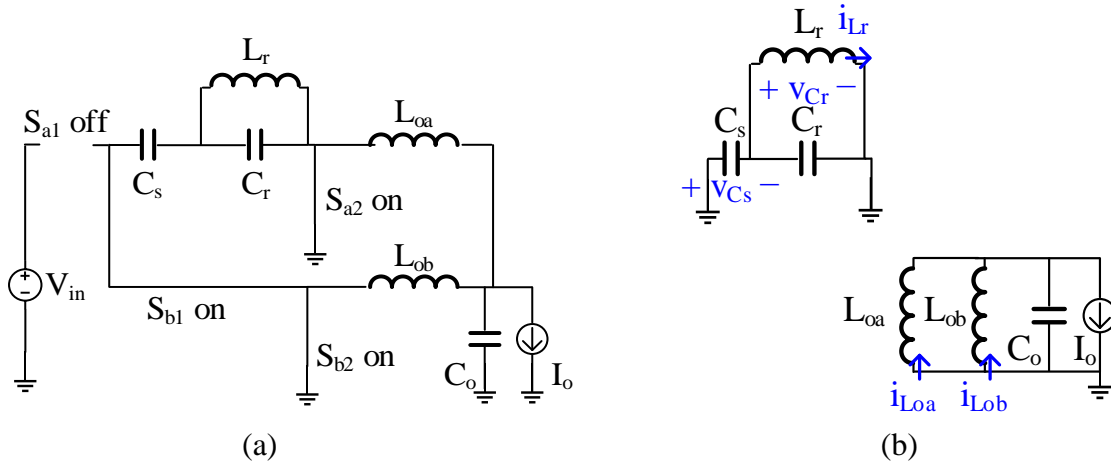


Fig. 2-8. (a) Circuit during interval  $t_4 - t_5$  defined in Fig. 2-4 and (b) corresponding simplified schematic.

### 2.4.5 Subinterval [ $t_5, t_6$ ]

The switch  $S_{b2}$  turns off from zero-current (ZCOFF) at  $t_5$ . The switches  $S_{a2}$  and  $S_{b1}$  are on; the switches  $S_{a1}$  and  $S_{b2}$  are off as shown Fig. 2-9.

The voltage  $v_{dsa1}$  is  $V_{in}$ . The voltage  $v_{dsb2}$  is dependent on  $v_{Cs}$  and  $v_{Cr}$ . The currents  $i_{b1}$  and  $i_{a2}$  are dependent on the output inductor current. The inductor  $L_{oa}$  is linearly discharged by  $V_o$ . The equivalent switch output capacitor  $C_{ossb2}$  is charged by the current dependent of  $i_{b1}$  and  $i_{Lob}$ .

This subinterval ends when the switch  $S_{b1}$  receives the turn-off signal at  $t_6$ .

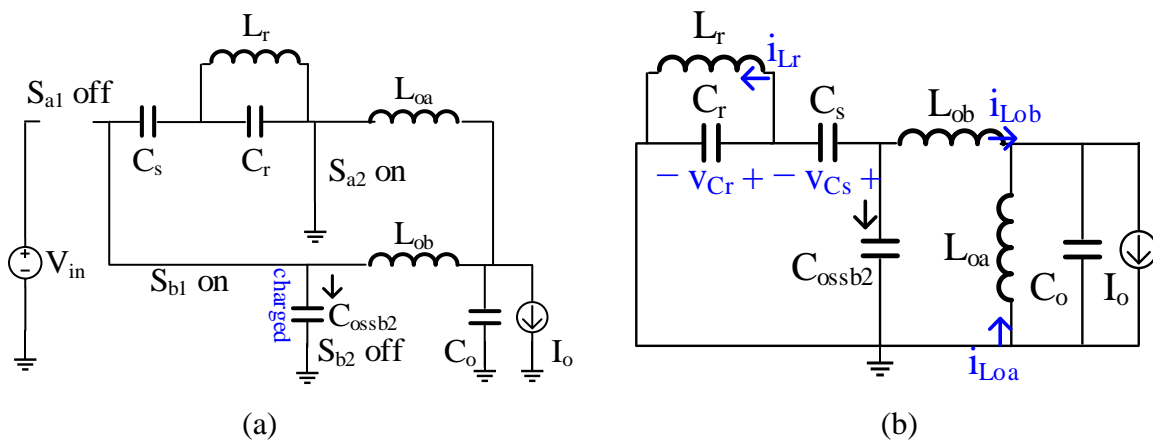


Fig. 2-9. (a) Circuit during interval  $t_5 - t_6$  defined in Fig. 2-4 and (b) corresponding simplified schematic.

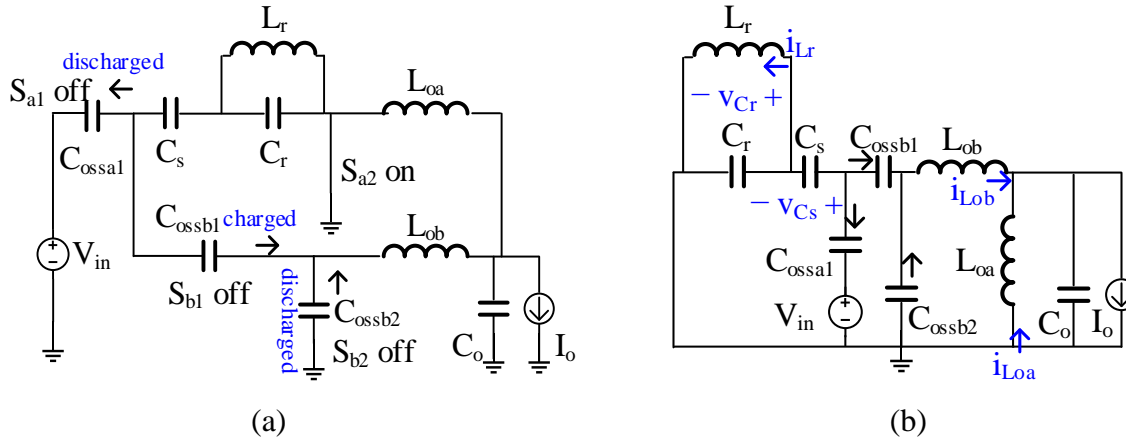


Fig. 2-10. (a) Circuit during interval  $t_6 - t_7$  defined in Fig. 2-4 and (b) corresponding simplified schematic.

#### 2.4.6 Subinterval [ $t_6, t_7$ ]

The switch  $S_{b1}$  receives the turn-off signal at  $t_6$ . The switch  $S_{a2}$  is on; the switches  $S_{a1}$ ,  $S_{b1}$ , and  $S_{b2}$  are off as shown in Fig. 2-10.

The inductor  $L_{oa}$  is linearly discharged by  $V_o$ . The current  $i_{Lob}$  charges  $C_{ossb1}$ , and discharges  $C_{ossa1}$  and  $C_{ossb2}$ . The time taken depends on the input voltage, the load condition, and the output inductor ripple.

This interval ends when  $v_{b2}$  reaches zero. The switch  $S_{b2}$  turns on into zero-voltage (ZVOn) at  $t_7$ .

#### 2.4.7 Subinterval [ $t_7, t_8$ ]

The switch  $S_{b2}$  turns on into zero-voltage (ZVOn) at  $t_7$ . The switches  $S_{a2}$  and  $S_{b2}$  are on; the switches  $S_{a1}$  and  $S_{b1}$  are off as shown in Fig. 2-11.

The inductors  $L_{oa}$  and  $L_{ob}$  are linearly discharged by  $V_o$ . The capacitors  $C_r$ ,  $C_{ossa1}$ , and  $C_{ossb1}$  are in parallel effectively if  $C_s \gg C_r$ . The current  $i_{Lr}$  charges  $C_{ossb1}$  and  $C_r$ , and discharges  $C_{ossa1}$ . The time taken depends on the current  $i_{Lr}$  and the resonant tank design.

This interval ends when  $v_{a1}$  and  $v_{b1}$  resonate to zero. The switch  $S_{a1}$  turns on into zero-voltage

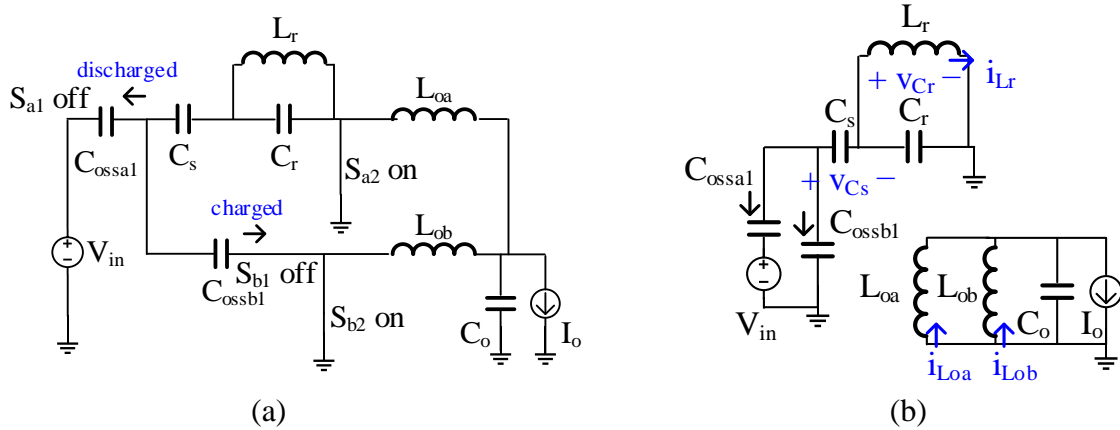


Fig. 2-11. (a) Circuit during interval  $t_7 - t_8$  defined in Fig. 2-4 and (b) corresponding simplified schematic.

(ZVOn) at  $t_8$ .

### 2.4.8 Subinterval [ $t_8, t_1$ ]

The switch  $S_{a1}$  turns on into zero-voltage (ZVOn) at  $t_8$ . The switches  $S_{a1}$ ,  $S_{a2}$ , and  $S_{b2}$  are on; the switch  $S_{b1}$  is off as shown in Fig. 2-12.

The voltage  $v_{dsb1}$  is  $V_{in}$ . The current  $i_{a1}$  is dependent on the resonant inductor current. The currents  $i_{a2}$  and  $i_{b2}$  are dependent on the output inductor current and the resonant inductor current. The inductors  $L_{ob}$  and  $L_{ob}$  are linearly discharged by  $V_o$ .

This subinterval ends when the switch current  $i_{b2}$  resonates to zero at  $t_1$ .

## 2.5 Steady-State Model with Series Resonator

The following assumptions are made:

- 1) The peak-to-peak switching ripples of  $v_{Cs}$ ,  $i_{Loa}$ , and  $i_{Lob}$  are less than 20% of their dc bias.
- 2) The switching frequency  $f_s$  is much larger than the highest natural frequency of the low-pass filter and the series capacitor. The state variables  $v_{Co}$ ,  $i_{Loa}$ ,  $i_{Lob}$ , and  $v_{Cs}$  are treated as constant in one switching cycle.

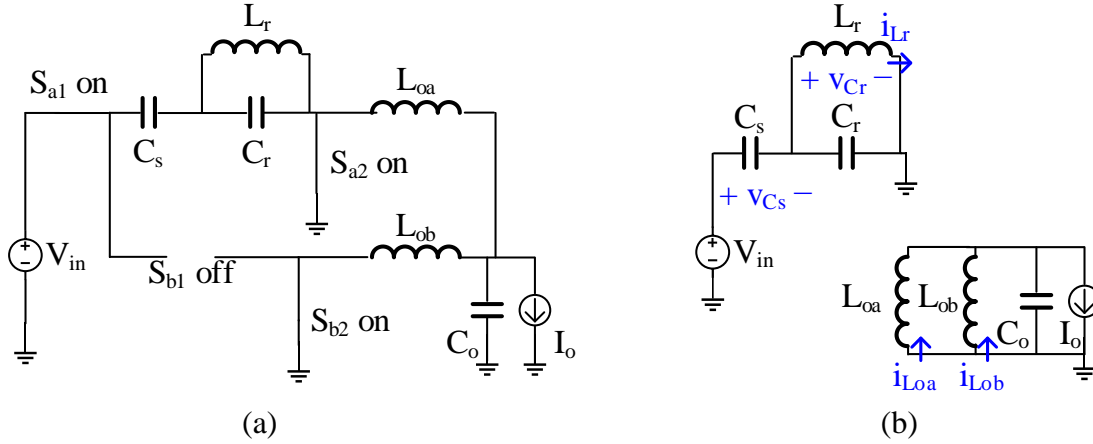


Fig. 2-12. (a) Circuit during interval  $t_s - t_1$  defined in Fig. 2-4 and (b) corresponding simplified schematic.

3) Two output inductors are the same:  $L_o = L_{oa} = L_{ob}$  and  $R_{Lo} = R_{Loa} = R_{Lob}$ .

4) All the switches and capacitors are ideal.

### Subinterval 1 ( $t_1 \rightarrow t_2$ )

The time  $t_1$  is the instant  $i_{a2}$  reaches zero, and  $S_{a2}$  turns off from zero current (ZCOFF). In the controller, the counter is reset, and starts counting toward  $t_{off}$ . At  $t_2 = t_1 + t_{off}$ ,  $S_{a1}$  is turned off. In subinterval 1,  $S_{a1}$  and  $S_{b2}$  are on. The equivalent circuit is shown in Fig. 2-13. The differential equations for all the subintervals are summarized in (2-19). The solutions for  $v_{Cr}$  and  $i_{Lr}$  in subinterval 1 consist of a natural response dependent on the initial conditions  $i_{Lr@t_1} = i_{Loa}(C_r + C_s)/C_s \approx i_{Loa}$ ,  $V_{Cr@t_1} = V_{in} - v_{Cs}$  and a forced response dependent on  $i_{Loa}$ :

$$v_{Cr}(t) = \cos(\omega_r t) (V_{in} - v_{Cs}), t_1 \leq t < t_2 \quad (2-1)$$

$$i_{Lr}(t) = \frac{1}{Z_r} \sin(\omega_r t) (V_{in} - v_{Cs}) + i_{Loa}, t_1 \leq t < t_2 \quad (2-2)$$

The length of this subinterval  $\tau_1$  is

$$\tau_1 = t_{off} \quad (2-3)$$

### Subinterval 2 and Subinterval 3 ( $t_2 \rightarrow t_4$ )

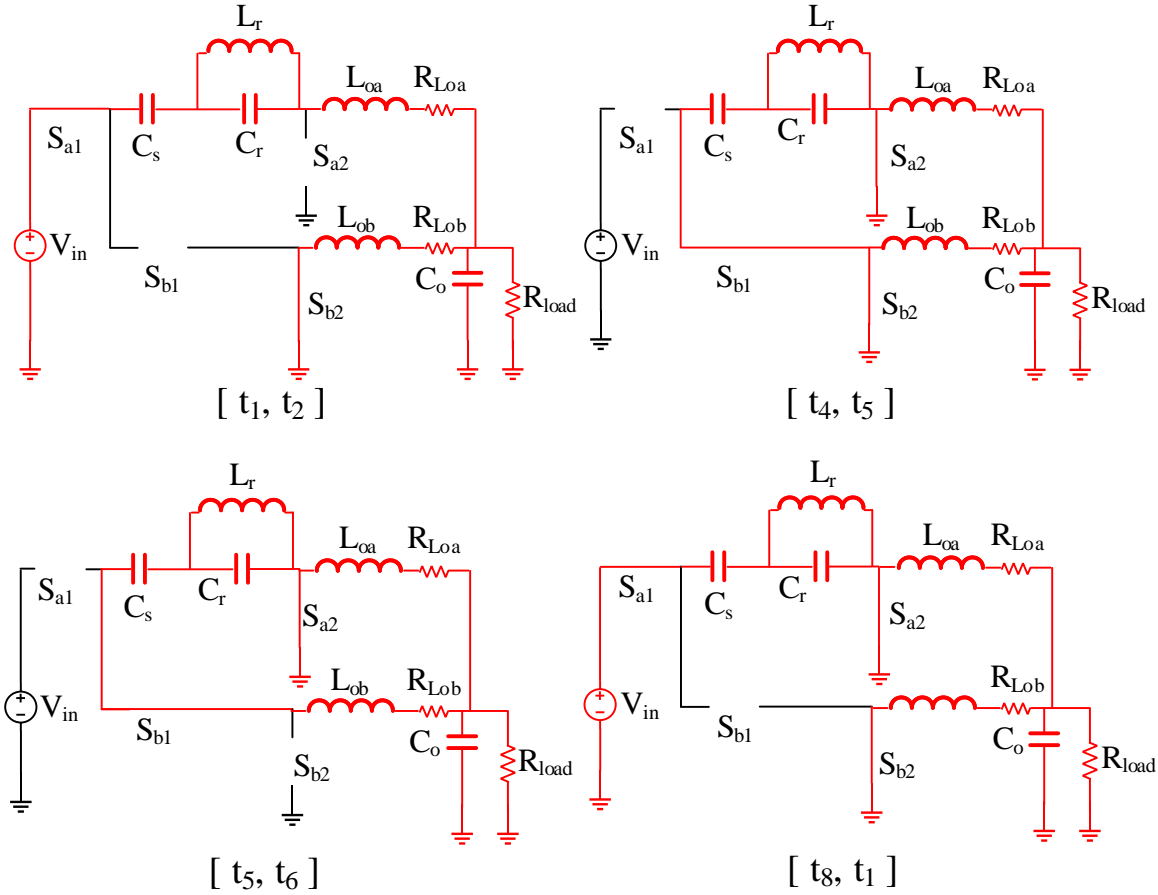


**Fig. 2-13.** The equivalent circuits of the subintervals defined in Fig. 2-4 of the SRB converter in Fig. 2-1 on page 22.

The ideal switch  $S_{a2}$  is turned on at  $t_2$ . The equivalent circuits of the subinterval  $t_2 - t_3$  and  $t_3 - t_4$  are combined in Fig. 2-13.

After  $S_{a1}$  is turned off at  $t_2$ ,  $C_r$  is charged to  $-V_{in}/2$  by  $i_{Lr}$  to bring  $v_{DSb1} = v_{Cs} + v_{Cr}$  to zero. The switch  $S_{b1}$  turns on into zero voltage (ZVOn) at  $t_4$ . The solutions for  $v_{Cr}$  and  $i_{Lr}$  are

$$v_{Cr}(t) = \cos(w_r t) V_{Cr@t_2} - Z_r \sin(w_r t) I_{Lr@t_2}, t_2 \leq t < t_4 \quad (2-4)$$

$$i_{Lr}(t) = \frac{1}{Z_r} \sin(w_r t) V_{Cr@t_2} + \cos(w_r t) I_{Lr@t_2}, t_2 \leq t < t_4 \quad (2-5)$$

where the initial conditions  $V_{Cr@t_2}$  and  $I_{Lr@t_2}$  are calculated with (2-1), (2-2), and (2-3). The detailed calculation of  $\tau_2 + \tau_3$  is documented in Appendix. The subinterval length is

$$\tau_2 + \tau_3 = \frac{2}{\omega_r} \arctan \left( \frac{Z_r I_{Lr@t_2} - \sqrt{(Z_r I_{Lr@t_2})^2 - (v_{Cs} - V_{Cr@t_2})(v_{Cs} + V_{Cr@t_2})}}{(v_{Cs} - V_{Cr@t_2})} \right) \quad (2-6)$$

This interval can be ignored if  $\tau_2 + \tau_3 < 5\%T_s$ . This ensures the transition period for charging and discharging  $C_{oss}$  accounts for less than 10% of one switching cycle, and therefore can be ignored in the steady-state analysis.

According to (2-6) and (2-20), the equation  $\tau_2 + \tau_3 < 5\%T_s$  can be confirmed by Matlab at  $0.1 < J < 10$ . This condition results in  $I_{Lr@t_4} \approx I_{Lr@t_2}$  and  $\tau_2 + \tau_3 \approx 0$ , which applies to most designs.

#### **Subinterval 4 ( $t_4 \rightarrow t_5$ )**

After  $S_{b1}$  is turned on at  $t_4$ , the current of  $L_r$  ramps up. The switch current  $i_{b2}$  decreases toward zero. This subinterval ends at  $t_5$  when  $S_{b2}$  turns off at zero current (ZCOff).

In subinterval 4,  $S_{a2}$ ,  $S_{b1}$ , and  $S_{b2}$  are on. The equivalent circuit is shown in Fig. 2-13. The series capacitor is equivalent to a voltage source. Two capacitors  $C_s$  and  $C_r$  are in parallel. The resonant inductor  $L_r$  is charged by  $-v_{Cs}$ . The solutions for  $v_{Cr}$  and  $i_{Lr}$  in subinterval 4 are

$$v_{Cr}(t) = -v_{Cs}, t_4 \leq t < t_5 \quad (2-7)$$

$$i_{Lr}(t) = I_{Lr@t_4} + \frac{-v_{Cs}}{L_r} t, t_4 \leq t < t_5 \quad (2-8)$$

where the initial condition  $I_{Lr@t_4} \approx I_{Lr@t_2}$  is calculated with (2-1), (2-2), and (2-3). The detailed calculation of  $\tau_4$  is documented in Appendix. The length of this subinterval  $\tau_4$  is

$$\tau_4 \approx \frac{L_r}{-v_{Cs}} (-i_{Lob} - I_{Lr@t_4}) \quad (2-9)$$

#### **Subinterval 5 ( $t_5 \rightarrow t_6$ )**

The time  $t_5$  is the instant  $i_{b2}$  reaches zero, and  $S_{b2}$  turns off from zero current (ZCOff). In the

controller, the counter is reset, and starts counting toward  $t_{\text{off}}$ . At  $t_6 = t_5 + t_{\text{off}}$ ,  $S_{b1}$  is turned off. In subinterval 5,  $S_{b1}$  and  $S_{a2}$  are on. The equivalent circuit is shown in Fig. 2-13. The solutions for  $v_{Cr}$  and  $i_{Lr}$  consist of a natural response dependent on the initial conditions  $I_{Lr@t_5} = i_{Lob}(C_r + C_s)/C_s \approx i_{Lob}$ ,  $V_{Cr@t_5} = -v_{Cs}$  and a forced response dependent on  $i_{Lob}$ :

$$v_{Cr}(t) = -\cos(w_r t) v_{Cs}, t_5 \leq t < t_6 \quad (2-10)$$

$$i_{Lr}(t) = \frac{1}{Z_r} \sin(w_r t) (-v_{Cs}) + (-i_{Lob}), t_5 \leq t < t_6 \quad (2-11)$$

The length of this subinterval  $\tau_5$  is

$$\tau_5 = t_{\text{off}} \quad (2-12)$$

### Subinterval 6 and Subinterval 7 ( $t_6 \rightarrow t_8$ )

The ideal switch  $S_{b2}$  is turned on at  $t_6$ . The equivalent circuits of the subinterval  $t_6 - t_7$  and  $t_7 - t_8$  are combined in Fig. 2-13.

After  $S_{b1}$  is turned off at  $t_6$ ,  $C_r$  is charged to  $V_{in}/2$  by  $i_{Lr}$  to bring  $v_{DSa1} = V_{in} - v_{Cs}$  to zero.

The switch  $S_{a1}$  turns on into zero voltage (ZVOn) at  $t_8$ . The solutions for  $v_{Cr}$  and  $i_{Lr}$  are

$$v_{Cr}(t) = \cos(w_r t) V_{Cr@t_6} - Z_r \sin(w_r t) I_{Lr@t_6}, t_6 \leq t < t_8 \quad (2-13)$$

$$i_{Lr}(t) = \frac{1}{Z_r} \sin(w_r t) V_{Cr@t_6} + \cos(w_r t) I_{Lr@t_6}, t_6 \leq t < t_8 \quad (2-14)$$

where the initial conditions  $V_{Cr@t_6}$  and  $I_{Lr@t_6}$  are calculated with (2-10), (2-11), and (2-12). The detailed calculation of  $\tau_6 + \tau_7$  is documented in Appendix. The subinterval length is

$$\tau_6 + \tau_7 = \frac{2}{w_r} \arctan \left( \frac{Z_r I_{Lr@t_6} - \sqrt{(Z_r I_{Lr@t_6})^2 - (v_{Cs} - V_{Cr@t_6})(v_{Cs} + V_{Cr@t_6})}}{(v_{Cs} - V_{Cr@t_6})} \right) \quad (2-15)$$

This interval can be ignored if  $\tau_6 + \tau_7 < 5\%T_s$ . This ensures the transition period for charging and discharging  $C_{\text{oss}}$  accounts for less than 10% of one switching cycle, and therefore can be

ignored in the steady-state analysis.

According to (2-6) and (2-20), the equation  $\tau_2 + \tau_3 < 5\%T_s$  can be confirmed by Matlab at  $0.1 < J < 10$ . This results in  $I_{Lr@t_8} \approx I_{Lr@t_6}$  and  $\tau_6 + \tau_7 \approx 0$ , which applies to most designs.

### **Subinterval 8 ( $t_8 \rightarrow t_1$ )**

After  $S_{a1}$  is turned on at  $t_8$ , the current of  $L_r$  ramps up. The switch current  $i_{a2}$  decreases toward zero. This subinterval ends at  $t_1$  when  $S_{a2}$  turns off at zero current (ZCOff).

In subinterval 8,  $S_{b2}$ ,  $S_{a1}$ , and  $S_{a2}$  are on. The equivalent circuit is shown in Fig. 2-13. The series capacitor is equivalent to a voltage source. Two capacitors  $C_s$  and  $C_r$  are in parallel. The resonant inductor  $L_r$  is charged by  $v_{C_s}$ . The solutions of  $v_{C_r}$  and  $i_{L_r}$  in subinterval 8 are

$$v_{C_r}(t) = v_{C_s}, t_8 \leq t < t_1 \quad (2-16)$$

$$i_{L_r}(t) = I_{Lr@t_8} + \frac{-v_{C_s}}{L_r} t, t_8 \leq t < t_1 \quad (2-17)$$

where the initial conditions  $V_{C_r@t_8} \approx V_{C_r@t_6}$  and  $I_{L_r@t_8} \approx I_{L_r@t_6}$  are calculated with (2-10), (2-11), and (2-12). The length of this subinterval  $\tau_8$  is

$$\tau_8 \approx \frac{L_r}{v_{C_s}} (-i_{Loa} - I_{Lr@t_8}) \quad (2-18)$$

### **Single Switching Cycle ( $t_1 \rightarrow T_s + t_1$ )**

This section analyzes subintervals 1 through 8, and lists the steady-state solution for the state variables of the resonant elements. All subinterval lengths are calculated according to the solutions of the resonant state variables.

The theoretical model is built in Matlab using the analytical solutions listed in this section. The calculation time of the analytical-based model is significantly faster than that of the numerical-based model.

Consider the series resonator's state variables as input variables. Keep the low-pass filter state variables. Each switched stage is modeled using matrix equations one by one.

Based on the concept of the generalized state-space averaging [106], the reduced-order state equations of the SRB converter are listed as follows:

$$K\dot{x} = Cx + D$$

$$K = \begin{bmatrix} C_s & 0 & 0 & 0 \\ 0 & C_o & 0 & 0 \\ 0 & 0 & L_{oa} & 0 \\ 0 & 0 & 0 & L_{ob} \end{bmatrix}, \dot{x} = \begin{bmatrix} \frac{dv_{Cs}}{dt} \\ \frac{dv_{Co}}{dt} \\ \frac{di_{Loa}}{dt} \\ \frac{di_{Lob}}{dt} \end{bmatrix}, x = \begin{bmatrix} v_{Cs} \\ v_{Co} \\ i_{Loa} \\ i_{Lob} \end{bmatrix},$$

$$A_1 = \begin{bmatrix} 0 & 0 & 1 & 0 \\ 0 & -\frac{1}{R_{load}} & 1 & 1 \\ -1 & -1 & 0 & 0 \\ 0 & -1 & 0 & 0 \end{bmatrix}, A_2 = A_3 = A_4 = \begin{bmatrix} 0 & 0 & 0 & 0 \\ 0 & -\frac{1}{R_{load}} & 1 & 1 \\ 0 & -1 & 0 & 0 \\ 0 & -1 & 0 & 0 \end{bmatrix}, \quad (2-19)$$

$$A_5 = \begin{bmatrix} 0 & 0 & 0 & -1 \\ 0 & -\frac{1}{R_{load}} & 1 & 1 \\ 0 & -1 & 0 & 0 \\ 1 & -1 & 0 & 0 \end{bmatrix}, A_6 = A_7 = A_8 = \begin{bmatrix} 0 & 0 & 0 & 0 \\ 0 & -\frac{1}{R_{load}} & 1 & 1 \\ 0 & -1 & 0 & 0 \\ 0 & -1 & 0 & 0 \end{bmatrix},$$

$$B_1 = \begin{bmatrix} 0 \\ 0 \\ V_{in} - v_{Cr} \\ 0 \end{bmatrix}, B_5 = \begin{bmatrix} 0 \\ 0 \\ 0 \\ v_{Cr} \end{bmatrix}, B_4 = B_8 = \begin{bmatrix} i_{Lr} \\ 0 \\ 0 \\ 0 \end{bmatrix}, B_2 = B_3 = B_6 = B_7 = \begin{bmatrix} 0 \\ 0 \\ 0 \\ 0 \end{bmatrix},$$

$$C = \left\{ \sum_{i=1}^k d_i A_i \right\}, D = \frac{1}{t_s} \sum_{i=1}^k \int_{t_{i-1}}^{t_i} B_i(\lambda) d\lambda$$

where  $d_i$  is defined as  $d_i = \frac{\tau_i}{t_s}$ . There are  $k = 8$  different subintervals in one switching cycle.

According to (2-1) to (2-18), the switching period is calculated by adding (2-3), (2-9), (2-12), and

(2-18)

$$t_s = \sum_{i=1}^k \tau_i \approx 2t_{off} + \frac{L_r(i_{Loa} + i_{Lob} + \frac{v_{Cs} \sin(w_r t_{off})}{Z_r})}{V_{in} - v_{Cs}} + \frac{L_r(i_{Loa} + i_{Lob} + \frac{(V_{in} - v_{Cs}) \sin(w_r t_{off})}{Z_r})}{v_{Cs}} \quad (2-20)$$

Equation (2-19) is set to equal to zero. The steady-state solutions are

$$X = -C^{-1}D = [V_{in}/2 \quad V_o \quad V_o/R_{load}/2 \quad V_o/R_{load}/2]^T \quad (2-21)$$

where according to voltage-second balance, (2-1), and (2-20),  $V_o$  is calculated with

$$V_o = \frac{1}{t_s} \sum_{i=1}^8 \int_{t_i}^{t_{i+1}} v_{dsa2}(\lambda) d\lambda = \frac{1}{t_s} \int_{t_1}^{t_2} v_{dsa2}(\lambda) d\lambda = \frac{1}{t_s} \int_{t_1}^{t_2} (V_{in} - V_{Cs} - v_{Cr}(\lambda)) d\lambda \quad (2-22)$$

This solution suggests the dc bias of  $v_{Cs}$  is half of the input voltage. The two inductor currents are equal to  $V_o/R_{load}/2$ . The solution in (2-21) can be added to (2-20) for the switching period  $T_s$  in the steady state

$$T_s \approx \frac{2}{w_r} (2J + w_r T_{off} + \sin(w_r T_{off})) \quad (2-23)$$

Matlab was used to calculate the modeled waveforms using (2-1) – (2-20). The Matlab code is attached to Appendix on page 254. The solutions of the state variables were calculated one subinterval by one subinterval sequentially over one switching cycle. The modeled waveforms and the simulated waveforms were compared. The waveforms were simulated in LTspice using ideal components. The gate signals of the high-side switches were provided by a voltage source with a preset switching frequency and duty ratio as exemplified in Fig. 2-3. The output voltage could be changed by adjusting the switching frequency of the high-side gate signals. Fig. 2-14 shows waveforms of resonant capacitor voltage  $v_{Cr}$  and resonant inductor current  $i_{Lr}$  at the full-load

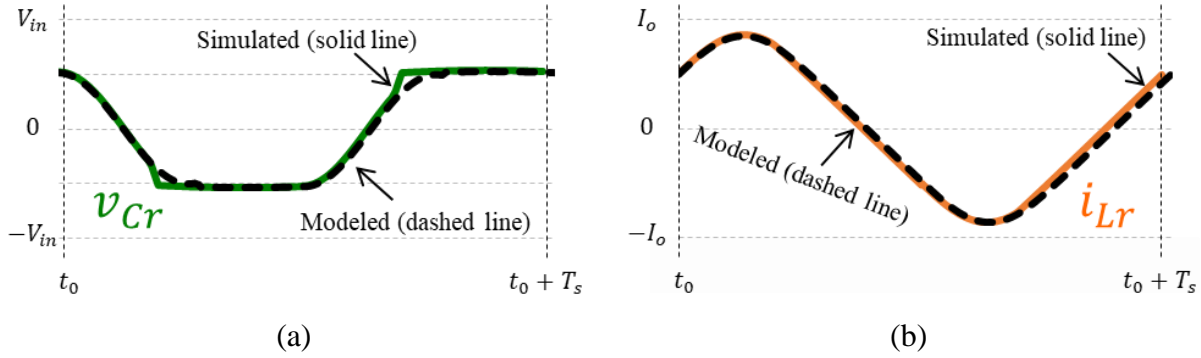


**Fig. 2-14.** The modeled waveforms using the schematic in Fig. 2-1 on page 22 match the simulated ones in the steady state. The waveforms were simulated in LTspice using ideal components with  $V_{in} = 48\text{ V}$ ,  $f_s = 2.0\text{ MHz}$ ,  $V_o = 7\text{ V}$ ,  $I_o = 20\text{ A}$ ,  $L_{oa} = L_{ob} = 1.2\text{ }\mu\text{H}$ ,  $L_r = 150\text{ nH}$ ,  $C_r = 12\text{ nF}$ , and  $C_o = 4\text{ }\mu\text{F}$ . The fine tune of deadtime is not required because ideal components are used.

condition. The error is less than 1%, calculated by one minus Pearson correlation coefficient.

Fig. 2-15 shows the waveforms of resonant capacitor voltage  $v_{Cr}$  and resonant inductor current  $i_{Lr}$  at the 5A load condition. The error is less than 3%, calculated by one minus Pearson correlation coefficient.

The condition  $J = 0.3$  is the worst case in the range of  $0.3 < J < 10$ . The interval length  $\tau_2$  and  $\tau_6$  (approximated to be zero in the model) increases as  $J$  decreases. The magnitude of the normalized control variable  $t_{off}f_r$  has a smaller impact on the error because the load condition dominates in the calculation of  $\tau_2$  and  $\tau_6$ . The error is expected to be more than 3% with  $J < 0.3$ .

The switching frequency error in (2-23) is less than 9%. The error is primarily caused by the assumption of zero  $\tau_2$  and  $\tau_6$ . The equation (2-23) depends on the control variable. A simplified switching cycle equation is presented in Chapter 4 on page 100.

The components  $C_s$ ,  $L_{oa}$ , and  $L_{ob}$  are treated as constant voltage or current sources given the 20% peak-to-peak ripple assumption. The worst-case error is expected to be more than 3% with larger ripples. The model assumes  $\tau_2 = 0$  and  $\tau_6 = 0$ . A larger ripple design reduces the peak current of  $L_r$ , and increases the time needed ( $\tau_2$  and  $\tau_6$ ) to charge  $C_r$ .

The steady-state model for the SRB converter is proven to provide good accuracy, and will help to illustrate the design tradeoff in the power stage design. The steady-state model assumes the inductor peak-to-peak current ripples. The capacitor peak-to-peak voltage ripples are less than 20% of their dc values. Fig. 2-15 confirms the error is less than 3% for the normalized load range larger than 0.3. A smaller load current adds the transition time needed to charge and discharge the switch  $C_{oss}$ , and makes the steady-state model less accurate. Fig. 2-14 and Fig. 2-15 show the error is less than 3% at the border of validity.

## 2.6 Soft-Switching Boundary

The ZVS boundary of the high-side switches  $S_{a1}$  and  $S_{b1}$  can be calculated as follows.

The energy in the resonant tank ( $L_r$  and  $C_r$ ) stored at  $t_2$  should be sufficient to charge  $C_r$  to half of the input voltage  $-V_{in}/2$ :

$$\frac{1}{2}C_r\left(-\frac{V_{in}}{2}\right)^2 \leq \frac{1}{2}L_r I_{Lr@t_2}^2 + \frac{1}{2}C_r V_{Cr@t_2}^2 \quad (2-24)$$

Calculate (2-24) by setting (2-19) equal to zero:

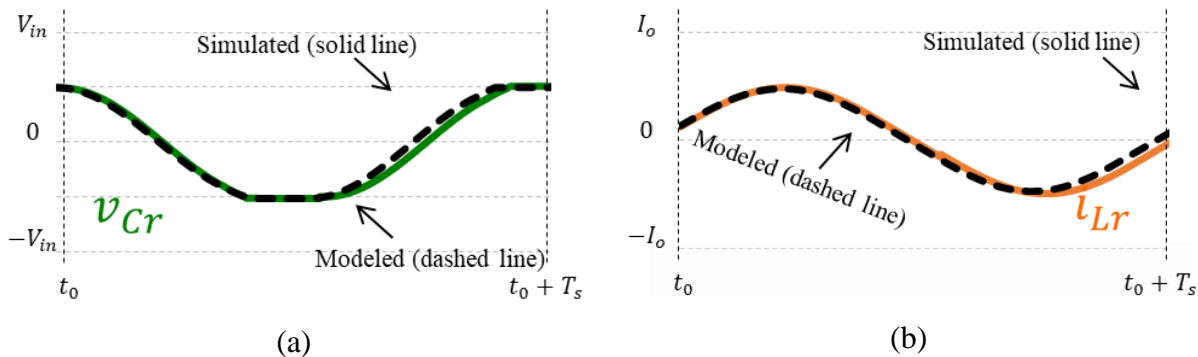


**Fig. 2-15.** The modeled waveforms using the schematic in Fig. 2-1 on page 22 match the simulated ones in the steady state. The waveforms were simulated in LTspice using ideal components with  $V_{in} = 48\text{ V}$ ,  $f_s = 3.1\text{ MHz}$ ,  $V_o = 7\text{ V}$ ,  $I_o = 5\text{ A}$ ,  $L_{oa} = L_{ob} = 1.2\text{ }\mu\text{H}$ ,  $L_r = 150\text{ nH}$ ,  $C_r = 12\text{ nF}$ , and  $C_o = 4\text{ }\mu\text{F}$ . The fine tune of deadtime is not required because ideal components are used.

$$1 \leq (\sin(w_r t_{off}) + J)^2 + (\cos(w_r t_{off}))^2 \quad (2-25)$$

where  $(\sin(w_r t_{off}) + J)^2 + (\cos(w_r t_{off}))^2$  is the energy in the parallel resonant tank normalized by  $C_r(V_{in}/2)^2$ .

The ZVS condition can be further simplified as

$$J \geq -2 \sin(w_r t_{off}) \quad (2-26)$$

The inequality holds for  $0 < w_r t_{off} < \pi$  as the normalized load current  $J \geq 0$ . A minimum load current constraint exists for the other region  $\pi < w_r t_{off} < 2\pi$  or  $\frac{\pi}{w_r} < t_{off} < \frac{2\pi}{w_r}$ . the normalized load current  $J$  needs to satisfy (2-26) for the ZVS condition.

The condition  $J = 0.3$  is the worst case in the range of  $0.3 < J < 10$  for the ZVS equation (2-26). The interval length  $\tau_2$  and  $\tau_6$  (approximated to be zero in the model) increases as  $J$  decreases. The error is expected to be more than 3% with  $J < 0.3$ . The components  $C_s$ ,  $L_{oa}$ , and  $L_{ob}$  are treated as constant voltage or current sources given the 20% peak-to-peak ripple assumption. The worst-case error is expected to be more than 3% with larger ripples (>20%). The model assumes  $\tau_2 = 0$  and  $\tau_6 = 0$ . A larger ripple design reduces the peak current of  $L_r$ , and increases the time needed ( $\tau_2$  and  $\tau_6$ ) to charge  $C_r$ . The equation (2-26) outlines the maximum  $w_r t_{off}$  given the load condition  $J$ . The error caused by the zero-ripple approximation makes the calculated maximum  $w_r t_{off}$  is larger than the simulated one.

Fig. 2-16 shows the minimum normalized load current  $J$  versus normalized control variable  $t_{off} f_r$ . A larger normalized load current is needed as the normalized control variable increases. There is no minimum  $J$  concern for  $w_r t_{off} < \pi$  or  $t_{off} < \frac{\pi}{w_r}$  because the right term in (2-26) goes below zero.

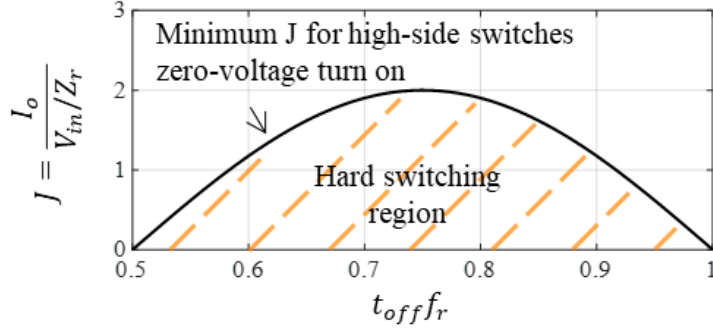


Fig. 2-16. Minimum normalized load current  $J$  calculated by (2-26) for the high-side switch ( $S_{a1}$  and  $S_{b1}$  labeled in Fig. 2-1) soft switching versus normalized control variable  $t_{off}$  defined in Fig. 2-3 normalized by  $1/f_r$ .

## 2.7 Gain Curve

By solving (2-19), the converter voltage gain of the SRB converter is

$$M = \frac{V_o}{V_{in}} = \frac{1}{4} \frac{w_r T_{off} - \sin(w_r T_{off})}{2J + w_r T_{off} + \sin(w_r T_{off})} \quad (2-27)$$

Fig. 2-17 shows voltage gain  $M$  versus the control variable  $t_{off}$  normalized by  $T_r$  using (2-27). The detailed derivation could be found in the Appendix. The condition  $J = 0.3$  is the worst case in the range of  $0.3 < J < 10$ . The interval length  $\tau_2$  and  $\tau_6$  (approximated to be zero in the model) in Fig. 2-4 increases as  $J$  decreases. The normalized control variable  $w_r T_{off}$  have less impact on the gain curve error compared to the normalized load condition  $J$ . The gain curve error was less than 9% at the valid boundary  $J = 0.3$ , and was less than 4% at  $J = 10$ . The error was less than 9% within the range of validity  $0.3 \leq J \leq 10$ .

The voltage gain of the SRB converter is reorganized by lumping the (2-23) as  $T_s$  as

$$M = \frac{1}{2} \frac{T_{off} - \frac{\sin(w_r T_{off})}{w_r}}{T_s} \quad (2-28)$$

The term  $\frac{1}{2} \frac{T_{off} - \frac{\sin(w_r T_{off})}{w_r}}{T_s}$  is the average of the switch node voltage normalized by the input voltage in the SRB converter. The parallel resonant tank brings in large switching ripples which add the sine term into the gain equation. The detailed equation characterizing the switching node voltage is (xxiii) documented in the Appendix.

In a conventional SCB converter, there is a rectangular waveform without a sinusoid component. The average of the switching-node voltage normalized by the input voltage is  $\frac{1}{2} \frac{T_{off}}{T_s}$ . The switching cycle  $T_s$  is controlled by the controller. The voltage gain of the SCB converter is

$$\frac{1}{2} \frac{T_{off}}{T_s} = \frac{D}{2}$$

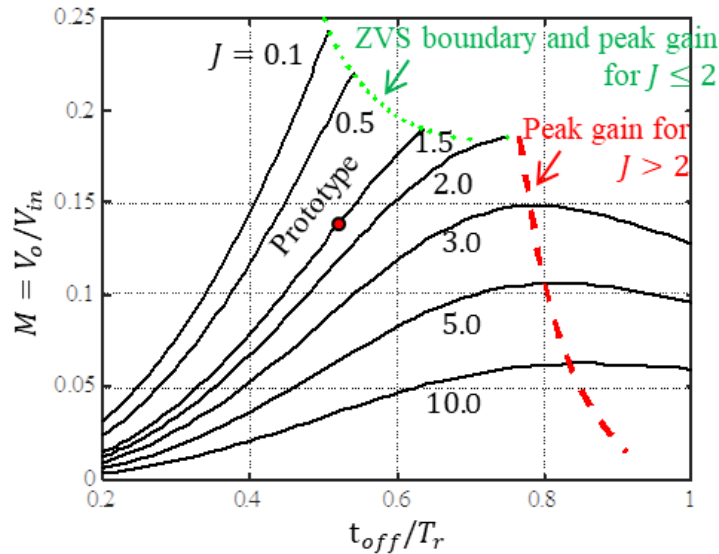


Fig. 2-17. Voltage gain  $M$  calculated by (2-28) versus control variable  $t_{off}$  defined in Fig. 2-3 normalized by  $T_r$ . The boundary of peak gain for  $J \leq 2$  in dotted line is plotted using (2-41). The boundary of peak gain for  $J > 2$  in dashed line is plotted using (2-36).

If the resonant tank is removed from the SRB converter, the  $v_{Cr}$  ripple is set to zero. The SRB

gain  $\frac{1}{2} \frac{T_{off} - \frac{\sin(w_r T_{off})}{w_r}}{T_s} \stackrel{*0}{=} \frac{1}{2} \frac{T_{off}}{T_s}$  is converted into the SCB gain.

Fig. 2-17 shows voltage gain M versus the control variable  $t_{off}$  normalized by  $T_r$ . The gain curves for  $J \leq 2$  end at the ZVS boundary (drawn as a dotted line). The high-side switches lose soft switching beyond the dotted line. The peak gains for  $J > 2$  are connected with the dashed line. There are no soft-switching boundaries for the minimum voltage gain.

A large J corresponds to a large  $L_r$  design resulting in a longer duration for subintervals 4 and 8 which do not deliver energy to the load. Less energy is delivered to the load, and therefore there is a smaller maximum voltage gain. A smaller J results in less energy reserved in resonant inductor  $L_r$  for soft switching in subinterval 2. This results in a limited ZVS region. A smaller J design offers a larger peak voltage gain at the expense of higher resonant tank energy.

The peak gain of the SRB converter is calculated by solving

$$\frac{dM}{dT_{off}} = J + \sin(w_r T_{off}) - J \cos(w_r T_{off}) - w_r T_{off} \cos(w_r T_{off}) = 0 \quad (2-29)$$

The trigonometric functions are approximated at  $\frac{3}{2}\pi < T_{off} f_r < 2\pi$  as follows

$$\sin(w_r T_{off}) \approx \frac{4}{\pi^2} \left( w_r T_{off} - \frac{3}{2}\pi \right)^2 - 1 \quad (2-30)$$

$$\cos(w_r T_{off}) \approx -\frac{4}{\pi^2} (w_r T_{off} - 2\pi)^2 + 1 \quad (2-31)$$

$$w_r T_{off} \cos(w_r T_{off}) \approx -\frac{8}{\pi} (w_r T_{off} - 2\pi)^2 + 2\pi \quad (2-32)$$

The approximations are with errors less than 15% in the range of  $\frac{3}{2}\pi < T_{off} f_r < 2\pi$ .

Two roots of  $dM/dT_{off} = 0$  with the approximated terms are

$$T_{offMPk1} \approx \frac{1}{w_r} \frac{\frac{4J + 8\pi + 3}{\pi} + \sqrt{\left(\frac{4J + 8\pi + 3}{\pi}\right)^2 - 4\frac{J + 2\pi + 1}{\pi^2}(4J + 7.5\pi + 2)}}{2\frac{J + 2\pi + 1}{\pi^2}} \quad (2-33)$$

$$T_{offMPk2} \approx \frac{1}{w_r} \frac{\frac{4J + 8\pi + 3}{\pi} - \sqrt{\left(\frac{4J + 8\pi + 3}{\pi}\right)^2 - 4\frac{J + 2\pi + 1}{\pi^2}(4J + 7.5\pi + 2)}}{2\frac{J + 2\pi + 1}{\pi^2}} \quad (2-34)$$

The first root in (2-33) is not valid as  $T_{offMPk1} > 2\pi/w_r$ . The contour of theoretical peak gain ( $w_r T_{offMPk2}, M_{Pk}(w_r T_{offMPk2}, J)$ ) for  $J > 2$  is drawn in the gain curve plot. According to Fig. 2-17, the difference between the peak gain  $M_{Pk}(w_r T_{offMPk2}, J)$  in red dashed line and approximated peak gain  $M(w_r T_{off} = \frac{3}{2}\pi, J)$  (or  $M(\frac{T_{off}}{T_r} = \frac{3}{4}, J)$ ) is less than 5% under the same J. Use the approximation (2-35) for peak voltage calculations.

$$w_r T_{offMPk2} \approx \frac{3}{2}\pi \quad (2-35)$$

The approximated peak gain for  $J > 2$  is

$$M_{pk} \approx \frac{1}{4} \frac{\frac{3\pi}{2} + 1}{2J + \frac{3\pi}{2} - 1}, \quad J > 2 \quad (2-36)$$

The calculation of the peak gain for  $J \leq 2$  is based on the boundary condition in subinterval

2. The energy in the resonant tank ( $L_r$  and  $C_r$ ) at  $t_2$  should be sufficient to charge  $C_r$  to  $(-V_{in}/2)$ :

$$\frac{1}{2} C_r \left(\frac{V_{in}}{2}\right)^2 \leq \frac{1}{2} L_r I_{Lr@t_2}^2 + \frac{1}{2} C_r V_{Cr@t_2}^2 \quad (2-37)$$

$$V_{Cr@t_2} = \cos(w_r T_{off}) \frac{V_{in}}{2}$$

$$I_{Lr@t_2} = \frac{1}{Z_r} \sin(w_r T_{off}) \frac{V_{in}}{2} + \frac{I_o}{2}$$

The equation can be simplified as

$$(\sin(w_r T_{off}) + J)^2 + (\cos(w_r T_{off}))^2 \geq 1 \quad (2-38)$$

The solution is

$$\sin(w_r T_{off}) \leq -\frac{J}{2} \quad (2-39)$$

or

$$T_{off} \leq \frac{\pi + \arcsin\left(\frac{J}{2}\right)}{w_r} \quad (2-40)$$

The peak gain for  $J \leq 2$  is

$$M_{pk} \approx \frac{1}{4} \frac{\frac{J}{2} + \pi + \arcsin\left(\frac{J}{2}\right)}{\frac{3J}{2} + \pi + \arcsin\left(\frac{J}{2}\right)}, \quad J \leq 2 \quad (2-41)$$

Fig. 2-18 shows the peak voltage gain  $M$  versus the normalized load current  $J$ . The peak voltage gains with  $J \leq 2$  are limited by the ZVS boundary defined in (2-26) outlined by the green dashed line in Fig. 2-17. The peak voltage gains with  $J > 2$  calculated with (2-36) are

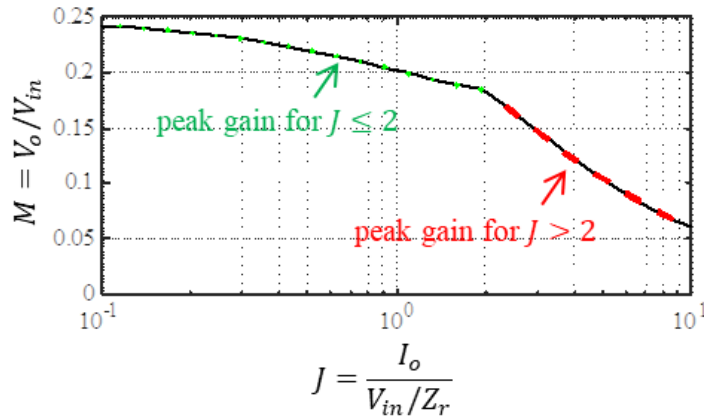


Fig. 2-18. Peak voltage gain calculated by (2-36) and (2-41) versus normalized load current  $J$ .

bounded by the red dashed line in Fig. 2-17. A larger  $J$  design results in a larger  $Z_r$  design. The voltage drop on the resonant tank is larger given the same  $I_o$ , and therefore reduces the maximum voltage gain. The predictions in Fig. 2-18 were compared with the simulation results. The peak gain error was less than 9% at the valid boundary  $J = 0.3$ , and was less than 4% at  $J = 10$ . The error was less than 9% within the range of validity  $0.3 \leq J \leq 10$ .

## 2.8 Experimental Verification

The prototype fabricated based on Table 2-1 is shown in Fig. 2-19. The detailed design procedures and bill of materials are presented in Section 4.8 on page 112. The schematic of the prototype in Fig. 2-19 is in Appendix.

The resonant inductor is the largest component in the converter. The magnetic design has a strong impact on power density and efficiency.

The converter operates at the minimum frequency at 100% load condition as the switching frequency decreases as the load increases.

**Table 2-1. Specifications of the SRB prototype**

Specified Parameters	Definitions	Value
$V_{in}$	Input voltage	48 V
$V_o$	Output voltage	7 V
$I_{oMax}$	Maximum output current	20 A
$I_{oMin}$	Minimum output current	5 A
$f_s$	Switching frequency	2 MHz

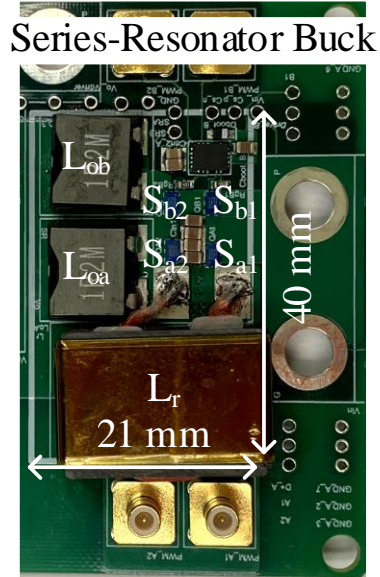


**Fig. 2-19.** The prototype of the Series-Resonator Buck (SRB) converter using the schematic in Fig. 2-1 on page 22 with  $L_{oa} = L_{ob} = 1.2 \mu H$ ,  $L_r = 150 nH$ ,  $C_r = 12 nF$ , and  $C_o = 20 \mu F$ . The maximum height of the prototype is 1 cm.

Fig. 2-19 shows a photo of the SRB prototype. All switches were enhancement-mode power transistor EPC2045 with  $R_{ds(on)} = 7 m\Omega$  and  $C_{oss} = 300 pF$ . A PLT core and an E core with ML-91s material from Hitachi were used to fabricate the resonant inductor  $L_r$ . The resonant capacitor  $C_r$  was eight discrete multilayer ceramic capacitors (CGA3E2NP02A152J080AA) in parallel. The series capacitor  $C_s$  was six discrete capacitors (C3216C0G2A104J160AC) in parallel. The input voltage was provided by the power supply UP60-14. The gate driving signals were provided by the signal generator AFG3102. The switching frequency and duty ratio of the gate signals were tuned until soft switching was achieved.

The measured drain-to-source voltages of all switches are shown in Fig. 2-20. The measurement results were exported from the oscilloscope MSO5104B.

All switches turn on at zero voltage. The area of the power loop and the gate driving loops were minimized to reduce the parasitic loop inductance. The currents in the switches were not

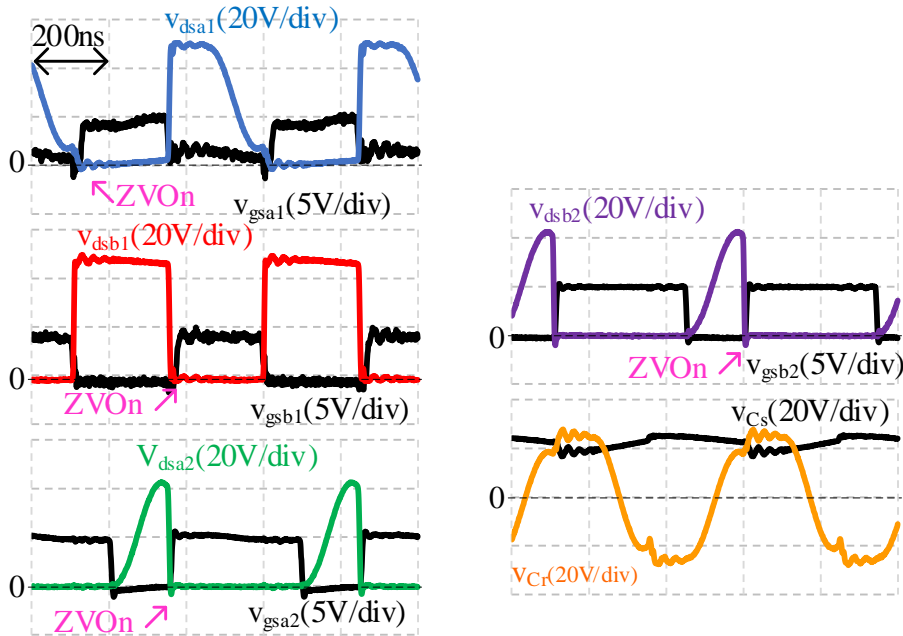


Fig. 2-20. Experimental voltage waveforms for all the switches labeled in Fig. 2-1 were measured by the oscilloscope. The prototype is shown in Fig. 2-19 using the schematic in Fig. 2-1 on page 22 with  $L_{oa} = L_{ob} = 1.2 \mu H$ ,  $L_r = 150 nH$ ,  $C_r = 12 nF$ , and  $C_o = 20 \mu F$  and operated at the specifications in Table 2-1.

measured since the insertion of current probes or shunts was undesirable in a tight layout.

The slopes of  $v_{dsa2}$  and  $v_{dsb2}$  are virtually zero at the off timing, suggesting  $S_{a2}$  and  $S_{b2}$  carried negligible currents at turn-off moments.

## 2.9 Conclusion

The steady-state operation of the SRB converter belongs to the class of quasi-resonant converters. The resonant frequency of the resonant components is higher than the switching frequency. The switch network waveforms are quasi-sinusoidal pulses.

The series resonator in the SRB converter amplifies the switching ripples. The larger ripple allows opportunities for soft switching. The gate-driving signals for the low-side switches of both the SCB and SRB converters are the same, and therefore their off-time ( $t_{off}$ ) is thus recommended

as the unified regulating variable.

Each switched stage of the SRB converter is modeled based on the concept of generalized state-space averaging. The modeled and simulated waveforms are compared. The error is less than 1% at the nominal operating point, and is less than 2% in the worst-case (minimal load condition). The soft-switching boundary of the high-side switches shown in Fig. 2-17 is derived. The analytical equations of the gain curves are presented. The peak voltage gain is limited by the soft-switching boundary of the high-side switches and the design of the resonant tank.

The soft-switching capability of the SRB converter is verified by a 2-MHz converter with 48 V input and 7 V at 20 A output. The measured waveforms demonstrate all the switches are turned on with zero voltage.

## Chapter 3      Transient-State Analysis of the SRB Converter

### Nomenclature

Symbol	Description
$A_i$	State matrix in (2-19) for the $i$ -th interval defined in Fig. 2-3
$B_i$	Input matrix in (2-19) for the $i$ -th interval defined in Fig. 2-3
$C_n$	Capacitance ratio of the resonant capacitor to the series capacitor in (1-3)
$C_o$	Output capacitor in Fig. 3-1
$C_r$	Resonant capacitor in Fig. 3-1
$C_s$	Series capacitor in Fig. 3-1
$d_i$	Subinterval length $(t_{i+1} - t_i)/T_s$ in (3-4)
$D_i$	Subinterval length $(t_{i+1} - t_i)/T_s$ in steady state in (3-19)
$f_{Co}$	Resonant frequency of the output inductor and capacitor in (3-2)
$f_{Cs}$	Resonant frequency of the output inductor and series capacitor in (3-2)
$f_r$	Resonant frequency of the resonant tank in (1-1)
$G_{in2Cs}(s)$	Input-to- $v_{Cs}$ transfer function in (3-24)
$G_{vv}(s)$	Input-to-output transfer function in (3-33)
$G_{vtoff}(s)$	Control-to-output transfer function in (3-38)
$H_{11}$	First element of input matrix associated with $\hat{v}_{in}$ in (3-22)
$H_{12}$	Second element of input matrix associated with $\hat{v}_{in}$ in (3-22)
$H_{13}$	Third element of input matrix associated with $\hat{v}_{in}$ in (3-22)
$H_{21}$	First element of input matrix associated with $\hat{t}_{off}$ in (3-22)
$H_{22}$	Second element of input matrix associated with $\hat{t}_{off}$ in (3-22)
$H_{23}$	Third element of input matrix associated with $\hat{t}_{off}$ in (3-22)
$J$	Normalized load current in (1-2)
$i_{a1}$	Current of switch $S_{a1}$ in Fig. 3-1
$i_{a2}$	Current of switch $S_{a2}$ in Fig. 3-1
$i_{b1}$	Current of switch $S_{b1}$ in Fig. 3-1
$i_{b2}$	Current of switch $S_{b2}$ in Fig. 3-1

$i_{Lr}$	Current of resonant inductor $L_r$ in Fig. 3-1
$i_1$	Equivalent current source in series with $V_{in}$ in Fig. 3-3
$i_2$	Equivalent current source in parallel with $C_s$ in Fig. 3-2
$i_{Loa}$	Current of output inductor $L_{oa}$ in Fig. 3-1
$i_{Lob}$	Current of output inductor $L_{ob}$ in Fig. 3-1
$I_o$	Converter output current consumed by the load in Fig. 3-1
$I_{Loa}$	Large-signal output inductor $L_{oa}$ current in (3-12)
$I_{Lob}$	Large-signal output inductor $L_{ob}$ current in (3-12)
$I_p$	Large-signal output current in (3-16)
$K$	Matrix containing the values of capacitance and inductance in (2-19)
$L_r$	Resonant inductor in Fig. 3-1
$L_{oa}$	Output inductor of the upper phase in Fig. 3-1
$L_{ob}$	Output inductor of the lower phase in Fig. 3-1
$L_n$	Inductance ratio of the resonant inductor to the output inductor in (1-4)
$M$	Voltage gain in Fig. 3-1
$R_e$	Small-signal equivalent resistor in series with output inductor in Fig. 3-15
$R_i$	Small-signal equivalent mutual resistor in Fig. 3-12
$R_{Lo}$	Inductor ESR in Fig. 3-2
$R_{Los}$	Small-signal equivalent inductor series resistor in Fig. 3-12
$R_{load}$	Load resistance in Fig. 3-2
$S_{a1}$	High-side switch of the upper phase in Fig. 3-1
$S_{b1}$	High-side switch of the lower phase in Fig. 3-1
$S_{a2}$	Low-side switch of the upper phase in Fig. 3-1
$S_{b2}$	Low-side switch of the lower phase in Fig. 3-1
$t_i$	Switching timing in Fig. 3-1
$t_{off}$	Off-time of the low-side switches in Fig. 3-1
$t_s$	Switching timing in (3-5)
$T_{off}$	Large signal control variable in (3-15)
$T_s$	Switching period in Fig. 3-1
$x$	State variables in (3-4)

$\dot{x}$	State derivatives in (3-4)
$X$	State variables in steady state in (3-19)
$U$	Input matrix in steady state in (3-19)
$v_1$	Equivalent voltage source in series with $L_{oa}$ in Fig. 3-2
$v_2$	Equivalent voltage source in series with $L_{ob}$ in Fig. 3-2
$v_{Co}$	Voltage of capacitor $C_o$ in Fig. 3-1
$v_{Cr}$	Voltage of capacitor $C_r$ in Fig. 3-1
$v_{Cs}$	Voltage of capacitor $C_s$ in Fig. 3-1
$v_{dsa1}$	Drain-source voltage of switch $S_{a1}$ in Fig. 3-1
$v_{dsa2}$	Drain-source voltage of switch $S_{a2}$ in Fig. 3-1
$v_{dsb1}$	Drain-source voltage of switch $S_{b1}$ in Fig. 3-1
$v_{dsb2}$	Drain-source voltage of switch $S_{b2}$ in Fig. 3-1
$V_{in}$	Input voltage in Fig. 3-1
$V_o$	Output voltage in Fig. 3-1
$V_{Co}$	Large-signal output capacitor voltage in (3-13)
$V_{Cs}$	Large-signal output capacitor voltage in (3-13)
$Z_r$	Characteristic impedance of the resonant tank in (1-2)
$Z_o(s)$	Characteristic impedance of the resonant tank in (1-2)
$\beta_{Cs}$	Scaling factor for $C_s$ in Fig. 3-12
$\beta_{Lo}$	Scaling factor for $L_o$ in Fig. 3-12
$\rho$	A set of derivatives defined in (3-19)
$\tau_i$	Subinterval length $t_{i+1} - t_i$ in Fig. 3-1
$\sigma_1$	Expanding factor in (3-35)
$\sigma_2$	Damping factor in (3-37)
$\sigma_3$	Correction factor in (3-39)
$\hat{d}_i$	Small-signal normalized subinterval length in (3-18)
$\hat{i}_{Loa}$	Small-signal output inductor $L_{oa}$ current in (3-12)
$\hat{i}_{Lob}$	Small-signal output inductor $L_{ob}$ current in (3-12)
$\hat{i}_p$	Small-signal output current in (3-16)

$\hat{t}_{off}$	Small signal control variable in (3-15)
$\hat{u}$	Small signal input matrix in (3-19)
$\hat{u}_1$	First element of small-signal input matrix in (3-19)
$\hat{u}_2$	Second element of small-signal input matrix in (3-19)
$\hat{u}_3$	Third element of small-signal input matrix in (3-19)
$\hat{u}_4$	Fourth element of small-signal input matrix in (3-19)
$\hat{v}_{Co}$	Small-signal output capacitor voltage in (3-13)
$\hat{v}_{Cs}$	Small-signal series capacitor voltage in (3-12)
$\hat{v}_{in}$	Small-signal input voltage in (3-14)
$\hat{x}$	Small-signal state variables in (3-18)

---

### 3.1 Introduction

The transient-state operation of the SRB converter belongs to the class of quasi-resonant converters [96] – [113]. The quasi-square-wave (QSW) converters were introduced in [109], and analyzed using the three-terminal switch model in [110]. The compensator design of QSW converters had depended on simulations until a small-signal equivalent circuit model of the QSW flyback converter was introduced [111]. The model in [111] is good for constant-frequency converters with resonant switches.

The multi-resonant (MR) converter with the multi-resonant switches has been introduced in [112], and it shares some similarities with the Series-Resonator Buck (SRB) converter: load-dependent switching frequency, unknown boundary conditions, and different resonant tanks involved in one switching cycle. No analytic solution for the small-signal transfer function of the MR converter has been given because there is no closed-form solution to the voltage gain equation [113].

This chapter starts with the large-signal modeling of the SRB converter utilizing the concept of generalized state-space averaging. The large-signal equivalent circuit is drawn and discussed.

The large-signal model is then linearized and perturbed for the small-signal analysis. The analytical small-signal transfer functions and equivalent circuits of the SRB converter are presented. The comparison between the small-signal behaviors of the SCB and SRB converters offers insights into the dynamic behavior and the design of the SRB converter.

### 3.2 Large-Signal Modeling with Generalized State-Space Averaging

The following assumptions are made:

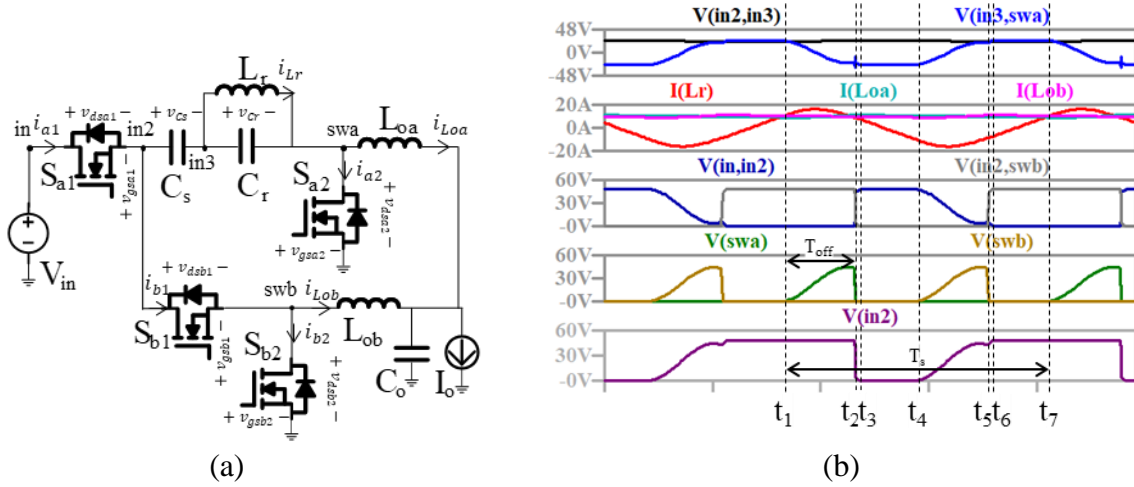
- 1) The peak-to-peak switching ripples of  $v_{CS}$ ,  $i_{Loa}$ , and  $i_{Lob}$  are less than 20% of their dc bias.
- 2) The switching frequency  $f_s$  and the resonant frequency of the resonant elements ( $L_r$  and  $C_r$ ) are more than 10 times larger than the highest natural frequency of the low-pass filter and the series capacitor. The ripples of the state variables  $v_{Co}$ ,  $i_{Loa}$ ,  $i_{Lob}$ , and  $v_{CS}$  are averaged out. All the state variables are treated as constants in one switching cycle.
- 3) Two output inductors are the same and  $L_o = L_{oa} = L_{ob}$ .
- 4) All the switches, capacitors, and inductors are ideal.

Fig. 3-1 shows the schematic of the SRB converter. The simulated waveforms of the state variable labeled in Fig. 3-1(a) are drawn in Fig. 3-1 (b). The  $v_{Cr}$  ripple is twice the value of  $V_{in}$ . The  $v_{CS}$  ripple is 20%  $V_{in}$ . The  $i_{Lr}$  ripple is twice the value of  $I_o$ . The  $i_{Loa}(i_{Lob})$  ripple is 20%  $I_o/2$ . The  $v_{CS}$  and  $i_{Loa}(i_{Lob})$  are treated as dc voltage and current sources because of their small ripples.

The resonant frequency  $f_r$  of the resonant elements is

$$f_r = 1/(2\pi\sqrt{L_r C_r}) \quad (3-1)$$

The natural frequencies  $f_{Co}$  and  $f_{CS}$  of the equivalent circuits of the subintervals in Fig. 3-1 (b) are



**Fig. 3-1. (a) Schematic and (b) state-variable waveforms of the SRB converter with  $V_{in} = 48\text{ V}$ ,  $V_o = 7\text{ V}$ ,  $I_o = 20\text{ A}$ ,  $f_s = 2\text{ MHz}$ ,  $L_{oa} = L_{ob} = 1.2\text{ }\mu\text{H}$ ,  $L_r = 150\text{ nH}$ ,  $C_s = 600\text{ nF}$ ,  $C_r = 12\text{ nF}$ , and  $C_o = 4\text{ }\mu\text{F}$ . The converter was simulated with ideal inductors with  $2\text{ m}\Omega$  equivalent series resistors. Other components were ideal.**

$$f_{Co} = 1/(2\pi\sqrt{C_o L_o/2}) \quad (3-2)$$

$$f_{Cs} = 1/(2\pi\sqrt{C_s L_o/2}) \quad (3-3)$$

The assumption of 20% peak-to-peak switching ripples of  $v_{Cs}$ ,  $i_{Loa}$ , and  $i_{Lob}$  results in  $f_{Co} < 0.1f_s$  and  $f_{Cs} < 0.1f_s$ .

The state variables  $v_{Co}$ ,  $i_{Loa}$ ,  $i_{Lob}$ , and  $v_{Cs}$  are treated as constants in one switching cycle as  $f_{Co} < 0.1f_s$  and  $f_{Cs} < 0.1f_s$ . The model is built in Matlab using the analytical solutions listed in this section. The calculation time of the analytical-based model is significantly smaller than the numerical-based model. The series resonator's state variables are considered as input variables. The low-pass filter state variables are the system state variables.

The switching sequences and operations of the SRB converter are presented in Section 2.4 on page 24. Based on the analysis of the one-switching cycle in Section 2.5 on page 30, the reduced-order state equations of the SRB converter are listed as follows:

$$K\dot{x} = \left\{ \sum_{i=1}^k d_i A_i \right\} x + \frac{1}{t_s} \sum_{i=1}^k \int_{t_{i-1}}^{t_i} B_i(\lambda) d\lambda$$

$$K = \begin{bmatrix} C_s & 0 & 0 & 0 \\ 0 & C_o & 0 & 0 \\ 0 & 0 & L_{oa} & 0 \\ 0 & 0 & 0 & L_{ob} \end{bmatrix}, \dot{x} = \begin{bmatrix} \frac{dv_{Cs}}{dt} \\ \frac{dv_{Co}}{dt} \\ \frac{di_{Loa}}{dt} \\ \frac{di_{Lob}}{dt} \end{bmatrix}, x = \begin{bmatrix} v_{Cs} \\ v_{Co} \\ i_{Loa} \\ i_{Lob} \end{bmatrix},$$

$$A_1 = \begin{bmatrix} 0 & 0 & 1 & 0 \\ 0 & -\frac{1}{R_{load}} & 1 & 1 \\ -1 & -1 & -R_{Loa} & 0 \\ 0 & -1 & 0 & -R_{Lob} \end{bmatrix}, A_2 = A_3 = A_4 = \begin{bmatrix} 0 & 0 & 0 & 0 \\ 0 & -\frac{1}{R_{load}} & 1 & 1 \\ 0 & -1 & -R_{Loa} & 0 \\ 0 & -1 & 0 & -R_{Lob} \end{bmatrix}, \quad (3-4)$$

$$A_5 = \begin{bmatrix} 0 & 0 & 0 & -1 \\ 0 & -\frac{1}{R_{load}} & 1 & 1 \\ 0 & -1 & -R_{Loa} & 0 \\ 1 & -1 & 0 & 0 \end{bmatrix}, A_6 = A_7 = A_8 = \begin{bmatrix} 0 & 0 & 0 & 0 \\ 0 & -\frac{1}{R_{load}} & 1 & 1 \\ 0 & -1 & -R_{Loa} & 0 \\ 0 & -1 & 0 & 0 \end{bmatrix},$$

$$B_1 = \begin{bmatrix} 0 \\ 0 \\ V_{in} - v_{Cr} \\ 0 \end{bmatrix}, B_5 = \begin{bmatrix} 0 \\ 0 \\ 0 \\ v_{Cr} \end{bmatrix}, B_4 = B_8 = \begin{bmatrix} i_{Lr} \\ 0 \\ 0 \\ 0 \end{bmatrix}, B_2 = B_3 = B_6 = B_7 = \begin{bmatrix} 0 \\ 0 \\ 0 \\ 0 \end{bmatrix},$$

where  $d_i$  is defined as  $d_i = \frac{\tau_i}{t_s}$ . There are  $k = 8$  different subintervals in one switching cycle. The

equation (3-4) is first presented as (2-19).

The equation (3-4) listed above is based on the steady-state analysis on page 30. The detailed derivation is documented in Appendix on page 185. The flowchart of the calculation using Matlab code is also attached to the Appendix.

The switching period is calculated as

$$\begin{aligned}
t_s = \sum_{i=1}^k \tau_i = 2t_{off} + \frac{L_r(i_{Loa} + i_{Lob} + \frac{v_{Cs} \sin(\omega_r t_{off})}{Z_r})}{V_{in} - v_{Cs}} \\
+ \frac{L_r(i_{Loa} + i_{Lob} + \frac{(V_{in} - v_{Cs}) \sin(\omega_r t_{off})}{Z_r})}{v_{Cs}}
\end{aligned} \tag{3-5}$$

The equation (3-5) is listed based on the steady-state analysis on page 30. The detailed derivation is documented in Appendix on page 143. This model and its equivalent circuits shown in Fig. 3-2 and Fig. 3-3 are valid within the ZVS boundary characterized in Fig. 2-17. The error in the range of validity is less than 3%, calculated by one minus Pearson correlation coefficient. The large-signal model characterized by (3-5) is converted to an equivalent circuit shown below.

Fig. 3-2 shows the large-signal equivalent circuit of the SRB converter. The dependent sources in the circuit are

$$i_1 = \frac{t_{off}}{t_s} i_{Loa} + \frac{1}{t_s} \int_{t_8}^{t_1} i_{Lr}(\lambda) d\lambda \tag{3-6}$$

$$i_2 = \frac{1}{t_{off}} \left( \int_{t_4}^{t_5} i_{Lr}(\lambda) d\lambda + \int_{t_8}^{t_1} i_{Lr}(\lambda) d\lambda \right) \tag{3-7}$$

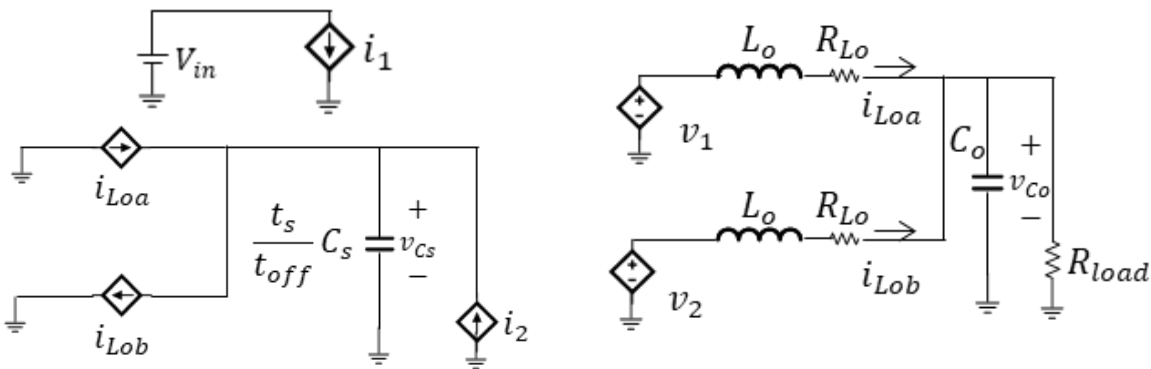


Fig. 3-2. Equivalent circuit of the large-signal model shown in (3-4) of the SRB converter in Fig. 3-1.

$$v_1 = \frac{t_{off}}{t_s}(v_{in} - v_{Cs}) - \frac{1}{t_s} \int_{t_1}^{t_2} v_{Cr}(\lambda) d\lambda \quad (3-8)$$

$$v_2 = \frac{t_{off}}{t_s} v_{Cs} + \frac{1}{t_s} \int_{t_5}^{t_6} v_{Cr}(\lambda) d\lambda \quad (3-9)$$

The equivalent circuit can be viewed as three parts. The ESR of the output inductors is added because it is at least 10 times larger than the ESR of the other components. The other ESR is not included to simplify the equations. The timings in the equations from (3-6) to (3-11) could be solved with the help of the solutions listed in the section on page 30. The detailed calculation is listed in Appendix on page 143.

The first part in the top left of Fig. 3-2 is associated with the input source. The input current drawn from the source is modeled. The dependent source  $i_1$  is calculated by integrating the  $S_{a1}$  current, and divided by  $t_s$ . The equation (3-6) is derived by averaging the sum of the input current in subintervals 1 and 8.

The second part in the bottom left of Fig. 3-2 is associated with the response of the series capacitor  $C_s$ . The equivalent capacitor in Fig. 3-2(a) is impacted by the control variable, and it responds to the difference between the two output inductor currents. The dependent current source  $i_2$  depends on the design of resonant elements  $C_r$  and  $L_r$ . There is no such branch in the conventional SCB converter.

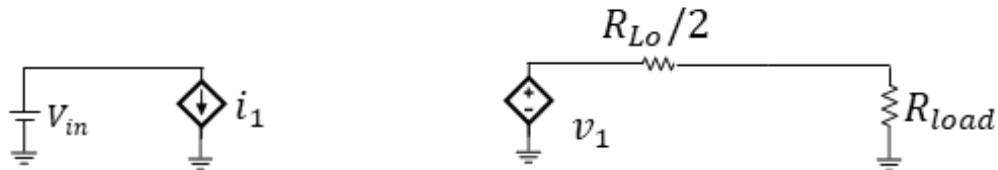


**Fig. 3-3. Steady-state equivalent circuit of the large-signal model shown in (3-4) of the SRB converter in Fig. 3-1. The capacitors are open, and the inductors are shorted in Fig. 3-2.**

The third part in the bottom right of Fig. 3-2(b) is associated with the response of the output capacitor  $C_o$ . The impact of the resonant elements is modeled in the dependent voltage sources  $v_1$  and  $v_2$ . The output capacitor  $C_o$  responds to the sum of the two inductor currents.

Fig. 3-3 shows the equivalent circuit of the large-signal model of the SRB converter in the steady state. The capacitors are opened, and the inductors are shorted in Fig. 3-2. The dependent current source  $i_2$  and the current  $i_{Loa} - i_{Lob}$  are zero according to the steady state solution shown in (2-21). The currents in all the branches are equal to zero in the bottom left circuit in Fig. 3-2. Those branches connected with the series capacitor  $C_s$  can be removed in the steady-state circuit in Fig. 3-3. There are two voltage-dependent sources with equal values in the steady state (according to voltage-second balance) in the right half of Fig. 3-2. Only one branch is needed to characterize the steady-state behavior. The branch with  $v_2$  is removed in Fig. 3-3.

The dependent sources are

$$i_1 = \frac{t_{off}}{t_s} i_{Loa} + \frac{1}{t_s} \int_{t_8}^{t_1} i_{Lr}(\lambda) d\lambda \quad (3-10)$$

$$v_1 = \frac{t_{off}}{t_s} (v_{in} - v_{Cs}) - \frac{1}{t_s} \int_{t_1}^{t_2} v_{Cr}(\lambda) d\lambda \quad (3-11)$$

Fig. 3-4 shows a gate-driving circuit formed by two soft-switching detectors and a timer to control the off time of the low-side switches  $S_{a2}$  labeled in Fig. 3-1.

The circuit in Fig. 3-4 is built in Simplis using Simplis gates. Simplis has built-in models for the eight common gate types: AND, NAND, OR, NOR, XOR, XNOR, Inverter, and Non-inverting Buffer. Each gate type implements both non-inverted and inverted outputs, reducing the actual number of models to four. The switch body diodes are ideal in the simulation. The ideal diode configuration simplifies the gate drive circuits, and complimentary signals can be used to drive the

SRB converter.

The  $S_{a1}$  on timing (when the  $S_{a1}$  channel is turned on) is when the detector in Fig. 3-4 detects  $i_{Lr} > 0$ . The switch current  $i_{a1} = i_{Lr}(C_s + C_r)/C_s$  becomes positive with  $i_{Lr} > 0$ . The gate signal of  $S_{a2}$  is switched to low when  $S_{a1}$  is turned on. The  $S_{a2}$  current goes through the ideal body diode after the  $S_{a2}$  channel is turned off. The current  $i_{Lr}$  goes up after  $S_{a1}$  is turned on. At the moment  $i_{Lr} = i_{Loa}$ , the switch  $S_1$  in the timer in Fig. 3-4 is turned on, and the current of  $S_{a2}$  decreases to zero. The timer (formed by an ideal current source and an ideal current source) starts counting toward  $t_{off}$ . The ratio of the timer capacitor  $C_1$  to the current source  $I_{timer}$  depends on  $t_{offMax}$  (dependent on circuit design) and  $V_{ctoffMax}$  (recommended be in the range of 100 mV to 1 V).

The control variable  $t_{off}$  in Fig. Fig. 2-3(b) on page 23 is programmed by the dc voltage source at the Vctoff node in Fig. 3-4(a). The conversion ratio of  $t_{off}$  to  $V_{ctoff}$  in Fig. 3-4 is

$$\frac{t_{offMax}}{V_{ctoffMax}} = 10^{-6} \text{ s/V}.$$

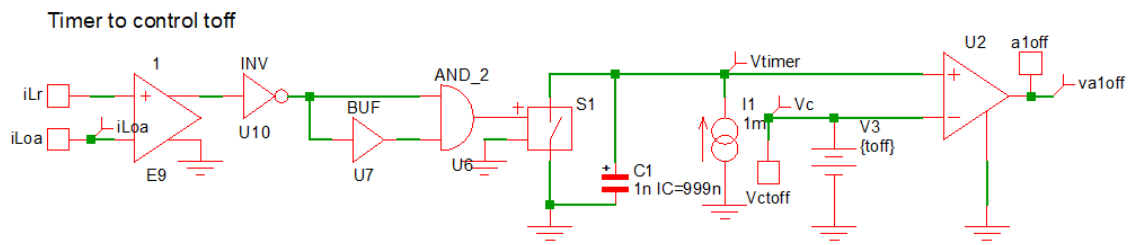
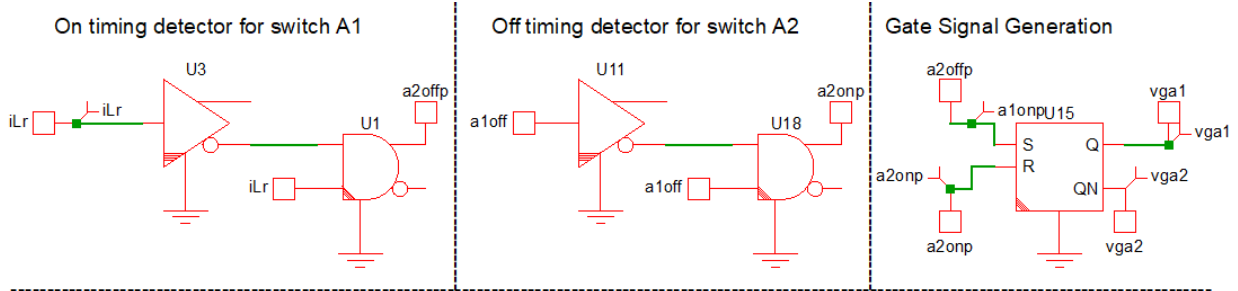
In the example shown in Fig. 3-4, given  $C_1 V_{ctoffMax} = I_{timer} t_{offMax}$ , there is  $\frac{C_1}{I_{timer}} =$

$$\frac{t_{offMax}}{V_{ctoffMax}} = \frac{150 \text{ ns}}{150 \text{ mV}} = 10^{-6} \text{ s/V}.$$

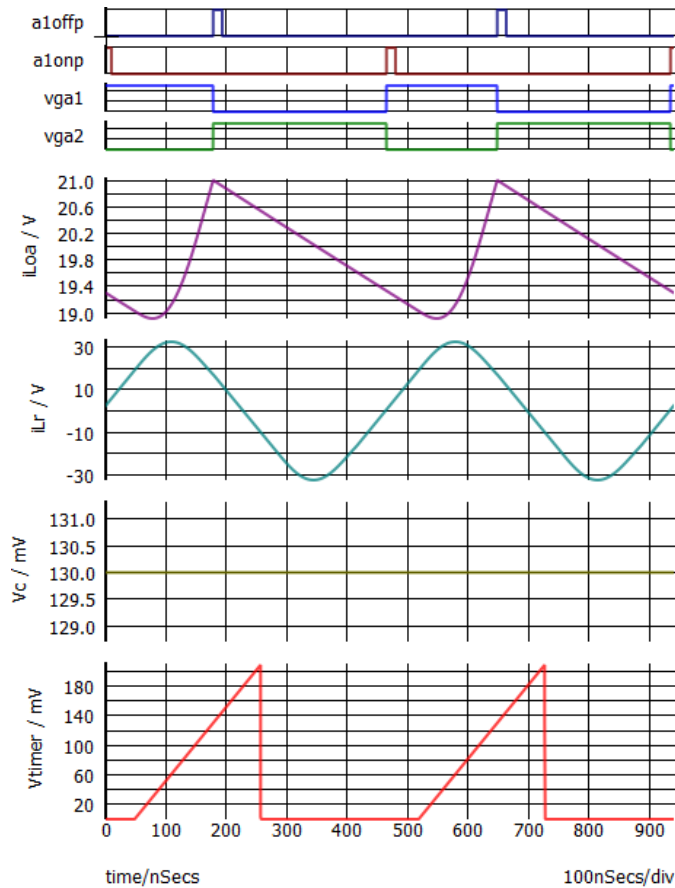
The current source  $I_{timer}$  is designed as 1 mA (recommended be 1 mA – 100 mA), and the timer capacitor  $C_1$  is 1 nF. The off timing for  $S_{a1}$  (on timing for  $S_{a2}$ ) is when the detector in Fig. 3-4 detects  $v_{timer} > v_c$ .

The gate-driving circuit for  $S_{b1}$  replaces  $i_{Loa}$  with  $i_{Lob}$ . The other parts are the same.

Fig. 3-5 shows the modeled and simulated converter state variable waveforms with a step change in  $v_{in}$ . The theoretical waveforms match the results obtained in Simplis. Two output inductor currents are not balanced during the transient period.



(a)



(b)

**Fig. 3-4. Gate-driving circuits with soft-switching detectors and timer for the Simplis simulations in this chapter. The high-side switches  $S_{a1}$  and component currents are labeled in Fig. 3-1.**

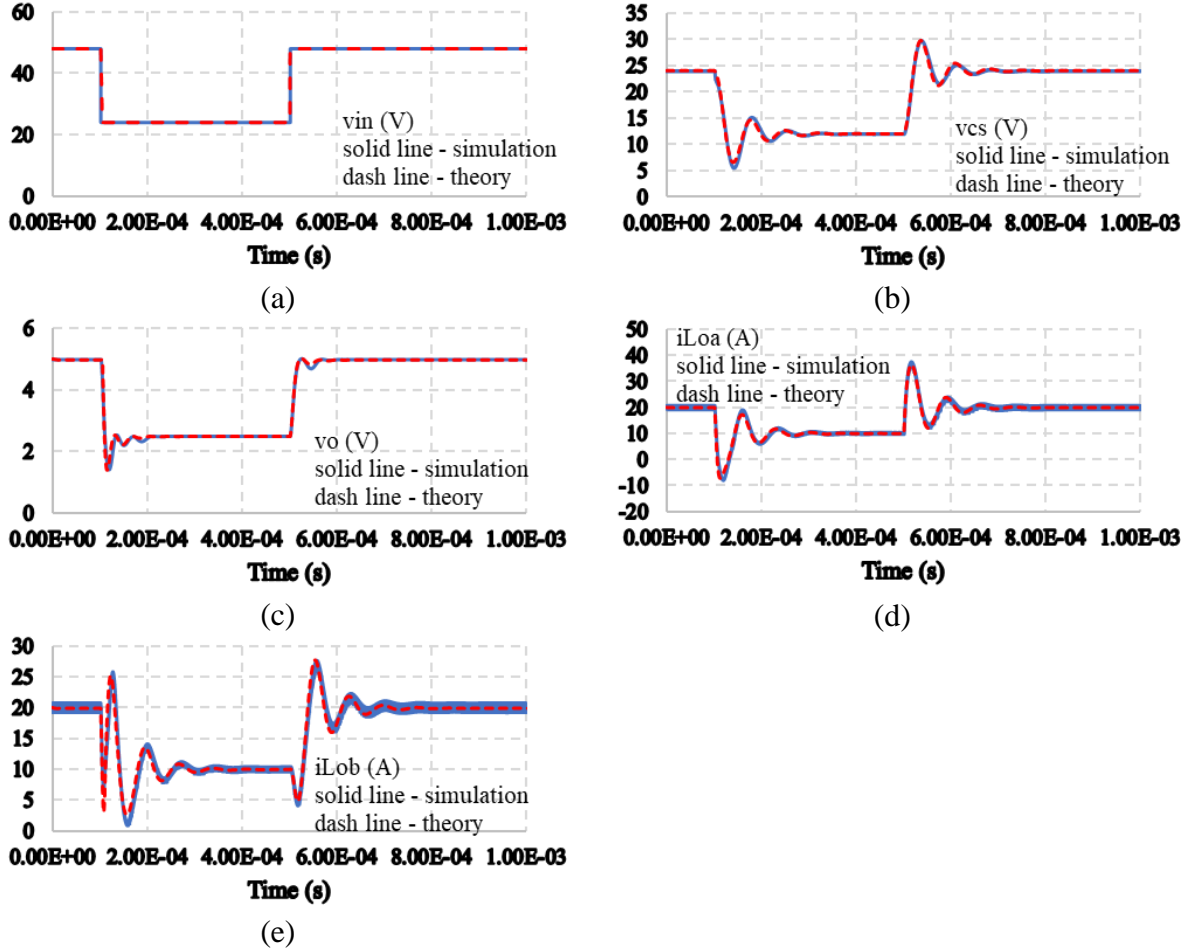


Fig. 3-5. Modeled using (3-4) and simulated converter state variable waveforms when a  $v_{in}$  step change is applied to the SRB converter in Fig. 3-1 on page 55 using the gate driving circuit in Fig. 3-4 on page 61. The control variable  $t_{off} = 120 \text{ ns}$  is set by the dc source V3 with the conversion ratio  $\frac{t_{off}}{v_{ctoff}} = 10^{-6} \frac{\text{s}}{\text{V}}$  in Fig. 3-4 on page 61. The theoretical model using (3-4) matches the simulated results in Simplis with  $V_{in} = 48 \text{ V}$ ,  $\Delta V_{in} = 24 \text{ V}$ ,  $R_{load} = 0.125 \Omega$ ,  $R_{Lo} = 0.01 \Omega$ ,  $L_{oa} = L_{ob} = 1.5 \mu\text{H}$ ,  $L_r = 80 \text{ nH}$ ,  $C_s = 20 \mu\text{F}$ ,  $C_r = 1 \text{ nF}$ , and  $C_o = 47 \mu\text{F}$ .

The waveforms for  $v_{Cs}$  and  $i_{Loa}$  have similar shapes because  $C_s$  is charged by  $i_{Loa}$  in the transient period. The  $i_{Loa}$  becomes negative to offload the energy stored in  $C_s$  at the beginning of the step change. The  $v_{Cs}$  follows the step change of  $v_{in}$ . Its settling time depends on the resonance between  $C_s$  and  $L_{oa}(L_{ob})$ . The control signal  $t_{off}$  is constant during the  $v_{in}$  transient in Fig. 3-5. A more advanced control scheme for smaller settling time of  $v_{in}$  transient is part of the future

work. The  $C_s$  equalizes  $i_{Loa}$  and  $i_{Lob}$  at  $I_o/2$  after  $v_{Cs}$  settles down. The overshoot of  $v_{Cs}$  is higher than that of  $v_{Co}$ . Calculation of the length of individual switching cycles using the large-signal model is not recommended. Error larger than 50% is expected when the SRB converter enters non-ZVS operating region during the transient. A model that characterizes the hard-switching behavior in large-signal transients is part of future work.

Fig. 3-6 shows the modeled and simulated resonant element waveforms with a step change in  $v_{in}$ . The envelopes of  $v_{Cr}$  and  $i_{Lr}$  are modeled, and compared with the results obtained in Simplis.  $i_{Lr}$  peaks in subinterval 1, and bottoms in subinterval 5 (the detailed waveform and equivalent circuit in Section 2.5 on page 30).  $i_{Lr}$  envelop is modeled as  $i_{LrMax} = \frac{v_{cs}}{Z_r} + i_{Loa}$  and  $i_{LrMin} = -\frac{v_{cs}}{Z_r} - i_{Lob}$  which are calculated in each switching cycle.  $v_{Cr}$  peaks in subinterval 8, and bottoms in subinterval 4 (the detailed waveform and equivalent circuit in Section 2.5 on page 30). The  $v_{Cr}$  envelop is modeled as  $v_{CrMax} = v_{in} - v_{cs}$ . The lower envelop is the smaller value of  $-v_{cs}$  and  $-(v_{in} - v_{cs})$ . The waveforms are zoomed-in to show the switching ripples and their envelopes. The theoretical waveforms match the simulation.

Fig. 3-7 shows the modeled and simulated converter state variable waveforms with a step change in  $t_{off}$ . The step change of  $t_{off}$  is added at  $t_{step} = 502\mu s$  in this example. There is no difference if the step change timing  $t_{step}$  is moved to a different timing location (same for the examples in Fig. 3-5 and Fig. 3-8). The theoretical waveforms match the results obtained in Simplis. The low-frequency transient parts of the  $i_{Loa}$  and  $i_{Lob}$  waveforms are similar. Only  $i_{Lob}$  is shown in the figure. Both output inductor currents are balanced in the transient period.  $v_{Cs}$  is constant.

Fig. 3-8 shows the modeled and simulated converter state variable waveforms with a step

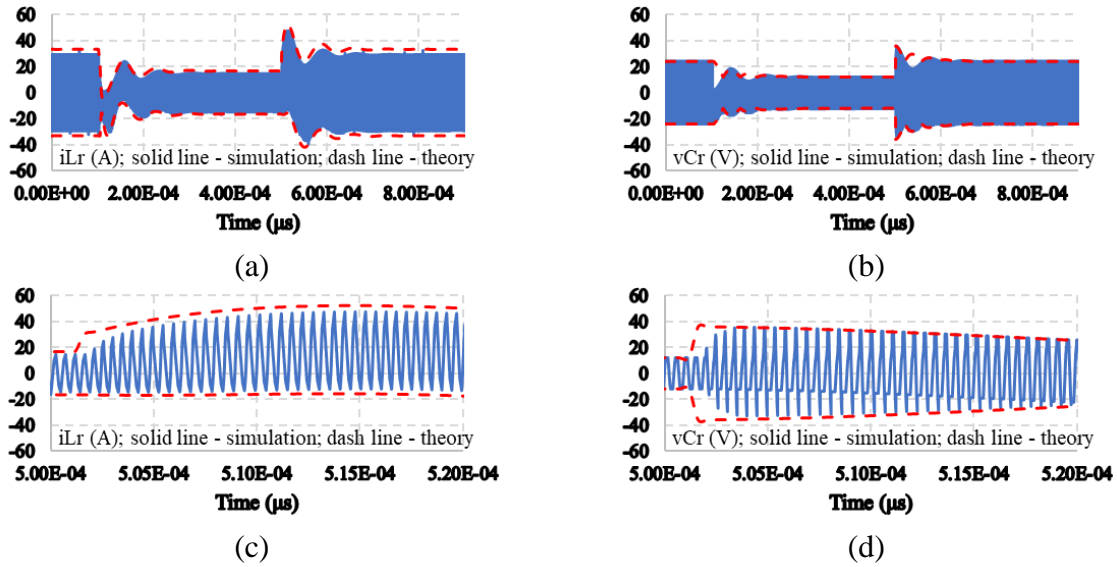


Fig. 3-6. Modeled using (3-4) and simulated resonant element waveforms when a  $v_{in}$  step change is applied to the SRB converter in Fig. 3-1 on page 55 using the gate driving circuit in Fig. 3-4 on page 61. The waveforms are zoomed in to show the switching ripples and their envelopes with  $V_{in} = 48 V$ ,  $\Delta V_{in} = 24 V$ ,  $V_o = 5 V$ ,  $I_o = 40 A$ ,  $L_{oa} = L_{ob} = 1.5 \mu H$ ,  $L_r = 80 nH$ ,  $C_s = 20 \mu F$ ,  $C_r = 21 nF$ , and  $C_o = 47 \mu F$ .

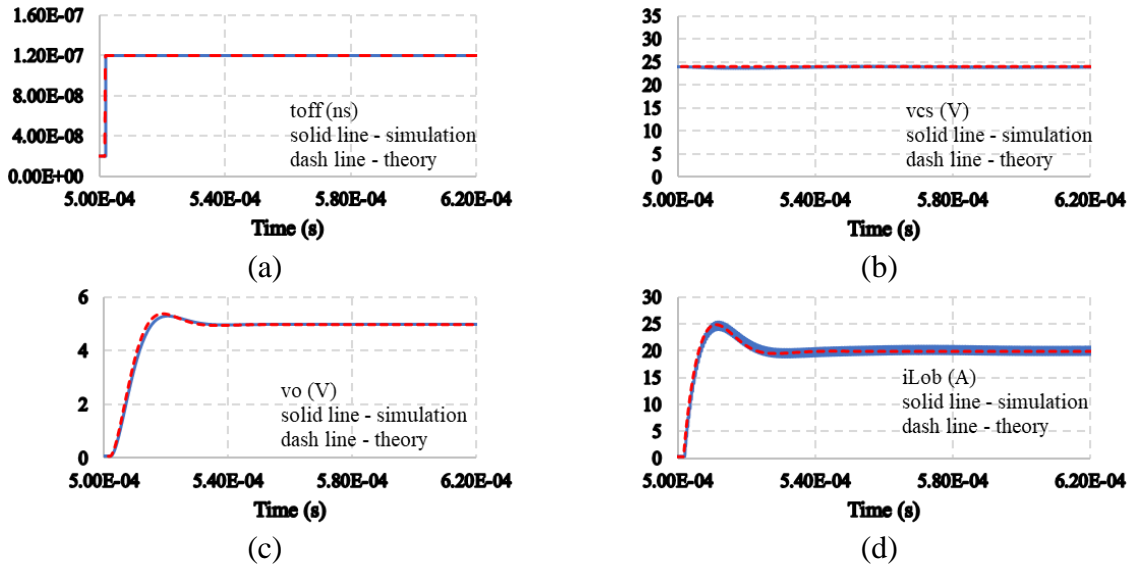


Fig. 3-7. Modeled and simulated converter state variable waveforms when a  $t_{off}$  step change is applied to the SRB converter in Fig. 3-1 on page 55 using the gate driving circuit in Fig. 3-4 on page 61. The control variable  $t_{off} = 120 ns$  is set by the dc source V3 with the conversion ratio  $\frac{t_{off}}{V_{ctoff}} = 10^{-6} \frac{s}{V}$  in Fig. 3-4 on page 61. The theoretical model using (3-4) matches the simulated results in Simplis with  $V_{in} = 48 V$ ,  $t_{off} = 120 ns$ ,  $\Delta t_{off} = 100 ns$ ,  $R_{load} = 0.125 \Omega$ ,  $R_{Lo} = 0.01 \Omega$ ,  $L_{oa} = L_{ob} = 1.5 \mu H$ ,  $L_r = 80 nH$ ,  $C_s = 20 \mu F$ ,  $C_r = 21 nF$ , and  $C_o = 47 \mu F$ .

change in  $i_o$ . The theoretical waveforms match the results obtained in Simplis. The low-frequency transient parts of the  $i_{Loa}$  and  $i_{Lob}$  waveforms are similar. Only  $i_{Lob}$  is shown in the figure. Both output inductor currents are balanced in the transient period as the  $v_{Cs}$  is virtually unchanged.

In Fig. 3-9, the responses of the state variables  $i_{Loa}$ ,  $i_{Lob}$ , and  $v_{Cs}$  are shown for the difference in the design of  $C_n$ . The waveforms with larger ripples in Fig. 3-9(a) are simulated using Simplis. The waveforms with smaller ripples in Fig. 3-9(a) are calculated using (3-4).

The detailed calculation is documented in Appendix on page 185. The calculated waveforms lie in the envelopes outlined by the switching ripples indicating an error that is less than 10%. The calculated ringing matches well with the simulated one. The one with a larger  $C_n$  design in

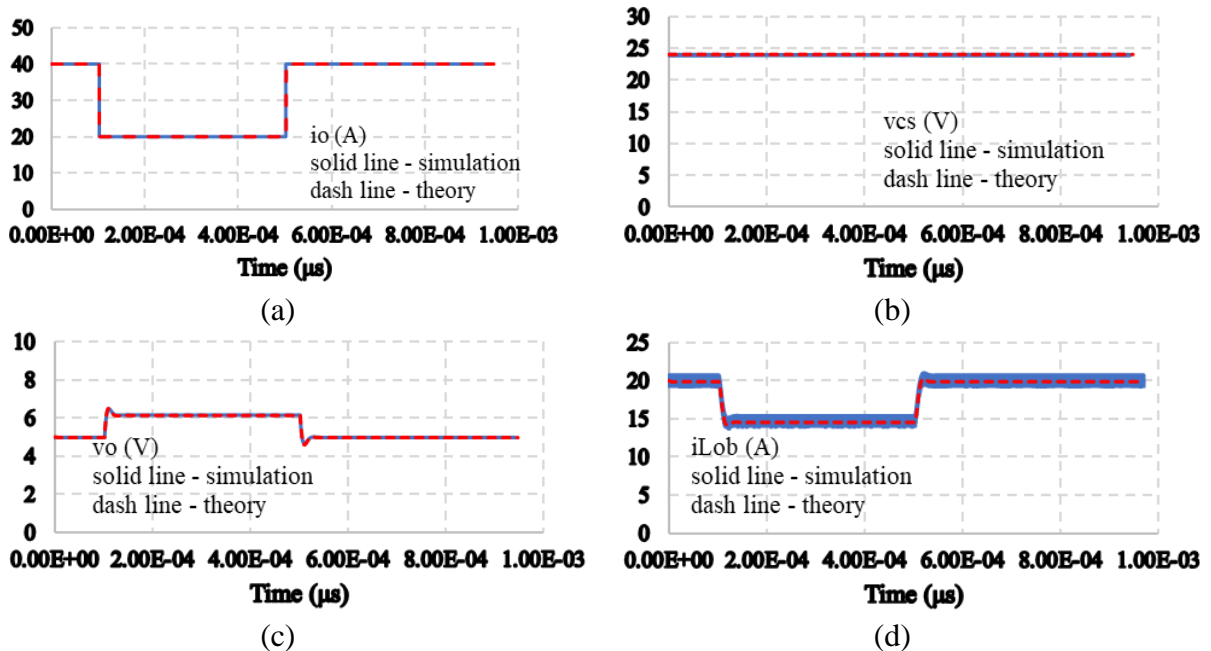


Fig. 3-8. Modeled and simulated converter state variable waveforms when a  $i_o$  step change is applied to the SRB converter in Fig. 3-1 on page 55 using the gate driving circuit in Fig. 3-4 on page 61. The control variable  $t_{off} = 120 \text{ ns}$  is set by the dc source V3 with the conversion ratio  $\frac{t_{off}}{v_{ctoff}} = 10^{-6} \frac{\text{s}}{\text{V}}$  in Fig. 3-4 on page 61. The theoretical model using (3-4) matches the simulated results in Simplis with  $V_{in} = 48 \text{ V}$ ,  $t_{off} = 120 \text{ ns}$ ,  $\Delta i_o = 20 \text{ A}$ ,  $R_{load} = 0.125 \Omega$ ,  $R_{Lo} = 0.05 \Omega$ ,  $L_{oa} = L_{ob} = 1.5 \mu\text{H}$ ,  $L_r = 80 \text{ nH}$ ,  $C_s = 20 \mu\text{F}$ ,  $C_r = 1 \text{ nF}$ , and  $C_o = 47 \mu\text{F}$ .

Fig. 3-9(a) results in a convergence in all state variables. The simulated one settles down slightly faster than the calculated one.

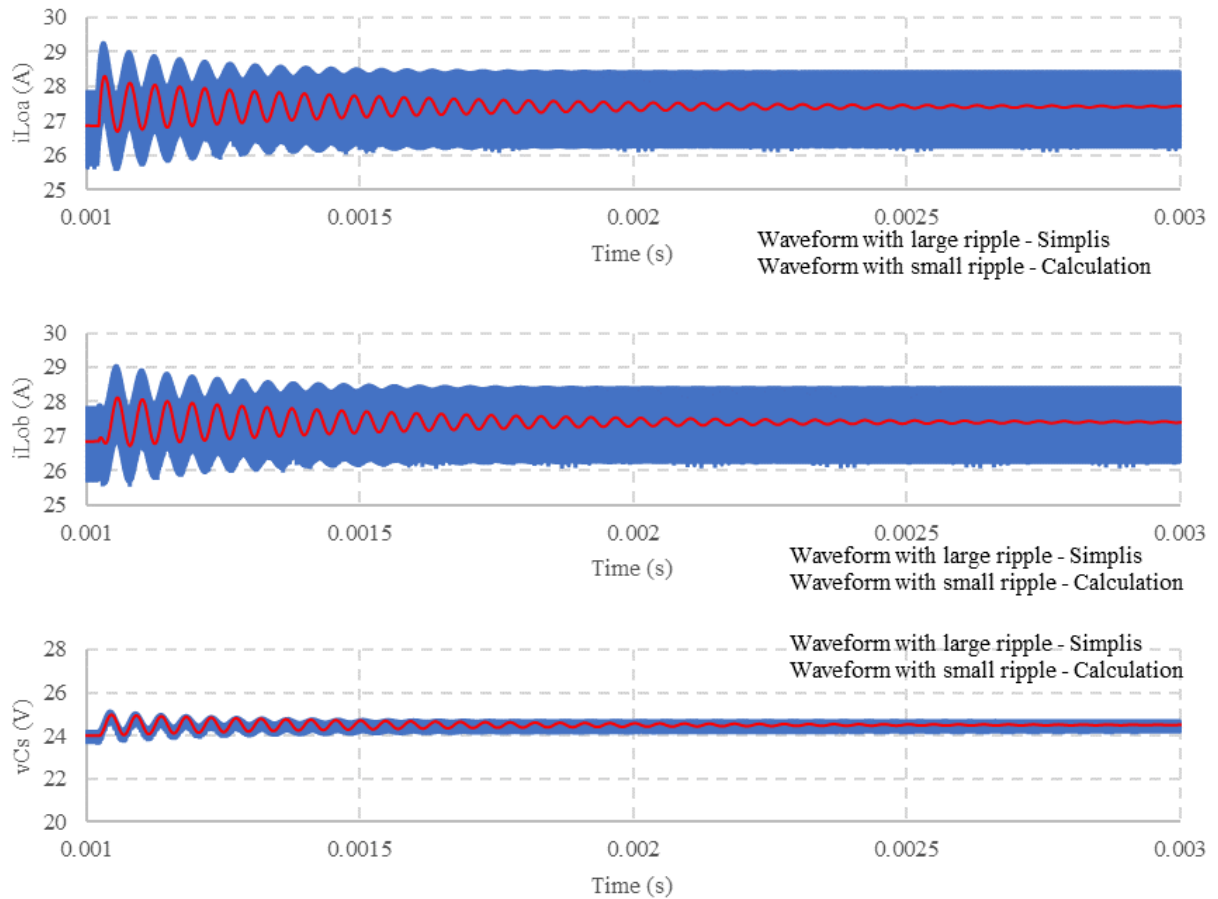
The other one with smaller  $C_n$  design in Fig. 3-9(b) shows divergence. The waveforms with endless oscillation in Fig. 3-9(b) are simulated using Simplis. This oscillation is partly associated with the dependent current source  $i_2$  in Fig. 3-2. The resonant components ( $L_r$  and  $C_r$ ) add a negative damping effect to the equivalent circuit. The waveforms ending at 0.0012s in Fig. 3-9(b) are calculated using (3-4). The error of the calculation increases significantly after the time  $\sim 0.0011$ s. The error is caused by the change in the circuit operation when the state variables diverge. One more switching interval is added between  $t_5$  and  $t_6$  in Fig. 2-4. In the subinterval 5 starting at  $t_5$ , the sum of the capacitor voltages  $v_{Cr} + v_{Cs}$  exceeds the input voltage  $v_{in}$  in the large-signal transient, and forces  $S_{a1}$  to turn on earlier than  $t_6$ . The capacitor voltage  $v_{Cr}$  is then clamped as  $v_{in} = v_{Cr} + v_{Cs}$ . This clamping effect is not modeled in (3-4). The calculated waveforms diverge much faster than the simulated ones.

The magnitude of each step of input voltage, load current, and control variable  $t_{off}$  is up to half of the initial value. The modeled waveform is with less than 10% error with step-down changes. The worst case is the one with the step-down change of the input voltage. The state variables  $v_{Cs}$ ,  $v_{Co}$ ,  $i_{Loa}$ , and  $i_{Lob}$  experience large swings and a larger number of operating points. The error is expected to be higher than 3% at the operating point with  $i_{Loa}$  and  $i_{Lob}$  smaller than 5A which makes  $\tau_2$  and  $\tau_6$  larger.

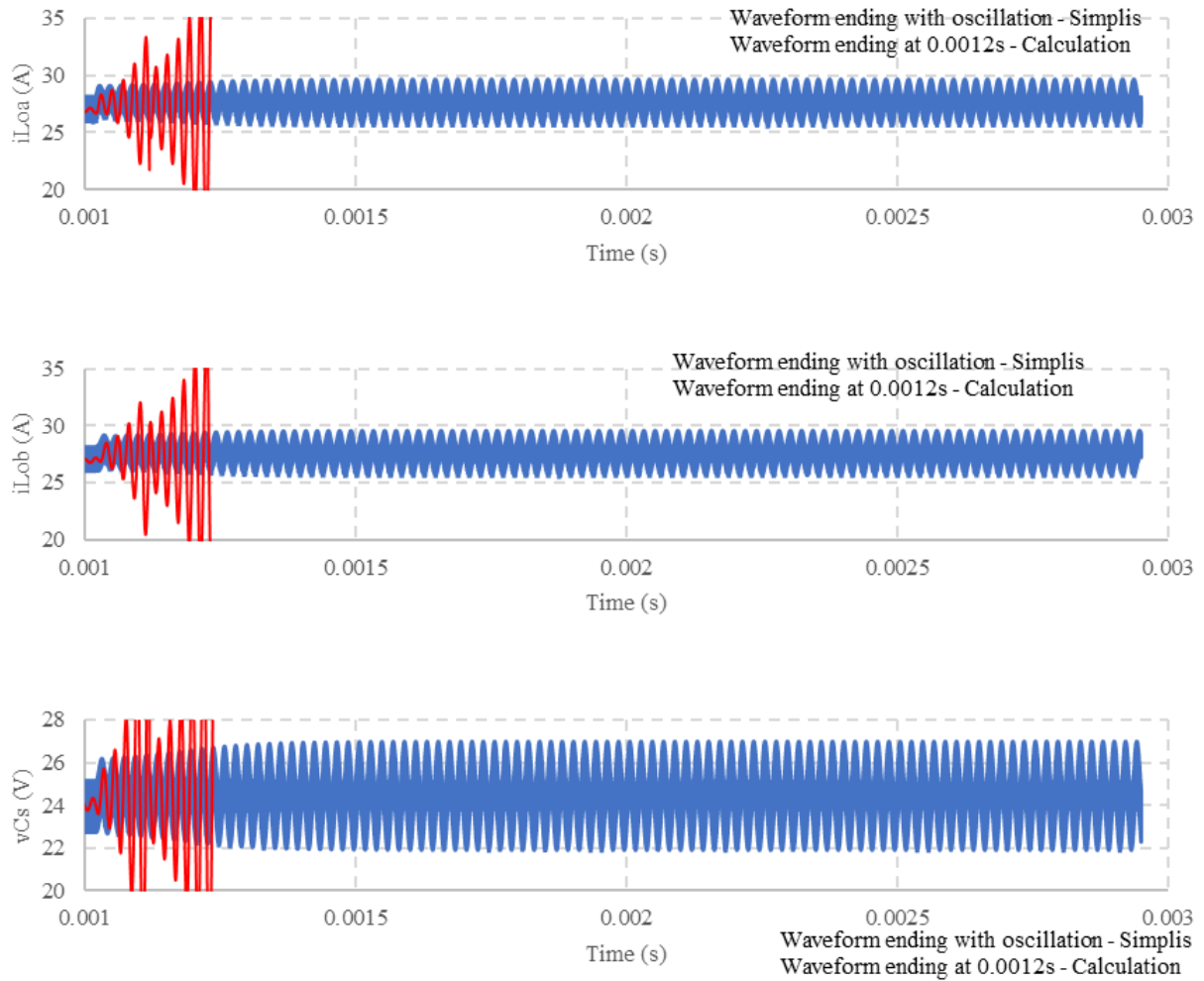
The model assumes the peak-to-peak ripples of  $i_{Loa}$ ,  $i_{Lob}$ , and  $v_{Cs}$  are less than 20% of their dc values. The error will grow larger if the ripple size exceeds 20%. The model assumes  $\tau_2 = 0$  and  $\tau_6 = 0$ . A larger ripple design reduces the peak current of  $L_r$ , and increases the time needed ( $\tau_2$  and  $\tau_6$ ) to charge  $C_r$ .

The error exceeds 10% when the SRB converter operates outside the ZVS region labeled in Fig. 2-17. The boundary conditions at each subinterval are not valid with the hard-switching operation. A large control variable  $t_{off}f_r > 0.5$  may cause error higher than 10% as shown in Fig. 3-9. Excessive energy is pumped into the series resonator, and forces  $S_{a1}$  to turn on earlier than  $t_6$  in Fig. 2-4. This extra switching interval is not modeled. This interval is not shown up with  $t_{off}f_r < 0.5$ , and therefore the error is smaller than 10%.

Fig. 3-10 shows the minimum design requirement of the capacitance ratio  $C_n$ . The area with green stripes refers to a good design region with good convergence.



(a)



(b)

**Fig. 3-9.** The SRB converter in Fig. 3-1 on page 55 and the gate driving circuit in Fig. 3-4 on page 61 with (a) convergence using  $C_n = 500$  and with (b) divergence using  $C_n = 100$ . The waveforms were simulated in Simplis with  $V_{in} = 48\text{ V}$ ,  $t_{off} = 150\text{ ns}$ ,  $R_{load} = 0.125\ \Omega$ ,  $L_{oa} = L_{ob} = 1.5\ \mu\text{H}$ ,  $R_{Lo} = 0.02\ \Omega$ ,  $L_r = 80\text{ nH}$ ,  $C_r = 20\text{ nF}$ , and  $C_o = 47\ \mu\text{F}$ . A 1-V step change in the input voltage is applied at  $t = 1\text{ ms}$ . The control variable  $t_{off}$  is set by the dc source V3 with the conversion ratio  $\frac{t_{off}}{V_{ctoff}} = 10^{-6}\ \frac{\text{s}}{\text{V}}$  in Fig. 3-4 on page 61.

A design with good convergence is a case in which no low-frequency oscillations at 1 ms after the step change is introduced. The output inductor equivalent series resistors (ESR) were modeled as  $10\text{ m}\Omega$  in Fig. 3-10. Simplis is used to find out the minimum  $C_n$  to avoid constant oscillations of the state variables at a given control variable  $t_{off}f_r$ . This figure shows three curves that correspond to three different  $L_n$  designs. Larger  $L_n$  requires a larger  $C_n$  as specified in Fig. 3-10 for a good convergent design. A design with  $L_n > 20$  results in an output inductor ripple smaller than 10%. It requires large inductance, and is not practical. A larger control variable  $t_{off}f_r$  makes the SRB converter more susceptible to divergence.

The minimum  $C_n$  needed for convergence decreases in the cases with an output inductor ESR larger than  $10\text{ m}\Omega$ . The design curves of minimum  $C_n$  are expected to be shifted higher with an

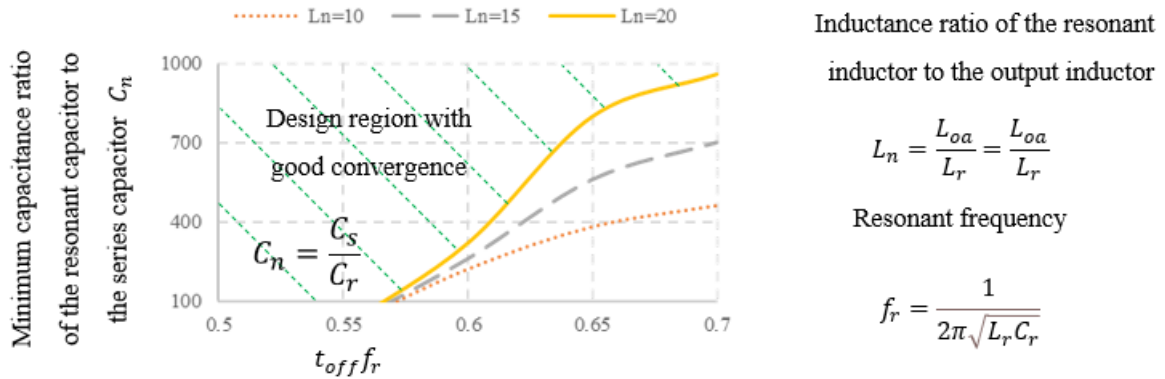
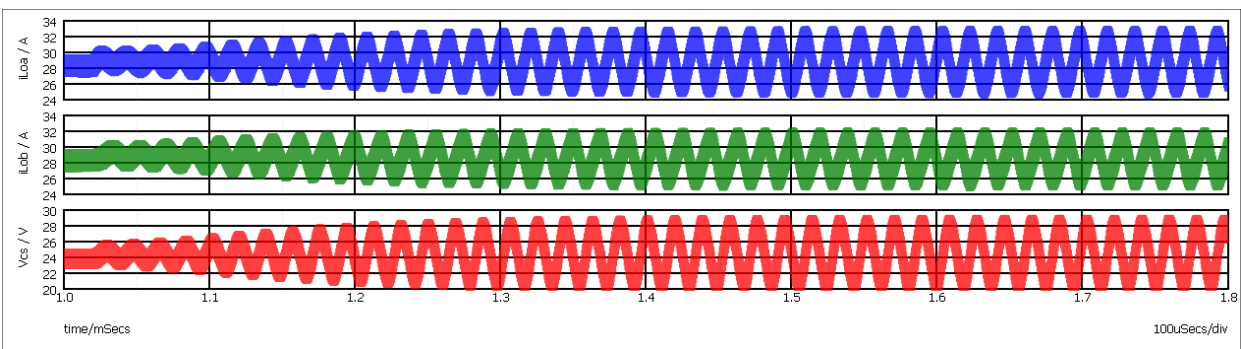


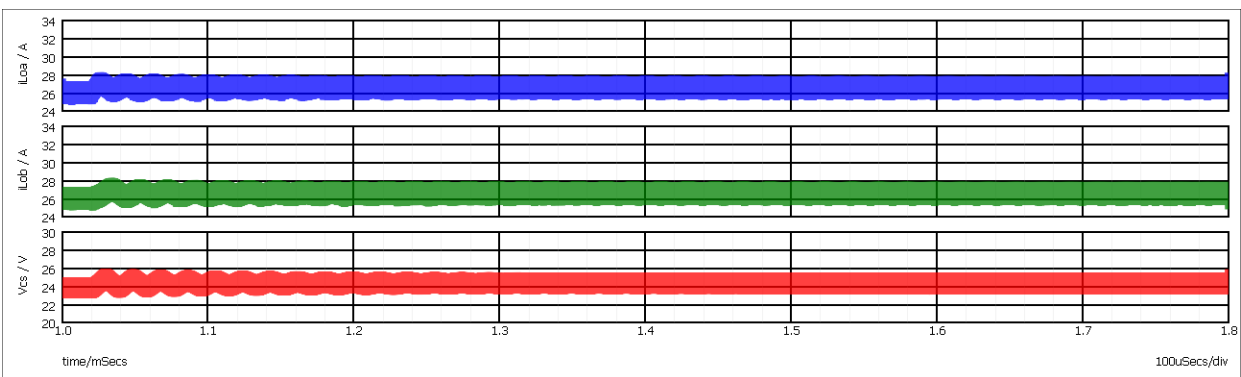
**Fig. 3-10.** Minimum  $C_n$  defined in (1-3) on page 9 for convergence versus control variable  $t_{off}$  defined in Fig. 2-3 on page 23 normalized by  $\frac{1}{f_r}$  parametric with  $L_n$  defined in (1-4) on page 10 for the design of the SRB converter in Fig. 3-1 on page 55. The region with good convergence as shown in Fig. 3-8(a) is shaped in green. The graph was simulated using Simplis with  $V_{in} = 48\text{ V}$ ,  $R_{load} = 0.125\ \Omega$ ,  $L_r = 80\text{ nH}$ ,  $C_r = 20\text{ nF}$ , and  $C_o = 47\ \mu\text{F}$ . The control variable  $t_{off}$  is set by the dc source V3 with the conversion ratio  $\frac{t_{off}}{V_{ctoff}} = 10^{-6} \frac{\text{s}}{\text{V}}$  in Fig. 3-4 on page 61.

ESR value smaller than  $10\text{ m}\Omega$ . The converter shows divergent issues with an inductor ESR of zero, given the practical  $C_n$  design ( $C_n < 10000$ ). It is not recommended to increase the inductor's ESR for a good convergence design as the ESR varies with the inductor design.

Fig. 3-11 compares the SRB converter operating in two different operating conditions. One operating condition results in good convergence with not oscillations in the state variables. The



(a)



(b)

**Fig. 3-11.** The SRB converter in Fig. 3-1 on page 55 using the gate driving circuit in Fig. 3-4 on page 61 with (a) divergence using  $t_{off}f_r = 0.6$  and with (b) convergence using  $t_{off}f_r = 0.55$ . The waveforms were simulated in Simplis with  $V_{in} = 48\text{ V}$ ,  $R_{load} = 0.125\ \Omega$ ,  $L_{oa} = L_{ob} = 1.5\ \mu\text{H}$ ,  $C_n = 100$ ,  $R_{Loa} = R_{Lob} = 0$ ,  $L_r = 80\ \text{nH}$ ,  $C_r = 20\ \text{nF}$ , and  $C_o = 47\ \mu\text{F}$ . A 1 V step change in the input voltage is applied at  $t = 1\ \text{ms}$ .

other operating condition leads to a divergence behavior. Zero inductor ESR resistance is assumed.

Fig. 3-11(a) shows divergence with a control variable  $t_{off}f_r = 0.6$ . The output inductor currents oscillate with the series capacitor voltage.

A condition of  $t_{off}f_r < 0.55$  could be used to design for stable according to Fig. 3-10. The  $C_n$  design for good convergence does not depend on the  $L_n$  design. It is recommended for stability because this condition has little impact on the other design parameters or converter performance such as efficiency, component stresses, and load regulation.

One limitation of adding this condition is that the maximum voltage gain at minimal circulating operation  $J = 1.5$  (this topic will be discussed in Chapter 4) reduces by about 8%. However, this negative impact is trivial. Typically, that 8% region is not recommended because some margin is needed in a practical design. The condition of  $t_{off}f_r < 0.55$  has no impact on the light load condition.

Some advanced control schemes could be used to bring in an extra damping effect to the SRB converter to avoid divergence in certain operating regions. This will be part of future work.

Fig. 3-11(b) shows the divergence is turned into convergence by reducing the  $t_{off}f_r$  to 0.55. The output inductor currents and the series capacitor voltage settle down. Fig. 3-11(b) uses the same scale in Fig. 3-11(a) for easy comparison.

It is therefore recommended to design  $t_{off}f_r < 0.55$  ensuring a good convergence of  $v_{Cr}$ ,  $i_{Loa}$ , and  $i_{Lob}$ .

### 3.3 Small-Signal Modeling of the SRB Converters

To perform small-signal analysis, the following perturbations are introduced:

$$i_{Loa} = I_{Loa} + \hat{i}_{Loa}, i_{Lob} = I_{Lob} + \hat{i}_{Lob} \quad (3-12)$$

$$v_{Co} = V_{Co} + \hat{v}_{Co}, v_{Cs} = V_{Cs} + \hat{v}_{Cs} \quad (3-13)$$

$$v_{in} = V_{in} + \hat{v}_{in} \quad (3-14)$$

$$t_{off} = T_{off} + \hat{t}_{off} \quad (3-15)$$

$$i_p = I_p + \hat{i}_p \quad (3-16)$$

The following assumptions are made

$$I_{Lo} \gg \hat{i}_{Lo}, V_{Co} \gg \hat{v}_{Co}, V_{in} \gg \hat{v}_{in}, T_{off} \gg \hat{t}_{off}, I_p \gg \hat{i}_p \quad (3-17)$$

where capital letters are dc steady-state components. The load current is  $I_p = \frac{V_o}{R_{load}}$ .

$\hat{i}_{Lo}, \hat{v}_{Co}, \hat{v}_{in}, \hat{t}_{off}$ , and  $\hat{i}_p$  are the small-signal perturbations.

Small signal perturbations are added into the GSSA equation yields:

$$K \left( \frac{dX}{dt} + \frac{d\hat{x}}{dt} \right) = \left\{ \sum_{i=1}^k (D_i + \hat{d}_i) A_i \right\} (X + \hat{x}) + (U + \hat{u}) \quad (3-18)$$

The second and higher-order terms of the small-signal perturbations are neglected. The ac small-signal state equation is

$$K \frac{d\hat{x}}{dt} = \left\{ \sum_{i=1}^k \hat{d}_i A_i \right\} X + \left\{ \sum_{i=1}^k D_i A_i \right\} \hat{x} + \hat{u} \quad (3-19)$$

$$K = \begin{bmatrix} C_s & 0 & 0 & 0 \\ 0 & C_o & 0 & 0 \\ 0 & 0 & L_{oa} & 0 \\ 0 & 0 & 0 & L_{ob} \end{bmatrix}, \hat{x} = \begin{bmatrix} \hat{v}_{Cs} \\ \hat{v}_{Co} \\ \hat{i}_{Loa} \\ \hat{i}_{Lob} \end{bmatrix}, X = \begin{bmatrix} V_{Cs} \\ V_{Co} \\ I_{Loa} \\ I_{Lob} \end{bmatrix}, \hat{u} = \begin{bmatrix} \hat{u}_1 \\ \hat{u}_2 \\ \hat{u}_3 \\ \hat{u}_4 \end{bmatrix}$$

$$A_1 = \begin{bmatrix} 0 & 0 & 1 & 0 \\ 0 & -\frac{1}{R_{load}} & 1 & 1 \\ -1 & -1 & 0 & 0 \\ 0 & -1 & 0 & 0 \end{bmatrix}, A_2 = A_3 = A_4 = \begin{bmatrix} 0 & 0 & 0 & 0 \\ 0 & -\frac{1}{R_{load}} & 1 & 1 \\ 0 & -1 & 0 & 0 \\ 0 & -1 & 0 & 0 \end{bmatrix},$$

$$A_5 = \begin{bmatrix} 0 & 0 & 0 & -1 \\ 0 & -\frac{1}{R_{load}} & 1 & 1 \\ 0 & -1 & 0 & 0 \\ 1 & -1 & 0 & 0 \end{bmatrix}, A_6 = A_7 = A_8 = \begin{bmatrix} 0 & 0 & 0 & 0 \\ 0 & -\frac{1}{R_{load}} & 1 & 1 \\ 0 & -1 & 0 & 0 \\ 0 & -1 & 0 & 0 \end{bmatrix},$$

$$B_1 = \begin{bmatrix} 0 \\ 0 \\ V_{in} - v_{Cr} \\ 0 \end{bmatrix}, B_5 = \begin{bmatrix} 0 \\ 0 \\ 0 \\ v_{Cr} \end{bmatrix}, B_4 = B_8 = \begin{bmatrix} i_{Lr} \\ 0 \\ 0 \\ 0 \end{bmatrix}, B_2 = B_3 = B_6 = B_7 = \begin{bmatrix} 0 \\ 0 \\ 0 \\ 0 \end{bmatrix},$$

$$\frac{d\hat{x}}{dt} = \begin{bmatrix} \frac{d\hat{v}_{Cs}}{dt} \\ \frac{d\hat{v}_{Co}}{dt} \\ \frac{d\hat{i}_{Loa}}{dt} \\ \frac{d\hat{i}_{Lob}}{dt} \end{bmatrix}, \sum_{i=1}^k D_i A_i = \begin{bmatrix} 0 & 0 & \frac{T_1}{T_s} & -\frac{T_4}{T_s} \\ 0 & -\frac{1}{R_{load}} & 1 & 1 \\ -\frac{T_1}{T_s} & -1 & -R_{Loa} & 0 \\ \frac{T_4}{T_s} & -1 & 0 & -R_{Lob} \end{bmatrix},$$

$$\rho = \frac{\partial \frac{t_{off}}{T_s}}{\partial v_{Cs}} \hat{v}_{Cs} + \frac{\partial \frac{t_{off}}{T_s}}{\partial i_{Loa}} \hat{i}_{Loa} + \frac{\partial \frac{t_{off}}{T_s}}{\partial i_{Lob}} \hat{i}_{Lob} + \frac{\partial \frac{t_{off}}{T_s}}{\partial v_{in}} \hat{v}_{in} + \frac{\partial \frac{t_{off}}{T_s}}{\partial t_{off}} \hat{t}_{off},$$

$$\sum_{i=1}^k \hat{d}_i A_i = \begin{bmatrix} 0 & 0 & \rho & -\rho \\ 0 & 0 & 0 & 0 \\ -\rho & 0 & 0 & 0 \\ \rho & 0 & 0 & 0 \end{bmatrix}, U = \begin{bmatrix} u_1 \\ u_2 \\ u_3 \\ u_4 \end{bmatrix}, u_i = \frac{1}{t_s} \sum_{i=1}^k \int_{t_{i-1}}^{t_i} B_i(\lambda) d\lambda$$

$$\hat{u} = \begin{bmatrix} \hat{u}_1 \\ \hat{u}_2 \\ \hat{u}_3 \\ \hat{u}_4 \end{bmatrix} = \begin{bmatrix} \frac{\partial u_1}{\partial v_{Cs}} \hat{v}_{Cs} + \frac{\partial u_1}{\partial i_{Loa}} \hat{i}_{Loa} + \frac{\partial u_1}{\partial i_{Lob}} \hat{i}_{Lob} + \frac{\partial u_1}{\partial v_{in}} \hat{v}_{in} + \frac{\partial u_1}{\partial t_{off}} \hat{t}_{off} \\ \hat{i}_p \\ \frac{\partial u_3}{\partial v_{Cs}} \hat{v}_{Cs} + \frac{\partial u_3}{\partial i_{Loa}} \hat{i}_{Loa} + \frac{\partial u_3}{\partial i_{Lob}} \hat{i}_{Lob} + \frac{\partial u_3}{\partial v_{in}} \hat{v}_{in} + \frac{\partial u_3}{\partial t_{off}} \hat{t}_{off} \\ \frac{\partial u_4}{\partial v_{Cs}} \hat{v}_{Cs} + \frac{\partial u_4}{\partial i_{Loa}} \hat{i}_{Loa} + \frac{\partial u_4}{\partial i_{Lob}} \hat{i}_{Lob} + \frac{\partial u_4}{\partial v_{in}} \hat{v}_{in} + \frac{\partial u_4}{\partial t_{off}} \hat{t}_{off} \end{bmatrix}$$

in which

$$\frac{\partial \frac{t_{off}}{T_s}}{\partial v_{Cs}} = 0$$

$$\frac{\partial \frac{t_{off}}{T_s}}{\partial i_{Loa}} = - \left( \frac{1 F_s}{\pi F_r} \right)^2 (w_r T_{off}) \frac{Z_r}{V_{in}}$$

$$\frac{\partial \frac{t_{off}}{T_s}}{\partial i_{Lob}} = \frac{\partial \frac{t_{off}}{T_s}}{\partial i_{Loa}}$$

$$\frac{\partial \frac{t_{off}}{T_s}}{\partial v_{in}} = \left( \frac{1 F_s}{\pi F_r} \right)^2 (w_r T_{off}) \frac{J}{V_{in}}$$

$$\frac{\partial \frac{t_{off}}{T_s}}{\partial t_{off}} = \frac{1 f_s w_r}{\pi f_r 2}$$

$$\frac{\partial u_1}{\partial v_{Cs}} = -2 \frac{\partial u_1}{\partial v_{in}} \tag{3-20}$$

$$\frac{\partial u_1}{\partial i_{Loa}} = \frac{1 F_s}{2\pi F_r} (2J + \sin(w_r T_{off}))$$

$$\frac{\partial u_1}{\partial i_{Lob}} = - \frac{\partial u_1}{\partial i_{Loa}}$$

$$\frac{\partial u_1}{\partial v_{in}} = \frac{1 F_s}{Z_r F_r} \frac{\sin(w_r T_{off})}{\pi} \left( J + \frac{3}{4} \sin(w_r T_{off}) \right)$$

$$\frac{\partial u_1}{\partial t_{off}} = 0$$

$$\frac{\partial u_3}{\partial v_{Cs}} = \frac{F_s \sin(w_r T_{off})}{F_r 2\pi}$$

$$\frac{\partial u_3}{\partial i_{Loa}} = \left( \frac{1 F_s}{\pi F_r} \right)^2 Z_r \left( \frac{\sin(w_r t_{off})}{2} - w_r T_{off} \right)$$

$$\frac{\partial u_3}{\partial i_{Lob}} = \frac{\partial u_3}{\partial i_{Loa}}$$

$$\frac{\partial u_3}{\partial v_{in}} = \frac{1}{2\pi} \frac{F_s}{F_r} (w_r T_{off} - \sin(w_r T_{off})) +$$

$$\left( \frac{1}{2\pi} \frac{F_s}{F_r} \right)^2 \left( 4J \left( w_r T_{off} - \frac{1}{2} \sin(w_r T_{off}) \right) \right)$$

$$\frac{\partial u_3}{\partial t_{off}} = \frac{1}{\pi} \frac{f_s}{f_r} \frac{3V_{in} w_r}{4}$$

$$\frac{\partial u_4}{\partial v_{Cs}} = -\frac{\partial u_3}{\partial v_{Cs}}$$

$$\frac{\partial u_4}{\partial i_{Loa}} = \left( \frac{1}{\pi} \frac{F_s}{F_r} \right)^2 \frac{Z_r}{2} \sin(w_r T_{off})$$

$$\frac{\partial u_4}{\partial i_{Lob}} = \frac{\partial u_4}{\partial i_{Loa}}$$

$$\frac{\partial u_4}{\partial v_{in}} = \left( \frac{1}{2\pi} \frac{F_s}{F_r} \right)^2 2J \sin(w_r T_{off})$$

$$\frac{\partial u_4}{\partial t_{off}} = \frac{1}{\pi} \frac{f_s}{f_r} \frac{V_{in} w_r}{4}$$

The detailed calculation and the Matlab are attached to Appendix on page 202. The responses of  $\hat{v}_{Cs}$  and  $\hat{v}_{Co}$  are decoupled. The solutions of (3-19) and (3-20) can be separated into two parts.

The first part of the solution is associated with the response of  $\hat{v}_{Cs}$ . The portion associated with  $\hat{v}_{Co}$  (the second row and the second column) in the equation (3-19) is taken out. The load perturbation is not shown in the equations as it is only associated with the response of  $\hat{v}_{Co}$ . The new equation for  $\hat{v}_{Cs}$  is re-written as

$$K \frac{d\hat{x}}{dt} = \left\{ \sum_{i=1}^k \hat{d}_i A_i \right\} X + \left\{ \sum_{i=1}^k D_i A_i \right\} \hat{x} + \hat{u}$$

$$K = \begin{bmatrix} C_s & 0 & 0 \\ 0 & L_o & 0 \\ 0 & 0 & L_o \end{bmatrix}, \frac{d\hat{x}}{dt} = \begin{bmatrix} \frac{d\hat{v}_{Cs}}{dt} \\ \frac{d\hat{i}_{Loa}}{dt} \\ \frac{d\hat{i}_{Lob}}{dt} \end{bmatrix}, X = \begin{bmatrix} V_{Cs} \\ I_{Loa} \\ I_{Lob} \end{bmatrix}, \hat{x} = \begin{bmatrix} \hat{v}_{Cs} \\ \hat{i}_{Loa} \\ \hat{i}_{Lob} \end{bmatrix}, \hat{u} = \begin{bmatrix} \hat{u}_1 \\ \hat{u}_2 \\ \hat{u}_3 \end{bmatrix},$$

$$\sum_{i=1}^k \hat{d}_i A_i = \begin{bmatrix} 0 & 0 & 0 \\ -\rho & 0 & 0 \\ \rho & 0 & 0 \end{bmatrix}, \sum_{i=1}^k D_i A_i = \begin{bmatrix} 0 & \frac{T_{off}}{T_s} & -\frac{T_{off}}{T_s} \\ -\frac{T_{off}}{T_s} & -R_{Lo} & 0 \\ \frac{T_{off}}{T_s} & 0 & -R_{Lo} \end{bmatrix}, \quad (3-21)$$

$$\rho = \frac{\partial \frac{t_{off}}{T_s}}{\partial v_{Cs}} \hat{v}_{Cs} + \frac{\partial \frac{t_{off}}{T_s}}{\partial i_{Loa}} \hat{i}_{Loa} + \frac{\partial \frac{t_{off}}{T_s}}{\partial i_{Lob}} \hat{i}_{Lob} + \frac{\partial \frac{t_{off}}{T_s}}{\partial v_{in}} \hat{v}_{in} + \frac{\partial \frac{t_{off}}{T_s}}{\partial t_{off}} \hat{t}_{off},$$

$$\hat{u} = \begin{bmatrix} -2 \frac{\partial u_1}{\partial v_{Cs}} \hat{v}_{Cs} + \frac{\partial u_1}{\partial i_{Loa}} \hat{i}_{Loa} - \frac{\partial u_1}{\partial i_{Lob}} \hat{i}_{Lob} + \frac{\partial u_1}{\partial v_{in}} \hat{v}_{in} + \frac{\partial u_1}{\partial t_{off}} \hat{t}_{off} \\ \frac{\partial u_2}{\partial v_{Cs}} \hat{v}_{Cs} + \frac{\partial u_2}{\partial i_{Loa}} \hat{i}_{Loa} + \frac{\partial u_2}{\partial i_{Lob}} \hat{i}_{Lob} + \frac{\partial u_2}{\partial v_{in}} \hat{v}_{in} + \frac{\partial u_2}{\partial t_{off}} \hat{t}_{off} \\ -\frac{\partial u_2}{\partial v_{Cs}} \hat{v}_{Cs} + \frac{\partial u_3}{\partial i_{Loa}} \hat{i}_{Loa} + \frac{\partial u_3}{\partial i_{Lob}} \hat{i}_{Lob} + \frac{\partial u_3}{\partial v_{in}} \hat{v}_{in} + \frac{\partial u_3}{\partial t_{off}} \hat{t}_{off} \end{bmatrix}$$

The terms associated with  $\hat{i}_{Loa}$  and  $\hat{i}_{Lob}$  in (3-21) are the same as those in (3-19). The detailed derivation of (3-19) is shown in Appendix on page 202. The equation above is reorganized:

$$\begin{bmatrix} C_s & 0 & 0 \\ 0 & L_o & 0 \\ 0 & 0 & L_o \end{bmatrix} \begin{bmatrix} \frac{d\hat{v}_{Cs}}{dt} \\ \frac{d\hat{i}_{Loa}}{dt} \\ \frac{d\hat{i}_{Lob}}{dt} \end{bmatrix} = \begin{bmatrix} -2H_1 & \beta_{Cs} & -\beta_{Cs} \\ -\beta_{Lo} & -R_{Los} & -R_i \\ \beta_{Lo} & -R_i & -R_{Los} \end{bmatrix} \begin{bmatrix} \hat{v}_{Cs} \\ \hat{i}_{Loa} \\ \hat{i}_{Lob} \end{bmatrix} + \begin{bmatrix} H_{11} \\ H_{12} \\ H_{13} \end{bmatrix} \hat{v}_{in} + \begin{bmatrix} H_{21} \\ H_{22} \\ H_{23} \end{bmatrix} \hat{t}_{off} \quad (3-22)$$

$$\beta_{Cs} = \frac{1}{2\pi} \frac{F_s}{F_r} (w_r T_{off} + \sin(w_r T_{off}) + 2J)$$

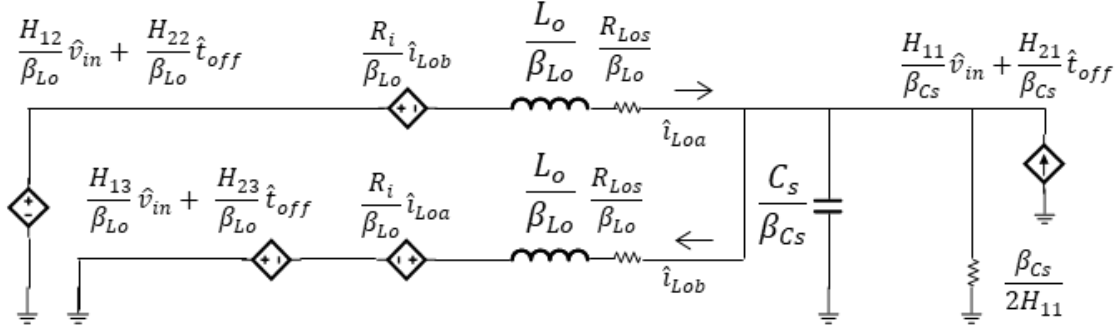


Fig. 3-12. Small-signal equivalent circuit of the SRB converter in Fig. 3-1 on page 55 is modeled using (3-4) on page 56 for the response of  $\hat{v}_{Cs}$ .

$$\beta_{Lo} = \frac{1}{2\pi} \frac{F_s}{F_r} (w_r T_{off} - \sin(w_r T_{off}))$$

$$R_{Los} = R_{Lo} + \left(\frac{1}{\pi} \frac{F_s}{F_r}\right)^2 \frac{Z_r}{2} (w_r T_{off} - \sin(w_r T_{off}))$$

$$R_i = \left(\frac{1}{\pi} \frac{F_s}{F_r}\right)^2 \frac{Z_r}{2} (w_r T_{off} - \sin(w_r T_{off}))$$

$$H_{11} = \frac{1}{Z_r} \frac{F_s}{F_r} \frac{\sin(w_r T_{off})}{\pi} \left(J + \frac{3}{4} \sin(w_r T_{off})\right)$$

$$H_{12} = \frac{1}{2\pi} \frac{F_s}{F_r} (w_r T_{off} - \sin(w_r T_{off})) + \left(\frac{1}{2\pi} \frac{F_s}{F_r}\right)^2 2J (w_r T_{off} - \sin(w_r T_{off}))$$

$$H_{13} = \left(\frac{1}{2\pi} \frac{F_s}{F_r}\right)^2 2J (w_r T_{off} + \sin(w_r T_{off}))$$

$$H_{21} = H_{22} = H_{23} = 0$$

Numerical examples of the variables listed in (3-22) are listed in Table 3-1. The first line of (3-22) is divided by  $\beta_{Cs}$ . The second and the third lines of (3-22) are divided by  $\beta_{Lo}$ . The new equation is

$$\begin{bmatrix} \frac{C_s}{\beta_{Cs}} & 0 & 0 \\ 0 & \frac{L_o}{\beta_{Lo}} & 0 \\ 0 & 0 & \frac{L_o}{\beta_{Lo}} \end{bmatrix} \begin{bmatrix} \frac{d\hat{v}_{Cs}}{dt} \\ \frac{d\hat{i}_{Loa}}{dt} \\ \frac{d\hat{i}_{Lob}}{dt} \end{bmatrix} = \begin{bmatrix} -\frac{2H_1}{\beta_{Cs}} & 1 & -1 \\ -1 & -\frac{R_{Los}}{\beta_{Lo}} & -\frac{R_i}{\beta_{Lo}} \\ 1 & -\frac{R_i}{\beta_{Lo}} & -\frac{R_{Los}}{\beta_{Lo}} \end{bmatrix} \begin{bmatrix} \hat{v}_{Cs} \\ \hat{i}_{Loa} \\ \hat{i}_{Lob} \end{bmatrix} + \begin{bmatrix} H_{11} \\ \beta_{Cs} \\ H_{12} \\ \beta_{Lo} \\ H_{13} \\ \beta_{Lo} \end{bmatrix} \hat{v}_{in} + \begin{bmatrix} H_{21} \\ \beta_{Cs} \\ H_{22} \\ \beta_{Lo} \\ H_{23} \\ \beta_{Lo} \end{bmatrix} \hat{t}_{off} \quad (3-23)$$

**Table 3-1. Numerical examples of variables in (3-22) using  $V_{in} = 48 V$ ,  $R_{load} = 0.125 \Omega$ ,  $R_{Lo} = 0.05 \Omega$ ,  $L_r = 80 nH$ ,  $L_{oa} = L_{ob} = 1.5 \mu H$ ,  $C_s = 20 \mu F$ ,  $C_r = 21 nF$ , and  $C_o = 47 \mu F$**

	#1	#2	#3	#4	#5
$t_{off}f_r$	<b>0.20</b>	<b>0.30</b>	<b>0.40</b>	<b>0.50</b>	<b>0.60</b>
$V_{in}(V)$	<b>48</b>	<b>48</b>	<b>48</b>	<b>48</b>	<b>48</b>
$V_{Cs}(V)$	<b>24</b>	<b>24</b>	<b>24</b>	<b>24</b>	<b>24</b>
$V_{Co}(V)$	<b>0.7</b>	<b>0.8</b>	<b>3.1</b>	<b>4.9</b>	<b>6.8</b>
$I_{Loa}(A)$	<b>2.8</b>	<b>7.7</b>	<b>15.1</b>	<b>24.6</b>	<b>33.8</b>
$I_{Lob}(A)$	<b>2.8</b>	<b>7.7</b>	<b>15.1</b>	<b>24.6</b>	<b>33.8</b>
$V_o(V)$	<b>0.8</b>	<b>1.0</b>	<b>3.8</b>	<b>6.1</b>	<b>8.5</b>
$\beta_{Cs}$	<b>0.42</b>	<b>0.48</b>	<b>0.50</b>	<b>0.50</b>	<b>0.50</b>
$\beta_{Lo}$	<b>0.02</b>	<b>0.08</b>	<b>0.16</b>	<b>0.26</b>	<b>0.35</b>
$R_{Los}(\Omega)$	<b>0.06</b>	<b>0.07</b>	<b>0.10</b>	<b>0.13</b>	<b>0.15</b>
$R_i(\Omega)$	<b>0.01</b>	<b>0.02</b>	<b>0.05</b>	<b>0.08</b>	<b>0.10</b>
$H_{11}(S)$	<b>0.19</b>	<b>0.19</b>	<b>0.10</b>	$2 \times 10^{-17}$	<b>-0.06</b>
$H_{12}(S)$	<b>0.03</b>	<b>0.09</b>	<b>0.20</b>	<b>0.32</b>	<b>0.44</b>
$H_{13}(S)$	<b>0.01</b>	<b>0.02</b>	<b>0.04</b>	<b>0.06</b>	<b>0.09</b>

Fig. 3-12 shows the small-signal equivalent circuit of the SRB converter for the response of  $\hat{v}_{C_s}$ . The response is dominated by the resonance between  $C_s/\beta_{C_s}$  and  $L_o/\beta_{L_o}$ . The scaling factors  $\beta_{C_s}$  and  $\beta_{L_o}$  depend on the design of the series resonator and the operating point.

There are two branches paralleled with  $C_s$  brought in by the parallel resonant tank. The polarity of  $H_{11}$  depends on the converter operating point. Negative damping is introduced as  $H_{11} < 0$ . Table 3-1 shows  $H_{11}$  is a positive number with  $t_{off}f_r < 0.5$ . The resistor branch in parallel with  $C_s$  offers a damping effect in the equivalent circuit.  $H_{11}$  turns into a negative number at the operating point with  $t_{off}f_r = 0.6$ . The resistor branch in parallel with  $C_s$  is with negative resistance. As a result, the poles move into the right half plane. Other variables in Table 3-1 vary with the change of the converter operating points, and impact the quality factor as shown in (3-24).

The two dependent voltage sources in the middle of the graph suggest the coupling effect of the two inductor currents.

$\hat{t}_{off}$  is set to zero. The solution of the input-to- $v_{C_s}$  transfer function shown in Fig. 3-13 is

$$\begin{aligned}
 G_{in2C_s}(s) &= \frac{\hat{v}_{C_s}(s)}{\hat{v}_{in}(s)} = G_{in2C_s0} \frac{1 + \frac{s}{w_{sz}}}{1 + \frac{s}{w_s Q} + \frac{s^2}{w_s^2}} \\
 G_{in2C_s0} &= \frac{1}{2} \frac{\beta_{C_s}(H_{12} - H_{13}) + H_{11}(R_{Los} - R_i)}{\beta_{C_s}\beta_{L_o} + H_{11}(R_{Los} - R_i)} \\
 w_{sz} &= \frac{\beta_{C_s}(H_{12} - H_{13}) + H_{11}(R_{Los} - R_i)}{H_{11}L_o} \\
 w_s &= \sqrt{\frac{\beta_{C_s}\beta_{L_o} + H_{11}(R_{Los} - R_i)}{C_s L_o}}
 \end{aligned} \tag{3-24}$$

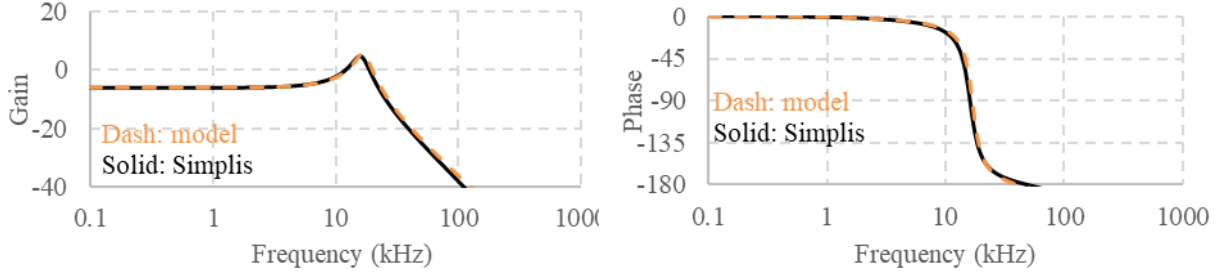


**Fig. 3-13.** The input-to- $\hat{v}_{C_s}$  transfer function of the modeled and simulated converter in Fig. 3-1 on page 54 using the gate driving circuit in Fig. 3-4 on page 61. The theoretical result using (3-4) on page 56 matches the simulated one in Simplis with  $V_{in} = 48\text{ V}$ ,  $V_o = 5\text{ V}$ ,  $R_{load} = 0.125\ \Omega$ ,  $L_r = 80\text{ nH}$ ,  $L_{oa} = L_{ob} = 1.5\ \mu\text{H}$ ,  $C_s = 20\ \mu\text{F}$ ,  $C_r = 21\text{ nF}$ , and  $C_o = 47\ \mu\text{F}$ . The control variable  $t_{off} = 120\text{ ns}$  is set by the dc source V3 with the conversion ratio  $\frac{t_{off}}{v_{ctoff}} = 10^{-6} \frac{\text{s}}{\text{V}}$  in Fig. 3-4 on page 61.

$$Q_s = \sqrt{\frac{2L_o \beta_{C_s} \beta_{L_o} + H_{11}(R_{L_{os}} - R_i)}{C_s \beta_{L_o}^2}} \frac{\beta_{L_{os}} - \frac{R_s}{\beta_{L_o}} + \frac{2H_{11}L_o}{\beta_{L_o} C_s}}{\beta_{L_o} - \frac{R_s}{\beta_{L_o}} + \frac{2H_{11}L_o}{\beta_{L_o} C_s}}$$

The solutions of  $\beta_{C_s}$ ,  $\beta_{L_o}$ ,  $R_{L_{os}}$ ,  $R_i$ ,  $H_{11}$ ,  $H_{12}$ , and  $H_{13}$  are documented in (3-22). Since  $\beta_{C_s}(H_{12} - H_{13}) \gg H_{11}(R_{L_{os}} - R_i)$  and  $\beta_{C_s}\beta_{L_o} \gg H_{11}(R_{L_{os}} - R_i)$ , the following approximations can be applied.

$$G_{in2C_s0} \approx \frac{1}{2}$$

$$w_{sz} \approx \frac{\beta_{C_s}(H_{12} - H_{13})}{H_{11}L_o} \quad (3-25)$$

Fig. 3-13 shows the modeled and simulated input-to- $\hat{v}_{C_s}$  transfer function. The low-frequency voltage gain is  $-6\text{ dB}$ , suggesting  $v_{C_s} = v_{in}/2$  at dc.

The location of the double poles depends on the control variable and the design of  $C_s$  and  $L_o$ . The theoretical result matches the simulated one in Simplis.

To ensure stability, the double poles need to be placed in the left-half plane. The locations of the double poles are

$$\begin{aligned}
p_1 &= -\zeta\omega_s + j\omega_s\sqrt{1-\zeta^2} \\
p_2 &= -\zeta\omega_s - j\omega_s\sqrt{1-\zeta^2}
\end{aligned} \tag{3-26}$$

The damping factor is

$$\zeta = \frac{1}{2Q_s} \tag{3-27}$$

If  $Q_s < 0$ , two poles move into the right half plane in the pole-zero map. Equation (3-28) is added to ensure the converter stability and avoid the right half-plane pole

$$Q_s = \frac{\sqrt{\frac{L_o}{2C_s} \frac{\beta_{Cs}}{\beta_{Lo}}}}{\frac{1}{2} \left( \frac{R_{Los} - R_s}{\beta_{Lo}} + \frac{2H_{11} L_o}{\beta_{Lo} C_s} \right)} > 0 \tag{3-28}$$

which is equivalent to

$$R_{Lo} + \frac{2L_o}{C_s} H_{11} > 0 \tag{3-29}$$

and

$$\frac{1}{\sin(\omega_r T_{off})} > - \left( \frac{C_n}{2L_n} \frac{2 + \frac{\pi}{J}}{\sin^2(\omega_r T_{off})} \frac{R_{Lo}}{Z_r} + \frac{31}{4J} \right) \tag{3-30}$$

In general, the double poles could be moved away from the right half plane by

1. Increasing  $C_n$ ;
2. Increasing  $R_{Lo}/Z_r$ ;
3. Reducing  $L_n$ ;
4. Reducing  $J$ ;
5. Reducing  $\sin(\omega_r t_{off})$ .

If  $0 < f_r T_{off} < 0.5$  is satisfied, there is  $\sin(\omega_r T_{off}) > 0$ . The left term in (3-30) is positive.

**Table 3-2. Numerical examples of variables from (3-22) to (3-30) using  $V_{in} = 48 V$ ,  $R_{load} = 0.125 \Omega$ ,  $R_{Lo} = 0.005 \Omega$ ,  $L_r = 80 nH$ ,  $L_{oa} = L_{ob} = 1.5 \mu H$ ,  $C_s = 20 \mu F$ ,  $C_r = 21 nF$ , and  $C_o = 47 \mu F$**

	Equation	#1 $t_{offf_r} = 0.4$	#2 $t_{offf_r} = 0.5$	#3 $t_{offf_r} = 0.6$
$V_{Cs}(V)$	(3-4)	24	24	24
$V_{Co}(V)$	(3-4)	3.8	6.1	8.5
$I_{Loo}(A)$	(3-4)	15.1	24.6	33.8
$I_{Lob}(A)$	(3-4)	15.1	24.6	33.8
$\beta_{Cs}$	(3-22)	0.50	0.50	0.50
$\beta_{Lo}$	(3-22)	0.16	0.26	0.35
$R_{Los}(\Omega)$	(3-22)	0.05	0.08	0.11
$R_i(\Omega)$	(3-22)	0.05	0.08	0.10
$H_{11}(S)$	(3-22)	0.10	$-1.7 \times 10^{-17}$	-0.06
$H_{12}(S)$	(3-22)	0.20	0.32	0.44
$H_{13}(S)$	(3-22)	0.04	0.06	0.09
$G_{in2Cs0}$	(3-24)	0.50	0.50	0.50
$w_s(rad/s)$	(3-24)	$7.1 \times 10^4$	$8.9 \times 10^4$	$9.9 \times 10^4$
$Q_s$	(3-24)	5.41	26.7	-55.3
$w_{sz}(rad/s)$	(3-24)	$5.1 \times 10^5$	$5.1 \times 10^{21}$	$-2.1 \times 10^6$
$w_{sz}(rad/s)$	(3-25)	$5.1 \times 10^5$	$5.1 \times 10^{21}$	$-2.1 \times 10^6$
$\zeta$	(3-27)	0.09	0.02	-0.01
$Q_s$	(3-28)	5.41	26.7	-55.3
$R_{Lo} + \frac{2L_o}{C_s} H_{11}$	(3-29)	0.02	0.01	-0.01
$\frac{1}{\sin(w_r T_{off})}$	(3-30)	1.70	$8 \times 10^{15}$	-1.70
$-\left(\frac{C_n}{2L_n} \frac{2 + \frac{\pi}{J}}{\sin^2(w_r T_{off})} \frac{R_{Lo}}{Z_r} + \frac{31}{4J}\right)$	(3-30)	-1.38	$-2 \times 10^{30}$	-1.38
Convergence	Simplis	Yes	Yes	No

Meanwhile, the right term in (3-30) is negative, ensuring  $Q_s > 0$ . This condition works for the load condition in the range of  $0.3 < J < 10$ , and the SRB converter needs to operate in the ZVS region defined in Fig. 2-17. The validity of this condition is demonstrated by the Simplis simulation shown in Table 3-2. The small-signal instability in (3-24) explains the divergence of the large-signal behavior in Fig. 3-11.

The perturbation from  $\hat{t}_{off}$  is canceled out as  $H_{21} = 0$  and  $H_{22} - H_{23} = 0$ . The  $\hat{v}_{Cs}$  primarily depends on  $\hat{v}_{in}$ .  $\hat{t}_{off}$  has no impact on  $\hat{v}_{Cs}$ .

Table 3-2 gives numerical examples of the small signal variables listed from (3-22) to (3-30). The large-signal variables are calculated using (3-4). The small-signal variables in Fig. 3-12 are calculated using (3-22).

The approximated equation of  $\mathbf{w}_{sz}$  in (3-25) and  $\mathbf{Q}_s$  in (3-28) are compared with the ones without approximation in (3-24). The calculation results show the equations with approximation match well with the original equations. The absolute magnitude of  $Q_s$  increases significantly as the normalized control variable  $\mathbf{t}_{off} \mathbf{f}_r$  increases.  $\mathbf{Q}_s$  in (3-28) turns into a negative value when the state variables  $v_{Cs}$ ,  $i_{Loa}$ , and  $i_{Lob}$  oscillate after the  $v_{in}$  transient. Equation (3-29) could be used to check the convergence of the SRB converter.  $R_{Lo} + \frac{2L_o}{C_s} H_{11}$  is a negative value in #3 in Table 3-2 suggesting nonconvergence. Condition (3-30) is equivalent to (3-29). Both of them are effective for the transient stability design as demonstrated by Table 3-2. Simplis simulation confirms the divergence if the condition (3-29) (or (3-30)) is not met.

The second part of the solution is associated with the response of  $\hat{v}_{Co}$ . The output inductor current is combined as  $i_{Lo} = i_{Loa} + i_{Lob}$  in (3-19). The response associated with  $\hat{v}_{Co}$  is removed. The equation associated with the response of  $\hat{v}_{Co}$  in (3-19) is written as follows:

$$K \frac{d\hat{x}}{dt} = \left\{ \sum_{i=1}^k \hat{d}_i A_i \right\} X + \left\{ \sum_{i=1}^k D_i A_i \right\} \hat{x} + \hat{u}$$

$$K = \begin{bmatrix} L_o/2 & 0 \\ 0 & C_o \end{bmatrix}, \frac{d\hat{x}}{dt} = \begin{bmatrix} \frac{d\hat{i}_{Lo}}{dt} \\ \frac{d\hat{v}_{Co}}{dt} \end{bmatrix}, X = \begin{bmatrix} I_{Lo} \\ V_{Co} \end{bmatrix}, \hat{x} = \begin{bmatrix} \hat{i}_{Lo} \\ \hat{v}_{Co} \end{bmatrix},$$

$$\sum_{i=1}^k \hat{d}_i A_i = 0, \sum_{i=1}^k D_i A_i = \begin{bmatrix} -\frac{R_{Lo}}{2} & -1 \\ 1 & -\frac{1}{R_{load}} \end{bmatrix}, \hat{u} = \begin{bmatrix} \frac{\partial u_1}{\partial i_{Lo}} \hat{i}_{Lo} + \frac{\partial u_1}{\partial v_{in}} \hat{v}_{in} + \frac{\partial u_1}{\partial t_{off}} \hat{t}_{off} \\ \hat{i}_p \end{bmatrix} \quad (3-31)$$

$$\frac{\partial u_1}{\partial i_{Lo}} = -\frac{R_{load}}{1 + \frac{\pi}{2} J}$$

$$\frac{\partial u_1}{\partial v_{in}} = \left( \frac{2T_{off} - \frac{\pi}{w_r}}{2T_s} \right) \left( 1 + \frac{1}{1 + \frac{\pi}{2} J} \right)$$

$$\frac{\partial u_1}{\partial t_{off}} = \frac{V_{in}}{T_s}$$

The terms associated with  $\hat{i}_{Loa}$  and  $\hat{i}_{Lob}$  in (3-31) are the same as those in (3-19). The detailed derivation of (3-19) is shown in Appendix on page 202.

The model in equation (3-31) is converted into an equivalent circuit to illustrate the physical insights of the small-signal behavior of the SRB converter.

There are three dependent sources in total. Dependent source  $\partial u_1 / \partial t_{off}$  models the perturbation from the control signal.

Dependent source  $\partial u_1 / \partial v_{in}$  models the perturbation from the input voltage. The last source,  $\partial u_1 / \partial i_{Lo}$ , can be converted into an equivalent damping resistor as shown in Fig. 3-14.

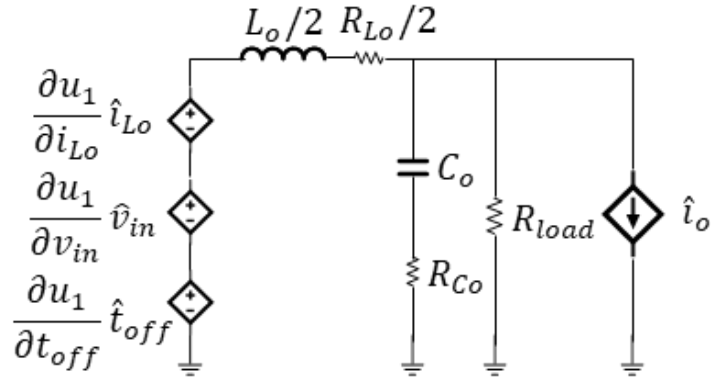


Fig. 3-14. Small-signal equivalent circuit of the SRB converter in Fig. 3-1 on page 55 is modeled using (3-4) on page 56 for the response of  $\hat{v}_{C_o}$ .

Fig. 3-14 shows the small-signal equivalent circuit of the SRB converter for the response of  $\hat{v}_{C_o}$ . The response is dominated by the resonance between  $L_o/2$  and  $C_o$ . The series resonator brings in a dependent voltage source associated with  $\hat{i}_{L_o}$ , which does not exist in a conventional SCB converter.

Fig. 3-15 shows the small-signal equivalent circuit with the damping resistor  $R_e$  of the SRB converter for the response of  $\hat{v}_{C_o}$ . The damping resistor  $R_e$  is not a physical resistor consuming energy. It is an equivalent resistor determined by the voltage-current relationship of the dependent current source  $(\partial u_1/\partial i_{L_o})\hat{i}_{L_o}$ , such that

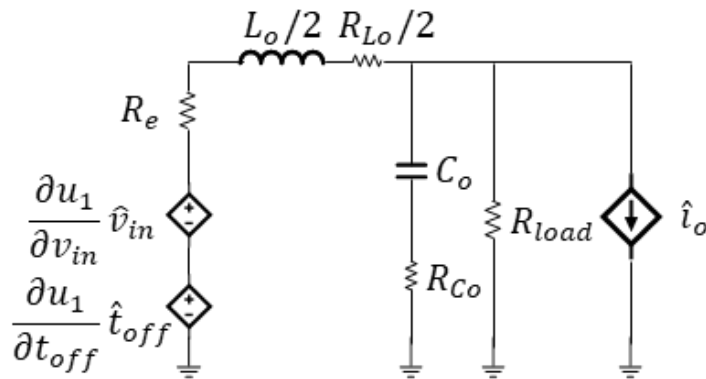


Fig. 3-15. Small-signal equivalent circuit with the damping resistor  $R_e$  modeled in (3-32) of the SRB converter in Fig. 3-1 on page 55 modeled using (3-4) on page 56 for the response of  $\hat{v}_{C_o}$ .

$$R_e = \frac{R_{load}}{1 + \frac{\pi}{2} J} \quad (3-32)$$

The  $R_e$  depends on the normalized load condition  $J$ . It models the damping effect brought in by the parallel resonant tank in the SRB converter.

The input-to-output transfer function shown in Fig. 3-16 is derived by applying the Laplace transformation:

$$G_{vv}(s) = \frac{\hat{v}_o(s)}{\hat{v}_{in}(s)} = G_{vv0} \frac{\left(1 + \frac{s}{w_z}\right)}{1 + \frac{s}{w_o Q} + \frac{s^2}{w_o^2}}$$

$$w_z = \frac{1}{C_o R_{Co}}$$

$$w_o = \frac{1}{\sqrt{\frac{L_o}{2}} C_o} \sqrt{1 + \frac{1}{2} \frac{R_{Lo}}{R_{load}} + \frac{1}{1 + \frac{\pi}{2} J}}$$

$$Q = \frac{R_{load}}{Z_o} \frac{\sqrt{1 + \frac{R_{Lo}}{2R_{load}} + \frac{1}{1 + \frac{\pi}{2} J}}}{1 + \frac{1}{2} \frac{R_{load} R_{Lo}}{Z_o^2} + \frac{1}{1 + \frac{\pi}{2} J} \frac{R_{load}^2}{Z_o^2}} \quad (3-33)$$

$$Z_o = \sqrt{\frac{C_o}{\frac{L_o}{2}}}$$

$$G_{vv0} = M \frac{1 + \frac{1}{1 + \frac{\pi}{2} J}}{1 + \frac{R_{Lo}}{2R_{load}} + \frac{1}{1 + \frac{\pi}{2} J}}$$

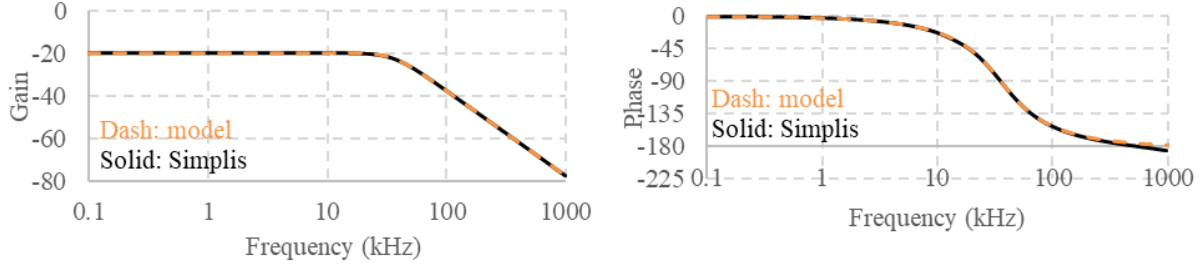


**Fig. 3-16.** The input-to-output transfer function of the modeled and simulated converter in Fig. 3-1 on page 55. The theoretical result using (3-4) on page 56 matches the simulated one in Simplis with  $V_{in} = 48\text{ V}$ ,  $V_o = 5\text{ V}$ ,  $R_{load} = 0.125\ \Omega$ ,  $L_r = 80\text{ nH}$ ,  $L_{oa} = L_{ob} = 1.5\ \mu\text{H}$ ,  $C_s = 20\ \mu\text{F}$ ,  $C_r = 21\text{ nF}$ , and  $C_o = 47\ \mu\text{F}$ . The control variable  $t_{off} = 120\text{ ns}$  is set by the dc source V3 with the conversion ratio  $\frac{t_{off}}{V_{ctoff}} = 10^{-6}\ \frac{\text{s}}{\text{V}}$  in Fig. 3-4 on page 61.

The detailed derivation of (3-23) is shown in Appendix. Fig. 3-16 shows the modeled and simulated input-to-output transfer function. The theoretical result matches the simulation.

Fig. 3-17 compares the input-to-output transfer function of the SRB and SCB converters. Assume ideal components for this comparison. Take  $w_{oSCB}$  as the double poles' frequency in the SCB converter.

$$w_{oSCB} = \frac{1}{\sqrt{\frac{L_o}{2} C_o}} \quad (3-34)$$

An expanding factor  $\sigma_1$  is used to bridge between two converters

$$\sigma_1 = \frac{w_o}{w_{oSCB}} = \sqrt{1 + \frac{1}{1 + \frac{\pi}{2} J}} \quad (3-35)$$

Expanding factor  $\sigma_1$  models the impact of the damping effect from the parallel resonant tank on the shift of the pole location. Compared to the pole location of the SCB converter, the shift of  $w_o$  depends on the normalized load condition. The expanding factor drops as  $J$  decreases. If the parallel resonant tank in the SRB converter is removed, the characteristic impedance of resonant

tank  $Z_r \rightarrow 0$ ,  $J \rightarrow 0$ , and expanding factor  $\sigma_1 \rightarrow 1$ .

Fig. 3-17(b) shows expanding factor  $\sigma_1$  versus normalized load condition  $J$ . The  $\sigma_1$  grows from one as  $J$  increases from 0.01, and grows faster near  $J = 1$ . The  $\sigma_1$  reaches  $\sqrt{2}$  as  $J$  approaches 100.  $\sigma_1 > 1$  over the full-load range suggests the pole frequency of the SRB converter is always larger than that of the SCB converter.

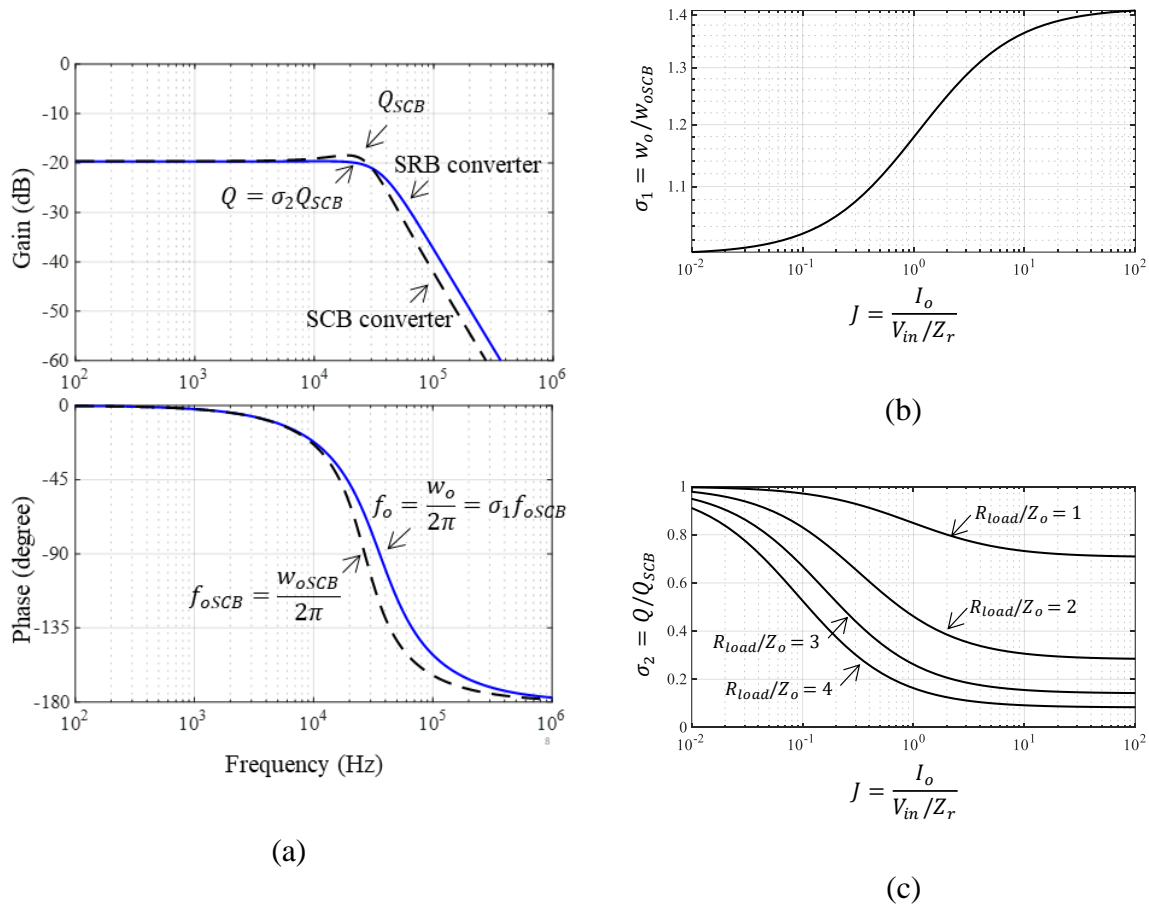


**Fig. 3-17.** (a) The input-to-output transfer functions of the SRB and SCB converters in Fig. 3-1 on page 55 with  $V_{in} = 48\text{ V}$ ,  $V_o = 5\text{ V}$ ,  $R_{load} = 0.125\ \Omega$ ,  $L_{oa} = L_{ob} = 1.5\ \mu\text{H}$ ,  $L_r = 80\ \text{nH}$ ,  $C_s = 20\ \mu\text{F}$ ,  $C_r = 21\ \text{nF}$ , and  $C_o = 47\ \mu\text{F}$ . (b) The ratio of the SRB pole frequency to the SCB pole frequency modeled by (3-35). (c) The ratio of the Q value of the SRB converter to that of the SCB converter parametric with  $R_{load}/Z_o$  modeled by (3-37).

$Q_{SCB}$  is considered as the quality factor in the SCB converter.

$$Q_{SCB} = R_{load} \sqrt{\frac{C_o}{\frac{L_o}{2}}} \quad (3-36)$$

A damping factor,  $\sigma_2$ , is used to bridge between two converters, such that

$$\sigma_2 = \frac{Q}{Q_{SCB}} = \frac{\sigma_1}{1 + \frac{1}{1 + \frac{\pi}{2} J} \frac{R_{load}^2}{Z_o^2}} \quad (3-37)$$

Damping factor  $\sigma_2$  models the damping effect introduced by the parallel resonant tank, and depends on the load condition, the design of the parallel resonant tank, and the characteristic impedance of the output filter  $Z_o = \sqrt{L_o/C_o}$ . As  $J$  increases, the switching ripple introduced by the resonant tank becomes larger, and then  $\sigma_2$  drops, meaning a stronger damping effect. If the parallel resonant tank in the SRB converter is removed, the characteristic impedance of resonant tank  $Z_r \rightarrow 0$ ,  $J \rightarrow 0$ , and damping factor  $\sigma_2 \rightarrow 1$ .

Fig. 3-17(c) shows damping factor  $\sigma_2$  versus the normalized load condition  $J$  as a parametric with  $R_{load}/Z_o$ . The  $\sigma_2$  drops from one as  $J$  increases.  $\sigma_2 < 1$  over the full-load range suggests the Q value of the SRB converter is always smaller than that of the SCB converter. A smaller Q value generally results in a smaller overshoot, which benefits the transient performance. A larger ratio of  $R_{load}/Z_o$  shifts the curve down indicating a more significant Q value drop compared to the SCB converter.

The dc gain of the input-to-output transfer function is  $G_{vv0SCB} = D/2$  for the SCB converter and  $G_{vv0} = M$  for the SRB converter.

The Laplace transform is applied to derive the following control-to-output transfer function:

$$G_{vtoff}(s) = \frac{\hat{v}_o(s)}{w_r \hat{t}_{off}(s)} = G_{do} \frac{(1 + \frac{s}{w_z})}{1 + \frac{s}{w_o Q} + \frac{s^2}{w_o^2}}$$

$$w_z = \frac{1}{C_o R_{Co}}$$

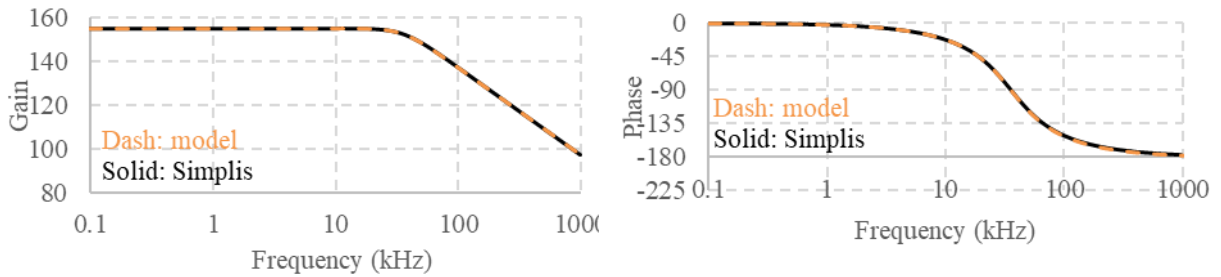
$$w_o = \frac{1}{\sqrt{\frac{L_o}{2} C_o}} \sqrt{1 + \frac{1}{2} \frac{R_{Lo}}{R_{load}} + \frac{1}{1 + \frac{\pi}{2J}}}$$

$$Q = \frac{R_{load}}{Z_o} \frac{\sqrt{1 + \frac{R_{Lo}}{2R_{load}} + \frac{1}{1 + \frac{\pi}{2J}}}}{1 + \frac{1}{2} \frac{R_{load} R_{Lo}}{Z_o^2} + \frac{1}{1 + \frac{\pi}{2J}} \frac{R_{load}^2}{Z_o^2}}$$

$$G_{do} = \frac{\frac{1}{2\pi} \frac{f_s}{f_r} V_{in}}{1 + \frac{R_{Lo}}{2R_{load}} + \frac{1}{1 + \frac{\pi}{2J}}}$$

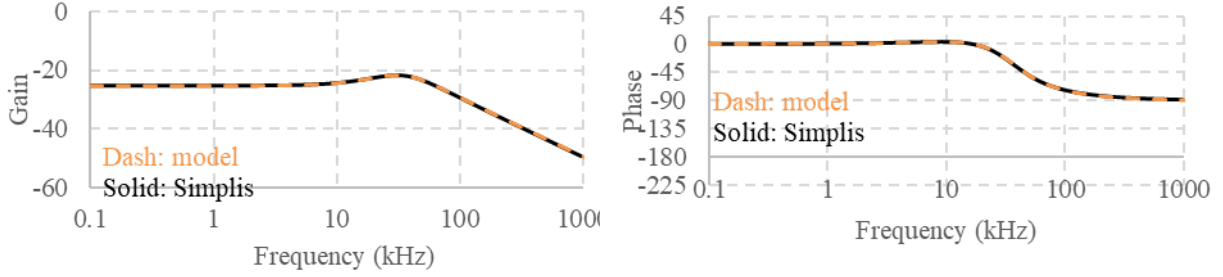
(3-38)

Fig. 3-18 shows the modeled and simulated converter control-to-output transfer function. The



**Fig. 3-18.** The control-to-output transfer function of the modeled and simulated converter in Fig. 3-1 on page 55. The theoretical result using (3-4) on page 56 matches the simulated one in Simplis with  $V_{in} = 48 V$ ,  $V_o = 5 V$ ,  $R_{load} = 0.125 \Omega$ ,  $L_r = 80 nH$ ,  $L_{oa} = L_{ob} = 1.5 \mu H$ ,  $C_s = 20 \mu F$ ,  $C_r = 21 nF$ , and  $C_o = 47 \mu F$ . The control variable  $t_{off} = 120 ns$  is set by the dc source V3 with the conversion ratio  $\frac{t_{off}}{V_{ctoff}} = 10^{-6} \frac{s}{V}$  in

Fig. 3-4 on page 61.



**Fig. 3-19.** The output impedance of the modeled and simulated converter in Fig. 3-1 on page 55. The theoretical result using (3-4) on page 56 matches the simulated one in Simplis with  $V_{in} = 48 V$ ,  $V_o = 5 V$ ,  $R_{load} = 0.125 \Omega$ ,  $L_{oa} = L_{ob} = 1.5 \mu H$ ,  $L_r = 80 nH$ ,  $C_s = 20 \mu F$ ,  $C_r = 21 nF$ , and  $C_o = 47 \mu F$ . The control variable  $t_{off} = 120 ns$  is set by the dc source V3 with the conversion ratio  $\frac{t_{off}}{V_{ctoff}} = 10^{-6} \frac{s}{V}$  in Fig. 3-4 on page 61.

theoretical result matches the simulated one.

$G_{d0SCB}$  is taken as the dc gain of the control-to-output transfer function in the SCB converter yields

$$G_{d0SCB} = \frac{V_o}{D} = V_{in} \quad (3-39)$$

Correction factor  $\sigma_3$  is used to bridge between the two converters, as follows.

$$\sigma_3 = \frac{G_{vt_{off}}}{G_{d0SCB}} = \frac{1}{2\pi} \frac{f_s}{f_r} \frac{1}{1 + \frac{1}{1 + \frac{\pi}{2} j}} \quad (3-40)$$

Laplace transformation is applied to derive the output impedance.

The modeled result is shown in Fig. 3-19 and the transfer function is

$$Z_o(s) = \frac{\hat{v}_o(s)}{\hat{i}_o(s)} = Z_{d0} \frac{(1 + \frac{s}{w_{zL}})(1 + \frac{s}{w_z})}{1 + \frac{s}{w_o Q} + \frac{s^2}{w_o^2}} \quad (3-41)$$

$$Z_{odc} = \frac{R_{load} \left( \frac{R_{Lo}}{2} + \frac{R_{load}}{1 + \frac{\pi}{2} J} \right)}{R_{load} + \left( \frac{R_{Lo}}{2} + \frac{R_{load}}{1 + \frac{\pi}{2} J} \right)}$$

$$w_{zL} = \frac{\frac{R_{Lo}}{2} + \frac{R_{load}}{1 + \frac{\pi}{2} J}}{\frac{L_o}{2}}$$

$$w_o = \frac{1}{\sqrt{\frac{L_o}{2} C_o}} \sqrt{1 + \frac{1}{2} \frac{R_{Lo}}{R_{load}} + \frac{1}{1 + \frac{\pi}{2} J}}$$

$$Q = \frac{R_{load}}{Z_o} \frac{\sqrt{1 + \frac{R_{Lo}}{2R_{load}} + \frac{1}{1 + \frac{\pi}{2} J}}}{1 + \frac{1}{2} \frac{R_{load} R_{Lo}}{Z_o^2} + \frac{1}{1 + \frac{\pi}{2} J} \frac{R_{load}^2}{Z_o^2}}$$

Fig. 3-19 shows the modeled and simulated converter output impedance. The theoretical result matches the simulation.

### 3.4 Conclusion

The large-signal and small-signal models are built to model the transient response of the SRB converter in this chapter.

The large-signal model of the SRB converter characterizes the low-frequency behavior of the low-pass filters with the series capacitor and the high-frequency behavior of the resonant elements. The large-signal model reveals the divergence response that occurs due to the oscillation between the series-capacitor  $C_s$  and the output inductors  $L_o$ . A design recommendation of  $C_n$  to avoid divergence is suggested in Fig. 3-10. Calculation of the length of individual switching cycles using

the large-signal model is not recommended. Error larger than 50% is expected when the SRB converter enters non-ZVS operating region during the transient. A model that characterizes the hard-switching behavior in large-signal transients is part of future work. The control signal  $t_{off}$  is constant during the  $v_{in}$  transient in Fig. 3-5. A more advanced control scheme for smaller settling time of  $v_{in}$  transient is part of the future work.

The major transfer functions are derived from the small-signal model of the SRB converter, and are compared with those in the SCB converter. The small-signal model reveals the damping effect caused by the resonant elements in the input-to-output transfer function. The double poles from the output filter move to high frequencies. The Q value drops in the SRB converter. The resonant tank in the SRB converter also adds a negative damping effect to the series resonance between the series capacitor  $C_s$  and the output inductors  $L_o$ . The oscillation is reinforced, and may lead to instability.

The design methodology based on the steady-state and transient-state analysis will be presented in the following chapter.

# Chapter 4 Design Methodology of the Series-Resonator Buck Converter

## Nomenclature

Symbol	Description
$C_n$	Capacitance ratio of the resonant capacitor to the series capacitor in (1-3)
$C_o$	Output capacitor in Fig. 2-1
$C_r$	Resonant capacitor in Fig. 2-1
$C_s$	Series capacitor in Fig. 2-1
$E_{tank}$	Normalized resonant tank energy in (4-1)
$f_r$	Resonant frequency of the resonant tank in (1-1)
$f_s$	Minimum switching frequency in Table 4-2
$i_{a1}$	Current of switch $S_{a1}$ in Fig. 2-1
$i_{a2}$	Current of switch $S_{a2}$ in Fig. 2-1
$i_{b1}$	Current of switch $S_{b1}$ in Fig. 2-1
$i_{b2}$	Current of switch $S_{b2}$ in Fig. 2-1
$i_{Lr}$	Current of resonant inductor $L_r$ in Fig. 2-1
$I_{a1}$	RMS current of switch $S_{a1}$ in (4-20)
$I_{a2}$	RMS current of switch $S_{a2}$ in (4-25)
$I_{b1}$	RMS current of switch $S_{b1}$ in (4-24)
$I_{b2}$	RMS current of switch $S_{b2}$ in (4-26)
$I_{CrRMS}$	Normalized peak resonant inductor current in (4-28)
$I_{CsRMS}$	Normalized peak resonant inductor current in (4-29)
$I_{LrPkN}$	Normalized peak resonant inductor current in (4-27)
$I_o$	Converter output current consumed by the load in Fig. 2-1
$J$	Normalized load current in (1-2)
$J_{Max}$	Maximum normalized load current in (4-9)
$J_{Min}$	Minimum normalized load current in (4-11)

$L_r$	Resonant inductor in Fig. 2-1
$L_{oa}$	Output inductor of the upper phase in Fig. 2-1
$L_{ob}$	Output inductor of the lower phase in Fig. 2-1
$L_n$	Inductance ratio of the resonant inductor to the output inductor in (1-4)
$M$	Voltage gain in Fig. 4-2
$M_{max}$	Maximum voltage gain in Table 4-2
$S_{a1}$	High-side switch of the upper phase in Fig. 2-1
$S_{b1}$	High-side switch of the lower phase in Fig. 2-1
$S_{a2}$	Low-side switch of the upper phase in Fig. 2-1
$S_{b2}$	Low-side switch of the lower phase in Fig. 2-1
$t_i$	Switching timing in Fig. 2-3
$t_{off}$	Off-time of the low-side switches in Fig. 2-3
$T_s$	Switching period in Fig. 2-3
$v_{Cr}$	Voltage of capacitor $C_r$ in Fig. 2-1
$v_{Cs}$	Voltage of capacitor $C_s$ in Fig. 2-1
$v_{dsa1}$	Drain-source voltage of switch $S_{a1}$ in Fig. 2-1
$v_{dsa2}$	Drain-source voltage of switch $S_{a2}$ in Fig. 2-1
$v_{dsb1}$	Drain-source voltage of switch $S_{b1}$ in Fig. 2-1
$v_{dsb2}$	Drain-source voltage of switch $S_{b2}$ in Fig. 2-1
$V_{in}$	Input voltage in Fig. 2-1
$V_{inMax}$	Maximum input voltage in Table 4-2
$V_{inMin}$	Minimum input voltage in Table 4-2
$V_o$	Output voltage in Fig. 2-1
$Z_r$	Characteristic impedance of the resonant tank in (1-2)
$\Delta v_{Cs}$	Voltage ripple of the series capacitor in (4-13)
$\Delta i_{Lo}$	Current ripple of the output inductor in (4-16)

---

## 4.1 Introduction

The Series-Resonator Buck (SRB) converter was realized by adding a resonant tank in series with the series-capacitor  $C_s$  in an SRB converter. No multi-winding inductors or snubbers are needed. Reference [93] considered the switches' output capacitance for soft-switching operating over a wide load range. The converter was simulated parametrically to understand its operation. Reference [94] calculated numerical solutions of the voltage gain, component peak voltages, and resonant inductor peak current. The power stage was designed with the help of the design curves generated numerically.

The circulating energy is defined as the sum of the peak energy stored in the resonant inductor and capacitor over one switching cycle. The reason for using the peak value rather than the instantaneous value is that the sizes of  $L_r$  and  $C_r$  depend on the peak current and peak voltage respectively. The lack of analytical equations of gain curves and circulating energy stops circuit designers from identifying the optimal operating point with minimum circulating energy. This work derives the closed-form solutions of the state variables, voltage gain, and component stresses of the SRB converter in the steady state. The understanding of the analytical relationships between the gain curves, component stresses, and design variables yields more insights into the power stage design.

## 4.2 Impedance Design for Minimizing Circulating Energy

The normalized resonant tank energy is defined as

$$E_{tank} = \frac{\frac{1}{2}(L_r I_{LrPk}^2 + C_r V_{CrPk}^2)}{\frac{V_o I_o}{f_r}} = \frac{(1+J)^2 + 1}{16\pi MJ} \quad (4-1)$$

where  $I_{LrPk}$  and  $V_{CrPk}$  are solved using the steady-state model. The detailed derivation is listed in

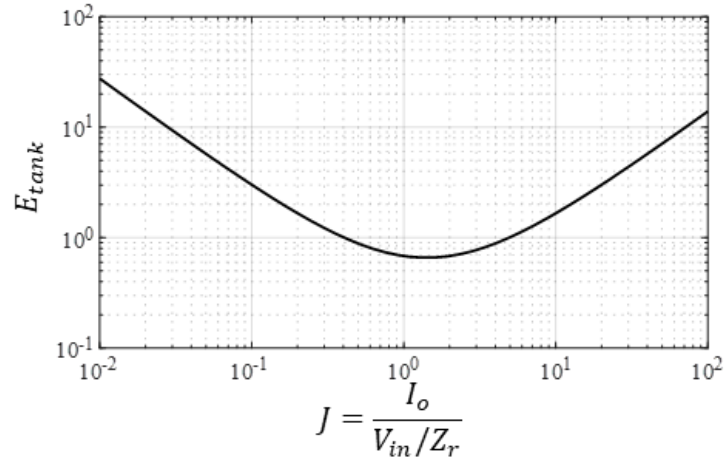


**Fig. 4-1. Normalized resonant tank energy  $E_{tank}$  calculated with (4-1) versus normalized load current  $J$ .**

Appendix on page 248. The validity of equation (4-1) depends on whether the assumptions on page 30 for the steady state model in Chapter 2 are satisfied. The calculation error of the circulating tank energy is generally less than 5% at optimal load conditions near  $J = 1.4$  compared to the simulated result. The worst-case condition for accuracy is at the light-load boundary ( $J = 0.3$ ). The error is not higher than 10%.

The worst-case error is expected to be more than 10% with larger output inductor ripples. The model assumes  $\tau_2 = 0$  and  $\tau_6 = 0$ . A larger ripple design reduces the peak current of  $L_r$ , and increases the time needed ( $\tau_2$  and  $\tau_6$ ) to charge  $C_r$ . A smaller load current ( $J < 0.3$ ) adds the transition time needed to charge and discharge the switch  $C_{oss}$ , and makes the circulating energy model less accurate.

Fig. 4-1 shows normalized resonant tank energy  $E_{tank}$  versus normalized load current  $J$  at  $M = 0.15$ . Small  $E_{tank}$  results in small peak energy stored in the resonant components, and therefore small circulating energy and component size. Small  $J$  leads to large  $C_r$  design and big  $C_r$  peak energy. Large  $J$  results in large  $L_r$  design and big  $L_r$  peak energy. Fig. 4-1 suggests there is a valley point of  $E_{tank}$  which results in a good balance of peak energy stored in  $C_r$  and  $L_r$ . This

balance results in minimal  $E_{tank}$ , and therefore minimal circulating energy in the converter.

The  $E_{tank}$  valley point is calculated by setting

$$\frac{dE_{tank}}{dJ} = 0 \quad (4-2)$$

which results in

$$J = \sqrt{2} \quad (4-3)$$

The detailed derivation is in the Matlab code listed in Appendix on page 250.

The operating point at  $J = \sqrt{2}$  balances the energy stored in the parallel resonant tank ( $L_r$  and  $C_r$ ). The normalized load current with minimal  $E_{tank}$  does not vary with voltage gain  $M$ .

### 4.3 Control Variable Design for Specified Gain Range

Fig. 4-2 shows voltage gain  $M$  versus the control variable  $t_{off}$  normalized by  $1/f_r$ . The detailed derivation of the voltage gain equation is in Chapter 2 on page 41. The gain equation in

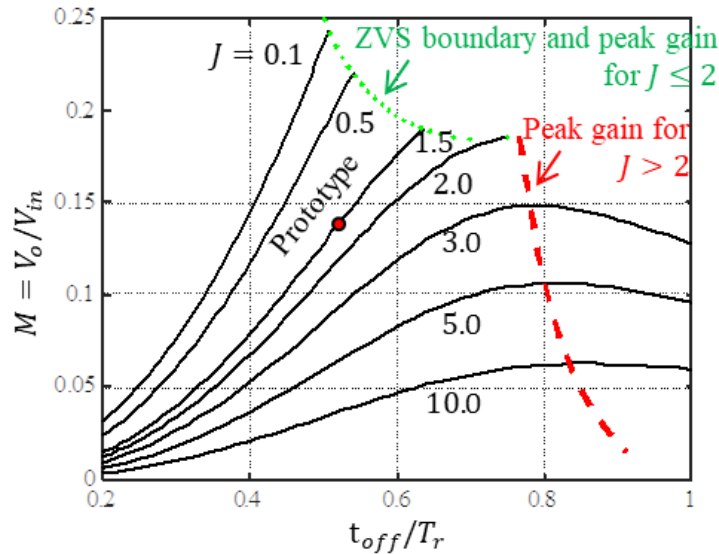


Fig. 4-2. Voltage gain  $M$  calculated with (4-4) versus control variable  $t_{off}$  defined in Fig. 2-3 on page 23 normalized by  $T_r$ .

(2-17) is listed below

$$M = \frac{V_o}{V_{in}} = \frac{1}{4} \frac{w_r T_{off} - \sin(w_r T_{off})}{2J + w_r T_{off} + \sin(w_r T_{off})} \quad (4-4)$$

The gain curves for  $J < 2$  ends at the ZVS boundary (drawn as a green dotted line). The condition  $J = 0.3$  is the worst case in the range of  $0.3 < J < 10$ . The interval length  $\tau_2$  and  $\tau_6$  (approximated to be zero in the model) in Fig. 2-4 increases as  $J$  decreases. The normalized control variable  $w_r T_{off}$  have less impact on the gain curve error compared to the normalized load condition  $J$ . The gain curve error was less than 9% at the valid boundary  $J = 0.3$ , and was less than 4% at  $J = 10$ . The error was less than 9% within the range of validity  $0.3 \leq J \leq 10$ .

The detailed derivation of the ZVS boundary is in Chapter 2 on page 39. The boundary equation in (2-26) is listed below

$$J \geq -2 \sin(w_r t_{off}) \quad (4-5)$$

The high-side switches lose soft switching beyond the dotted line.

The condition  $J = 0.3$  is the worst case in the range of  $0.3 < J < 10$  for the ZVS equation (2-26). The interval length  $\tau_2$  and  $\tau_6$  (approximated to be zero in the model) increases as  $J$  decreases. The error is expected to be more than 3% with  $J < 0.3$ . The components  $C_s$ ,  $L_{oa}$ , and  $L_{ob}$  are treated as constant voltage or current sources given the 20% peak-to-peak ripple assumption. The worst-case error is expected to be more than 3% with larger ripples (>20%). The model assumes  $\tau_2 = 0$  and  $\tau_6 = 0$ . A larger ripple design reduces the peak current of  $L_r$  and increases the time needed ( $\tau_2$  and  $\tau_6$ ) to charge  $C_r$ . The equation (2-26) outlines the maximum  $w_r t_{off}$  given the load condition  $J$ . The error caused by the zero-ripple approximation makes the calculated maximum  $w_r t_{off}$  is larger than the simulated one.

The peak gains for  $J > 2$  are connected with the red dashed line. The detailed derivation of the peak voltage gain for  $J > 2$  is in Chapter 2 on page 41. The peak gain equation in (2-36) is listed below

$$M_{pk} \approx \frac{1}{4} \frac{\frac{3\pi}{2} + 1}{2J + \frac{3\pi}{2} - 1}, \quad J > 2 \quad (4-6)$$

There are no soft-switching boundaries for the minimum voltage gain.

The condition  $J = 0.3$  is the worst case in the range of  $0.3 < J < 10$ . The interval length  $\tau_2$  and  $\tau_6$  (approximated to be zero in the model) in Fig. 2-4 increases as  $J$  decreases. The peak gain error was less than 9% at the valid boundary  $J = 0.3$ , and was less than 4% at  $J = 10$ . The error was less than 9% within the range of validity  $0.3 \leq J \leq 10$ .

Large  $J$  corresponds to a large  $L_r$  design resulting in a larger length of the subinterval 4 and 8, which does not deliver energy to the load. Less energy is delivered to the load. There is a smaller maximum voltage gain. Smaller  $J$  results in less energy reserved in resonant inductor  $L_r$  for soft switching in subinterval 2, and results in the limited ZVS region. A smaller  $J$  design offers a higher peak voltage gain at the expense of higher resonant tank energy.

#### 4.4 Resonant Frequency Design for Minimum Switching Frequency

The normalized switching period and switching frequency are calculated in (2-23) on page 44 in Chapter 2. The equation is listed below

$$w_r T_s \approx 2(2J + w_r T_{off} + \sin(w_r T_{off})) \quad (4-7)$$

which can be reorganized as

$$\frac{f_s}{f_r} \approx \frac{\pi}{2J + w_r T_{off} + \sin(w_r T_{off})} \quad (4-8)$$

For the same  $w_r T_{off}$ , the normalized switching period is longer as the normalized load current  $J$  increases, since the resonant inductor takes a longer time to be charged to  $-I_o/2$  in the subinterval  $t_4 - t_5$ , and charged to  $I_o/2$  in the subinterval  $t_8 - t_1$ . A larger load current or a larger  $L_r$  design results in a larger  $J$ , and therefore larger  $T_s$ .

The condition  $J = 0.3$  is the worst case in the range of  $0.3 < J < 10$ . The interval length  $\tau_2$  and  $\tau_6$  (approximated to be zero in the model) shown in Fig. 2-4 increases as  $J$  decreases. The magnitude of the normalized control variable  $t_{off} f_r$  has smaller impact on the error because the load condition dominates in the calculation of  $\tau_2$  and  $\tau_6$ . The error is expected to be more than 3% with  $J < 3$ .

The components  $C_s$ ,  $L_{oa}$ , and  $L_{ob}$  are treated as constant voltage or current sources given the 20% peak-to-peak ripple assumption. The worst-case error is expected to be more than 3% with larger ripples. The model assumes  $\tau_2 = 0$  and  $\tau_6 = 0$ . A larger ripple design reduces the peak current of  $L_r$ , and increases the time needed ( $\tau_2$  and  $\tau_6$ ) to charge  $C_r$ .

Fig. 4-3(a) shows the normalized switching frequency  $f_s/f_r$  versus normalized load current  $J$ . The curves shift higher as  $t_{off} f_r$  reduces from 0.5 to 0.2. The switching ripples across the resonant elements change slightly as the control variable increases.

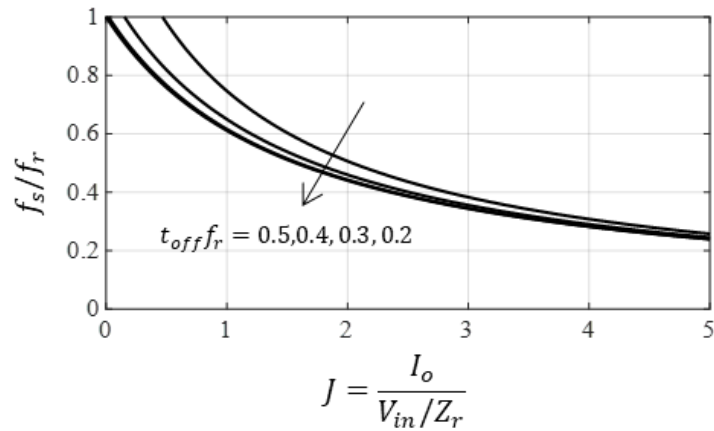
The curves for  $t_{off} f_r < 0.2$  are not drawn in Fig. 4-3(a) as their maximum voltage gain is smaller than 0.05.

Fig. 4-3(b) shows that the variance of the switching frequency as  $t_{off} f_r$  increases from 0.2 to 0.5. The ratio of switching frequency with  $t_{off} f_r = 0.5$  to switching frequency with  $t_{off} f_r = 0.2$  ranges from 0.8 to 1 for  $J > 0.8$ .

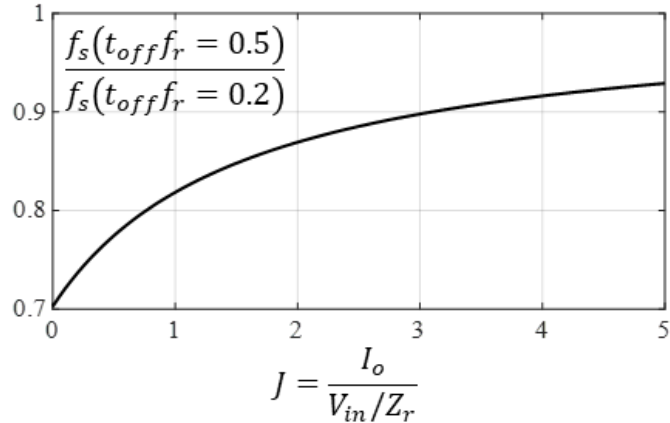
The switching frequency curve can be approximated to the curve with  $t_{off} f_r = 0.5$  for simple

calculation.

The variance of  $f_s$  with  $w_r T_{off}$  is less than 15% for  $0.2 < w_r T_{off} < 0.8$  and  $J > 1$ . A simple switching frequency design curve is generated by setting  $w_r T_{off} = \pi$  and results in



(a)



(b)

**Fig. 4-3. (a) Normalized switching frequency versus  $J$  calculated with (4-8). The curves shift higher as  $t_{off} f_r$  reduces from 0.5 to 0.2. The curves for  $t_{off} f_r < 0.2$  are not drawn as their maximum voltage gain is smaller than 0.05. (b) The ratio of switching frequency with  $t_{off} f_r = 0.5$  to switching frequency with  $t_{off} f_r = 0.2$  calculated with (4-8). The switching frequency curve can be approximated to the curve with  $t_{off} f_r = 0.5$  for simple calculation.**

$$\frac{f_s}{f_r} \approx \frac{1}{\frac{2J}{\pi} + 1} \quad (4-9)$$

The error of (4-9) is less than 15% within the range of validity  $0.3 \leq J \leq 10$ . The error is primarily caused by the approximation of  $w_r T_{off} = \pi$ . The approximated equation in (4-9) only depends on the normalized load condition J, and simplifies the design procedure. Designers can use the more acute switching frequency equation (4-8) if a more accurate switching frequency range with an error less than 9% is needed.

Fig. 4-4 shows normalized switching frequency versus J at  $w_r T_{off} = \pi$ . This curve serves as the design curve for setting the switching frequency. Fig. 4-4 suggests that the converter operates at the minimum switching frequency  $f_{sMin}$  at

$$J_{max} = \frac{I_{oMax}}{V_{inMin}/Z_r} \quad (4-10)$$

where the converter is with full-load condition  $I_{oMax}$  and minimum input voltage  $V_{inMin}$ . The specifications of the converter input and output are typically given. The design of  $f_{sMin}$  is by

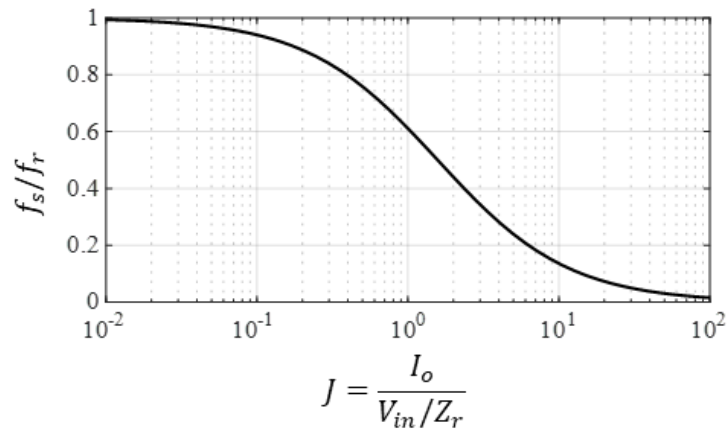


Fig. 4-4. Normalized switching frequency versus J as design curve calculated with (4-9).

controlling the design of  $Z_r$ . The converter moves to the maximum switching frequency  $f_{sMax}$  at

$$J_{min} = \frac{I_{oMin}}{V_{inMax}/Z_r} \quad (4-11)$$

where the converter is with minimal condition  $I_{oMin}$  and maximum input voltage  $V_{inMax}$ .

#### 4.5 Capacitance Ratio Design for Specified Voltage Ripple

By solving

$$C_s \Delta V_{C_s} = \left| \int_{t_8}^{t_1} i_{Lr}(\lambda) d\lambda + \int_{t_1}^{t_2} i_{Loa}(\lambda) d\lambda \right| \quad (4-12)$$

the peak-to-peak voltage ripple  $\Delta V_{C_s}$  normalized by  $V_{in}$  is

$$\frac{\Delta V_{C_s}}{V_{in}} = \frac{C_r}{C_s} \frac{(\sin(w_r T_{off}) + J)^2 + J^2 + 2w_r T_{off} J}{4} \quad (4-13)$$

Larger  $J$  results in a larger  $C_s$  current ripple and therefore larger  $\Delta V_{C_s}$ . A smaller voltage ripple design is typically preferred for smaller voltage stresses on the capacitors  $C_s$  and  $C_r$ . Smaller ripples could be achieved by increasing  $C_s$  and reducing the normalized load  $J$  by designing smaller characteristic impedance  $Z_r$ .

To design the capacitance ratio  $C_n$ , (4-13) is reorganized to

$$C_n = \frac{C_s}{C_r} = \frac{V_{in}}{\Delta V_{C_s}} \frac{(\sin(w_r T_{off}) + J)^2 + J^2 + 2w_r T_{off} J}{4} \quad (4-14)$$

$w_r t_{off} = \frac{3}{2}\pi$  is used for calculating the worst-case voltage ripple at given  $J$ . The  $C_s$  design can follow

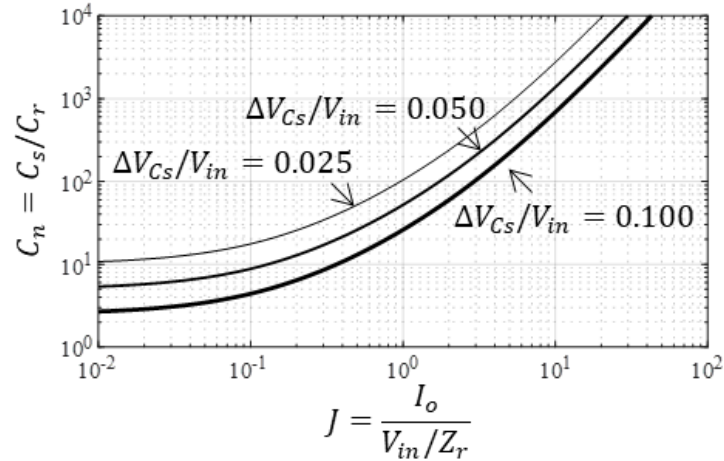


Fig. 4-5. Capacitance ratio  $C_n$  calculated with (4-15) versus normalized load current  $J$  parametric with the series capacitor voltage ripple  $\Delta V_{C_s}/V_{in}$ .

$$C_n = \frac{C_s}{C_r} = \frac{V_{in}}{\Delta V_{C_s}} \frac{(J-1)^2 + J^2 + 3\pi J}{4} \quad (4-15)$$

Fig. 4-5 shows the design curves for the capacitance ratio  $C_n$  design. The required  $C_n$  is plotted versus the normalized load condition  $J$  parametric with the  $v_{C_s}$  ripple.

The design of  $C_n$  also impacts the oscillation between the  $C_s$  and  $L_o$  which are analyzed in the chapter on transient-state analysis. It is recommended to design  $C_n$  according to the requirements of the steady-state voltage ripple and the transient response convergence.

The error of the calculated voltage ripple using equation (4-15) is less than 5% for the exemplary design in Table 4-3 on page 114. The error has not been fully analyzed over a wide load condition range of  $0.3 < J < 10$ . The study of the error caused by the normalized control variables  $w_r T_{off}$  and the normalized load condition will be part of the future work.

## 4.6 Inductance Ratio Design for Specified Current Ripple

By solving

$$L_o \Delta I_{L_o} = \int_{t_5}^{t_6} (v_{Cs}(\lambda) + v_{Cr}(\lambda) - V_o) d\lambda \quad (4-16)$$

the peak-to-peak current ripple  $\Delta I_{L_o}$  normalized by  $V_{in}/Z_r$  is

$$\frac{\Delta I}{\frac{V_{in}}{Z_r}} = \frac{L_r}{L_o} \left( \left( \frac{1}{2} - \frac{V_o}{V_{in}} \right) w_r T_{off} - \frac{\sin(w_r T_{off})}{2} \right) \quad (4-17)$$

The inductor current ripple depends on the control variable  $w_r T_{off}$  and the output inductance  $L_o$ . A smaller ripple is achieved by increasing  $L_o$ .

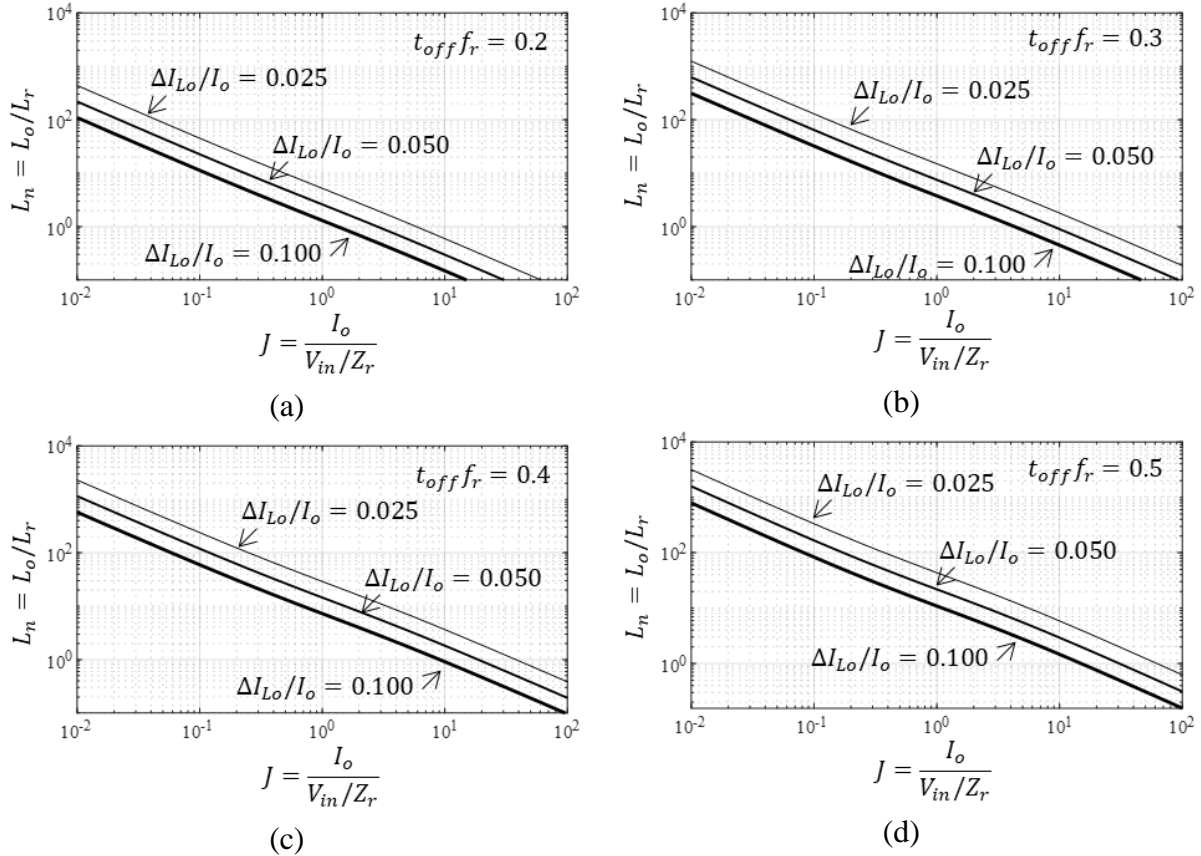


**Fig. 4-6. Inductance ratio  $L_n$  calculated with (4-18) versus normalized load current  $J$  parametric with the output inductor current ripple  $\Delta I_{L_o}/I_o$  and the normalized control variable  $t_{off} f_r$ .**

To design the inductance ratio  $L_n$ , (4-17) is reorganized to

$$L_n = \frac{L_o}{L_r} = \frac{I_o}{\Delta I} \frac{\left(1 - 2 \frac{V_o}{V_{in}}\right) w_r T_{off} - \sin(w_r T_{off})}{J} \quad (4-18)$$

Fig. 4-6 shows the design curves for the inductance ratio  $L_n$  design. The required  $L_n$  is plotted versus the normalized load condition  $J$  parametric with the  $i_{L_o}$  ripple and the normalized control variable  $t_{off} f_r$ .

The error of the calculated output inductor current ripple using equation (4-18) is less than 5% for the exemplary design in Table 4-3 on page 114. The error has not been fully analyzed over a wide load condition range of  $0.3 < J < 10$ . The study of the error caused by the normalized control variables  $w_r T_{off}$  and the normalized load condition will be part of the future work.

## 4.7 Component Stresses

In the steady state, output inductor current ripples are ignored for switch current stress calculation. The short subintervals 2, 3, 6, and 7 are approximated to be zero. The validity of this approximation is discussed in Section 2.5 on page 30.

The following approximation is made for a simpler calculation

$$I_{a1@t_8} = I_{Lr@t_8} = \frac{\sin[w_r T_{off}] V_{in}}{Z_r} \frac{I_o}{2} - \frac{I_o}{2} \approx -\frac{I_o}{2} \quad (4-19)$$

The RMS current of the switch  $S_{a1}$  is calculated as follows

$$\begin{aligned} I_{a1RMS} &= \sqrt{\frac{1}{T_s} \int_{t_1}^{t_1+T_s} i_{a1}^2(t) dt} \approx \sqrt{\frac{T_{off}}{T_s} \left(\frac{I_o}{2}\right)^2 + \frac{1}{3} \left(\frac{I_o}{2}\right)^2 \frac{T_8}{T_s} + \frac{1}{3} \left(\frac{I_o}{2}\right)^2 \frac{T_8}{T_s}} \\ &\approx \frac{I_o}{2} \sqrt{\frac{F_s}{F_r} \left(T_{off} F_r + \frac{J}{3\pi}\right)} \end{aligned} \quad (4-20)$$

The  $S_{a1}$  current stress is load-dependent with the term  $I_o/2$ . The  $S_{a1}$  current decreases as the load current drops, which is good for light-load efficiency.

The following approximations are applied to calculate the current stresses of the other switches

$$I_{b1@t_4} = -I_{Lr@t_4} = -\frac{\sin[w_r T_{off}] V_{in}}{Z_r} \frac{I_o}{2} - \frac{I_o}{2} \approx -\frac{I_o}{2} \quad (4-21)$$

$$I_{a2@t_8} = I_{a1@t_8} - I_{Loa@t_8} \approx -I_o \quad (4-22)$$

$$I_{b2@t_4} = I_{b1@t_4} - I_{Lob@t_4} \approx -I_o \quad (4-23)$$

The RMS current stresses of switches  $S_{b1}$ ,  $S_{a2}$ , and  $S_{b2}$  are calculated as

$$I_{b1RMS} \approx \sqrt{\frac{t_{off}}{T_s} \left(\frac{I_o}{2}\right)^2 + \frac{1}{3} \left(\frac{I_o}{2}\right)^2 \frac{T_4}{T_s} + \frac{1}{3} \left(\frac{I_o}{2}\right)^2 \frac{T_4}{T_s}} \approx \frac{I_o}{2} \sqrt{\frac{F_s}{F_r} \left(T_{off} F_r + \frac{J}{3\pi}\right)} \quad (4-24)$$

$$I_{a2RMS} \approx \sqrt{\frac{1}{3} I_o^2 \frac{T_4}{T_s} + \frac{T_{off}}{T_s} I_o^2 + \frac{1}{3} I_o^2 \frac{T_8}{T_s}} \approx \frac{I_o}{2} \sqrt{\frac{F_s}{F_r} \left(4T_{off} F_r + \frac{8J}{3\pi}\right)} \quad (4-25)$$

$$I_{b2RMS} \approx \sqrt{\frac{T_{off}}{T_s} \left(\frac{I_o}{2}\right)^2 + \frac{1}{3} I_o^2 \frac{T_4}{T_s} + \frac{T_8}{T_s} \left(\frac{I_o}{2}\right)^2} \approx \frac{I_o}{2} \sqrt{\frac{F_s}{F_r} \left(T_{off} F_r + \frac{7J}{3\pi}\right)} \quad (4-26)$$

All current stresses of the switches are load-dependent as shown in Fig. 4-7.

The detailed math derivation has been listed in Appendix on page 261.

$S_{b1}$  and  $S_{a1}$  share similar current stress as their shapes of the current waveforms are the same with a 180-degree phase shift.  $S_{a2}$  experiences the highest current stress. That is because  $S_{a2}$  is part of the inductor  $L_{ob}$  charging loop  $S_{a2}$ - $C_r$ - $C_s$ - $L_{ob}$ - $R_{load}$  in subinterval  $t_5 - t_6$ , while  $S_{b2}$  is not in the inductor  $L_{oa}$  charging loop in subinterval  $t_1 - t_2$ .

Fig. 4-8 shows the peak current of the resonant inductor normalized by the load current.

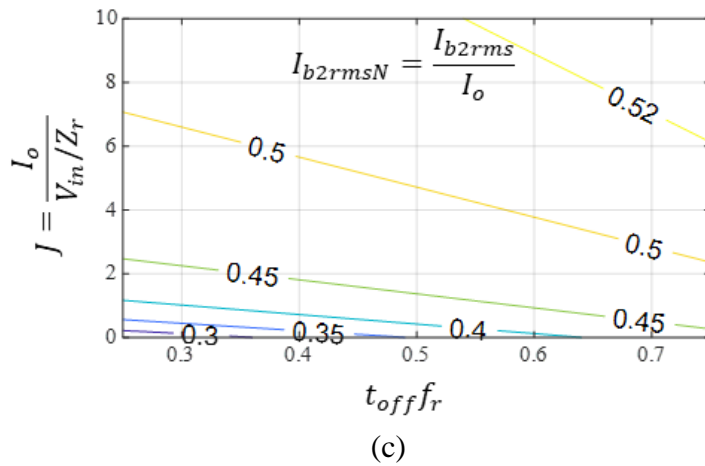
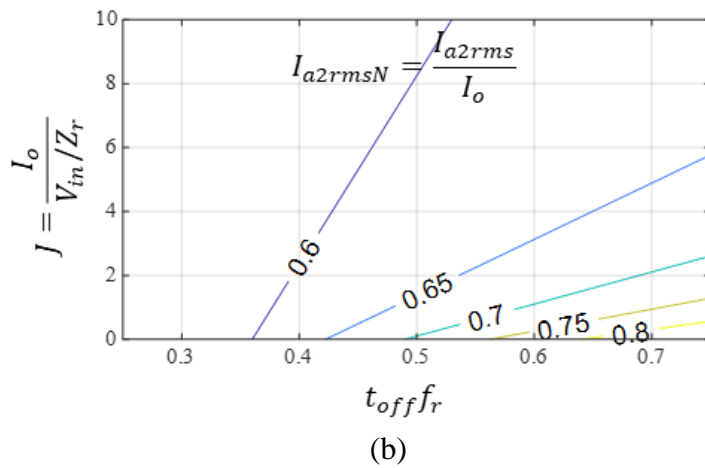
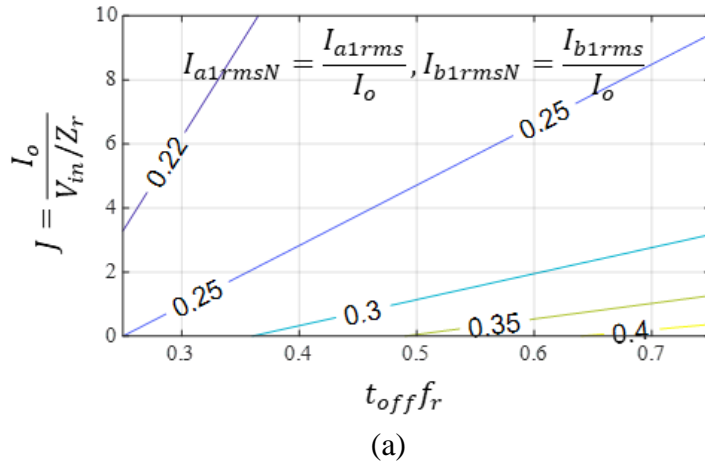


**Fig. 4-7. Normalized RMS current stresses of the switches (a)  $S_{a1}$  ( $S_{b1}$ ) calculated with (4-20), (b)  $S_{a2}$  calculated with (4-25), and (c)  $S_{b2}$  calculated with (4-26) in Fig. 3-1 on page 55. Large normalized control variable  $t_{off}f_r$  results in larger stress of  $S_{a1}$  because more power is delivered from the source to load. A large normalized load condition  $J$  leads to a larger voltage gain given the same  $t_{off}f_r$  and therefore higher current stress. The current stress variance of  $S_{a2}$  and  $S_{b2}$  are similar to the stress of  $S_{a1}$ .**

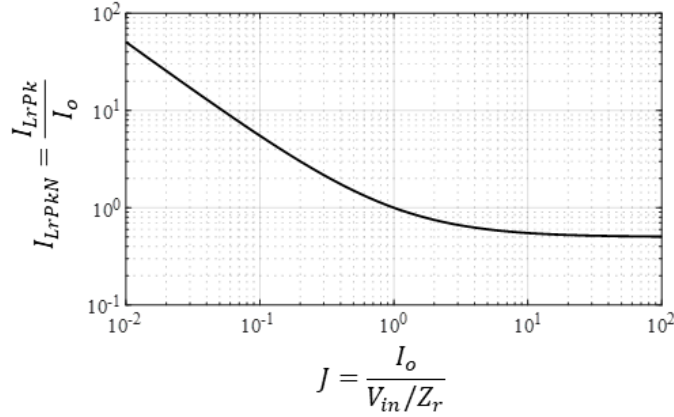


**Fig. 4-8. Peak current of resonant inductor normalized by the load current calculated with (4-27) versus the normalized load current. The resonant inductor current stress is load-dependent benefiting light-load efficiency. Larger characteristic impedance  $Z_r$  design helps reduce the peak resonant current.**

The peak current of the resonant inductor in Fig. 4-8 is

$$I_{LrPkN} = \frac{I_{LrPk}}{I_o} = \frac{\frac{1}{2} \left( \frac{V_{in}}{Z_r} + I_{oMax} \right)}{I_o} = \frac{1}{2} \left( \frac{1}{J} + 1 \right) \quad (4-27)$$

The resonant inductor current stress is load-dependent benefiting light-load efficiency. A larger characteristic impedance  $Z_r$  design helps reduce the peak resonant current. The absolute value of the resonant inductor drops as the load current decreases which benefits the converter light-load efficiency. A larger character impedance design reduces normalized resonant inductor current.

The RMS currents of  $C_s$  and  $C_r$  are

$$I_{CrRMS} = \sqrt{\frac{2}{T_s} \int_0^{T_{off}} i_{Cr}^2 dt} = \frac{V_{in}}{2Z_r} \sqrt{\frac{F_s}{F_r} \left( 2T_{off}F_r - \frac{\sin(4\pi T_{off}F_r)}{2\pi} \right)} \quad (4-28)$$

$$I_{CsRMS} = \sqrt{\frac{1}{T_s} \left( \int_0^{T_{off}} i_{a1}^2 dt + \int_0^{T_{off}} i_{b1}^2 dt \right)} = \frac{I_o}{2} \sqrt{2 \frac{F_s}{F_r} \left( T_{off}F_r + \frac{J}{3\pi} \right)} \quad (4-29)$$

The normalized control variable controls the energy flow into the converter. A larger  $T_{off}F_r$  increases the converter input current and therefore larger capacitor currents. The characteristic

impedance  $Z_r$  controls the distribution of the circulating energy between the resonant capacitor  $C_r$  and inductor  $L_r$ . A larger  $Z_r$  design reduces the circulating energy of the  $C_r$ , and therefore smaller  $I_{CrRMS}$ .

**Table 4-1. Component stresses in Fig. 3-1 on page 55 of the SRB prototype in Fig. 4-10 with components in Table 4-3**

	Equation	Calculation	Simulation	Error
$I_{a1RMS}$	(4-20)	6.0 A	5.6 A	7%
$I_{b1RMS}$	(4-24)	6.0 A	5.6 A	7%
$I_{a2RMS}$	(4-25)	13.4 A	12.9 A	4%
$I_{b2RMS}$	(4-26)	9.3 A	8.7A	6%
$I_{LrPk}$	(4-27)	17.0 A	16.2 A	5%
$I_{CrRMS}$	(4-28)	4.0 A	3.8 A	5%
$I_{CsRMS}$	(4-29)	8.6 A	7.9 A	8%

Table 4-1 compares the calculation results with the simulation results. The SRB converter operates at  $V_{inMin}$  and  $I_{oMax}$  in Table 4-2. The component specifications are listed in Table 4-3. The error is within 8%.

## 4.8 Design Flowchart and Experimental Verification

Fig. 4-9 shows the recommended sequential design for the SRB converter. The input includes

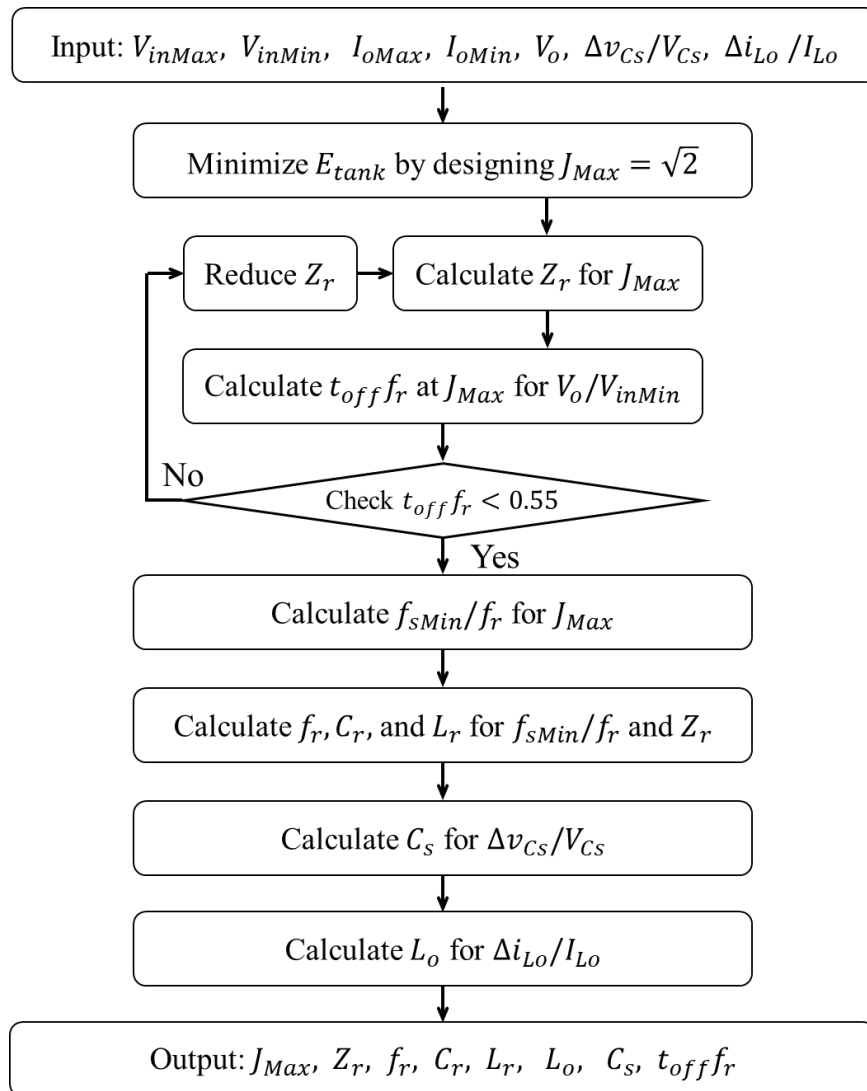


Fig. 4-9. Sequential design procedure of the SRB converter in Fig. 4-10. A design example using this procedure is in Table 4-3 using specifications in Table 4-2.

the range of input voltage, output voltage, and load current. The  $v_{C_s}$  and  $i_{L_o}$  ripples are specified. The characteristic impedance  $Z_r$  is designed first to reduce the circulating energy. It is important to check if the normalized control variable is larger than 0.55 which may cause a divergence issue in the transient response. Switch to a smaller  $Z_r$  design if the initial design is with a control variable higher than 0.55. The resonant frequency  $f_r$  of the resonant tank is then designed to meet the minimum frequency requirement. The  $C_s$  and  $L_o$  are followed to design for the given  $v_{C_s}$  and  $i_{L_o}$  ripples.

**Table 4-2. Specifications of the SRB prototype fed into the design procedure in Fig. 4-9 and resulting in the design in Table 4-3 and the prototype in Fig. 4-10**

Specified Parameters	Definitions	Value
$V_{inMax}$	Maximum input voltage	54 V
$V_{inMin}$	Minimum input voltage	48 V
$V_o$	Output voltage	7 V
$M_{max}$	Maximum gain	0.146
$I_{oMax}$	Maximum output current	20 A
$I_{oMin}$	Minimum output current	5 A
$\Delta v_{C_s}/V_{C_s}$	Peak-to-peak $v_{C_s}$ ripple	20%
$\Delta i_{L_o}/I_{L_o}$	Peak-to-peak $i_{L_o}$ ripple	20%
$f_{sMin}$	Minimum $f_s$ at $I_{oMax}$ and $V_{inMin}$	2 MHz

The design procedure is outlined in the first two columns, and the resultant values of the design variables are in the last column in Table 4-3. The efficiency and power density targets are not

specified because they depend heavily on the passive component designs, which are beyond the scope of this chapter.

**Table 4-3. Sequential design procedure of the SRB prototype in Fig. 4-10 using the design procedure in Fig. 4-9 and the specifications in Table 4-2**

	Design Methods	Value
$J_{max}$	Minimize $E_{tank}$ using (4-1)	$\sqrt{2}$
$Z_r$	Calculate $Z_r = J_{max}(V_{inMin}/I_{oMax})$ for $V_{inMin}$ and $I_{oMax}$ in Table 4-2	3.4 $\Omega$
$t_{off}f_r$	Calculate $t_{off}f_r$ at $J_{max}$ for $M_{max}$ in Table 4-2 using (2-27)	0.5
$t_{off}f_r$	Check $t_{off}f_r < 0.55$	Yes
$f_{sMin}/f_r$	Calculate $f_{sMin}/f_r$ for $J_{Max}$ in Table 4-2 using (4-9)	0.55
$f_r$	Calculate $f_r$ for $f_{sMin}$ in Table 4-2	3.7 MHz
$L_r$	Calculate $L_r = Z_r/(2\pi f_r)$	0.15 $\mu H$
$C_r$	Calculate $C_r = 1/L_r/(2\pi f_r)^2$	12 nF
$C_n$	Calculate $C_n$ using (4-15)	50
$C_s$	Calculate $C_s = C_n C_r$	0.6 $\mu F$
$L_n$	Calculate $L_n$ using (4-18)	8
$L_o$	Calculate $L_o = L_n L_r$	1.2 $\mu H$

The prototype was fabricated based on Table 4-2 and Table 4-3. The design of  $C_{in}$  and  $C_o$  depends on the design of the prior stage, which sources the SRB converter, and the SRB load requirements.

The ripple sizes are recommended to be less than 10%. The designer could use the simulation to design the  $C_{in}$  and  $C_o$  value.



**Fig. 4-10. Prototype of the Series-Resonator Buck (SRB) converter using the design procedure in Fig. 4-9, the specifications in Table 4-2, and the component values in Table 4-3.**

The hardware is shown in Fig. 4-10. The schematic is shown in the Appendix. GaNFET features small on-resistance and small switch equivalent output capacitance and therefore has been widely adopted for high-frequency converters. All switches were enhancement-mode power transistors EPC2045. The gate drivers were LMG1210 from Texas Instruments. The ferrite material ML-91s was selected for its low core loss density. The litz wire design is documented in [95]. The resonant capacitor  $C_r$  was eight discrete multilayer ceramic capacitors (CGA3E2NP02A152J080AA) in parallel. The series capacitor  $C_s$  was six discrete capacitors (C3216C0G2A104J160AC) in parallel. The input capacitor  $C_{in}$  was four ceramic capacitors (08051C105K4T2A). The output capacitor  $C_o$  was four discrete capacitors (GRM21BR61C226ME44L). The gate resistor was a 0603 resistor (ERJ-3BSJR20V). The overshoot voltage of the switch gate signals depends on the layout design. It is recommended to get started with a 2-ohm resistor. Then the gate resistance can be reduced gradually while the overshoot is monitored. The bootstrap diode was a Schottky barrier diode (BAT46WJ). The

bootstrap capacitor must be large enough to support charging the high-side FET. The bootstrap capacitor  $C_{boot}$  was designed by calculating  $C_{boot} \geq 10C_g = 2.96 \text{ nF}$  where  $C_g$  was equivalent gate-source capacitance of EPC2045.  $C_{boot}$  was designed to be 10 nF (08053C103KAT4A).

The input voltage was provided by the power supply UP60-14. The gate driving signals were provided by the signal generator AFG3102. The switching frequency and duty ratio of the gate signals were tuned until soft switching was achieved. The SMB connector supporting gate signals was 1-1337482-0. The load was six discrete resistors (HSA50R05J) in series.

The measured drain-source and gate-source voltages of all switches are shown in Fig. 4-11.

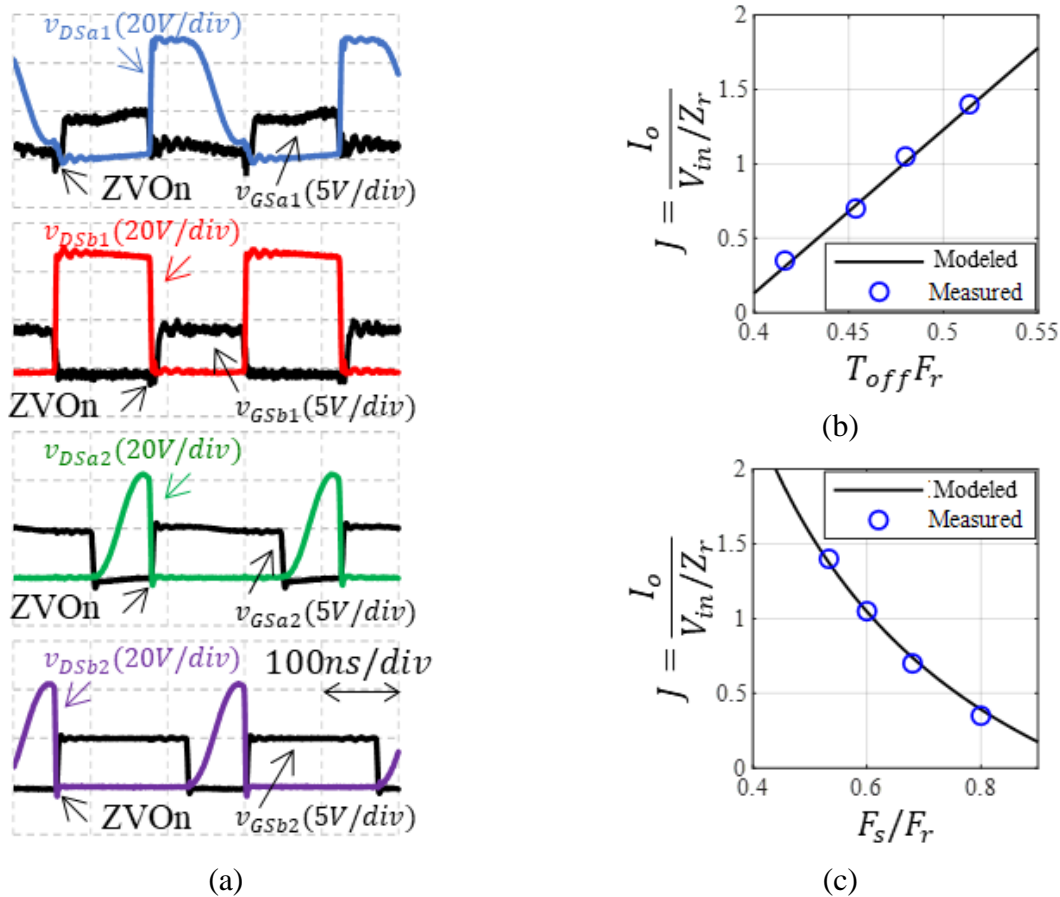


Fig. 4-11. (a) Experimental voltage waveforms of all the switches from the prototype in Fig. 4-10 measured by the oscilloscope; measured and modeled normalized load current versus (b) normalized control signal using (2-26) and (c) normalized switching frequency using (4-9).

The measurement results were exported from the oscilloscope MSO5104B. All switches were turned on at zero voltage. The area of the power loop and the gate driving loops were minimized to reduce the parasitic loop inductance.

The currents in the switches were not measured since the insertion of current probes or shunts was undesirable in a tight layout. The slopes of  $v_{DSa2}$  and  $v_{DSb2}$  were virtually zero at the off timing, suggesting  $S_{a2}$  and  $S_{b2}$  carried negligible currents at turn-off moments.

The full load efficiency was 97.3%. The measured and modeled normalized load versus the control variable is in Fig. 4-11(b), and the switching frequency is shown in Fig. 4-11(c). The measurement results were compared with the simulation. The discrepancy between the model and measurement was less than 3%.

The peak efficiency of the SRB prototype is 98.5%, and the full load efficiency is 97.3%, as shown in Fig. 4-12 (a). The switching frequency was adjusted with the load condition as shown in Fig. 4-12 (b). The measurement results were compared with the simulation.

The converter was simulated with the non-ideal switch model provided by EPC. Each capacitor was with an equivalent series resistor (ESR) at the switching frequency from the datasheets.

Each output inductor's loss was from TDK's inductor selection tool online, and was with an ESR according to the simulated loss.

This inductor was simulated with Finite Element Analysis (FEA) in Ansys Maxwell, and was with an ESR according to the FEA result. The discrepancy between simulation and measurement is less than 0.5%.

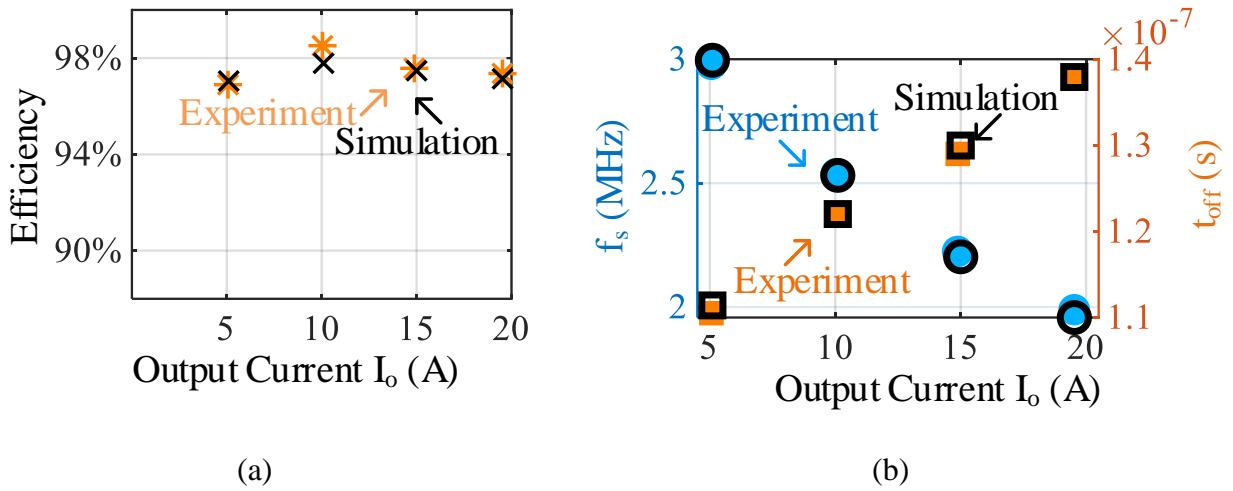
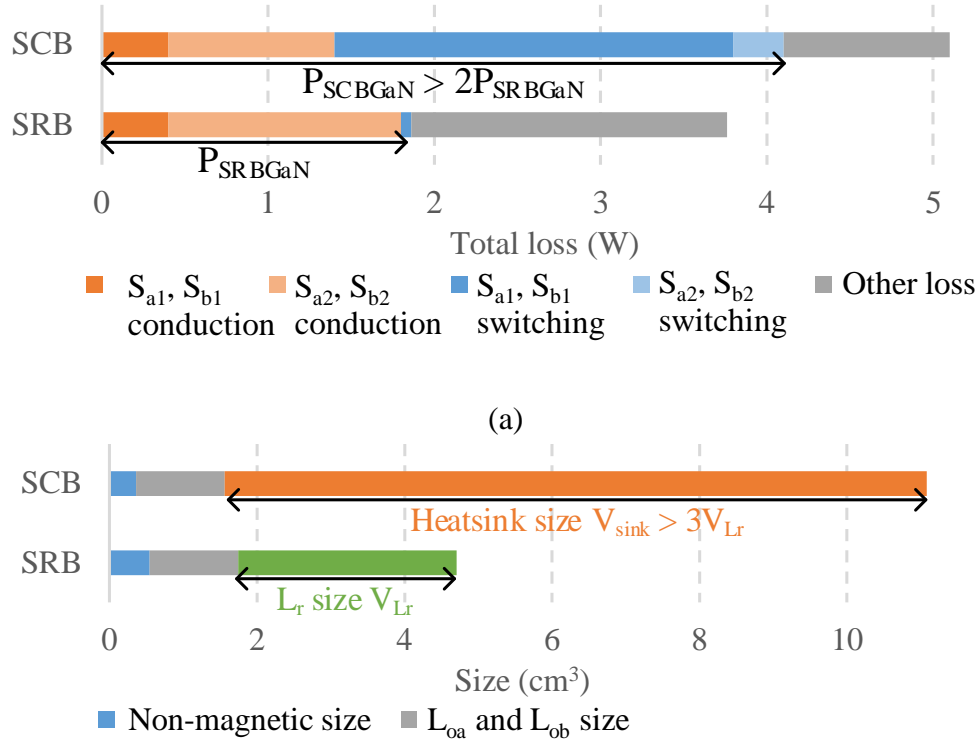


**Fig. 4-12. (a) Efficiency and (b) switching frequency modeled by (4-9) of the SRB prototype in Fig. 4-10 while keeping  $V_{in} = 48$  V and  $V_o = 7$  V (hollow circle:  $f_s$  in simulation, solid circle:  $f_s$  in experiment, and hollow square:  $t_{off}$  in simulation, solid square:  $t_{off}$  in experiment). The simulation utilized a non-ideal switch model from EPC and ideal passive components adding 2 m $\Omega$  inductor ESR.**

The major improvements with the series resonator are shown in Fig. 4-13. Two cases were compared using simulation at the same full-load operating point. GaN FET EPC2045 (100 V,  $R_{dson} = 7$  m $\Omega$ ,  $C_{oss} = 295$  pF) was selected for all the switches in the SRB converter. The low-side switches' voltage stress was  $V_{in}/2$  in the SCB converter. EPC2045 for the high-side switches and EPC2049 (40 V,  $R_{dson} = 5$  m $\Omega$ ,  $C_{oss} = 350$  pF) for the low-side switches were selected. The non-ideal switch models were provided by EPC.

The average switch junction temperatures of both cases are the same. A heatsink was added to the SCB converter due to hard-switching loss. The total loss was compared in Fig. 4-13 (a). The SCB converter had a switch loss that was twice the switch loss of the SRB converter. The series resonator saved about 30% of the overall converter loss. The size comparison is shown in Fig. 4-13 (b). Both cases have the same output inductors. The heatsink size of the SCB converter is three times larger than the resonant inductor size of the SRB converter.



(a)

(b)

Fig. 4-13. (a) Total loss and (b) converter size comparison between the SRB converter in Fig. 4-10 and the SCB converter with the same full load condition in Table I. The simulation utilized non-ideal switch models from EPC and ideal passive components adding 2 mΩ inductor ESR. A heatsink (374024B60023 made by Aavid Thermalloy) is added for the SCB converter to keep the switch's average junction temperature the same. The SRB converter reduces switch loss by a factor of 2. Its resonant inductor size is less than one-third of the heatsink size in the SCB converter.

## 4.9 Conclusion

The steady-state operation of the Series-Resonator Buck converter belongs to the class of quasi-resonant converters. The resonant frequency of the resonant components is higher than the switching frequency. The switch network waveforms are quasi-sinusoidal pulses.

The design  $J_{max} = \sqrt{2}$  minimizes the normalized resonant tank energy in (4-1) by balancing the peak energy in the resonant elements  $L_r$  and  $C_r$ . The gain equation in (2-27) models the load-

dependent characteristic and the peak gain boundary. The switching frequency can be calculated using (4-8). The  $f_s$  variation with voltage gain  $M$  is small because the resonant element switching ripples change little with different  $M$ . Equations (4-15) and (4-18) are provided to design the non-resonant passive components  $C_s$ ,  $L_{oa}$ , and  $L_{ob}$ , given the size of switching ripples. The error of the equations (4-15) and (4-18) over wide load condition  $0.3 < J < 10$  has not been fully studied, and will be part of future work.

The understanding of the analytical relationships between the resonant tank energy, voltage gain, component stresses, and the design parameters were utilized to guide the converter design. The prototype fabricated based on the specifications in was designed according to the procedures listed in Table 4-3. The theoretical analysis was validated by a 2-MHz SRB converter with 48 V at the input and 7 V, 20 A at the output. The discrepancy between the model, and measurement was less than 3%.

# Chapter 5 Rhombus-Window Resonant Inductor Design with Significant ac Flux

## Nomenclature

Symbol	Description
$A_L$	Footprint of the inductor in Fig. 5-3
$C_m$	Steinmetz coefficient of the magnetic material in Table 5-1
$f_s$	Switching frequency in Table 5-1
$h_c$	Height of the magnetic core in Fig. 5-3
$h_w$	Winding thickness in Table 5-1
$I_{acpk}$	Peak ac inductor current in Table 5-1
$i_{Lr}$	Resonant inductor current in Fig. 5-1
$L$	Inductance in Table 5-1
$k_y$	Ratio of the window height to core thickness in Fig. 5-3
$l_g$	Length of the air gap in Fig. 5-3
$l_c$	Length of the magnetic core in Fig. 5-3
$t_c$	Thickness of the magnetic core in Fig. 5-3
$R_{ag}$	Reluctance of the air gap in (5-3)
$R_{agin}$	Reluctance of the air gap inner path in (5-5)
$R_{agout}$	Reluctance of the air gap inner path in (5-4)
$R_{ml}$	Reluctance of the core reluctance in (5-2)
$R_{wfr}$	Reluctance of the window area in (5-6)
$v_{Lr}$	Resonant inductor voltage in Fig. 5-1
$w_c$	Width of the inductor in Fig. 5-3
$w_h$	Thickness of the inductor winding in Fig. 5-3
$w_w$	Width of the inductor winding in Fig. 5-3
$\alpha$	Steinmetz coefficient of the magnetic material in Table 5-1

$\beta$	Steinmetz coefficient of the magnetic material in Table 5-1
$\mu_r$	Relative permeability in Table 5-1

---

## 5.1 Introduction

Recent works on one-turn inductors focus on the reduction of inductor loss and size [114]-[122]. The lateral-flux inductor has a smaller winding loss with a shorter winding [114]-[116]. Its ac current handling capability is usually limited. The vertical-flux inductor typically has a larger cross-sectional area with a stronger ac current handling capability. A two-vertical gap inductor is suggested for inductors with high dc and ac currents [122]. This low-profile design demonstrates strong current handling capability. A more compact design was achieved after introducing the coupling effect [123].

The design of an inductor with significant ac flux at MHz switching frequency is challenging [124] – [140]. High switching frequency at the MHz level contributes to core loss and winding loss due to skin and proximity effects [124] – [129]. Air gap brings in a fringing magnetic field, which results in uneven current distribution and therefore higher winding loss.

A distributed airgap [130] – [133] was suggested to mitigate the fringing field caused by the air gap. Ref. [135] replaced the air gap with low-permeability material to reduce the fringing flux. Ref. [136] used the air gap fringing field to compensate for the adverse magnetic skin and proximity fields within the winding. Reconfiguring the winding structure was another option to reduce the winding loss [137], [140].

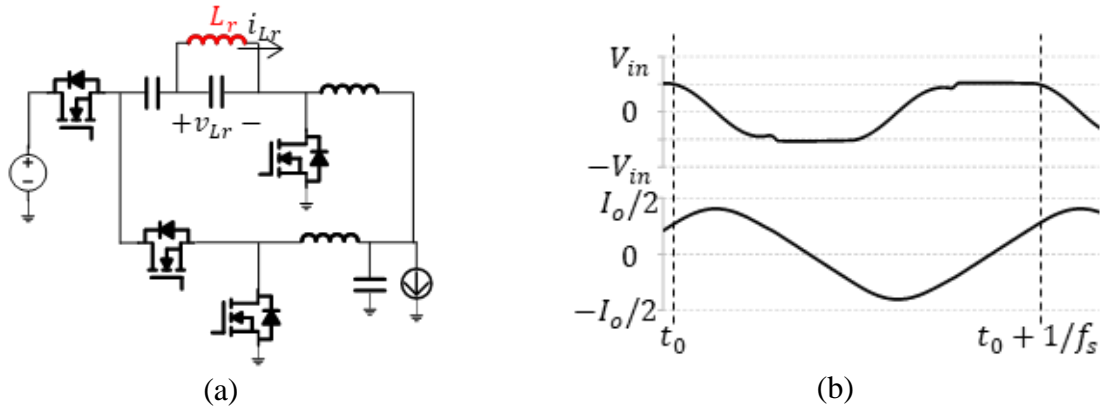


Fig. 5-1. (a) Schematic of the SRB converter with the resonant inductor being highlighted; (b) simulated resonant inductor current and voltage waveforms.

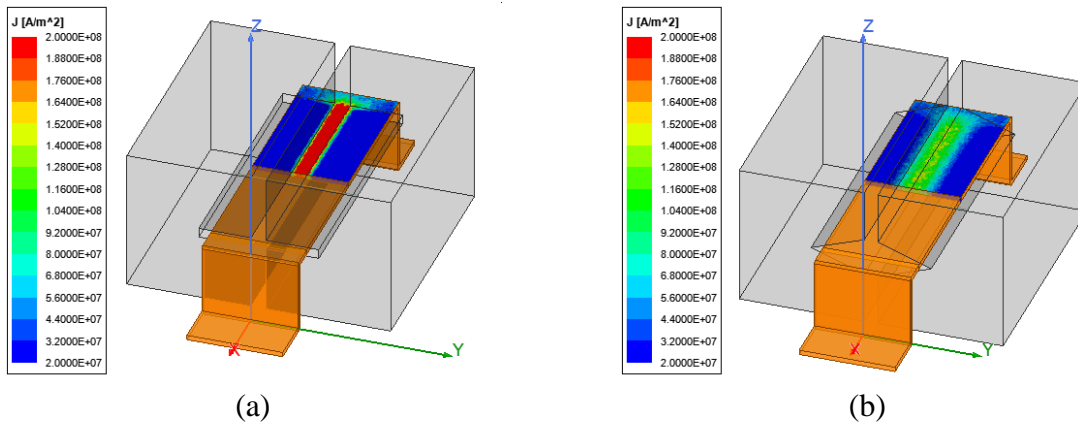


Fig. 5-2. (a) Conventional rectangular-window inductor with significant current crowding; and (b) rhombus-window inductor with better current distribution. The inductor specifications are labeled in Fig. 5-13. The inductor current excitation is 36A peak current at 2MHz. The type is set as “Solid”. It was simulated using eddy current mode in Ansys Maxwell 2D.

One example of an application using inductors with significant ac flux is the Series-Resonator Buck (SRB) converter. Fig. 5-1(a) shows the schematic of the Series-Resonator Buck converter. The resonant inductor is highlighted. The simulated current and voltage waveforms of the resonant inductor  $L_r$  are shown in Fig. 5-1(b).

This work replaces the conventional rectangular core window, shown in Fig. 5-2(a), with the rhombus core window shown in Fig. 5-2(b). The inductor volumes are the same in both designs.

The winding in the rectangular-window design is closer to the air gap, and exposed to a stronger fringing flux. The winding current crowds at the surface of the copper near the gap. The rhombus-window design provides extra space between the gap and the winding, and therefore the smaller winding loss caused by the fringing field. The winding current spreads out on the winding copper.

This chapter presents the design of a resonant inductor with significant ac flux. The conventional rectangular-window core was replaced by the rhombus-window core to reduce the fringing flux on the winding and therefore smaller winding loss. The inductance, core loss, and winding loss of the rhombus-window inductor are discussed. The step-by-step design procedure meeting the given exemplary specifications is given. Experimental results are discussed to verify the theoretical analysis.

### 5.2 Selection of 2-MHz Magnetic Material

The performances of the magnetic material are compared in references [141] – [148]. Some of the best materials include 3F4 [143], ML91s [144], DMR51 [145], and P61 [146] as shown in Fig. 5-3.

Fig. 5-3 compares the measured core loss density versus peak ac flux density at 2 MHz. 3F4

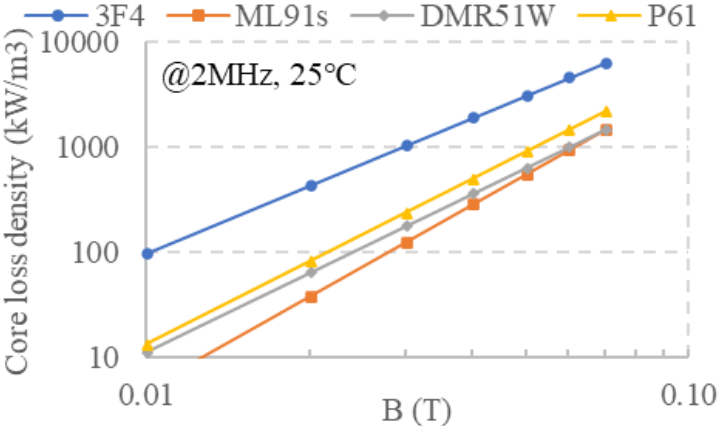


Fig. 5-3. Measured core loss density versus peak ac flux density at 2MHz.

shows the largest core loss density among the candidates. There is no significant difference between the core loss of ML91s, DMR51W, and P61. DMR51W and ML91s are recommended for their low loss at large peak ac flux density higher than 40 mT.

3F4 is a high-frequency power material made by Ferroxcube for use in power and general-purpose transformers at frequencies of 1 MHz – 2 MHz. ML91s is designed for use in transformers and inductors for automotive, data center, server, and telecommunication applications. DMR51 from Hengdian Group DMEGC targets high-frequency and high-temperature applications. P61 is made by ACME Electronics Corporation, and optimized for frequencies above 2 MHz.

DMR51 was selected for the inductor prototype in this study for its low core loss density.

### 5.3 Structural Design of the Rhombus-Window Inductor

Fig. 5-4 shows the front view of the rhombus-window inductor and the key design parameters are defined.  $t_c$  is the magnetic core thickness. The core height is twice the core thickness  $h_c = 2t_c$ .  $d_x$  is the clearance distance between the magnetic core and the inductor winding.  $w_w$  and  $w_h$  are the winding width and thickness. The length of the air gap is  $l_g$ . The length of the inductor along the x-axis is  $l_c$ .

The ratio  $k_y$  controls the thickness of the magnetic core. Smaller  $k_y$  results in a shorter distance  $k_y t_c$  between the air gap and the winding. The core loss of the magnetic material is characterized using the Steinmetz coefficients  $C_m$ ,  $\alpha$ , and  $\beta$ . The relative permeability of the magnetic material is  $\mu_r$ .

The width of the core is calculated as  $w_c = 2t_c + w_w + 2d_x$ . The inductor volume is  $V_L = l_c w_c h_c$ . The footprint is  $A_L = l_c w_c$ . The following section of this chapter discusses the inductance, core loss, and winding loss of the rhombus-window inductor.

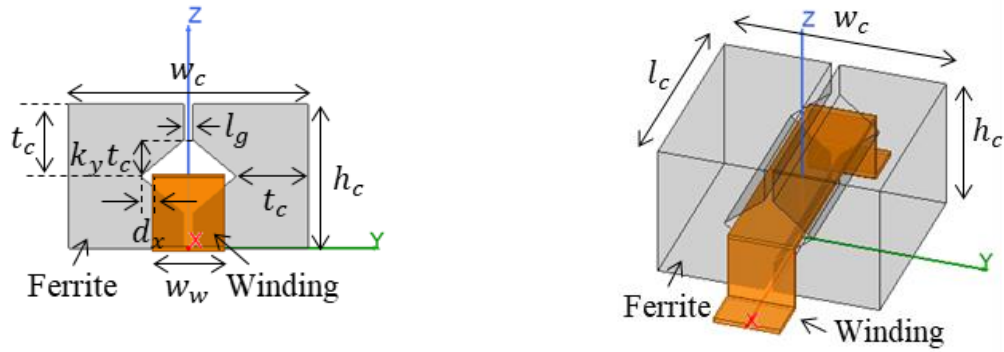


Fig. 5-4. Front view and 3-D view of the inductor with rhombus window. Key design parameters are listed above.

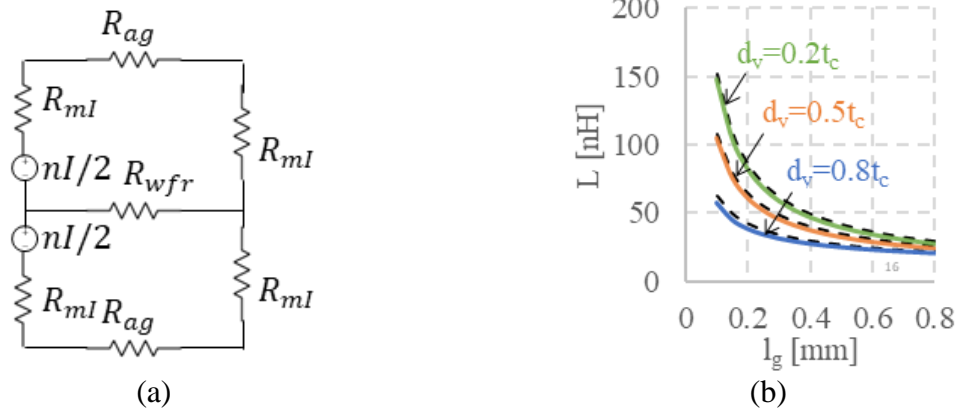


Fig. 5-5. (a) Magnetic circuit model of the rhombus-window inductor. (b) Simulated (dash line) and calculated (solid line) inductance versus the inductor air gap parametric with the window height ratio  $k_y$  with inductor specifications  $h_w = 100 \mu m$ ,  $w_w = 3 cm$ ,  $l_c = 9 cm$ ,  $t_c = 3 cm$ ,  $\mu_r = 900$ ,  $d_x = 1 mm$ ,  $w_c = 9 cm$ , and  $h_c = 6 cm$  labeled in Fig. 5-4. The inductor current excitation is 36A peak current at 2MHz. The type is set as “Solid”. The inductance was simulated using eddy current mode in Ansys Maxwell 2D.

## 5.4 Inductance of the Rhombus-Window Inductor

A magnetic circuit shown in Fig. 5-5 is drawn to calculate the inductance of the rhombus-window inductor. The winding is a source of magnetomotive force (MMF), of value  $nI$ . The core reluctance  $R_{ml}$  and air gap reluctance  $R_{ag}$  are effectively in series.

The solution of the magnetic circuit is

$$ni = \Phi((2R_{ag} + 4R_{ml}) // (R_{wfr} + R_{ag} + 2R_{ml})) \quad (5-1)$$

The capacitance-to-reluctance analogy was suggested by [149] to calculate the reluctance in typical magnetic core configurations. The core reluctance  $R_{ml}$  models the side legs, and is calculated as

$$R_{ml} = \frac{\frac{h_c - 2k_y t_c}{2}}{\mu_0 \mu_r t_c} \quad (5-2)$$

where  $\mu_r$  is the relative permeability of the magnetic core material, and  $\mu_0$  is the permeability of free space.

The air gap is modeled by the air gap reluctance  $R_{ag}$

$$R_{ag} = \frac{R_{agout} R_{agin}}{R_{agout} + R_{agin}} \quad (5-3)$$

$$R_{agout} = \frac{1}{\mu_0 \left( \frac{h_c - k_y t_c}{2l_g} + \frac{1}{\pi} \left( 1 + \ln \frac{\pi \frac{w_c - l_g}{2}}{2l_g} \right) \right)} \quad (5-4)$$

$$R_{agin} = \frac{1}{\mu_0 \left( \frac{h_c - k_y t_c}{2l_g} + \frac{1}{\pi} \left( 1 + \ln \frac{\pi \left( \frac{w_c - l_g}{2} - t_c \right)}{2l_g} \right) \right)} \quad (5-5)$$

The fringing effect of the window area is modeled by the reluctance  $R_{wfr}$

$$R_{wfr} = \frac{w_c - 2t_c}{\mu_0 \frac{h_c - 2(t_c - k_y t_c)}{2}} \quad (5-6)$$

The inductance of a one-turn inductor is modeled as

$$L = \frac{l_c}{(2R_{ag} + 4R_{ml}) // R_{wfr}} \quad (5-7)$$

Fig. 5-5 compares the calculated inductance using (5-2) – (5-7). The simulated inductance

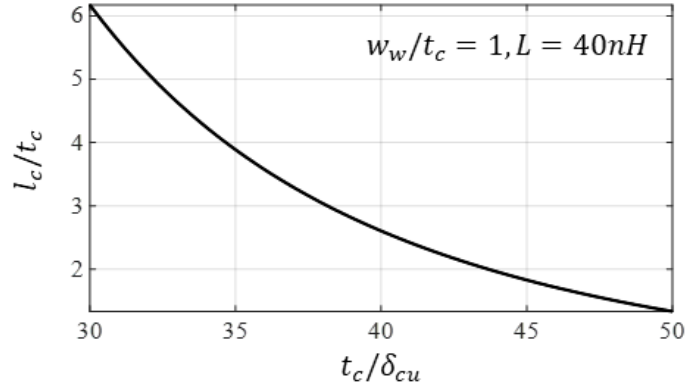


**Fig. 5-6. Inductor length  $l_c$  versus design variables the core thickness  $t_c$  labeled in Fig. 5-4. The inductor current excitation is 36A peak current at 2MHz. The type is set as “Solid”. The inductance was simulated using eddy current mode in Ansys Maxwell 2D.**

using an FEA simulation parametric with the window height ratio  $k_y$ . A larger  $k_y$  results in a smaller cross-sectional area  $(1 - k_y)t_c l_c$ , and therefore smaller inductance. The inductance is controlled by the design of the air gap length  $l_g$ , the window height ratio  $k_y$ , the length of the inductor  $l_c$ , and the thickness of the core  $t_c$ . It is recommended to control  $l_g$  to design the specified inductance. Leave other design parameters to meet other requirements. The calculated inductance error is less than 10% compared with Maxwell 2D simulation in the range of  $0.1mm < l_g < 0.8mm$  and  $5mm < l_c < 20mm$ . The error exceeds 10% for the case with  $l_c < 5mm$  because the model assumes 2D flux distribution assuming infinite  $l_c$ .

## 5.5 Winding and Core Loss of the Rhombus-Window Inductor

Fig. 5-6 shows the inductor length  $l_c$  versus the core thickness  $t_c$ . The skin depth of copper at 1 MHz is  $\delta_{cu} = 100\mu m$ . The inductor volume is kept as  $V_L = 1000mm^3$ . Large  $t_c$  design results in a shorter  $l_c$  and therefore short inductor winding. Smaller  $t_c$  design leads to a longer  $l_c$  and therefore a larger cross-sectional area.

Fig. 5-7(a) shows the inductor winding loss versus the window height ratio  $k_y$  parametric with

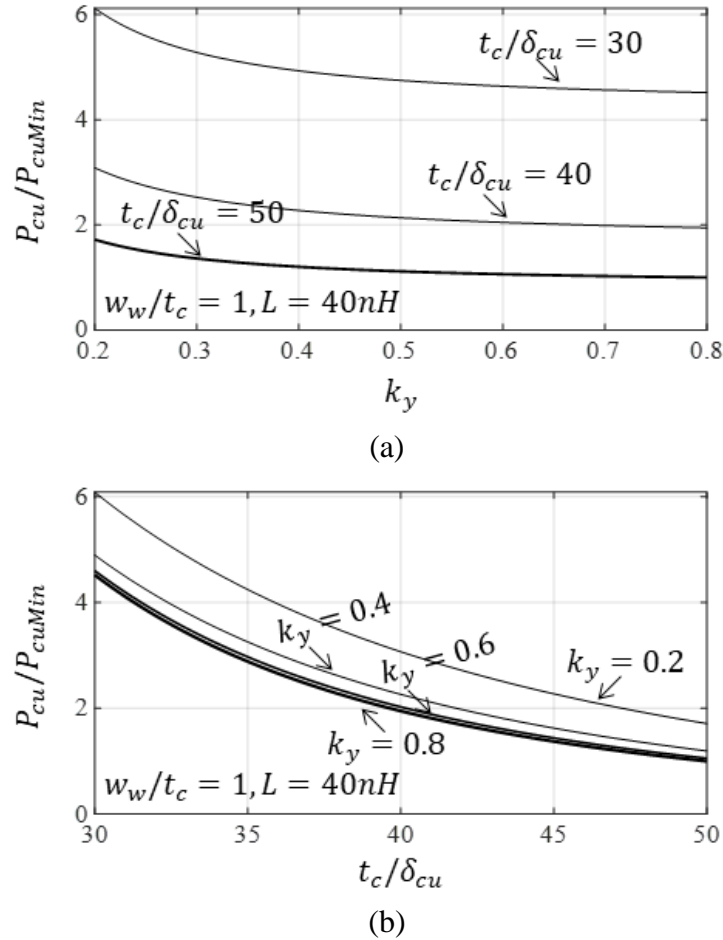


**Fig. 5-7.** The rhombus-window winding loss versus design variables the window height ratio  $k_y$  and the core thickness  $t_c$  labeled in Fig. 5-4. The inductor current excitation is 36A peak current at 2MHz. The type is set as “Solid”. The copper loss was simulated using eddy current mode in Ansys Maxwell 2D and current specifications in Table 5-1.

the core thickness  $t_c$ . Large  $k_y$  design adds the distance between the air gap and the winding, reducing the winding loss caused by the fringing effect. The loss reduction is less significant at  $k_y > 0.5$ .

Fig. 5-7(b) shows the inductor winding loss versus the core thickness  $t_c$  parametric with the window height ratio  $k_y$ . Large  $t_c$  design shortens the inductor winding length and reduces the inductor winding loss, which benefits all the designs with various  $k_y$ .

In general, the big  $k_y$  design alleviates the fringing effect loss. Large  $t_c$  design shortens the copper length. The reduction of inductor winding loss can be achieved by increasing  $k_y$  and enlarging  $t_c$ .

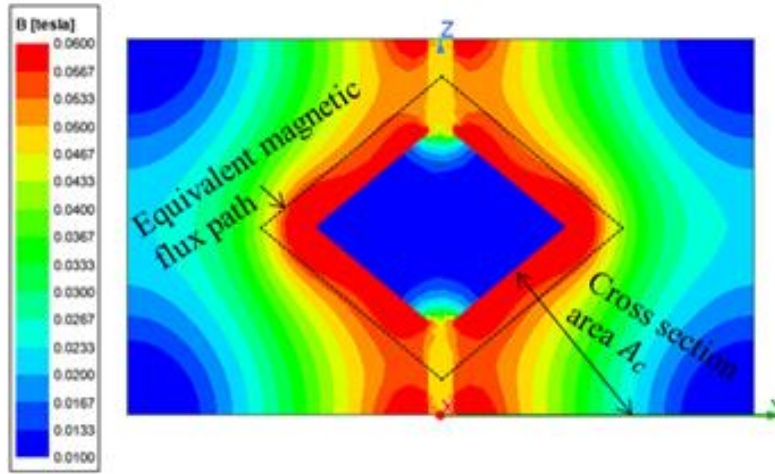
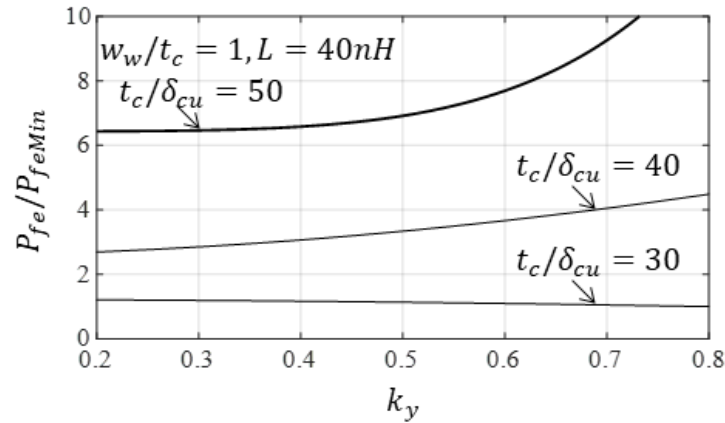


Fig. 5-8. AC flux density in the cross-sectional area of the rhombus-window inductor with  $h_w = 100 \mu\text{m}$ ,  $w_w = 3 \text{ cm}$ ,  $l_c = 9 \text{ cm}$ ,  $t_c = 3 \text{ cm}$ ,  $k_y = 0.5$ ,  $\mu_r = 900$ ,  $d_x = 1 \text{ mm}$ ,  $w_c = 9 \text{ cm}$ , and  $h_c = 6 \text{ cm}$  labeled in Fig. 5-4. The inductor current excitation is 36A peak current at 2MHz. The type is set as “Solid”. The flux was simulated using eddy current mode in Ansys Maxwell 2D using the current and material specifications in Table 5-1.

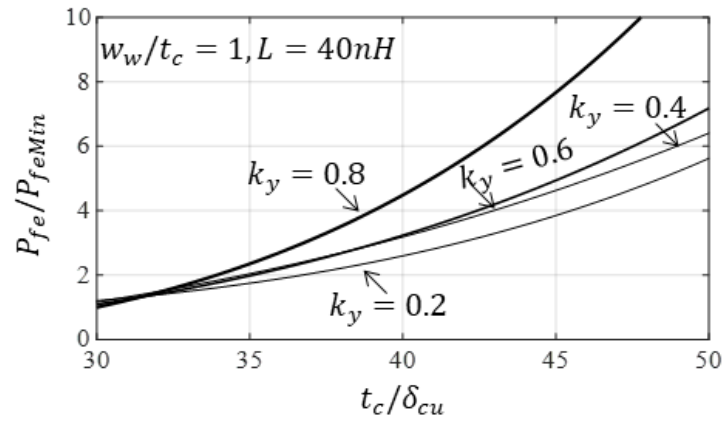
The magnetic flux density is typically assumed to be the same in a standard magnetic core, but this is not the case for the rhombus-window inductor. The simulated ac flux in the cross-sectional area of the rhombus-window inductor is shown in Fig. 5-8. The core legs above and below the winding are narrower, resulting in a larger flux density. The peak flux in the upper leg is about 1.5 times larger than the average flux density.

The equivalent magnetic flux path whose length is  $l_m$  is parallel to the edge of the rhombus window, and the cross-section area  $A_c$  varies along the path. The distribution of the ac flux density heavily depends on the design of  $k_y$ .

Fig. 5-9(a) shows the inductor core loss versus the window height ratio  $k_y$  parametric with



(a)



(b)

**Fig. 5-9. Inductor core loss versus design variables the window height ratio  $k_y$  and the core thickness  $t_c$  labeled in Fig. 5-4. The inductor current excitation is 36A peak current at 2MHz. The type is set as “Solid”. The core loss was simulated using eddy current mode in Ansys Maxwell 2D and specifications in Table 5-1.**

In general, small  $k_y$  design and small  $t_c$  design reduce core loss by increasing the cross-sectional area of the inductor.

The design of the rhombus-window inductor is to control the window height ratio  $k_y$  and the core thickness  $t_c$  to balance the winding loss and core loss of the inductor.

the core thickness  $t_c$ . Small  $k_y$  design increases the cross-sectional area of the magnetic material, and therefore smaller core loss. However, the core loss reduction is less significant at  $k_y < 0.4$  because the ac flux distribution is about the same in the range of  $0.2 < k_y < 0.4$ .

Fig. 5-9(b) shows the inductor core loss versus the core thickness  $t_c$  parametric with the window height ratio  $k_y$ . The increase of  $t_c$  reduces the inductor length  $l_c$ , and therefore smaller cross-sectional area. The core loss increases by more than 5 times as  $t_c$  doubles.

## 5.6 Design Procedures with Given Inductor Current and Loss Budget

A prototype meeting the exemplary specifications in Table 5-1 was designed.

Table 5-1. Specifications labeled in Fig. 5-4 on page 126 and fed into the inductor design procedure in

Fig. 5-10

Specified Parameters	Definitions	Value
$L$	Inductance	43 nH
$I_{acpk}$	Peak ac current	36A
$f_s$	Switching frequency	2MHz
$C_m$	Steinmetz coefficient	$7.58 \times 10^{-10}$
$\alpha$	Steinmetz coefficient	2.41
$\beta$	Steinmetz coefficient	2.51
$\mu_r$	Relative permeability	900
$h_w$	Winding thickness	100 $\mu m$
$w_{wMin}, w_{wMax}$	In Fig. 5-4	2 mm, 5mm
$t_{cMin}, t_{cMax}$	In Fig. 5-4	2 mm, 5mm
$l_{cMin}, l_{cMax}$	In Fig. 5-4	5 mm, 15mm
$k_{yMin}, k_{yMax}$	In Fig. 5-4	0.2, 0.8

The inductance and switching frequency used are from the SRB circuit design. The peak ac current was simulated given the circuit design. The Steinmetz coefficients were calculated from the core loss measurement of DMR51. The relative permeability is from the datasheet of DMR51 provided by the manufacturer.

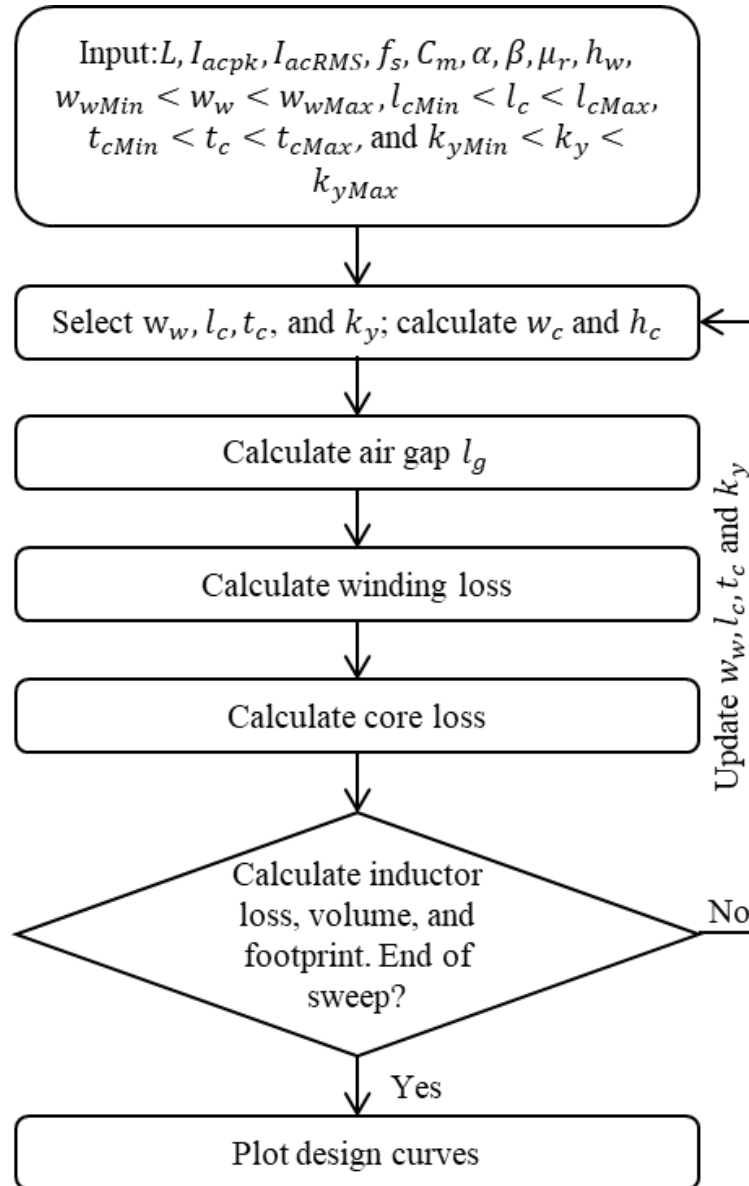
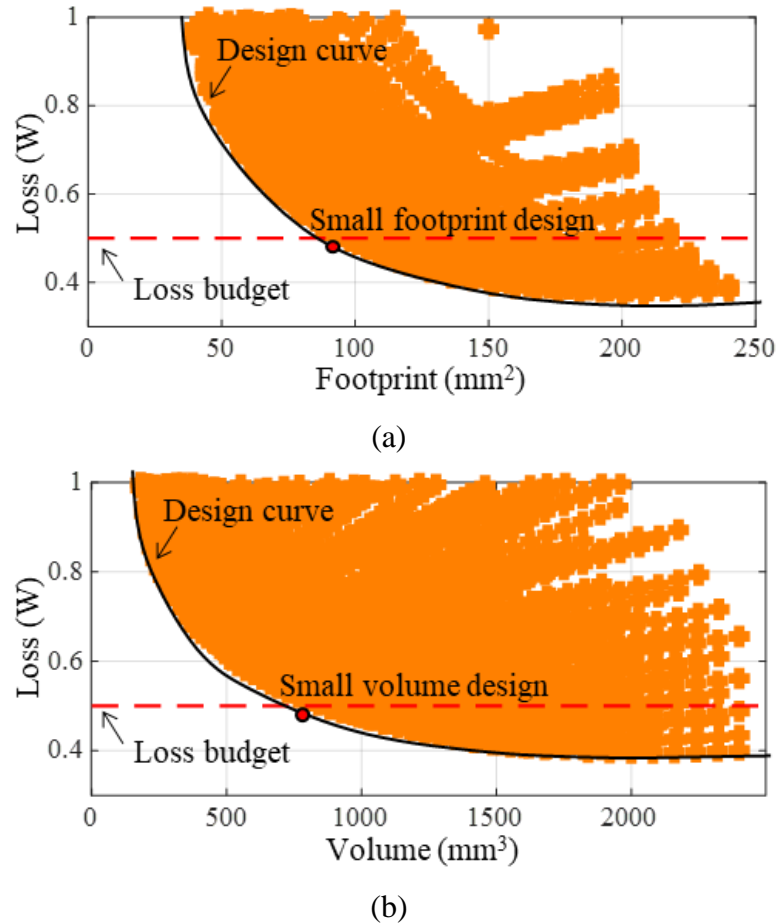


Fig. 5-10. Design flowchart of the rhombus-window inductor labeled in Fig. 5-4 on page 126. A design example using specifications in Table 5-1 is shown in Fig. 5-11 and Fig. 5-12.

Fig. 5-10 shows the design flowchart used to design the resonant inductor meeting the specifications in Table 5-1. It was designed for a Series-Resonator Buck (SRB) converter and a circuit design example was given in Chapter 4.



**Fig. 5-11. Design curves of inductor loss versus (a) footprint and (b) size meeting the inductor specifications in Table 5-1 as part of the design procedure in Fig. 5-10. The inductor loss was simulated using eddy current mode in Ansys Maxwell 2D.**

Fig. 5-11 shows the resultant design curves following the design procedure in Fig. 5-10 and meeting the inductor specifications in Table 5-1. Fig. 5-11(a) shows the inductor loss versus the inductor footprint. The resultant small footprint design and its dimensions are shown in Fig. 5-12(a). The small footprint design features a short inductor length  $l_c$ . Fig. 5-11(b) shows the inductor loss versus the inductor volume. The resultant small volume design and its dimension are

shown in Fig. 5-12(b). The small-volume design features a small inductor height  $h_c$ .

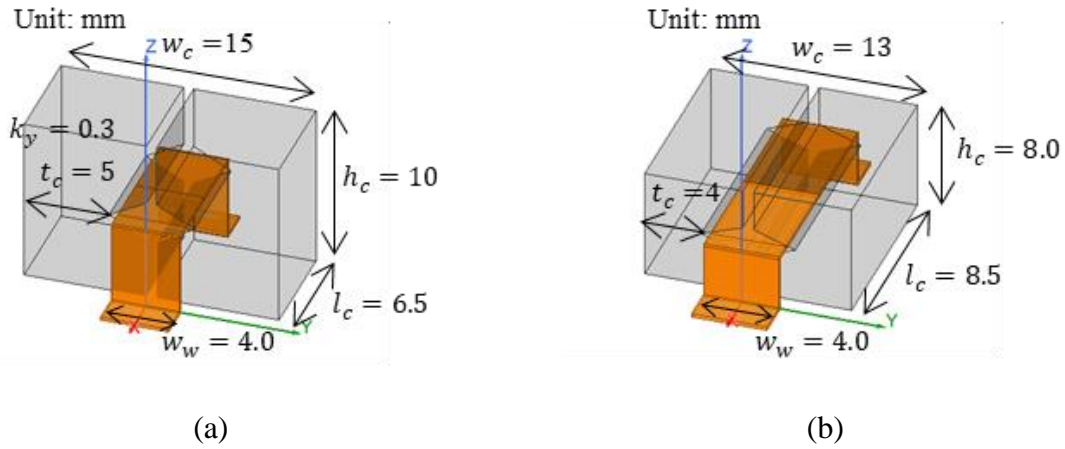


**Fig. 5-12. (a) Small footprint design and (b) small volume design meeting the inductor specifications in Table 5-1 and following the design procedure in Fig. 5-10.**

Fig. 5-12 shows the dimensions of the inductor meeting the inductor specifications in Table 5-1.

The small volume design was selected to fabricate the inductor prototype, and is shown in the following section.

Fig. 5-13 compares the losses between the conventional rectangular-window inductor and the rhombus-window inductor given the same component size.

The winding width of the rectangular-window design is larger, but the winding loss is 60% larger due to the fringing-effect loss. The rhombus-window design reduces the loss by 40%.

The 2D and 3D simulation models of the design in Fig. 5-13 are compared and the error is less than 8%. The error will exceed 8% if the inductor length  $l_c$  is less than 5mm, because the 2D simulation assumes infinite  $l_c$ .

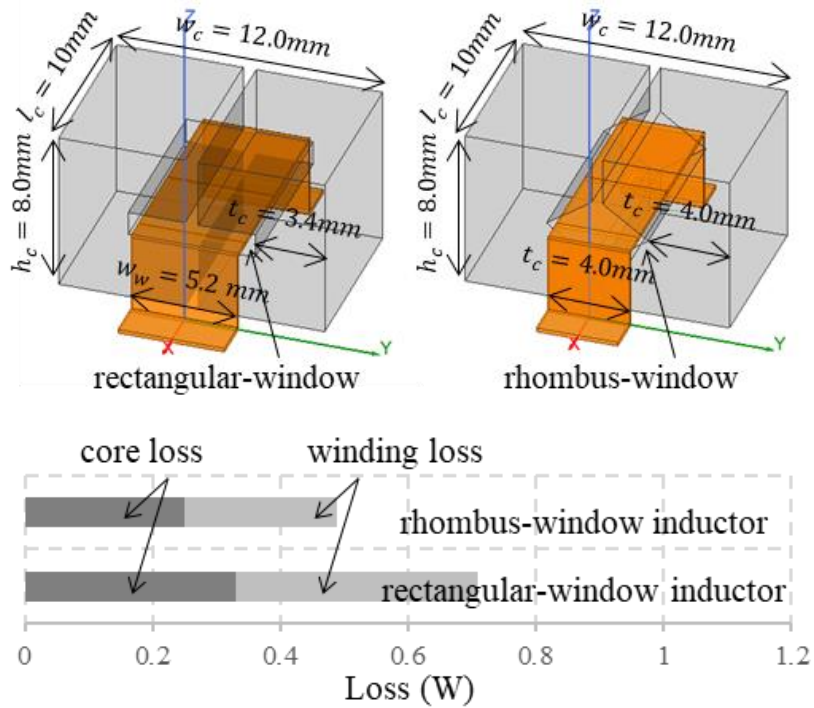


Fig. 5-13. Loss comparison between the conventional rectangular-window inductor and the rhombus-window inductor given the same component size. The inductor loss was simulated using eddy current mode in Ansys Maxwell 2D. The current and material specifications are in Table 5-1.

## 5.7 Experimental Verification of the Rhombus-Window Inductor

Fig. 5-14 shows the experimental hardware used to validate the design of the rhombus-window inductor. The inductor prototype in Fig. 5-14(b) was built using the small volume design with the specifications in Table 5-1. The prototype was placed into a 200 W SRB converter at 48 V input voltage and 40 A output current in Fig. 5-14(a).

The magnetic material used was DMR51 made by Hengdian Group Inc. Copper foil was used to make the inductor winding.

Nomex paper from DuPont was used to control the air gap above and below the inductor winding.

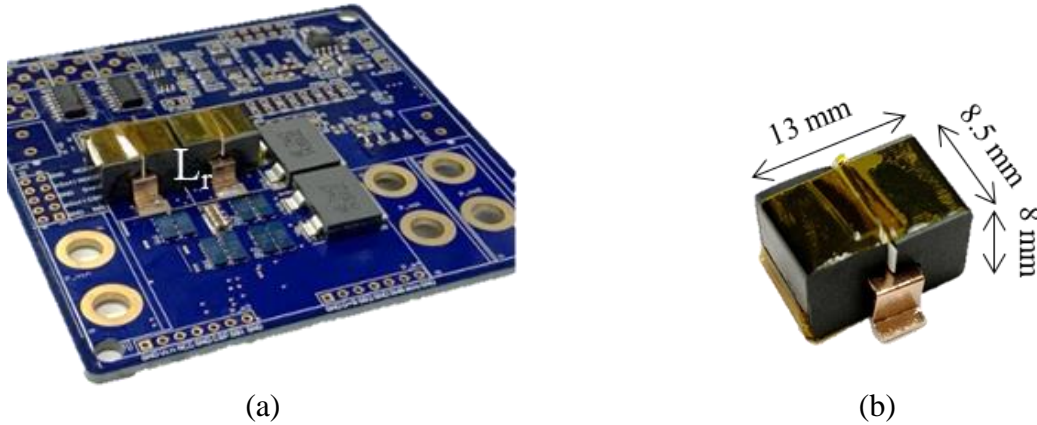


Fig. 5-14. (a) Prototype of the Series-Resonator Buck (SRB) converter using (b) the rhombus-window inductor using the inductor specifications in Fig. 5-12, Table 5-1 and following the design procedure in Fig. 5-10. The converter was with  $V_{in} = 48\text{ V}$ ,  $V_o = 5\text{ V}$ ,  $R_{load} = 0.125\ \Omega$ ,  $L_{oa} = L_{ob} = 0.3\ \mu\text{H}$ ,  $L_r = 80\text{ nH}$ ,  $C_s = 20\ \mu\text{F}$ ,  $C_r = 21\text{ nF}$ , and  $C_o = 4\ \mu\text{F}$ .

Fig. 5-15 shows the experimental inductor voltage and current waveforms. The inductor operates at the full-load condition.

## 5.8 Conclusion

One example of an application using inductors with significant ac flux is the Series-Resonator Buck (SRB) converter. The conventional rectangular-window core is replaced by the rhombus-window core to reduce the fringing flux on the winding, resulting in a smaller winding loss.

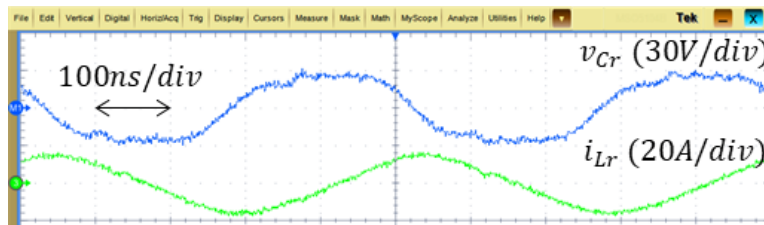


Fig. 5-15. Measured voltage and inductor waveforms labeled in Fig. 5-1 on page 123 of the resonant inductor in Fig. 5-14 and specifications in the caption of Fig. 5-14 using oscilloscope MSO5104B.

Detailed discussions of the inductance, core loss, and winding loss for the rhombus-window inductor are presented. The step-by-step design procedures meeting the given exemplary specifications are given. Experimental results are discussed to verify the theoretical analysis.

## Chapter 6 Conclusions and Future Work

### 6.1 Summary

The Series-Resonator Buck (SRB) converter is synthesized by adding a resonant tank in series with the series-capacitor  $C_s$ . The presence of the resonant tank in the SRB converter reduces all switches' voltages to zero at turn-on, and all low-side switches' currents to zero before turn-off.

A steady-state model of the SRB converter is built to calculate the voltage gain, component peak voltages, and resonant inductor peak current. The error is less than 1% in the nominal operating point, and is less than 2% in the worst case (minimal load condition).

The large-signal and small-signal models are built to model the transient response of the SRB converter. The large-signal model of the SRB converter characterizes the low-frequency behavior of the low-pass filters with the series capacitor and the high-frequency behavior of the resonant elements. The large-signal model reveals the divergence response due to the oscillation between the series-capacitor  $C_s$  and the output inductors  $L_o$ . A design recommendation of  $C_n$  to avoid divergence is suggested. The major transfer functions are derived from the small-signal model of the SRB converter, and are compared with those in the SCB converter. The small-signal model reveals the damping effect caused by the resonant elements in the input-to-output transfer function. The double poles from the output filter move to high frequency. The Q value drops in the SRB converter. The resonant tank in the SRB converter also adds a negative damping effect to the series resonance between the series-capacitor  $C_s$  and the output inductors  $L_o$ . The oscillation is reinforced, and may lead to instability.

The converter specifications such as voltage gain, switching frequency, and component stresses couple with multiple design variables in the SRB converter. A sequential design procedure

help reduce the time spent on simulations and design iterations. A 2-MHz prototype with a peak efficiency of 98.5%, 48 V at the input and 7 V, 20 A at the output was built. The full-load efficiency is improved by 1.1%. The light-load efficiency increases by 3.7%.

One example of an application using inductors with significant ac flux is the Series-Resonator Buck (SRB) converter. The conventional rectangular-window core is replaced by the rhombus-window core to reduce the fringing flux on the winding resulting in a smaller winding loss. Detailed discussions of the inductance, core loss, and winding loss for the rhombus-window inductor are presented. The step-by-step design procedures meeting the given exemplary specifications are given. Experimental results are discussed to verify the theoretical analysis.

## 6.2 Future Work

The ripples of the output inductors are ignored in this work because the 2<sup>nd</sup> order system is easier to understand and use. A steady-state model considering large inductor ripples is needed for a small output inductor design. The impact of smaller output inductance on the voltage gain, ZVS boundary, and component stresses will be part of future work.

A larger error is noticed in the calculation of large-signal behavior with  $t_{off}f_r > 0.5$ . Modeling the extra switching interval added in the large-signal transient is part of future work. A mathematical equation in an explicit form for the minimum  $C_n$  design will offer more insights into the SRB converter design. The converter does not operate in the soft-switching region in the start-up period. A control method for the start-up period could be optimized for minimal component stresses.

Most of the terms in the transfer functions of the SRB converter are documented using intermediate variables rather than design variables. It is because the substitution of the intermediate

variables with the design variables results in a very long equation that offers limited insights into the converter design. A simplified design-oriented transfer function without the intermediate variables will be part of future work.

The core loss in the high-frequency magnetic material limits the switching frequency of the SRB converter. An air core inductor with no core loss may benefit the SRB converter efficiency at MHz-level switching frequency. Future work will include the study of the air gap winding geometry and a different design methodology for the SRB converters using air core inductors.

## 6.3 List of Publications

### 6.3.1 Journal Papers

- C. Tu, R. Chen, and K. D. T. Ngo, "Steady-State Analysis of Series-Resonator Buck Converter," in *IEEE Transactions on Power Electronics*, vol. 37, no. 10, pp. 12327-12335, Oct. 2022.
- C. Tu, R. Chen, and K. D. T. Ngo, "Series-Resonator Buck Converter—Viability Demonstration," in *IEEE Transactions on Power Electronics*, vol. 36, no. 9, pp. 9693-9697, Sept. 2021.
- C. Tu and K. D. T. Ngo, "Design Methodology of the Series-Resonator Buck Converter," in *IEEE Transactions on Power Electronics*, in review.
- C. Tu and K. D. T. Ngo, "One-Turn Inductor using Rhombus Window," in *IEEE Transactions on Power Electronics*, in review.
- Y. Yan, L. Geng, L. Zhang, C. Tu, R. Sriramdas et al., "High-Power Magnetolectric Voltage Tunable Inductors," in *IEEE Transactions on Industrial Electronics*, vol. 68, no. 6, pp. 5355-5365, June 2021.

### 6.3.2 Conference Papers

- **C. Tu**, K. D. T. Ngo, and R. Chen, "A Fast Non-Iterative Design Approach of One-Turn Inductor with Significant AC Flux using Commercially Available Components," *2022 IEEE Applied Power Electronics Conference and Exposition (APEC)*, 2022, pp. 1486-1491.
- **C. Tu**, K. D. T. Ngo, and R. Chen, "Series-Capacitor Buck Converter with Soft Turn-On," *2020 IEEE Applied Power Electronics Conference and Exposition (APEC)*, New Orleans, LA, USA, 2020, pp. 41-47.
- **C. Tu** and K. D. T. Ngo, " Design of Series-Resonator Buck Converter with Minimal Circulating Energy," *2023 IEEE Applied Power Electronics Conference and Exposition (APEC)*, accepted.
- **C. Tu** and K. D. T. Ngo, " Rhombus-Window Resonant Inductor with Significant AC Flux," *2023 IEEE Applied Power Electronics Conference and Exposition (APEC)*, accepted.

### 6.3.3 Patents

- **C. Tu**, K. Ngo, T. Ge, and R. Chen, "Series-Resonator Converter," U.S. Patent 17154094, in review.

## Appendix

### A. Calculation of Switching Cycle

At the beginning of subinterval 4, switch  $S_{b1}$  is turned on at zero drain-source voltage. The length of subintervals 2 and 3  $\tau_2 + \tau_3$  is calculated with

$$v_{dsb1@t_4} = V_{Cr@t_4} + v_{Cs} = 0 \quad (i)$$

The following substitutions are made

$$2\alpha = \omega_r(\tau_2 + \tau_3)$$

$$\cos 2\alpha = \frac{1 - \tan^2 \alpha}{1 + \tan^2 \alpha} \quad (ii)$$

$$\sin 2\alpha = \frac{2 \tan \alpha}{1 + \tan^2 \alpha}$$

The solution of  $V_{Cr@t_4}$  is from (2-4). Equations (i) and (ii) are combined

$$(v_{Cs} - V_{Cr@t_2})\tan^2 \alpha - 2Z_r I_{Lr@t_2} \tan \alpha + v_{Cs} + V_{Cr@t_2} = 0 \quad (iii)$$

The calculations of the roots  $\alpha_1$  and  $\alpha_2$  is shown below

$$2\alpha = \omega_r t_{34}$$

$$\cos(2\alpha) V_{Cr@t_2} - Z_r \sin(2\alpha) I_{Lr@t_2} + v_{Cs} = 0$$

$$\frac{1 - \tan^2 \alpha}{1 + \tan^2 \alpha} V_{Cr@t_2} - Z_r \frac{2 \tan \alpha}{1 + \tan^2 \alpha} I_{Lr@t_2} + v_{Cs} = 0$$

$$(1 - \tan^2 \alpha) V_{Cr@t_2} - 2Z_r \tan \alpha I_{Lr@t_2} + (1 + \tan^2 \alpha) v_{Cs} = 0 \quad (iv)$$

$$(V_{Cr@t_2} - V_{Cr@t_2} \tan^2 \alpha) - 2Z_r \tan \alpha I_{Lr@t_2} + (v_{Cs} + v_{Cs} \tan^2 \alpha) = 0$$

$$\tan^2 \alpha (v_{Cs} - V_{Cr@t_2}) - 2Z_r \tan \alpha I_{Lr@t_2} + v_{Cs} + V_{Cr@t_2} = 0$$

---

$$\cos(w_r t_{34}) V_{Cr@t_2} - Z_r \sin(w_r t_{34}) I_{Lr@t_2} + v_{Cs} = 0$$

$$\Downarrow 2\alpha = w_r t_{34}$$

$$\frac{1 - \tan^2 \alpha}{1 + \tan^2 \alpha} V_{Cr@t_2} - Z_r \frac{2 \tan \alpha}{1 + \tan^2 \alpha} I_{Lr@t_2} + v_{Cs} = 0$$

$$\Downarrow$$

$$\tan^2 \alpha (v_{Cs} - V_{Cr@t_2}) - 2Z_r \tan \alpha I_{Lr@t_2} + v_{Cs} + V_{Cr@t_2} = 0$$

$$\Downarrow$$

$$\tan \alpha_{1,2} = \frac{Z_r I_{Lr@t_2} \pm \sqrt{[Z_r^2 I_{Lr@t_2}^2 + V_{Cr@t_2}^2 - v_{Cs}^2]}}{v_{Cs} - V_{Cr@t_2}}$$

$$\tan \alpha_2 > \tan \alpha_1 > 0$$

$$\Downarrow$$

$$\begin{aligned} \Delta &= 4Z_r^2 I_{Lr@t_2}^2 - 4(v_{Cs} - V_{Cr@t_2})(v_{Cs} + V_{Cr@t_2}) \\ &= 4Z_r^2 I_{Lr@t_2}^2 - 4(v_{Cs}^2 - V_{Cr@t_2}^2) \\ &= 4[Z_r^2 I_{Lr@t_2}^2 - (v_{Cs} - V_{Cr@t_2})^2] \\ &= 4[Z_r^2 I_{Lr@t_2}^2 + V_{Cr@t_2}^2 - v_{Cs}^2] \end{aligned}$$

$$\Downarrow$$

$$\tan \alpha_{1,2} = \frac{2Z_r I_{Lr@t_2} \pm 2\sqrt{[Z_r^2 I_{Lr@t_2}^2 - (v_{Cs} - V_{Cr@t_2})^2]}}{2(v_{Cs} - V_{Cr@t_2})}$$

The roots  $\alpha_1$  and  $\alpha_2$  of (iii) are listed below

$$\alpha_1 = \arctan \left( \frac{Z_r I_{Lr@t_2} - \sqrt{(Z_r I_{Lr@t_2})^2 - (v_{Cs} - V_{Cr@t_2})(v_{Cs} + V_{Cr@t_2})}}{(v_{Cs} - V_{Cr@t_2})} \right) \quad (v)$$

$$\alpha_2 = \arctan \left( \frac{Z_r I_{Lr@t_2} + \sqrt{(Z_r I_{Lr@t_2})^2 - (v_{Cs} - V_{Cr@t_2})(v_{Cs} + V_{Cr@t_2})}}{(v_{Cs} - V_{Cr@t_2})} \right) \quad (\text{vi})$$

Equations (2-1) – (2-3) are used to calculate  $V_{Cr@t_2}$  and  $I_{Lr@t_2}$ . Both roots are positive and  $\alpha_1 < \alpha_2$ . The smaller root is valid

$$\tau_2 + \tau_3 = \frac{2\alpha_2}{\omega_r} \quad (\text{vii})$$

At the beginning of subinterval 5, switch  $S_{b2}$  turns off from zero current (ZCOFF). The length of the subinterval 4  $\tau_4$  is calculated with

$$i_{b2@t_5} = -I_{Cs@t_5} - i_{Lob} = 0 \quad (\text{viii})$$

$$I_{Cs@t_5} = \frac{C_s}{C_s + C_r} I_{Lr@t_5} \approx I_{Lr@t_5} \quad (\text{ix})$$

Equation (2-8) is used to calculate  $I_{Lr@t_5}$ . The subinterval length  $\tau_4$  is calculated with (viii), (ix), and (2-8)

$$\tau_4 \approx \frac{L_r}{-v_{Cs}} (-i_{Lob} - I_{Lr@t_4}) \quad (\text{x})$$

Equations (2-1) – (2-3) are used to calculate  $I_{Lr@t_4}$  (or  $I_{Lr@t_2}$ ) in (x). The subinterval length  $\tau_4$  can be written as

$$\tau_4 \approx \frac{L_r (i_{Loa} + i_{Lob} + \frac{(V_{in} - v_{Cs}) \sin(\omega_r t_{off})}{Z_r})}{v_{Cs}} \quad (\text{xi})$$

At the beginning of subinterval 8, switch  $S_{a1}$  is turned on at zero drain-source voltage. The length of subintervals 6 and 7  $\tau_6 + \tau_7$  is calculated with

$$v_{dsa1@t_8} = V_{in} - (v_{Cs} + V_{Cr@t_8}) = 0 \quad (\text{xii})$$

The following substitutions are made

$$2\gamma = w_r(\tau_6 + \tau_7)$$

$$\cos 2\gamma = \frac{1 - \tan^2 \gamma}{1 + \tan^2 \gamma} \quad (\text{xiii})$$

$$\sin 2\gamma = \frac{2 \tan \gamma}{1 + \tan^2 \gamma}$$

The solution of  $V_{Cr@t_8}$  is from (2-13). Equations (xii) and (xiii) are combined

$$\left( (v_{Cs} - V_{in}) - V_{Cr@t_6} \right) \tan^2 \gamma - 2Z_r I_{Lr@t_6} \tan \gamma + (v_{Cs} - V_{in}) + V_{Cr@t_6} = 0 \quad (\text{xiv})$$

The roots of  $\gamma_1$  and  $\gamma_2$  of (xiv) are listed below

$\gamma_1$

$$= \frac{2}{w_r} \arctan \left( \frac{Z_r I_{Lr@t_6} - \sqrt{(Z_r I_{Lr@t_6})^2 - \left( (v_{Cs} - V_{in}) - V_{Cr@t_6} \right) \left( (v_{Cs} - V_{in}) + V_{Cr@t_6} \right)}}{\left( (v_{Cs} - V_{in}) - V_{Cr@t_6} \right)} \right) \quad (\text{xv})$$

$\gamma_2$

$$= \frac{2}{w_r} \arctan \left( \frac{Z_r I_{Lr@t_6} + \sqrt{(Z_r I_{Lr@t_6})^2 - \left( (v_{Cs} - V_{in}) - V_{Cr@t_6} \right) \left( (v_{Cs} - V_{in}) + V_{Cr@t_6} \right)}}{\left( (v_{Cs} - V_{in}) - V_{Cr@t_6} \right)} \right) \quad (\text{xvi})$$

Equations (2-10) – (2-12) are used to calculate  $V_{Cr@t_6}$  and  $I_{Lr@t_6}$ . Both roots are positive and  $\gamma_1 > \gamma_2$ . The smaller root is valid

$$\tau_6 + \tau_7 = \gamma_2 \quad (\text{xvii})$$

At the beginning of subinterval 1, switch  $S_{a2}$  turns off from zero current (ZCOFF). The length of the subinterval 8  $\tau_8$  is calculated with

$$i_{a2@t_1} = I_{Cs@t_1} - i_{Loa} = 0 \quad (\text{xviii})$$

$$I_{Cs@t_1} = \frac{C_s}{C_s + C_r} I_{Lr@t_1} \approx I_{Lr@t_1} \quad (\text{xix})$$

Equation (2-17) is used to calculate  $I_{Lr@t_1}$ . The subinterval length  $\tau_8$  is calculated with (viii),

(ix), and (2-8)

$$\tau_8 \approx \frac{L_r}{v_{Cs}} (-i_{Loa} - I_{Lr@t_8}) \quad (\text{xx})$$

Equations (2-10) – (2-12) are used to calculate  $I_{Lr@t_8}$  (or  $I_{Lr@t_6}$ ) in (x). The subinterval length  $\tau_8$  can be written as

$$\tau_8 \approx \frac{L_r (i_{Loa} + i_{Lob} + \frac{v_{Cs} \sin(w_r t_{off})}{Z_r})}{V_{in} - v_{Cs}} \quad (\text{xxi})$$

The Matlab code to solve  $\tau_2 + \tau_3$  is attached below

```
% ----- Clear Data _ start -----%
```

```
close all;clc; clear all; tic;
```

```
% set(0,'defaultFigureWindowStyle','docked');
```

```
% tt1=clock;
```

```
format compact
```

```
% ----- Clear Data _ END -----%
```

```
%% Color
```

```
C01=[1.0 0.0 0.0]; % red
```

```
C02=[1.0 0.5 0.0]; % dark orange
```

```
C03=[0.0 0.5 0.0]; % green
```

```
C04=[0.0 0.7 1.0]; % deep sky blue
```

```
C05=[0.0 0.0 1.0]; % blue
```

```
C06=[0.6 0.0 0.8]; % dark violet
```

```
C07=[1.0 0.0 1.0]; % magenta
```

```

C08=[0.8 0.4 0.1]; % chocolate
C09=[0.0 0.0 0.0]; % black
C10=[0.4 0.4 0.4]; % dim gray

c=[C01;C02;C03;C04;C05;C06;C07;C08;C09;C10];

%%

% component
Rload=sym('Rload');
Cr=sym('Cr');
Lr=sym('Lr');
Cs=sym('Cs');
Co=sym('Co');
Loa=sym('Loa');
Lob=sym('Lob');
RLoa=sym('RLoa');
RLob=sym('RLob');
Lob=Loa;
RLob=RLoa;

% large signal
vin=sym('vin');

```

```

toff=sym('toff');
vcs=sym('vcs');
vo=sym('vo');
iLoa=sym('iLoa');
iLob=sym('iLob');
io=sym('io');

% normalized
j=sym('j');
m=sym('m');

% symbolic combination
wr=1/sqrt(Lr*Cr);
fr=wr/2/pi;
Zr=sqrt(Lr/Cr);
wr3=1/sqrt(Lr*(Cs+Cr));
fr3=wr3/2/pi;
Zr3=sqrt(Lr/(Cs+Cr));

%%
wrtoff_sw=2*pi*linspace(0,1,500);
j=logspace(-2,2,500);

```

```

[wrtoff,j] = meshgrid(wrtoff_sw,j);
% wrtoff=2*pi*0.6
% j=0.01

tssw=2.*(2.*j+wrtoff+sin(wrtoff))./wr;

vcr_t2=cos(wrtoff)*vin/2;
iLr_t2=1/Zr.*sin(wrtoff).*vin./2 + 0.5.*vin./Zr.*j;
% tanalpha1=(Zr.*iLr_t2-sqrt((Zr.*iLr_t2).^2-(vin./2-vcr_t2).*(vin./2+vcr_t2)) )./(vin./2-
vcr_t2)
tanalpha1=(sin(wrtoff)+j-sqrt(2.*j.*sin(wrtoff)+j.^2) )./(1-cos(wrtoff)); % after
normalization

alpha1=tanalpha1; % alpha1=atan(tanalpha1); replace it for approximation x = tan(x)
t23x=2.*alpha1./wr;
t23x(imag(t23x)~=0)=-1e-9; % set complex number to -1e-9
t23x(t23x<0)=-1e-9; % set nagtive number to -1e-9

ratiosw=2*t23x./tssw;
tanalpha1(imag(tanalpha1)~=0)=-1e-9;

j_bound=j+2*sin(wrtoff);% Lr current zvs boundary
f31 = figure(31);

```

```

contour(wrtoff/2/pi,j,t23x,'ShowText','on','LevelList',[-0.98e-9 1e-9 10e-9]); hold on;%
tau2/Ts

% contour(wrtoff/2/pi,j,j_bound,'ShowText','on','LevelList',[0]); hold on;% Lr current zvs
boundary

set(gca,'Yscale','log','Xscale','linear')

set(gca,'linewidth',0.5,'fontsize',8,'FontName','Times New Roman');

figpo=[100 800 (1.7*2-0.2*(-2.5))*96 (2-0.2*0)*96]; set(f31,'InnerPosition',figpo); grid on;

f32 = figure(32);

contour(wrtoff/2/pi,j,ratiosw,'ShowText','on','LevelList',[0.1 0.5 2 5]); hold on;% tau2/Ts

contour(wrtoff/2/pi,j,j_bound,'ShowText','on','LevelList',[0]); hold on;% Lr current zvs
boundary

set(gca,'Yscale','log','Xscale','linear')

set(gca,'linewidth',0.5,'fontsize',8,'FontName','Times New Roman');

figpo=[100 500 (1.7*2-0.2*(-2.5))*96 (2-0.2*0)*96]; set(f32,'InnerPosition',figpo); grid on;

f33 = figure(33);

contour(wrtoff/2/pi,j,ratiosw,'ShowText','on','LevelList',[0.1 0.2]); hold on;% tau2/Ts

contour(wrtoff/2/pi,j,j_bound,'ShowText','on','LevelList',[0]); hold on;% Lr current zvs
boundary

xlim([0.25 0.75])

ylim([0 5])

set(gca,'Yscale','linear','Xscale','linear')

```

```

set(gca,'linewidth',0.5,'fontsize',8,'FontName','Times New Roman');
figpo=[100 200 (1.7*2-0.2*(-2.5))*96 (2-0.2*0)*96]; set(f33,'InnerPosition',figpo); grid on;

```

f34 = figure(34); % check for approximation  $x = \tan(x)$ , the majority of the area smaller than

0.2, good approximation

```

contour(wrtoff/2/pi,j,tanalpha1,'ShowText','on','LevelList',[0.2 0.6 1.8 5.4]); hold on;

```

```

% xlim([0.25 0.75])

```

```

% ylim([0.1 10])

```

```

set(gca,'Yscale','log','Xscale','linear')

```

```

set(gca,'linewidth',0.5,'fontsize',8,'FontName','Times New Roman');

```

```

figpo=[500 200 (1.7*2-0.2*(-2.5))*96 (2-0.2*0)*96]; set(f34,'InnerPosition',figpo); grid on;

```

```

%% The end

```

```

toc

```

The Matlab code to solve  $\tau_6 + \tau_7$  is attached below

```

% ----- Clear Data _ start -----%

```

```

close all;clc; clear all; tic;

```

```

% set(0,'defaultFigureWindowState','docked');

```

```

% tt1=clock;

```

```

format compact

```

```

% ----- Clear Data _ END -----%

```

%% Color

C01=[1.0 0.0 0.0]; % red

C02=[1.0 0.5 0.0]; % dark orange

C03=[0.0 0.5 0.0]; % green

C04=[0.0 0.7 1.0]; % deep sky blue

C05=[0.0 0.0 1.0]; % blue

C06=[0.6 0.0 0.8]; % dark violet

C07=[1.0 0.0 1.0]; % magenta

C08=[0.8 0.4 0.1]; % chocolate

C09=[0.0 0.0 0.0]; % black

C10=[0.4 0.4 0.4]; % dim gray

c=[C01;C02;C03;C04;C05;C06;C07;C08;C09;C10];

%%

% component

Rload=sym('Rload');

Cr=sym('Cr');

Lr=sym('Lr');

Cs=sym('Cs');

Co=sym('Co');

Loa=sym('Loa');

```

Lob=sym('Lob');
RLoa=sym('RLoa');
RLob=sym('RLob');
Lob=Loa;
RLob=RLoa;

% large signal
vin=sym('vin');
toff=sym('toff');
vcs=sym('vcs');
vo=sym('vo');
iLoa=sym('iLoa');
iLob=sym('iLob');
io=sym('io');

% normalized
j=sym('j');
m=sym('m');

% symbolic combination
wr=1/sqrt(Lr*Cr);
fr=wr/2/pi;
Zr=sqrt(Lr/Cr);

```

$$wr3=1/\text{sqrt}(Lr*(Cs+Cr));$$

$$fr3=wr3/2/\text{pi};$$

$$Zr3=\text{sqrt}(Lr/(Cs+Cr));$$

%%

$$\text{tau6\_00}=-\text{Lr}*(i\text{Loa} + i\text{Lob} + (\text{vcs}*(\text{pi} - \text{toff}/(\text{Cr}*\text{Lr})^{1/2}))/(\text{Lr}/\text{Cr})^{1/2}))/(\text{vcs} - \text{vin})$$

$$\text{tau6\_01}=(\text{Lr}*(\text{io} + (\text{vcs}*(\text{pi} - \text{toff}/(\text{Cr}*\text{Lr})^{1/2}))/(\text{Lr}/\text{Cr})^{1/2}))/\text{vcs}$$

$$\text{tau6\_02}=(\text{Lr}*(\text{io} + (\text{vcs}*(\text{pi} - \text{toff}*\text{wr}))/\text{Zr}))/\text{vcs}$$

$$\text{tau6\_03}=\text{Lr}*(\text{io}/\text{vcs} + (\text{pi} - \text{toff}*\text{wr})/\text{Zr})$$

$$\text{tau6\_04}=\text{Lr}*\text{io}/\text{vcs} + \text{Lr}*(\text{pi} - \text{toff}*\text{wr})/\text{Zr}$$

$$\text{tau6\_05}=\text{Lr}*\text{io}/\text{vcs} + (\text{pi}/\text{wr} - \text{toff})$$

$$\text{tau6\_06}=\text{Lr}*\text{io}/\text{vcs} + 0*(\text{pi}/\text{wr} - \text{toff})$$

%% The end

toc

## B. Calculation of Output Voltage

The output voltage in (2-22) is derived

$$V_o = \frac{1}{t_s} \sum_{i=1}^8 \int_{t_i}^{t_{i+1}} v_{dsa2}(\lambda) d\lambda = \frac{1}{t_s} \int_{t_1}^{t_2} v_{dsa2}(\lambda) d\lambda \quad (\text{xxii})$$

The calculation of  $\int_{t_1}^{t_2} v_{dsa2}(\lambda) d\lambda$  in subinterval 1 involves the solution of the state variables in (2-1)

$$\begin{aligned} \int_{t_1}^{t_2} v_{dsa2}(\lambda) d\lambda &= \int_{t_1}^{t_2} V_{in} - v_{Cs} - v_{Cr}(\lambda) d\lambda \\ &= \int_{t_1}^{t_2} V_{in} - v_{Cs} \\ &\quad - (\cos(w_r \lambda) V_{Cr@t_1} - Z_r \sin(w_r \lambda) I_{Lr@t_1} + Z_r \sin(w_r \lambda) i_{Loa}) d\lambda \\ &= V_{in} \tau_1 - V_{Cr@t_1} \left( \frac{\sin(w_r \tau_1)}{w_r} - \frac{\sin(0)}{w_r} \right) \\ &\quad - Z_r I_{Lr@t_1} \left( -\frac{\cos(w_r \tau_1)}{w_r} + \frac{\cos(0)}{w_r} \right) \\ &\quad + Z_r i_{Loa} \left( -\frac{\cos(w_r \tau_1)}{w_r} + \frac{\cos(0)}{w_r} \right) \\ &= V_{in} \tau_1 - V_{Cr@t_1} \frac{\sin(w_r \tau_1)}{w_r} - Z_r I_{Lr@t_1} \left( -\frac{\cos(w_r \tau_1)}{w_r} + \frac{1}{w_r} \right) \\ &\quad + Z_r i_{Loa} \left( -\frac{\cos(w_r \tau_1)}{w_r} + \frac{1}{w_r} \right) \end{aligned} \quad (\text{xxiii})$$

In the steady state, equation (xxiii) can be simplified with the initial conditions  $I_{Lr@t_1} = i_{Loa}(C_r + C_s)/C_s \approx i_{Loa}$ ,  $V_{Cr@t_1} = V_{in} - v_{Cs}$ ,  $\tau_1 = T_{off}$ , (2-20), and (2-21)

$$V_o \approx \frac{V_{in}}{4} \frac{w_r T_{off} - \sin(w_r T_{off})}{2J + w_r T_{off} + \sin(w_r T_{off})} \quad (\text{xxiv})$$

### C. Calculation of Steady-State State Variables

The Matlab code to solve  $\{\sum_{i=1}^k d_i A_i\}x + \frac{1}{t_s} \sum_{i=1}^k \int_{t_{i-1}}^{t_i} B_i(\lambda) d\lambda = 0$  from (2-19) is attached

below

```
% ----- Clear Data _ start -----%
close all;clc; clear all; tic;

% set(0,'defaultFigureWindowStyle','docked');

% ttl=clock;

format compact

% ----- Clear Data _ END -----%

%% Color

C01=[1.0 0.0 0.0]; % red
C02=[1.0 0.5 0.0]; % dark orange
C03=[0.0 0.5 0.0]; % green
C04=[0.0 0.7 1.0]; % deep sky blue
C05=[0.0 0.0 1.0]; % blue
C06=[0.6 0.0 0.8]; % dark violet
C07=[1.0 0.0 1.0]; % magenta
C08=[0.8 0.4 0.1]; % chocolate
C09=[0.0 0.0 0.0]; % black
C10=[0.4 0.4 0.4]; % dim gray

c=[C01;C02;C03;C04;C05;C06;C07;C08;C09;C10];
```

```
%% Steady-State Model
```

```
% components
```

```
Rload=sym('Rload');
```

```
Cr=sym('Cr');
```

```
Lr=sym('Lr');
```

```
Cs=sym('Cs');
```

```
Co=sym('Co');
```

```
Loa=sym('Loa');
```

```
Lob=sym('Lob');
```

```
RLoa=sym('RLoa');
```

```
RLob=sym('RLob');
```

```
% state variables
```

```
vcs=sym('vcs');
```

```
vco=sym('vco');
```

```
iLoa=sym('iLoa');
```

```
iLob=sym('iLob');
```

```
vin=sym('vin');
```

```

% symbolic combination
wr=1/sqrt(Lr*Cr);
Zr=sqrt(Lr/Cr);
wr3=1/sqrt(Lr*(Cs+Cr));
Zr3=sqrt(Lr/(Cs+Cr));

%% subintervals & resonant vcr and iLr
% initial condition
vcr_t1=vin-vcs;
iLr_t1=iLoa;
% subinterval 1
tau1=toff;
vcr_t2=cos(wr*tau1)*vcr_t1;
iLr_t2=1/Zr*(-wr*tau1+pi)*vcr_t1 + iLoa;
% subinterval 2
tau2=0;
vcr_t3=-vcs;
iLr_t3=iLr_t2;
% subinterval 3
tau3=(-iLob-iLr_t3)*Lr/(-vcs);
vcr_t4=vcr_t3;
iLr_t4=iLr_t3+(-vcs)*tau3/Lr;
% subinterval 4

```

```

tau4=toff;
vcr_t5=cos(wr*tau4)*vcr_t4;
iLr_t5=1/Zr*(-wr*tau4+pi)*vcr_t4 - iLob;
% subinterval 5
tau5=0;
vcr_t6=vin-vcs;
iLr_t6=iLr_t5;
% subinterval 6
tau6=(iLoa-iLr_t6)*Lr/(vin-vcs);
vcr_t7=vcr_t6;
iLr_t7=iLr_t6+(vin-vcs)*tau6/Lr;

% switching cycle
Ts = (tau1+tau2+tau3+tau4+tau5+tau6)*1;

%% matrices
K= [
    Cs 0 0 0;
    0 Co 0 0;
    0 0 Loa 0;
    0 0 0 Lob
];
A1= [

```

```
0 0 1 0;  
0 -1/Rload 1 1;  
-1 -1 -RLoa 0;  
0 -1 0 -RLob  
];
```

```
A2= [  
0 0 0 0;  
0 -1/Rload 1 1;  
0 -1 -RLoa 0;  
0 -1 0 -RLob  
];
```

```
A3= [  
0 0 0 0;  
0 -1/Rload 1 1;  
0 -1 -RLoa 0;  
0 -1 0 -RLob  
];
```

```
A4= [  
0 0 0 -1;  
0 -1/Rload 1 1;  
0 -1 -RLoa 0;  
1 -1 0 -RLob  
];
```

```

A5= [
      0 0 0 0;
      0 -1/Rload 1 1;
      0 -1 -RLoa 0;
      0 -1 0 -RLob
    ];

```

```

A6= [
      0 0 0 0;
      0 -1/Rload 1 1;
      0 -1 -RLoa 0;
      0 -1 0 -RLob
    ];

```

```

u1 = tau3/2*(-2*iLob-tau3*(-vcs)/Lr) + tau6/2*(2*iLoa-
tau6*(vin-vcs)/Lr);

```

```

u2 = 0;

```

```

u3 = vin*tau1 - vcr_t1*(-tau1+pi/wr);

```

```

u4 = vcr_t4*(-tau4+pi/wr);

```

```

U = [u1;0;u3;u4];

```

```
%% sum up for large-signal state space equation

A = A1*tau1+A2*tau2+A3*tau3+A4*tau4+A5*tau5+A6*tau6

C = simplify(inv(K)*A /Ts)

D = simplify(inv(K)*U /Ts)

X_sol = -inv(C)*D

Toc
```

## D. Calculation of ZVS Boundary

The Matlab code to Simplify the ZVS boundary characterized by (2-24) is attached below. It includes the derivation from (2-24) to (2-26).

```
% ----- Clear Data _ start -----%
close all;clc; clear all; tic;
% set(0,'defaultFigureWindowStyle','docked');
% ttl=clock;
format compact
% ----- Clear Data _ END -----%

%% Color
C01=[1.0 0.0 0.0]; % red
C02=[1.0 0.5 0.0]; % dark orange
C03=[0.0 0.5 0.0]; % green
C04=[0.0 0.7 1.0]; % deep sky blue
C05=[0.0 0.0 1.0]; % blue
C06=[0.6 0.0 0.8]; % dark violet
C07=[1.0 0.0 1.0]; % magenta
C08=[0.8 0.4 0.1]; % chocolate
C09=[0.0 0.0 0.0]; % black
C10=[0.4 0.4 0.4]; % dim gray

c=[C01;C02;C03;C04;C05;C06;C07;C08;C09;C10];
```

```

%% Model

% component

Rload=sym('Rload');

Cr=sym('Cr');

Lr=sym('Lr');

Cs=sym('Cs');

Co=sym('Co');

Loa=sym('Loa');

Lob=sym('Lob');

RLoa=sym('RLoa');

RLob=sym('RLob');

Lob=Loa;

RLob=RLoa;

% large signal

vin=sym('vin');

toff=sym('toff');

vcs=sym('vcs');

vo=sym('vo');

iLoa=sym('iLoa');

iLob=sym('iLob');

```

```

io=sym('io');

% normalized

j=sym('j');
m=sym('m');

% symbolic combination

wr=1/sqrt(Lr*Cr);
fr=wr/2/pi;
Zr=sqrt(Lr/Cr);
wr3=1/sqrt(Lr*(Cs+Cr));
fr3=wr3/2/pi;
Zr3=sqrt(Lr/(Cs+Cr));

%% Gain curve

M=0.25*(wr*toff-sin(wr*toff))/(2*j+wr*toff+sin(wr*toff));

% check wr*toff boundary

eq = j+2*sin(wr*toff)==0;

[s1] = solve(eq, toff);

```

```

M_dtoff=diff(M,toff);

% eq = M_dtoff==0;

% [s1] = solve(eq,toff)

% Derivation

x=sym('x');

M_dtoff_00=(1-cos(x))*(2*j+x+sin(x))-(x-sin(x))*(1+cos(x));

M_dtoff_01=2*j+2*sin(x)-2*j*cos(x)-2*x*cos(x);

M_dtoff_02=2*j+2*(4/pi/pi*(x-pi*3/2)^2-1)-2*j*(-4/pi/pi*(x-
2*pi)^2+1)-2*x*(-4/pi/pi*(x-2*pi)^2+1);

M_dtoff_03=2*j+2*(4/pi/pi*(x-pi*3/2)^2-1)-2*j*(-4/pi/pi*(x-
2*pi)^2+1)-2*(2*pi-8/pi*(x-2*pi)^2);

M_dtoff_04=2*(j+(4/pi/pi*(x-pi*3/2)^2-1)-j*(-4/pi/pi*(x-
2*pi)^2+1)-(2*pi-8/pi*(x-2*pi)^2));

M_dtoff_05=2*(j+4/pi/pi*x^2-12/pi*x+8+j*(4/pi/pi*x*x-
16/pi*x+15)+8/pi*x*x-32*x+30*pi);

m1=(j+2*pi+1)/pi/pi;

m2=- (4*j+8*pi+3)/pi;

m3=4*j+7.5*pi+2;

M_dtoff_06=4*2*( m1*x^2+m2*x+m3 );

root1=(-m2+sqrt(m2*m2-4*m1*m3))/2/m1;

root2=(-m2-sqrt(m2*m2-4*m1*m3))/2/m1;

roo12_01=( (4*j+8*pi+3)/pi-sqrt((- (4*j+8*pi+3)/pi)^2-

```

```
4*((j+2*pi+1)/pi/pi)*(4*j+7.5*pi+2)))/(2*(j+2*pi+1)/pi/pi);
```

```
% eval(M_dtoff_01)
```

```
% eval(M_dtoff_02)
```

```
% eval(M_dtoff_03)
```

```
% eval(M_dtoff_04)
```

```
% eval(M_dtoff_05)
```

```
% eval(M_dtoff_06)
```

```
% eval(root1)/pi
```

```
% eval(root2)/pi
```

```
% eval(roo12_01)/pi
```

```
%% The end
```

```
Toc
```

## E. Calculation of Gain Curve

The derivation of approximated trigonometric functions in (2-30), (2-31), and (2-32) is attached below

```
% ----- Clear Data _ start -----%
close all;clc; clear all; tic;
% set(0,'defaultFigureWindowStyle','docked');
% ttl=clock;
format compact
% ----- Clear Data _ END -----%

%% Color
C01=[1.0 0.0 0.0]; % red
C02=[1.0 0.5 0.0]; % dark orange
C03=[0.0 0.5 0.0]; % green
C04=[0.0 0.7 1.0]; % deep sky blue
C05=[0.0 0.0 1.0]; % blue
C06=[0.6 0.0 0.8]; % dark violet
C07=[1.0 0.0 1.0]; % magenta
C08=[0.8 0.4 0.1]; % chocolate
C09=[0.0 0.0 0.0]; % black
C10=[0.4 0.4 0.4]; % dim gray

c=[C01;C02;C03;C04;C05;C06;C07;C08;C09;C10];
```

```

%%

% component

Rload=sym('Rload');
Cr=sym('Cr');
Lr=sym('Lr');
Cs=sym('Cs');
Co=sym('Co');
Loa=sym('Loa');
Lob=sym('Lob');
RLoa=sym('RLoa');
RLob=sym('RLob');
Lob=Loa;
RLob=RLoa;

% large signal

vin=sym('vin');
toff=sym('toff');
vcs=sym('vcs');
vo=sym('vo');
iLoa=sym('iLoa');
iLob=sym('iLob');

```

```

io=sym('io');

% normalized

j=sym('j');
m=sym('m');

% symbolic combination

wr=1/sqrt(Lr*Cr);

fr=wr/2/pi;

Zr=sqrt(Lr/Cr);

wr3=1/sqrt(Lr*(Cs+Cr));

fr3=wr3/2/pi;

Zr3=sqrt(Lr/(Cs+Cr));

%%

%% Gain boundary - Numerical sinx and cosx

f31=figure(31);

x=linspace(1.5*pi,(1.8+0.2)*pi,50);

plot(x/pi,sin(x),'k-','linewidth',2);hold on;

plot(x/pi,(1/(pi/2)^2)*(x-3/2*pi).^2-1,'k--

','linewidth',2);hold on;

% plot(x/pi,x-2*pi,'b--','linewidth',2);hold on;

```

```

% plot(x/pi,2/pi*(x-2*pi),'r--','linewidth',2);hold on;

% plot(x/pi,cos(x),'b-','linewidth',2);hold on;

%           plot(x/pi,-(1/(pi/2)^2)*(x-2*pi).^2+1,'b--
','linewidth',2);hold on;

plot(x/pi,x.*cos(x),'r-','linewidth',2);hold on;
plot(x/pi,-8/pi*(x-2*pi).^2+2*pi,'r--','linewidth',2);hold on;
xlabel('x/pi');
ylabel('y app compare')
xlim([0 2])

set(gca,'linewidth',0.5,'fontsize',8,'FontName','Times      New
Roman'); grid on;

figpo=[100      100      (1.7*1-0.2*0)*96*2      (1.7-0.2*0)*96*2];
set(f31,'InnerPosition',figpo); grid on;

f32=figure(32);
x=linspace(1.5*pi,(1.8+0.2)*pi,50);
j=2;
M_dtoff_01=2*j+2.*sin(x)-2*j.*cos(x)-2*x.*cos(x);
M_dtoff_02=2*j+2.*(4./pi./pi.*(x-pi.*3./2).^2-1)-2.*j.*(-
4/pi/pi.*(x-2*pi).^2+1)-2.*x.*(-4./pi./pi.*(x-2.*pi).^2+1);
M_dtoff_03=2*j+2.*(4./pi./pi.*(x-pi.*3./2).^2-1)-2.*j.*(-

```

```

4/pi/pi.*(x-2*pi).^2+1)-2.*(2.*pi-8./pi.*(x-2.*pi).^2);

plot(x/pi,M_dtoff_01,'k-','linewidth',2);hold on;
plot(x/pi,M_dtoff_02,'g--','linewidth',2);hold on;
plot(x/pi,M_dtoff_03,'r--','linewidth',2);hold on;

xlabel('x/pi');

ylabel('y app compare')

xlim([0 2])

set(gca,'linewidth',0.5,'fontsize',8,'FontName','Times New
Roman'); grid on;

figpo=[100 100 (1.7*1-0.2*0)*96*2 (1.7-0.2*0)*96*2];
set(f32,'InnerPosition',figpo); grid on;

%% The end

Toc

```

The Matlab code for deriving the voltage gain in (2-27) is shown below

```

% ----- Clear Data _ start -----%

close all;clc; clear all; tic;

% set(0,'defaultFigureWindowStyle','docked');

% ttl=clock;

format compact

```

```

% ----- Clear Data _ END -----%

%% Color

C01=[1.0 0.0 0.0]; % red
C02=[1.0 0.5 0.0]; % dark orange
C03=[0.0 0.5 0.0]; % green
C04=[0.0 0.7 1.0]; % deep sky blue
C05=[0.0 0.0 1.0]; % blue
C06=[0.6 0.0 0.8]; % dark violet
C07=[1.0 0.0 1.0]; % magenta
C08=[0.8 0.4 0.1]; % chocolate
C09=[0.0 0.0 0.0]; % black
C10=[0.4 0.4 0.4]; % dim gray

c=[C01;C02;C03;C04;C05;C06;C07;C08;C09;C10];

%%

% component

Rload=sym('Rload');
Cr=sym('Cr');
Lr=sym('Lr');
Cs=sym('Cs');

```

```

Co=sym('Co');
Loa=sym('Loa');
Lob=sym('Lob');
RLoa=sym('RLoa');
RLob=sym('RLob');
Lob=Loa;
RLob=RLoa;

% large signal
vin=sym('vin');
toff=sym('toff');
vcs=sym('vcs');
vo=sym('vo');
iLoa=sym('iLoa');
iLob=sym('iLob');
io=sym('io');

% normalized
j=sym('j');
m=sym('m');

% symbolic combination
wr=1/sqrt(Lr*Cr);

```

```

fr=wr/2/pi;
Zr=sqrt(Lr/Cr);
wr3=1/sqrt(Lr*(Cs+Cr));
fr3=wr3/2/pi;
Zr3=sqrt(Lr/(Cs+Cr));

%%
% toff=110e-9;J=1.5;
M_00=(2*toff-pi/wr)/Ts/2
M_01=0.25*(2*wr*toff-pi)/(2*J+pi)
M_02=0.25*(wr*toff-sin(wr*toff))/(2*J+wr*toff+sin(wr*toff))
M_11=0.25*( (pi-asin(-J/2))-sin((pi-asin(-J/2))))/(2*J+(pi-
asin(-J/2))+sin((pi-asin(-J/2))))
M_12=0.25*( (J/2+pi+asin(J/2))/(3/2*J+pi+asin(J/2)))

%% The end

toc

```

The Matlab code for the gain curve in Fig. 2-17 using (2-27), (2-36), and (2-41) is shown below

```

% ----- Clear Data _ start -----%
close all;clc; clear all; tic;

```

```

% set(0,'defaultFigureWindowStyle','docked');

% ttl=clock;

format compact

% ----- Clear Data _ END -----%

%% Color

C01=[1.0 0.0 0.0]; % red
C02=[1.0 0.5 0.0]; % dark orange
C03=[0.0 0.5 0.0]; % green
C04=[0.0 0.7 1.0]; % deep sky blue
C05=[0.0 0.0 1.0]; % blue
C06=[0.6 0.0 0.8]; % dark violet
C07=[1.0 0.0 1.0]; % magenta
C08=[0.8 0.4 0.1]; % chocolate
C09=[0.0 0.0 0.0]; % black
C10=[0.4 0.4 0.4]; % dim gray

c=[C01;C02;C03;C04;C05;C06;C07;C08;C09;C10];

%%

% component

Rload=sym('Rload');

```

```
Cr=sym('Cr');
Lr=sym('Lr');
Cs=sym('Cs');
Co=sym('Co');
Loa=sym('Loa');
Lob=sym('Lob');
RLoa=sym('RLoa');
RLob=sym('RLob');
Lob=Loa;
RLob=RLoa;

% large signal
vin=sym('vin');
toff=sym('toff');
vcs=sym('vcs');
vo=sym('vo');
iLoa=sym('iLoa');
iLob=sym('iLob');
io=sym('io');

% normalized
j=sym('j');
m=sym('m');
```

```

% symbolic combination

wr=1/sqrt(Lr*Cr);

fr=wr/2/pi;

Zr=sqrt(Lr/Cr);

wr3=1/sqrt(Lr*(Cs+Cr));

fr3=wr3/2/pi;

Zr3=sqrt(Lr/(Cs+Cr));

%%

j_sw=linspace(0.01,2,20);

for i=1:length(j_sw) % M vs J with J<2

    j=j_sw(i);

    toff=(pi-asin(-j/2))/2/pi/fr;

    toff_zvs_sw(i)=toff;

    M_zvs_sw(i)=eval(M);

end

j_sw=linspace(2,50,20); % M vs J with wrtoff(j) and J>2

for i=1:length(j_sw)

    j=j_sw(i);

    toff=(
        (4*j+8*pi+3)/pi-sqrt((- (4*j+8*pi+3)/pi)^2-

```

```
4*((j+2*pi+1)/pi/pi)*(4*j+7.5*pi+2)))/(2*(j+2*pi+1)/pi/pi)/wr;
```

```
toff_Mmax_sw(i)=toff;
```

```
M_max_sw(i)=eval(M);
```

```
end
```

```
j_sw=linspace(2,50,20); % M vs J with wrtoff=3/2*pi and J>2
```

```
for i=1:length(j_sw)
```

```
    j=j_sw(i);
```

```
    toff=1.5*pi/wr;
```

```
    toff_Mmax_app1_sw(i)=toff;
```

```
    Mmax_app1=0.25*(1.5*pi+1)/(2*j+1.5*pi-1);
```

```
    M_max_app1_sw(i)=Mmax_app1;
```

```
end
```

```
N=50;
```

```
j=0.1;
```

```
toff_j01=linspace(0.2/fr,(pi-asin(-j/2))/2/pi/fr,N);
```

```
toff=toff_j01;
```

```
M_j01=eval(M);
```

```
j=0.5;
```

```

toff_j05=linspace(0.2/fr, (pi-asin(-j/2))/2/pi/fr,N);
toff=toff_j05;
M_j05=eval(M);

j=0.7;
toff_j07=linspace(0.2/fr, (pi-asin(-j/2))/2/pi/fr,N);
toff=toff_j07;
M_j07=eval(M);

j=1.5;
toff_j15=linspace(0.2/fr, (pi-asin(-j/2))/2/pi/fr,N);
toff=toff_j15;
M_j15=eval(M);

j=2.0;
toff_j20=linspace(0.2/fr, (pi-asin(-j/2))/2/pi/fr,N);
toff=toff_j20;
M_j20=eval(M);

j=3.0;
toff_j30=linspace(0.2/fr, 1/fr,N);
toff=toff_j30;
M_j30=eval(M);

```

```

j=5.0;

toff_j50=linspace(0.2/fr,1/fr,N);

toff=toff_j50;

M_j50=eval(M);

j=10;

toff=linspace(0.2/fr,1/fr,N);

M_j10=eval(M);

f12=figure(12);

plot(toff_j01*fr,M_j01,'k-','linewidth',1.0);hold on;
plot(toff_j05*fr,M_j05,'k-','linewidth',1.0);hold on;
plot(toff_j15*fr,M_j15,'k-','linewidth',1.0);hold on;
plot(toff_j20*fr,M_j20,'k-','linewidth',1.0);hold on;
plot(toff_j30*fr,M_j30,'k-','linewidth',1.0);hold on;
plot(toff_j50*fr,M_j50,'k-','linewidth',1.0);hold on;
plot(toff*fr,M_j10,'k-','linewidth',1.0);hold on;
plot(toff_zvs_sw*fr,M_zvs_sw,'g.','linewidth',2);hold on;
plot(toff_Mmax_sw*fr,M_max_sw,'r--','linewidth',2);hold on;
%           plot(toff_Mmax_appl_sw*fr,M_max_appl_sw,'r--
','linewidth',2);hold on;

xlabel(' '); % fr*toff

```

```

ylabel('    ') % M
% xlim([0.2 0.7])
ylim([0 0.25])
set(gca,'linewidth',0.5,'fontsize',8,'FontName','Times New
Roman'); grid on;
figpo=[100 100 (1.7*1-0.2*0)*96*2 (1.7-0.2*0)*96*1.5];
set(f12,'InnerPosition',figpo); grid on;

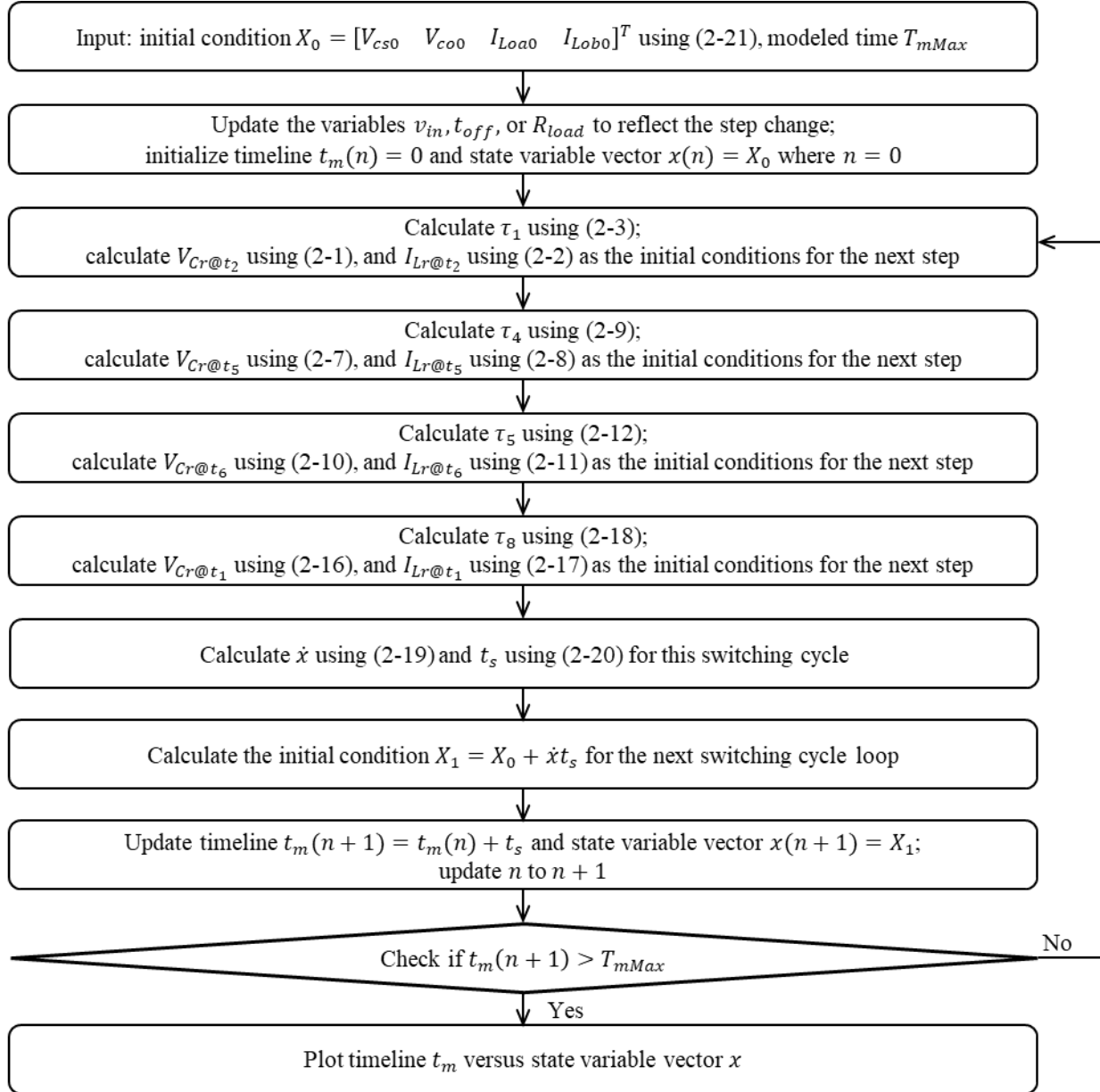
%% The end

toc

```

## F. Calculation of Large Signal Equations

The flowchart for the calculation of the large-signal equations (3-4) is shown below



The Matlab code to solve (3-4) is attached below

```

% ----- Clear Data _ start -----%

close all;clc; clear all;

% set(0,'defaultFigureWindowStyle','docked'); tt1=clock;

```

```
format compact
% ----- Clear Data _ END -----%
%% Color
C01=[1.0 0.0 0.0]; % red
C02=[1.0 0.5 0.0]; % dark orange
C03=[0.0 0.5 0.0]; % green
C04=[0.0 0.7 1.0]; % deep sky blue
C05=[0.0 0.0 1.0]; % blue
C06=[0.6 0.0 0.8]; % dark violet
C07=[1.0 0.0 1.0]; % magenta
C08=[0.8 0.4 0.1]; % chocolate
C09=[0.0 0.0 0.0]; % black
C10=[0.4 0.4 0.4]; % dim gray

c=[C01;C02;C03;C04;C05;C06;C07;C08;C09;C10];
```

```

%% Theoretical Model

X0 = [24.0;5.0;20.0;20.0]; % vCs,vCo,iLoa,iLob average value

% X0 = [24.0;7.0;10.0;10.0]; % vCs,vCo,iLoa,iLob average value

t0 = 0;

V0 = [48;5/40;50e-3;120e-9;0];

Sv = [X0;t0;V0];

for i=1:1:(102e-6/475e-9)*1

    i;

    [X1,t1] = Large_220526(X0,t0,V0);

    X0 = X1; t0 = t1;

    Sv = [Sv [X1;t1;V0]];

end

Excel=zeros(5,length(Sv(1,:)));

Excel(1,:)=Sv(5,:);

Excel(2:5,:)=Sv(1:4,:);

Excel(6,:)=Sv(9,:);

Excel=Excel';

%% comparison

X0 = [5.0;40.0]; % vCo,iLo average value

```

```

t0 = 0;
V0 = [48;5/40;50e-3;120e-9;0];
Sv2 = [X0;t0;V0];
for i=1:1:(102e-6/475e-9)*1
    i;
    [X1,t1] = Small_220616(X0,t0,V0);
    X0 = X1; t0 = t1;
    Sv2 = [Sv2 [X1;t1;V0]];
end

```

```

V0 = [54;5/40;50e-3;120e-9;0];
for i=1:1:(400e-6/475e-9)*1
    i;
    [X1,t1] = Small_220616(X0,t0,V0);
    X0 = X1; t0 = t1;
    Sv2 = [Sv2 [X1;t1;V0]];
end

```

```

V0 = [48;5/40;50e-3;120e-9;0];
for i=1:1:(500e-6/475e-9)*1
    i;
    [X1,t1] = Small_220616(X0,t0,V0);
    X0 = X1; t0 = t1;

```

```

    Sv2 = [Sv2 [X1;t1;V0]];
end

Excel2=zeros(4,length(Sv2(1,:)));
Excel2(1,:)=Sv2(3,:);
Excel2(2:3,:)=Sv2(1:2,:);
Excel2(4,:)=Sv2(4,:);
Excel2=Excel2';

%% Figures

f11=figure(11);
% plot(Sv(end,:),Sv(1:4,:),'-', 'Color',c(9,:), 'linewidth',1);hold on;
% plot(Sv(5,:)*1e6,Sv(3:4,:),'-', 'linewidth',1);hold on;
plot(Sv(5,:)*1e6,Sv(1:4,:),'-', 'linewidth',2);hold on;
plot(Sv(5,:)*1e6,Sv(3,:)+Sv(4,:),'-', 'linewidth',2);hold on;
plot(Sv2(3,:)*1e6,Sv2(1:2,:),'-', 'linewidth',2);hold on;
xlabel('Time','FontSize',11);
ylabel('vCs [V]')
% xlim([100 200])
% ylim([-30 30])

set(gca,'linewidth',0.5,'fontsize',8,'FontName','Times New Roman'); grid on;

```

```
figpo=[100 100 (1.7*2-0.2*0)*96*2 (2-0.2*0)*96*2]; set(f11,'InnerPosition',figpo); grid on;
```

```
f12=figure(12);
```

```
plot(Sv(5,:)*1e6,Sv(2,:)*1,'-', 'linewidth',1);hold on;
```

```
plot(Sv2(3,:)*1e6,Sv2(1,:),'.', 'linewidth',2);hold on;
```

```
xlabel('Time','FontSize',11);
```

```
ylabel('vo [V]')
```

```
% xlim([100 200])
```

```
set(gca,'linewidth',0.5,'fontsize',8,'FontName','Times New Roman'); grid on;
```

```
figpo=[100 800 (1.7*2-0.2*0)*96*1 (2-0.2*0)*96*1]; set(f12,'InnerPosition',figpo); grid on;
```

```
%% -----
```

```
%% FUNCTIONS
```

```
%% -----
```

```
function [X1,t1] = Large_220526(X0,t0,V0)
```

```
%% Temp
```

```
% toff=140e-9;
```

```
% toff=120e-9;
```

```
%% Specs
```

```

% % ----- Components _ start _ 1-----%

% fr=3.77e6;

% Zr=3.5;

% Lr=Zr/2/pi/fr;

% Cr=1/2/pi/fr/Zr;

% Cn=50*1;

% Cs=Cr*Cn;

% Co=47e-6;

% wr=1/sqrt(Lr*Cr);

% wr3=1/sqrt(Lr*(Cs+Cr));

% Zr3=sqrt(Lr/(Cs+Cr));

% Loa=1200e-9*2;

% Lob=Loa;

%

% Vin=V0(1);

% Rload=V0(2);

% % ----- Components _ start _ 1-----%

% ----- Components _ start _ 2-----%

fr=4.1e6;

Zr=1.8;

Lr=Zr/2/pi/fr;

Cr=1/2/pi/fr/Zr;

```

```

Cn=1000*1;
Cs=Cr*Cn;
Co=47e-6;
wr=1/sqrt(Lr*Cr);
wr3=1/sqrt(Lr*(Cs+Cr));
Zr3=sqrt(Lr/(Cs+Cr));
Loa=1500e-9;
Lob=Loa;

Vin=V0(1);
Rload=V0(2);
RLo=V0(3);
toff=V0(4);
delI=V0(5);
% ----- Components _ start _ 2-----%

%% IC

Vcs=X0(1);
Vco=X0(2);
Iloa=X0(3);
Ilob=X0(4);

```

```

vcr_t1=Vin-Vcs;

iLr_t1=Iloa;

N_sample=50;

%% #1

tv=linspace(0,toff,N_sample);

tv_1_sample=tv(2)-tv(1);

vcr_v1=cos(wr.*tv)*vcr_t1;

iLr_v1=1/Zr*(-wr.*tv+pi)*vcr_t1 + Iloa;

vcr_t2=vcr_v1(end);

iLr_t2=iLr_v1(end);

%% #2

% t23x=Cr*(-Vcs-vcr_t2)/(-iLr_t2);

% tv=linspace(0,t23x,N_sample);

% iLr_v2=iLr_t2+vcr_t2.*tv/Lr

% vcr_t3=-Vcs;

% iLr_t3=iLr_v2(end);

```

```

t23x=0;

vcr_t3=-Vcs;

iLr_t3=iLr_v1(end);

%% #3

t34x=(Ilob+iLr_t3)*Lr/Vcs;

tv=linspace(0,t34x,N_sample);

vcr_v3=-Vcs;

iLr_v3=iLr_t3+(-Vcs).*tv/Lr;

vcr_t4=vcr_v3(end);

iLr_t4=(-Ilob);

%% #4

tv=linspace(0,toff,N_sample);

tv_4_sample=tv(2)-tv(1);

vcr_v4=cos(wr.*tv)*vcr_t4;

iLr_v4=1/Zr*(-wr.*tv+pi)*vcr_t4 + (-Ilob);

vcr_t5=vcr_v4(end);

```

```

iLr_t5=iLr_v4(end);

%% #5
% t56x=Cr*( (Vin-Vcs) -vcr_t5)/(-iLr_t5);
% tv=linspace(0,t56x,N_sample);
% iLr_v5=iLr_t5+vcr_t5.*tv/Lr;
% vcr_t6=Vin-Vcs;
% iLr_t6=iLr_v5(end);

t56x=0;
vcr_t6=Vin-Vcs;
iLr_t6=iLr_v4(end);

%% #6
t67x=(Iloa-iLr_t6)*Lr/(Vin-Vcs);
tv=linspace(0,t67x,N_sample);

vcr_v6=Vin-Vcs;
iLr_v6=iLr_t6+(Vin-Vcs).*tv/Lr;

vcr_t7=vcr_v6(end);
iLr_t7=Iloa;

```

```

%% Sumup
Ts = toff+t23x+t34x+toff+t56x+t67x;

if imag(t34x)~= 0
    disp('complex number!')
end

%% Integrate short period (B matrices)
b1 = t34x/2*(-2*Ilob+t34x*Vcs/Lr) + t67x/2*(2*Iloa-t67x*(Vin-Vcs)/Lr);
b1 = b1/Cs;

b2 = (-delI)*Ts/Co;

b3 = Vin*toff - vcr_t1*(-toff+pi/wr);
b3 = b3/Loa;

b4 = vcr_t4*(-toff+pi/wr);
b4 = b4/Lob;

Bsum= [b1;b2;b3;b4]/Ts;

%% A matrices
A1= [

```

$0 \ 0 \ 1/C_s \ 0;$   
 $0 \ 1^*-1/R_{load}/C_o \ 1/C_o \ 1/C_o;$   
 $-1/L_oa \ -1/L_oa \ -R_{Lo}/L_oa \ 0;$   
 $0 \ -1/L_{ob} \ 0 \ -R_{Lo}/L_{ob}$   
 $];$

$A_2 = [$   
 $0 \ 0 \ 0 \ 0;$   
 $0 \ 1^*-1/R_{load}/C_o \ 1/C_o \ 1/C_o;$   
 $0 \ -1/L_oa \ -R_{Lo}/L_oa \ 0;$   
 $0 \ -1/L_{ob} \ 0 \ -R_{Lo}/L_{ob}$   
 $];$

$A_3 = [$   
 $0 \ 0 \ 0 \ 0;$   
 $0 \ 1^*-1/R_{load}/C_o \ 1/C_o \ 1/C_o;$   
 $0 \ -1/L_oa \ -R_{Lo}/L_oa \ 0;$   
 $0 \ -1/L_{ob} \ 0 \ -R_{Lo}/L_{ob}$   
 $];$

$A_4 = [$   
 $0 \ 0 \ 0 \ -1/C_s;$   
 $0 \ 1^*-1/R_{load}/C_o \ 1/C_o \ 1/C_o;$   
 $0 \ -1/L_oa \ -R_{Lo}/L_oa \ 0;$   
 $1/L_{ob} \ -1/L_{ob} \ 0 \ -R_{Lo}/L_{ob}$   
 $];$

```

A5= [
    0 0 0 0;
    0 1*-1/Rload/Co 1/Co 1/Co;
    0 -1/Loa -RLo/Loa 0;
    0 -1/Lob 0 -RLo/Lob
];

```

```

A6= [
    0 0 0 0;
    0 1*-1/Rload/Co 1/Co 1/Co;
    0 -1/Loa -RLo/Loa 0;
    0 -1/Lob 0 -RLo/Lob
];

```

$A_{sum} = (t_{off} * A1 + t_{23x} * A2 + t_{34x} * A3 + t_{off} * A4 + t_{56x} * A5 + t_{67x} * A6) / T_s;$

$\dot{x} = (A_{sum} * X0 + B_{sum});$

$X1 = X0 + \dot{x} * T_s;$

$t1 = t0 + T_s;$

%% debug

$T_{scal} = 2 * t_{off} + 4 * L_r * (I_{loa} + I_{lob} + V_{in} / 2 * (\pi - t_{off} * \omega_r) / Z_r) / V_{in};$  % w/ sin app

$V_{ocal} = (V_{in} / 2) * (2 * t_{off} - \pi / \omega_r) / T_{scal} - R_{Lo} / 2 * (I_{loa} + I_{lob});$

$V_{odel} = V_{co} - V_{ocal};$

```
% toff
% t23x
% t34x
% iLr_t3
% t34x=(Ilob+iLr_t3)*Lr/Vcs
% t67x=(Iloa-iLr_t6)*Lr/(Vin-Vcs)
```

```
% Iloa+Ilob
% Loa
% Lob
% b3/Ts*Ts
% Asum*X0*Ts
% Ts =Ts
```

```
end
```

```
%%
```

```
function [X1,t1] = Small_220616(X0,t0,V0)
```

```
%% Temp
```

```
% ----- Components _ start _ 2-----%
```

```
fr=4.1e6;
```

```
Zr=1.8;
```

```
Lr=Zr/2/pi/fr;
```

```
Cr=1/2/pi/fr/Zr;
```

```
Cn=1000*1;
```

```
Cs=Cr*Cn;
```

```
Co=47e-6;
```

```
wr=1/sqrt(Lr*Cr);
```

```
wr3=1/sqrt(Lr*(Cs+Cr));
```

```
Zr3=sqrt(Lr/(Cs+Cr));
```

```
Loa=1500e-9;
```

```
Lob=Loa;
```

```
Vin=V0(1);
```

```
Rload=V0(2);
```

```
RLo=V0(3);
```

```
toff=V0(4);
```

```

delI=V0(5);

% ----- Components _ start _ 2-----%

%% IC

Vco=X0(1);

Ilo=X0(2);

%% state equations

Ts=2*toff+4*Lr*( Ilo+Vin/2*(pi-toff*wr)/Zr )/Vin;

dvco=(-Vco/Rload+Ilo)/Co;

diLo=(Vin/2*(2*toff-pi/wr)/Ts-Vco-RLo/2*Ilo)/(Loa/2);

X1(1,1) = X0(1) + dvco*Ts;

X1(2,1) = X0(2) + diLo*Ts;

% toff

Vocal=Vin*( toff/2/Ts-RLo/2*Ilo/Vin);

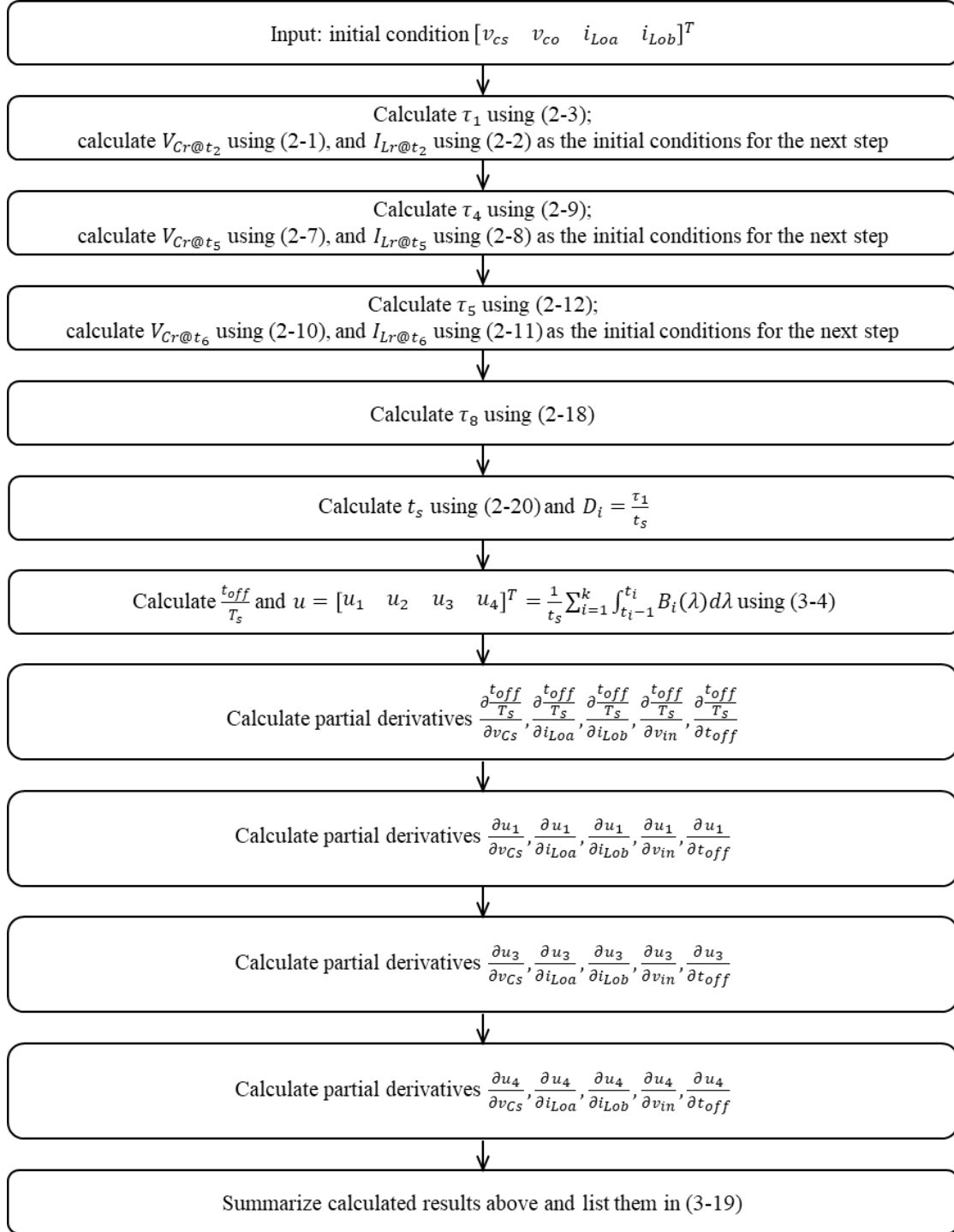
t1= t0+Ts;

end

```

## G. Calculation of Small Signal Equations

The flowchart for the calculation of the large-signal equations (3-4) is shown below



The first portion of the Matlab code is to calculate  $t_{off}/T_s$  and  $u = [u_1 \ u_2 \ u_3 \ u_4]^T = \frac{1}{t_s} \sum_{i=1}^k \int_{t_{i-1}}^{t_i} B_i(\lambda) d\lambda$ . The results are used as the input for the second portion. The second portion of the Matlab code is to calculate and simplify the partial derivatives. The equations of the partial derivatives are presented in the shortest form in (3-20).

The first portion of the Matlab code is:

```
% ----- Clear Data _ start -----%
close all;clc; clear all; tic;
% set(0,'defaultFigureWindowStyle','docked');
% ttl=clock;
format compact
% ----- Clear Data _ END -----%
```

%% Color

C01=[1.0 0.0 0.0]; % red

C02=[1.0 0.5 0.0]; % dark orange

C03=[0.0 0.5 0.0]; % green

C04=[0.0 0.7 1.0]; % deep sky blue

C05=[0.0 0.0 1.0]; % blue

C06=[0.6 0.0 0.8]; % dark violet

C07=[1.0 0.0 1.0]; % magenta

C08=[0.8 0.4 0.1]; % chocolate

C09=[0.0 0.0 0.0]; % black

C10=[0.4 0.4 0.4]; % dim gray

```
c=[C01;C02;C03;C04;C05;C06;C07;C08;C09;C10];
```

```
%% My model with Req
```

```
% management diff perturbation
```

```
EN_vinhat=1
```

```
EN_toffhat=0
```

```
EN_iohat=0
```

```
% simplified symbolic solution
```

```
Ts=sym('Ts');
```

```
tau4=sym('tau4');
```

```
tau6=sym('tau6');
```

```
% small signal hat
```

```
vcshat=sym('vcshat');
```

```
% vcohat=sym('vcohat');
```

```
iLoahat=sym('iLoahat');
```

```
iLobhat=sym('iLobhat');
```

```
vinhat=sym('vinhat');
```

```
toffhat=sym('toffhat');
```

```
iohat=sym('iohat');
```

```
% Laplace
s=sym('s');

% component
Rload=sym('Rload');
Cr=sym('Cr');
Lr=sym('Lr');
Cs=sym('Cs');
% Co=sym('Co');
Loa=sym('Loa');
Lob=sym('Lob');
RLoa=sym('RLoa');
RLob=sym('RLob');
Lob=Loa;
RLob=RLoa;

% large signal
vin=sym('vin');
toff=sym('toff');
vcs=sym('vcs');
% vco=sym('vco');
iLoa=sym('iLoa');
iLob=sym('iLob');
```

```

% symbolic combination

wr=1/sqrt(Lr*Cr);

Zr=sqrt(Lr/Cr);

wr3=1/sqrt(Lr*(Cs+Cr));

Zr3=sqrt(Lr/(Cs+Cr));

%% subintervals & resonant vcr and iLr

% initial condition

vcr_t1=vin-vcs;

iLr_t1=iLoa;

% subinterval 1

tau1=toff;

% vcr_t2=cos(wr*tau1)*vcr_t1;

iLr_t2=1/Zr*(-wr*tau1+pi)*vcr_t1 + iLoa;

% subinterval 2 - ignored

tau3=0;

vcr_t3=-vcs;

iLr_t3=iLr_t2;

% subinterval 3

tau4=(-iLob-iLr_t3)*Lr/(-vcs);

vcr_t4=vcr_t3;

iLr_t4=iLr_t3+(-vcs)*tau4/Lr;

```

```

% subinterval 4

tau4=toff;

% vcr_t5=cos(wr*tau4)*vcr_t4;

iLr_t5=1/Zr*(-wr*tau4+pi)*vcr_t4 - iLob;

% subinterval 5 - ignored

tau5=0;

vcr_t6=vin-vcs;

iLr_t6=iLr_t5;

% subinterval 6

tau6=(iLoa-iLr_t6)*Lr/(vin-vcs);

vcr_t7=vcr_t6;

iLr_t7=iLr_t6+(vin-vcs)*tau6/Lr;

%% matrices

K= [

    Cs 0 0;

    0 Loa 0;

    0 0 Lob

];

u1 = tau4/2*(-2*iLob-tau4*(-vcs)/Lr) + tau6/2*(2*iLoa-tau6*(vin-vcs)/Lr)

u3 = vin/2*tau1*2 - vcr_t1*(-tau1+pi/wr); %4th order

u4 = vin/2*tau4*0 + vcr_t4*(-tau4+pi/wr); %4th order

```

```
u1=u1/Ts;
```

```
u3=u3/Ts;
```

```
u4=u4/Ts;
```

```
U = [u1;u3;u4];
```

```
%% calculate partial derivative
```

```
p=toff/Ts;
```

```
dpdvcs = diff(p,vcs);
```

```
dpdiLoa = diff(p,iLoa);
```

```
dpdiLob = diff(p,iLob);
```

```
dpdvin = diff(p,vin);
```

```
dpdtoff = diff(p,toff);
```

```
du1dvcs=diff(u1,vcs)
```

```
du1diLoa=diff(u1,iLoa);
```

```
du1diLob=diff(u1,iLob);
```

```
du1dvin=diff(u1,vin);
```

```
du1dtoff=diff(u1,toff);
```

```
du3dvcs=diff(u3,vcs);
```

```
du3diLoa=diff(u3,iLoa);
```

du3diLob=diff(u3,iLob);

du3dvin=diff(u3,vin);

du3dtoff=diff(u3,toff);

du4dvcs=diff(u4,vcs);

du4diLoa=diff(u4,iLoa);

du4diLob=diff(u4,iLob);

du4dvin=diff(u4,vin);

du4dtoff=diff(u4,toff);

dp =dpdvcs\*vcs $\hat{a}$  +dpdiLoa\*iLoa $\hat{a}$  +dpdiLob\*iLob $\hat{a}$  +EN\_vin $\hat{a}$ \*dpdvin\*vin $\hat{a}$   
+EN\_toff $\hat{a}$ \*dpdtoff\*toff $\hat{a}$ ;

du1=du1dvcs\*vcs $\hat{a}$ +du1diLoa\*iLoa $\hat{a}$ +du1diLob\*iLob $\hat{a}$ +EN\_vin $\hat{a}$ \*du1dvin\*vin $\hat{a}$ +  
EN\_toff $\hat{a}$ \*du1dtoff\*toff $\hat{a}$ ;

du3=du3dvcs\*vcs $\hat{a}$ +du3diLoa\*iLoa $\hat{a}$ +du3diLob\*iLob $\hat{a}$ +EN\_vin $\hat{a}$ \*du3dvin\*vin $\hat{a}$ +  
EN\_toff $\hat{a}$ \*du3dtoff\*toff $\hat{a}$ ;

du4=du4dvcs\*vcs $\hat{a}$ +du4diLoa\*iLoa $\hat{a}$ +du4diLob\*iLob $\hat{a}$ +EN\_vin $\hat{a}$ \*du4dvin\*vin $\hat{a}$ +  
EN\_toff $\hat{a}$ \*du4dtoff\*toff $\hat{a}$ ;

toc

The second portion of Matlab code is:

```

% ----- Clear Data _ start -----%

close all;clc; clear all; tic;

% set(0,'defaultFigureWindowState','docked');

% tt1=clock;

format compact

% ----- Clear Data _ END -----%

%% Color

C01=[1.0 0.0 0.0]; % red

C02=[1.0 0.5 0.0]; % dark orange

C03=[0.0 0.5 0.0]; % green

C04=[0.0 0.7 1.0]; % deep sky blue

C05=[0.0 0.0 1.0]; % blue

C06=[0.6 0.0 0.8]; % dark violet

C07=[1.0 0.0 1.0]; % magenta

C08=[0.8 0.4 0.1]; % chocolate

C09=[0.0 0.0 0.0]; % black

C10=[0.4 0.4 0.4]; % dim gray

c=[C01;C02;C03;C04;C05;C06;C07;C08;C09;C10];

```

```
%%  
  
% New variables  
wr=sym('wr');  
Zr=sym('Zr');  
io=sym('io');  
Ts=sym('Ts');  
wss=sym('wss');  
  
% management diff perturbation  
EN_vinhat=1;  
EN_toffhat=0;  
EN_iohat=0;  
  
% component  
Rload=sym('Rload');  
Cr=sym('Cr');  
Lr=sym('Lr');  
Cs=sym('Cs');  
Loa=sym('Loa');  
Lob=sym('Lob');  
RLoa=sym('RLoa');
```

```

RLob=sym('RLob');
Lob=Loa;
RLob=RLoa;

% large signal
vin=sym('vin');
toff=sym('toff');
vcs=sym('vcs');
iLoa=sym('iLoa');
iLob=sym('iLob');

%%

ts_00 = 2*toff - (Lr*(iLoa + iLob + (vcs*(pi - toff/(Cr*Lr)^(1/2)))/(Lr/Cr)^(1/2)))/(vcs - vin)
+ (Lr*(iLoa + iLob - ((vcs - vin)*(pi - toff/(Cr*Lr)^(1/2)))/(Lr/Cr)^(1/2)))/vcs;

ts_01 = subs(ts_00,iLob,iLoa); % s-new = subs(s-old,old,new)
ts_02 = subs(ts_01,vcs,vin/2);
ts_03 = subs(ts_02,1/(Cr*Lr)^(1/2),wr);
ts_04 = subs(ts_03,(Lr/Cr)^(1/2),Zr);
ts_05 = subs(ts_04,2*iLoa,io)
ts_06 = 2*toff + (4*Lr*(io + (vin*sin(wr*toff))/(2*Zr)))/vin;

du1dvcs_00 = ((Lr*(iLob - iLoa + ((vcs - vin)*(pi - toff/(Cr*Lr)^(1/2)))/(Lr/Cr)^(1/2)))*(iLoa

```

$$\begin{aligned}
& + iLob - ((vcs - vin)*(pi - toff/(Cr*Lr)^{(1/2)}))/(Lr/Cr)^{(1/2)})/(2*vcs^2) - (Lr*(iLoa + iLob + \\
& (vcs*(pi - toff/(Cr*Lr)^{(1/2)}))/(Lr/Cr)^{(1/2)})*(iLob - iLoa + (vcs*(pi - \\
& toff/(Cr*Lr)^{(1/2)}))/(Lr/Cr)^{(1/2)}))/(2*(vcs - vin)^2) + (Lr*(pi - toff/(Cr*Lr)^{(1/2)})*(iLob - iLoa \\
& + (vcs*(pi - toff/(Cr*Lr)^{(1/2)}))/(Lr/Cr)^{(1/2)}))/(2*(Lr/Cr)^{(1/2)}*(vcs - vin)) + (Lr*(pi - \\
& toff/(Cr*Lr)^{(1/2)})*(iLob - iLoa + ((vcs - vin)*(pi - \\
& toff/(Cr*Lr)^{(1/2)}))/(Lr/Cr)^{(1/2)}))/(2*vcs*(Lr/Cr)^{(1/2)}) + (Lr*(pi - toff/(Cr*Lr)^{(1/2)})*(iLoa + \\
& iLob + (vcs*(pi - toff/(Cr*Lr)^{(1/2)}))/(Lr/Cr)^{(1/2)}))/(2*(Lr/Cr)^{(1/2)}*(vcs - vin)) - (Lr*(pi - \\
& toff/(Cr*Lr)^{(1/2)})*(iLoa + iLob - ((vcs - vin)*(pi - \\
& toff/(Cr*Lr)^{(1/2)}))/(Lr/Cr)^{(1/2)}))/(2*vcs*(Lr/Cr)^{(1/2)})/(2*toff - (Lr*(iLoa + iLob + (vcs*(pi \\
& - toff/(Cr*Lr)^{(1/2)}))/(Lr/Cr)^{(1/2)}))/(vcs - vin) + (Lr*(iLoa + iLob - ((vcs - vin)*(pi - \\
& toff/(Cr*Lr)^{(1/2)}))/(Lr/Cr)^{(1/2)}))/vcs) + (((Lr*(iLoa + iLob + (vcs*(pi - \\
& toff/(Cr*Lr)^{(1/2)}))/(Lr/Cr)^{(1/2)})*(iLob - iLoa + (vcs*(pi - \\
& toff/(Cr*Lr)^{(1/2)}))/(Lr/Cr)^{(1/2)}))/(2*(vcs - vin)) - (Lr*(iLob - iLoa + ((vcs - vin)*(pi - \\
& toff/(Cr*Lr)^{(1/2)}))/(Lr/Cr)^{(1/2)})*(iLoa + iLob - ((vcs - vin)*(pi - \\
& toff/(Cr*Lr)^{(1/2)}))/(Lr/Cr)^{(1/2)}))/(2*vcs))*((Lr*(iLoa + iLob - ((vcs - vin)*(pi - \\
& toff/(Cr*Lr)^{(1/2)}))/(Lr/Cr)^{(1/2)))/vcs^2 - (Lr*(iLoa + iLob + (vcs*(pi - \\
& toff/(Cr*Lr)^{(1/2)}))/(Lr/Cr)^{(1/2)))/vcs - vin)^2 + (Lr*(pi - \\
& toff/(Cr*Lr)^{(1/2)))/vcs*(Lr/Cr)^{(1/2)}) + (Lr*(pi - toff/(Cr*Lr)^{(1/2)))/((Lr/Cr)^{(1/2)}*(vcs - \\
& vin)))/(2*toff - (Lr*(iLoa + iLob + (vcs*(pi - toff/(Cr*Lr)^{(1/2)}))/(Lr/Cr)^{(1/2)))/vcs - vin) + \\
& (Lr*(iLoa + iLob - ((vcs - vin)*(pi - toff/(Cr*Lr)^{(1/2)}))/(Lr/Cr)^{(1/2)))/vcs)^2;
\end{aligned}$$

du1dvcs\_01 = subs(du1dvcs\_00,iLob,iLoa); % s-new = subs(s-old,old,new)

du1dvcs\_02 = subs(du1dvcs\_01,vcs,vin/2);

du1dvcs\_03 = subs(du1dvcs\_02,1/(Cr\*Lr)^{(1/2),wr);

du1dvcs\_04 = subs(du1dvcs\_03,(Lr/Cr)^(1/2),Zr);

du1dvcs\_05 = subs(du1dvcs\_04,2\*iLoa,io);

du1dvcs\_06 = subs(du1dvcs\_05,ts\_05,Ts)

du1diLoa\_00 = - ((Lr\*(iLoa + iLob + (vcs\*(pi - toff/(Cr\*Lr)^(1/2)))/(Lr/Cr)^(1/2)))/(Lr/Cr)^(1/2))/(2\*(vcs - vin)) - (Lr\*(iLoa + iLob - ((vcs - vin)\*(pi - toff/(Cr\*Lr)^(1/2)))/(Lr/Cr)^(1/2)))/(2\*vcs) - (Lr\*(iLob - iLoa + (vcs\*(pi - toff/(Cr\*Lr)^(1/2)))/(Lr/Cr)^(1/2)))/(2\*(vcs - vin)) + (Lr\*(iLob - iLoa + ((vcs - vin)\*(pi - toff/(Cr\*Lr)^(1/2)))/(Lr/Cr)^(1/2)))/(2\*vcs))/(2\*toff - (Lr\*(iLoa + iLob + (vcs\*(pi - toff/(Cr\*Lr)^(1/2)))/(Lr/Cr)^(1/2)))/(vcs - vin) + (Lr\*(iLoa + iLob - ((vcs - vin)\*(pi - toff/(Cr\*Lr)^(1/2)))/(Lr/Cr)^(1/2)))/vcs) - ((Lr/vcs - Lr/(vcs - vin))\*((Lr\*(iLoa + iLob + (vcs\*(pi - toff/(Cr\*Lr)^(1/2)))/(Lr/Cr)^(1/2))\*iLob - iLoa + (vcs\*(pi - toff/(Cr\*Lr)^(1/2)))/(Lr/Cr)^(1/2)))/(2\*(vcs - vin)) - (Lr\*(iLob - iLoa + ((vcs - vin)\*(pi - toff/(Cr\*Lr)^(1/2)))/(Lr/Cr)^(1/2))\*iLoa + iLob - ((vcs - vin)\*(pi - toff/(Cr\*Lr)^(1/2)))/(Lr/Cr)^(1/2)))/(2\*vcs))/(2\*toff - (Lr\*(iLoa + iLob + (vcs\*(pi - toff/(Cr\*Lr)^(1/2)))/(Lr/Cr)^(1/2)))/(vcs - vin) + (Lr\*(iLoa + iLob - ((vcs - vin)\*(pi - toff/(Cr\*Lr)^(1/2)))/(Lr/Cr)^(1/2)))/vcs)^2;

du1diLoa\_01 = subs(du1diLoa\_00,iLob,iLoa); % s-new = subs(s-old,old,new)

du1diLoa\_02 = subs(du1diLoa\_01,vcs,vin/2);

du1diLoa\_03 = subs(du1diLoa\_02,1/(Cr\*Lr)^(1/2),wr);

du1diLoa\_04 = subs(du1diLoa\_03,(Lr/Cr)^(1/2),Zr);

du1diLoa\_05 = subs(du1diLoa\_04,2\*iLoa,io);

du1diLoa\_06 = subs(du1diLoa\_05,ts\_05,Ts)

$$\begin{aligned}
du1dvin\_00 = & ((Lr*(iLoa + iLob + (vcs*(pi - toff/(Cr*Lr)^{(1/2)})))/(Lr/Cr)^{(1/2)})) / (Lr/Cr)^{(1/2)} * (iLob - iLoa \\
+ & (vcs*(pi - toff/(Cr*Lr)^{(1/2)})) / (Lr/Cr)^{(1/2)}) / (2*(vcs - vin)^2) - (Lr*(pi - \\
toff/(Cr*Lr)^{(1/2)}) * (iLob & - iLoa + ((vcs - vin)*(pi - \\
toff/(Cr*Lr)^{(1/2)})) / (Lr/Cr)^{(1/2)}) / (2*vcs*(Lr/Cr)^{(1/2)}) + (Lr*(pi - toff/(Cr*Lr)^{(1/2)}) * (iLoa + \\
iLob - ((vcs - vin)*(pi - toff/(Cr*Lr)^{(1/2)})) / (Lr/Cr)^{(1/2)}) / (2*vcs*(Lr/Cr)^{(1/2)}) / (2*toff - \\
(Lr*(iLoa + iLob + (vcs*(pi - toff/(Cr*Lr)^{(1/2)})) / (Lr/Cr)^{(1/2)})) / (vcs - vin) + (Lr*(iLoa + iLob - \\
((vcs - vin)*(pi - toff/(Cr*Lr)^{(1/2)})) / (Lr/Cr)^{(1/2)})) / vcs) + (((Lr*(iLoa + iLob + (vcs*(pi - \\
toff/(Cr*Lr)^{(1/2)})) / (Lr/Cr)^{(1/2)})) / (vcs & - vin)^2 - (Lr*(pi - \\
toff/(Cr*Lr)^{(1/2)})) / (vcs*(Lr/Cr)^{(1/2)})) * ((Lr*(iLoa + iLob + (vcs*(pi - \\
toff/(Cr*Lr)^{(1/2)})) / (Lr/Cr)^{(1/2)}) * (iLob & - iLoa + (vcs*(pi - \\
toff/(Cr*Lr)^{(1/2)})) / (Lr/Cr)^{(1/2)})) / (2*(vcs - vin)) - (Lr*(iLob - iLoa + ((vcs - vin)*(pi - \\
toff/(Cr*Lr)^{(1/2)})) / (Lr/Cr)^{(1/2)}) * (iLoa + iLob - ((vcs - vin)*(pi - \\
toff/(Cr*Lr)^{(1/2)})) / (Lr/Cr)^{(1/2)})) / (2*vcs))) / (2*toff - (Lr*(iLoa + iLob + (vcs*(pi - \\
toff/(Cr*Lr)^{(1/2)})) / (Lr/Cr)^{(1/2)})) / (vcs - vin) + (Lr*(iLoa + iLob - ((vcs - vin)*(pi - \\
toff/(Cr*Lr)^{(1/2)})) / (Lr/Cr)^{(1/2)})) / vcs)^2;
\end{aligned}$$

$$du1dvin\_01 = \text{subs}(du1dvin\_00, iLob, iLoa); \% s\text{-new} = \text{subs}(s\text{-old}, old, new)$$

$$du1dvin\_02 = \text{subs}(du1dvin\_01, vcs, vin/2);$$

$$du1dvin\_03 = \text{subs}(du1dvin\_02, 1/(Cr*Lr)^{(1/2)}, wr);$$

$$du1dvin\_04 = \text{subs}(du1dvin\_03, (Lr/Cr)^{(1/2)}, Zr);$$

$$du1dvin\_05 = \text{subs}(du1dvin\_04, 2*iLoa, io);$$

$$du1dvin\_06 = \text{subs}(du1dvin\_05, ts\_05, Ts)$$

$$du1dvcs = du1dvcs\_06;$$

du1diLoa = du1diLoa\_06;

du2dvcs\_00 = ((toff\*vin - (vcs - vin)\*(toff - pi\*(Cr\*Lr)^(1/2)))\*(Lr\*(iLoa + iLob - ((vcs - vin)\*(pi - toff/(Cr\*Lr)^(1/2)))/(Lr/Cr)^(1/2)))/vcs^2 - (Lr\*(iLoa + iLob + (vcs\*(pi - toff/(Cr\*Lr)^(1/2)))/(Lr/Cr)^(1/2)))/(vcs - vin)^2 + (Lr\*(pi - toff/(Cr\*Lr)^(1/2)))/(vcs\*(Lr/Cr)^(1/2)) + (Lr\*(pi - toff/(Cr\*Lr)^(1/2)))/((Lr/Cr)^(1/2)\*(vcs - vin)))/(2\*toff - (Lr\*(iLoa + iLob + (vcs\*(pi - toff/(Cr\*Lr)^(1/2)))/(Lr/Cr)^(1/2)))/(vcs - vin) + (Lr\*(iLoa + iLob - ((vcs - vin)\*(pi - toff/(Cr\*Lr)^(1/2)))/(Lr/Cr)^(1/2)))/vcs^2 - (toff - pi\*(Cr\*Lr)^(1/2))/(2\*toff - (Lr\*(iLoa + iLob + (vcs\*(pi - toff/(Cr\*Lr)^(1/2)))/(Lr/Cr)^(1/2)))/(vcs - vin) + (Lr\*(iLoa + iLob - ((vcs - vin)\*(pi - toff/(Cr\*Lr)^(1/2)))/(Lr/Cr)^(1/2)))/vcs);

du2dvcs\_01 = subs(du2dvcs\_00,iLob,iLoa); % s-new = subs(s-old,old,new)

du2dvcs\_02 = subs(du2dvcs\_01,vcs,vin/2);

du2dvcs\_03 = subs(du2dvcs\_02,1/(Cr\*Lr)^(1/2),wr);

du2dvcs\_04 = subs(du2dvcs\_03,(Lr/Cr)^(1/2),Zr);

du2dvcs\_05 = subs(du2dvcs\_04,2\*iLoa,io);

du2dvcs\_06 = subs(du2dvcs\_05,ts\_05,Ts)

du2diLoa\_00 = -((toff\*vin - (vcs - vin)\*(toff - pi\*(Cr\*Lr)^(1/2)))\*(Lr/vcs - Lr/(vcs - vin)))/(2\*toff - (Lr\*(iLoa + iLob + (vcs\*(pi - toff/(Cr\*Lr)^(1/2)))/(Lr/Cr)^(1/2)))/(vcs - vin) + (Lr\*(iLoa + iLob - ((vcs - vin)\*(pi - toff/(Cr\*Lr)^(1/2)))/(Lr/Cr)^(1/2)))/vcs^2);

du2diLoa\_01 = subs(du2diLoa\_00,iLob,iLoa); % s-new = subs(s-old,old,new)

du2diLoa\_02 = subs(du2diLoa\_01,vcs,vin/2);

du2diLoa\_03 = subs(du2diLoa\_02,1/(Cr\*Lr)^(1/2),wr);

$$\text{du2diLoa\_04} = \text{subs}(\text{du2diLoa\_03}, (\text{Lr}/\text{Cr})^{1/2}, \text{Zr});$$

$$\text{du2diLoa\_05} = \text{subs}(\text{du2diLoa\_04}, 2 * \text{iLoa}, \text{io});$$

$$\text{du2diLoa\_06} = \text{subs}(\text{du2diLoa\_05}, \text{ts\_05}, \text{Ts})$$

$$\begin{aligned} \text{du2dvin\_00} = & (2 * \text{toff} - \text{pi} * (\text{Cr} * \text{Lr})^{1/2}) / (2 * \text{toff} - (\text{Lr} * (\text{iLoa} + \text{iLob} + (\text{vcs} * (\text{pi} - \\ & \text{toff} / (\text{Cr} * \text{Lr})^{1/2}))) / (\text{Lr} / \text{Cr})^{1/2})) / (\text{vcs} - \text{vin}) + (\text{Lr} * (\text{iLoa} + \text{iLob} - ((\text{vcs} - \text{vin}) * (\text{pi} - \\ & \text{toff} / (\text{Cr} * \text{Lr})^{1/2}))) / (\text{Lr} / \text{Cr})^{1/2})) / \text{vcs} + ((\text{toff} * \text{vin} - (\text{vcs} - \text{vin}) * (\text{toff} - \\ & \text{pi} * (\text{Cr} * \text{Lr})^{1/2})) * ((\text{Lr} * (\text{iLoa} + \text{iLob} + (\text{vcs} * (\text{pi} - \text{toff} / (\text{Cr} * \text{Lr})^{1/2}))) / (\text{Lr} / \text{Cr})^{1/2})) / (\text{vcs} - \\ & \text{vin})^2 - (\text{Lr} * (\text{pi} - \text{toff} / (\text{Cr} * \text{Lr})^{1/2})) / (\text{vcs} * (\text{Lr} / \text{Cr})^{1/2})) / (2 * \text{toff} - (\text{Lr} * (\text{iLoa} + \text{iLob} + (\text{vcs} * (\text{pi} \\ & - \text{toff} / (\text{Cr} * \text{Lr})^{1/2}))) / (\text{Lr} / \text{Cr})^{1/2})) / (\text{vcs} - \text{vin}) + (\text{Lr} * (\text{iLoa} + \text{iLob} - ((\text{vcs} - \text{vin}) * (\text{pi} - \\ & \text{toff} / (\text{Cr} * \text{Lr})^{1/2}))) / (\text{Lr} / \text{Cr})^{1/2})) / \text{vcs})^2; \end{aligned}$$

$$\text{du2dvin\_01} = \text{subs}(\text{du2dvin\_00}, \text{iLob}, \text{iLoa}); \quad \% \text{ s-new} = \text{subs}(\text{s-old}, \text{old}, \text{new})$$

$$\text{du2dvin\_02} = \text{subs}(\text{du2dvin\_01}, \text{vcs}, \text{vin}/2);$$

$$\text{du2dvin\_03} = \text{subs}(\text{du2dvin\_02}, 1 / (\text{Cr} * \text{Lr})^{1/2}, \text{wr});$$

$$\text{du2dvin\_04} = \text{subs}(\text{du2dvin\_03}, (\text{Lr}/\text{Cr})^{1/2}, \text{Zr});$$

$$\text{du2dvin\_05} = \text{subs}(\text{du2dvin\_04}, 2 * \text{iLoa}, \text{io});$$

$$\text{du2dvin\_06} = \text{subs}(\text{du2dvin\_05}, \text{ts\_05}, \text{Ts})$$

$$\begin{aligned} \text{du2dvin\_000} = & (\text{toff} - \text{sin}(\text{toff} / (\text{Cr} * \text{Lr})^{1/2}) * (\text{Cr} * \text{Lr})^{1/2}) / (2 * \text{toff} - (\text{Lr} * (\text{iLoa} + \text{iLob} + \\ & (\text{vcs} * \text{sin}(\text{toff} / (\text{Cr} * \text{Lr})^{1/2})) / (\text{Lr} / \text{Cr})^{1/2})) / (\text{vcs} - \text{vin}) + (\text{Lr} * (\text{iLoa} + \text{iLob} - \\ & (\text{sin}(\text{toff} / (\text{Cr} * \text{Lr})^{1/2}) * (\text{vcs} - \text{vin})) / (\text{Lr} / \text{Cr})^{1/2})) / \text{vcs} + (((\text{Lr} * (\text{iLoa} + \text{iLob} + \\ & (\text{vcs} * \text{sin}(\text{toff} / (\text{Cr} * \text{Lr})^{1/2})) / (\text{Lr} / \text{Cr})^{1/2})) / (\text{vcs} - \text{vin})^2 - \\ & (\text{Lr} * \text{sin}(\text{toff} / (\text{Cr} * \text{Lr})^{1/2})) / (\text{vcs} * (\text{Lr} / \text{Cr})^{1/2})) * (\text{toff} * \text{vin} + \text{sin}(\text{toff} / (\text{Cr} * \text{Lr})^{1/2}) * (\text{vcs} - \end{aligned}$$

$$\begin{aligned} & \text{vin}*(\text{Cr}*\text{Lr})^{(1/2)})/(2*\text{toff} - (\text{Lr}*(\text{iLoa} + \text{iLob} + \\ & (\text{vcs}*\sin(\text{toff}/(\text{Cr}*\text{Lr})^{(1/2)}))/(\text{Lr}/\text{Cr})^{(1/2)}))/(\text{vcs} - \text{vin}) + (\text{Lr}*(\text{iLoa} + \text{iLob} - \\ & (\sin(\text{toff}/(\text{Cr}*\text{Lr})^{(1/2)}))*(\text{vcs} - \text{vin}))/(\text{Lr}/\text{Cr})^{(1/2)}))/\text{vcs}^2; \end{aligned}$$

$$\text{du2dvin}_001 = \text{subs}(\text{du2dvin}_000, \text{iLob}, \text{iLoa}); \% \text{ s-new} = \text{subs}(\text{s-old}, \text{old}, \text{new})$$

$$\text{du2dvin}_002 = \text{subs}(\text{du2dvin}_001, \text{vcs}, \text{vin}/2);$$

$$\text{du2dvin}_003 = \text{subs}(\text{du2dvin}_002, 1/(\text{Cr}*\text{Lr})^{(1/2)}, \text{wr});$$

$$\text{du2dvin}_004 = \text{subs}(\text{du2dvin}_003, (\text{Lr}/\text{Cr})^{(1/2)}, \text{Zr});$$

$$\text{du2dvin}_005 = \text{subs}(\text{du2dvin}_004, 2*\text{iLoa}, \text{io});$$

$$\text{du2dvin}_006 = \text{subs}(\text{du2dvin}_005, \text{ts}_06, \text{Ts})$$

$$\begin{aligned} \text{du3dvcs}_00 = & (\sin(\text{toff}/(\text{Cr}*\text{Lr})^{(1/2)}))*(\text{Cr}*\text{Lr})^{(1/2)}/(2*\text{toff} - (\text{Lr}*(\text{iLoa} + \text{iLob} + \\ & (\text{vcs}*\sin(\text{toff}/(\text{Cr}*\text{Lr})^{(1/2)}))/(\text{Lr}/\text{Cr})^{(1/2)}))/(\text{vcs} - \text{vin}) + (\text{Lr}*(\text{iLoa} + \text{iLob} - \\ & (\sin(\text{toff}/(\text{Cr}*\text{Lr})^{(1/2)}))*(\text{vcs} - \text{vin}))/(\text{Lr}/\text{Cr})^{(1/2)}))/\text{vcs} - \\ & (\text{vcs}*\sin(\text{toff}/(\text{Cr}*\text{Lr})^{(1/2)}))*(\text{Cr}*\text{Lr})^{(1/2)}*((\text{Lr}*(\text{iLoa} + \text{iLob} - (\sin(\text{toff}/(\text{Cr}*\text{Lr})^{(1/2)}))*(\text{vcs} - \\ & \text{vin}))/(\text{Lr}/\text{Cr})^{(1/2)}))/\text{vcs}^2 - (\text{Lr}*(\text{iLoa} + \text{iLob} + (\text{vcs}*\sin(\text{toff}/(\text{Cr}*\text{Lr})^{(1/2)}))/(\text{Lr}/\text{Cr})^{(1/2)}))/(\text{vcs} \\ & - \text{vin})^2 + (\text{Lr}*\sin(\text{toff}/(\text{Cr}*\text{Lr})^{(1/2)}))/(\text{vcs}*(\text{Lr}/\text{Cr})^{(1/2)}) + \\ & (\text{Lr}*\sin(\text{toff}/(\text{Cr}*\text{Lr})^{(1/2)}))/((\text{Lr}/\text{Cr})^{(1/2)}*(\text{vcs} - \text{vin}))) / (2*\text{toff} - (\text{Lr}*(\text{iLoa} + \text{iLob} + \\ & (\text{vcs}*\sin(\text{toff}/(\text{Cr}*\text{Lr})^{(1/2)}))/(\text{Lr}/\text{Cr})^{(1/2)}))/(\text{vcs} - \text{vin}) + (\text{Lr}*(\text{iLoa} + \text{iLob} - \\ & (\sin(\text{toff}/(\text{Cr}*\text{Lr})^{(1/2)}))*(\text{vcs} - \text{vin}))/(\text{Lr}/\text{Cr})^{(1/2)}))/\text{vcs}^2; \end{aligned}$$

$$\text{du3dvcs}_01 = \text{subs}(\text{du3dvcs}_00, \text{iLob}, \text{iLoa}); \% \text{ s-new} = \text{subs}(\text{s-old}, \text{old}, \text{new})$$

$$\text{du3dvcs}_02 = \text{subs}(\text{du3dvcs}_01, \text{vcs}, \text{vin}/2);$$

$$\text{du3dvcs}_03 = \text{subs}(\text{du3dvcs}_02, 1/(\text{Cr}*\text{Lr})^{(1/2)}, \text{wr});$$

$$\text{du3dvcs}_04 = \text{subs}(\text{du3dvcs}_03, (\text{Lr}/\text{Cr})^{(1/2)}, \text{Zr});$$

du3dvcs\_05 = subs(du3dvcs\_04,2\*iLoa,io);

du3dvcs\_06 = subs(du3dvcs\_05,ts\_06,Ts)

du3diLoa\_00 =(vcs\*sin(toff/(Cr\*Lr)^(1/2))\*(Lr/vcs - Lr/(vcs - vin))\*(Cr\*Lr)^(1/2))/(2\*toff -  
(Lr\*(iLoa + iLob + (vcs\*sin(toff/(Cr\*Lr)^(1/2)))/(Lr/Cr)^(1/2)))/(vcs - vin) + (Lr\*(iLoa + iLob -  
(sin(toff/(Cr\*Lr)^(1/2))\*(vcs - vin))/(Lr/Cr)^(1/2)))/vcs)^2;

du3diLoa\_01 = subs(du3diLoa\_00,iLob,iLoa); % s-new = subs(s-old,old,new)

du3diLoa\_02 = subs(du3diLoa\_01,vcs,vin/2);

du3diLoa\_03 = subs(du3diLoa\_02,1/(Cr\*Lr)^(1/2),wr);

du3diLoa\_04 = subs(du3diLoa\_03,(Lr/Cr)^(1/2),Zr);

du3diLoa\_05 = subs(du3diLoa\_04,2\*iLoa,io);

du3diLoa\_06 = subs(du3diLoa\_05,ts\_06,Ts)

du3dvin\_00 =-(vcs\*sin(toff/(Cr\*Lr)^(1/2))\*((Lr\*(iLoa + iLob +  
(vcs\*sin(toff/(Cr\*Lr)^(1/2)))/(Lr/Cr)^(1/2)))/(vcs - vin)^2 -  
(Lr\*sin(toff/(Cr\*Lr)^(1/2)))/(vcs\*(Lr/Cr)^(1/2)))\*(Cr\*Lr)^(1/2))/(2\*toff - (Lr\*(iLoa + iLob +  
(vcs\*sin(toff/(Cr\*Lr)^(1/2)))/(Lr/Cr)^(1/2)))/(vcs - vin) + (Lr\*(iLoa + iLob -  
(sin(toff/(Cr\*Lr)^(1/2))\*(vcs - vin))/(Lr/Cr)^(1/2)))/vcs)^2;

du3dvin\_01 = subs(du3dvin\_00,iLob,iLoa); % s-new = subs(s-old,old,new)

du3dvin\_02 = subs(du3dvin\_01,vcs,vin/2);

du3dvin\_03 = subs(du3dvin\_02,1/(Cr\*Lr)^(1/2),wr);

du3dvin\_04 = subs(du3dvin\_03,(Lr/Cr)^(1/2),Zr);

du3dvin\_05 = subs(du3dvin\_04,2\*iLoa,io);

du3dvin\_06 = subs(du3dvin\_05,ts\_06,Ts)

dpdiLoa\_00 = -(toff\*(Lr/vcs - Lr/(vcs - vin)))/(2\*toff - (Lr\*(iLoa + iLob +  
(vcs\*sin(toff/(Cr\*Lr)^(1/2)))/(Lr/Cr)^(1/2)))/(vcs - vin) + (Lr\*(iLoa + iLob -  
(sin(toff/(Cr\*Lr)^(1/2))\*(vcs - vin))/(Lr/Cr)^(1/2)))/vcs)^2;

dpdiLoa\_01 = subs(dpdiLoa\_00,iLob,iLoa); % s-new = subs(s-old,old,new)

dpdiLoa\_02 = subs(dpdiLoa\_01,vcs,vin/2);

dpdiLoa\_03 = subs(dpdiLoa\_02,1/(Cr\*Lr)^(1/2),wr);

dpdiLoa\_04 = subs(dpdiLoa\_03,(Lr/Cr)^(1/2),Zr);

dpdiLoa\_05 = subs(dpdiLoa\_04,2\*iLoa,io);

dpdiLoa\_06 = subs(dpdiLoa\_05,ts\_06,Ts)

dpdvin\_00 = (toff\*((Lr\*(iLoa + iLob + (vcs\*sin(toff/(Cr\*Lr)^(1/2)))/(Lr/Cr)^(1/2)))/(vcs -  
vin)^2 - (Lr\*sin(toff/(Cr\*Lr)^(1/2)))/(vcs\*(Lr/Cr)^(1/2)))/(2\*toff - (Lr\*(iLoa + iLob +  
(vcs\*sin(toff/(Cr\*Lr)^(1/2)))/(Lr/Cr)^(1/2)))/(vcs - vin) + (Lr\*(iLoa + iLob -  
(sin(toff/(Cr\*Lr)^(1/2))\*(vcs - vin))/(Lr/Cr)^(1/2)))/vcs)^2;

dpdvin\_01 = subs(dpdvin\_00,iLob,iLoa); % s-new = subs(s-old,old,new)

dpdvin\_02 = subs(dpdvin\_01,vcs,vin/2);

dpdvin\_03 = subs(dpdvin\_02,1/(Cr\*Lr)^(1/2),wr);

dpdvin\_04 = subs(dpdvin\_03,(Lr/Cr)^(1/2),Zr);

dpdvin\_05 = subs(dpdvin\_04,2\*iLoa,io);

dpdvin\_06 = subs(dpdvin\_05,ts\_06,Ts)

toc

% The END

## H. Calculation of Transfer Functions

The detailed derivation of (3-22) is shown below. The following equation is derived by combing the three matrices on the right of the equations and then grouping them by the small-signal state variables,  $\hat{v}_{in}$ , and  $\hat{t}_{off}$ . The new equation is shown below

$$\begin{bmatrix} C_s & 0 & 0 \\ 0 & L_o & 0 \\ 0 & 0 & L_o \end{bmatrix} \begin{bmatrix} \frac{d\hat{v}_{Cs}}{dt} \\ \frac{d\hat{i}_{Loa}}{dt} \\ \frac{d\hat{i}_{Lob}}{dt} \end{bmatrix} = \begin{bmatrix} -2\frac{\partial u_1}{\partial v_{in}} & \frac{T_{off}}{T_s} + \frac{\partial u_1}{\partial i_{Loa}} & -\frac{T_{off}}{T_s} - \frac{\partial u_1}{\partial i_{Loa}} \\ -\frac{T_{off}}{T_s} + \frac{\partial u_2}{\partial v_{Cs}} & -R_{Lo} + \frac{\partial u_2}{\partial i_{Loa}} - \frac{\partial \frac{t_{off}}{T_s}}{\partial i_{Loa}} V_{Cs} & \frac{\partial u_2}{\partial i_{Loa}} - \frac{\partial \frac{t_{off}}{T_s}}{\partial i_{Loa}} V_{Cs} \\ \frac{T_{off}}{T_s} - \frac{\partial u_2}{\partial v_{Cs}} & \frac{\partial u_3}{\partial i_{Loa}} + \frac{\partial \frac{t_{off}}{T_s}}{\partial i_{Loa}} V_{Cs} & -R_{Lo} + \frac{\partial u_3}{\partial i_{Loa}} + \frac{\partial \frac{t_{off}}{T_s}}{\partial i_{Loa}} V_{Cs} \end{bmatrix} \quad (xxv)$$

$$\begin{bmatrix} \hat{v}_{Cs} \\ \hat{i}_{Loa} \\ \hat{i}_{Lob} \end{bmatrix} + \begin{bmatrix} \frac{\partial u_1}{\partial v_{in}} \\ \frac{\partial u_2}{\partial v_{in}} - \frac{\partial \frac{t_{off}}{T_s}}{\partial v_{in}} V_{Cs} \\ \frac{\partial u_3}{\partial v_{in}} + \frac{\partial \frac{t_{off}}{T_s}}{\partial v_{in}} V_{Cs} \end{bmatrix} \hat{v}_{in} + \begin{bmatrix} 0 \\ \frac{\partial u_2}{\partial t_{off}} - \frac{\partial \frac{t_{off}}{T_s}}{\partial t_{off}} V_{Cs} \\ \frac{\partial u_3}{\partial t_{off}} + \frac{\partial \frac{t_{off}}{T_s}}{\partial t_{off}} V_{Cs} \end{bmatrix} \hat{t}_{off}$$

There are multiple terms for each element in the matrix and the vectors in the equation above.

The equation is reorganized by assigning new variables to each element

$$\begin{aligned}
& \begin{bmatrix} C_s & 0 & 0 \\ 0 & L_o & 0 \\ 0 & 0 & L_o \end{bmatrix} \begin{bmatrix} \frac{d\hat{v}_{Cs}}{dt} \\ \frac{d\hat{i}_{Loa}}{dt} \\ \frac{d\hat{i}_{Lob}}{dt} \end{bmatrix} \\
& = \begin{bmatrix} -2H_1 & \beta_{Cs} & -\beta_{Cs} \\ -\beta_{Lo} & -R_{Los} & -R_i \\ \beta_{Lo} & -R_i & -R_{Los} \end{bmatrix} \begin{bmatrix} \hat{v}_{Cs} \\ \hat{i}_{Loa} \\ \hat{i}_{Lob} \end{bmatrix} + \begin{bmatrix} H_{11} \\ H_{12} \\ H_{13} \end{bmatrix} \hat{v}_{in} + \begin{bmatrix} H_{21} \\ H_{22} \\ H_{23} \end{bmatrix} \hat{t}_{off} \\
& \beta_{Cs} = \frac{T_{off}}{T_s} + \frac{\partial u_1}{\partial i_{Loa}} \\
& \beta_{Lo} = \frac{T_{off}}{T_s} - \frac{\partial u_2}{\partial v_{Cs}} \\
& R_{Los} = R_{Lo} - \frac{\partial u_2}{\partial i_{Loa}} + \frac{\partial \frac{t_{off}}{T_s}}{\partial i_{Loa}} V_{Cs} \\
& R_i = -\frac{\partial u_2}{\partial i_{Loa}} + \frac{\partial \frac{t_{off}}{T_s}}{\partial i_{Loa}} V_{Cs} \\
& H_{11} = \frac{\partial u_1}{\partial v_{in}} \\
& H_{12} = \frac{\partial u_2}{\partial v_{in}} - \frac{\partial \frac{t_{off}}{T_s}}{\partial v_{in}} V_{Cs} \\
& H_{13} = \frac{\partial u_3}{\partial t_{off}} + \frac{\partial \frac{t_{off}}{T_s}}{\partial t_{off}} V_{Cs} \\
& H_{21} = 0 \\
& H_{22} = \frac{\partial u_2}{\partial t_{off}} - \frac{\partial \frac{t_{off}}{T_s}}{\partial t_{off}} V_{Cs}
\end{aligned} \tag{xxvi}$$

$$H_{23} = \frac{\partial u_3}{\partial t_{off}} + \frac{\partial \frac{t_{off}}{T_s}}{\partial t_{off}} V_{Cs}$$

All the partial derivatives are calculating when (3-19) is derived in Appendix on page 202.

The calculated results are shown in (3-22).

The equation is reorganized as

$$\begin{bmatrix} \frac{C_s}{\beta_{Cs}} & 0 & 0 \\ 0 & \frac{L_o}{\beta_{Lo}} & 0 \\ 0 & 0 & \frac{L_o}{\beta_{Lo}} \end{bmatrix} \begin{bmatrix} \frac{d\hat{v}_{Cs}}{dt} \\ \frac{d\hat{i}_{Loa}}{dt} \\ \frac{d\hat{i}_{Lob}}{dt} \end{bmatrix} = \begin{bmatrix} -\frac{2H_1}{\beta_{Cs}} & 1 & -1 \\ -1 & -\frac{R_{Los}}{\beta_{Lo}} & -\frac{R_i}{\beta_{Lo}} \\ 1 & -\frac{R_i}{\beta_{Lo}} & -\frac{R_{Los}}{\beta_{Lo}} \end{bmatrix} \begin{bmatrix} \hat{v}_{Cs} \\ \hat{i}_{Loa} \\ \hat{i}_{Lob} \end{bmatrix} + \begin{bmatrix} \frac{H_{11}}{\beta_{Cs}} \\ \frac{H_{12}}{\beta_{Lo}} \\ \frac{H_{13}}{\beta_{Lo}} \end{bmatrix} \hat{v}_{in} + \begin{bmatrix} \frac{H_{21}}{\beta_{Cs}} \\ \frac{H_{22}}{\beta_{Lo}} \\ \frac{H_{23}}{\beta_{Lo}} \end{bmatrix} \hat{t}_{off} \quad (xxvii)$$

The detailed derivation of (3-31) is shown below.

The large signal equation is from (3-4). The terms associated with  $v_{Cs}$  are removed. The terms associated with  $i_{Loa}$  and  $i_{Lob}$  are combined as  $i_{Loa} + i_{Lob}$ . The large-signal response of  $v_{Co}$  is

$$K \frac{L_o}{2} \frac{di_{Lo}}{dt} = -\frac{R_{Lo}}{2} i_{Lo} - v_{Co} + \frac{v_{in}}{2} \frac{2t_{off} - \frac{\pi}{w_r}}{T_s(i_{Lo}, v_{in}, t_{off})} \quad (xxviii)$$

$$C_o \frac{dv_{Co}}{dt} = i_{Lo} - \frac{1}{R_{load}} v_{Co}$$

where

$$T_s(I_{Lo}, V_{in}, T_{off}) = 2T_{off} + 4 \frac{L_r}{V_{in}} \left( I_{Lo} + \frac{V_{in}}{2Z_r} (\pi - w_r T_{off}) \right) \quad (xxix)$$

The state-space equation for the response of  $v_{Co}$  is shown below

$$K\dot{x} = \left\{ \sum_{i=1}^k d_i A_i \right\} x + U$$

$$x(t) = \begin{bmatrix} i_{Lo}(t) \\ v_{Co}(t) \end{bmatrix}, \dot{x}(t) = \frac{dx(t)}{dt}, K = \begin{bmatrix} L_o/2 & 0 \\ 0 & C_o \end{bmatrix},$$

$$A_1 = A_4 = A_5 = A_8 = \begin{bmatrix} -1 & -R_{Lo}/2 \\ -1/R_{load} & 1 \end{bmatrix}, A_2 = A_3 = A_6 = A_7 = 0, \quad (\text{xxx})$$

$$U = \frac{1}{T_s} \sum_{i=1}^k \int_{t_{i-1}}^{t_i} B_i(\lambda) d\lambda = \begin{bmatrix} u_1 \\ u_2 \end{bmatrix} = \begin{bmatrix} v_{in} \frac{2t_{off} - \frac{\pi}{w_r}}{2 T_s(i_{Lo}, v_{in}, t_{off})} \\ 0 \end{bmatrix}$$

The small-signal state-space equation for the response of  $\hat{v}_{Co}$  is shown below

$$K \frac{d\hat{x}}{dt} = \left\{ \sum_{i=1}^k \hat{d}_i A_i \right\} X + \left\{ \sum_{i=1}^k D_i A_i \right\} \hat{x} + \hat{u}$$

$$K = \begin{bmatrix} L_o/2 & 0 \\ 0 & C_o \end{bmatrix}, \frac{d\hat{x}}{dt} = \begin{bmatrix} \frac{d\hat{i}_{Lo}}{dt} \\ \frac{d\hat{v}_{Co}}{dt} \end{bmatrix}, X = \begin{bmatrix} I_{Lo} \\ V_{Co} \end{bmatrix}, \hat{x} = \begin{bmatrix} \hat{i}_{Lo} \\ \hat{v}_{Co} \end{bmatrix},$$

$$\sum_{i=1}^k \hat{d}_i A_i = 0, \sum_{i=1}^k D_i A_i = \begin{bmatrix} -\frac{R_{Lo}}{2} & -1 \\ 1 & -\frac{1}{R_{load}} \end{bmatrix}, \quad (\text{xxxi})$$

$$\hat{u} = \begin{bmatrix} \frac{\partial u_1}{\partial i_{Lo}} \hat{i}_{Lo} + \frac{\partial u_1}{\partial v_{in}} \hat{v}_{in} + \frac{\partial u_1}{\partial t_{off}} \hat{t}_{off} \\ \hat{i}_p \end{bmatrix}$$

$$= \begin{bmatrix} \frac{v_{in}}{2} \frac{2t_{off} - \frac{\pi}{w_r}}{2t_{off} + 4 \frac{L_r}{v_{in}} \left( i_{Lo} + \frac{v_{in}}{2Z_r} (\pi - w_r t_{off}) \right)} \\ 0 \end{bmatrix}$$

$$= \begin{bmatrix} v_{in} M(t_{off}, i_{Lo}, v_{in}) \\ 0 \end{bmatrix}$$

$$M(t_{off}, i_{Lo}, v_{in}) = \frac{1}{2} \frac{2t_{off} - \frac{\pi}{w_r}}{T_s(t_{off}, i_{Lo}, v_{in})}$$

$$\hat{u} = \begin{bmatrix} \frac{\partial u_1}{\partial i_{Lo}} \hat{i}_{Lo} + \frac{\partial u_1}{\partial v_{in}} \hat{v}_{in} + \frac{\partial u_1}{\partial t_{off}} \hat{t}_{off} \\ 0 \end{bmatrix}$$

where

$$\begin{aligned} \frac{\partial u_1}{\partial i_{Lo}} &= \frac{v_{in}}{2} (2t_{off} - \frac{\pi}{w_r}) \frac{-4 \frac{L_r}{v_{in}}}{(2t_{off} + 4 \frac{L_r}{v_{in}} (i_{Lo} + \frac{v_{in}}{2Z_r} (\pi - w_r t_{off})))^2} \\ &= \frac{-2L_r (2t_{off} - \frac{\pi}{w_r})}{\left(2t_{off} + 4 \frac{L_r}{v_{in}} (i_{Lo} + \frac{v_{in}}{2Z_r} (\pi - w_r t_{off}))\right)^2} \\ &= \frac{-2L_r (2t_{off} - \frac{\pi}{w_r})}{T_s^2} \tag{xxxii} \\ &= -\frac{4L_r M}{T_s} \\ &= -\frac{4w_r L_r M}{w_r T_s} \\ &= -\frac{4Z_r M}{w_r T_s} \\ &= -\frac{4Z_r M}{2\pi \frac{f_r}{f_s}} \end{aligned}$$

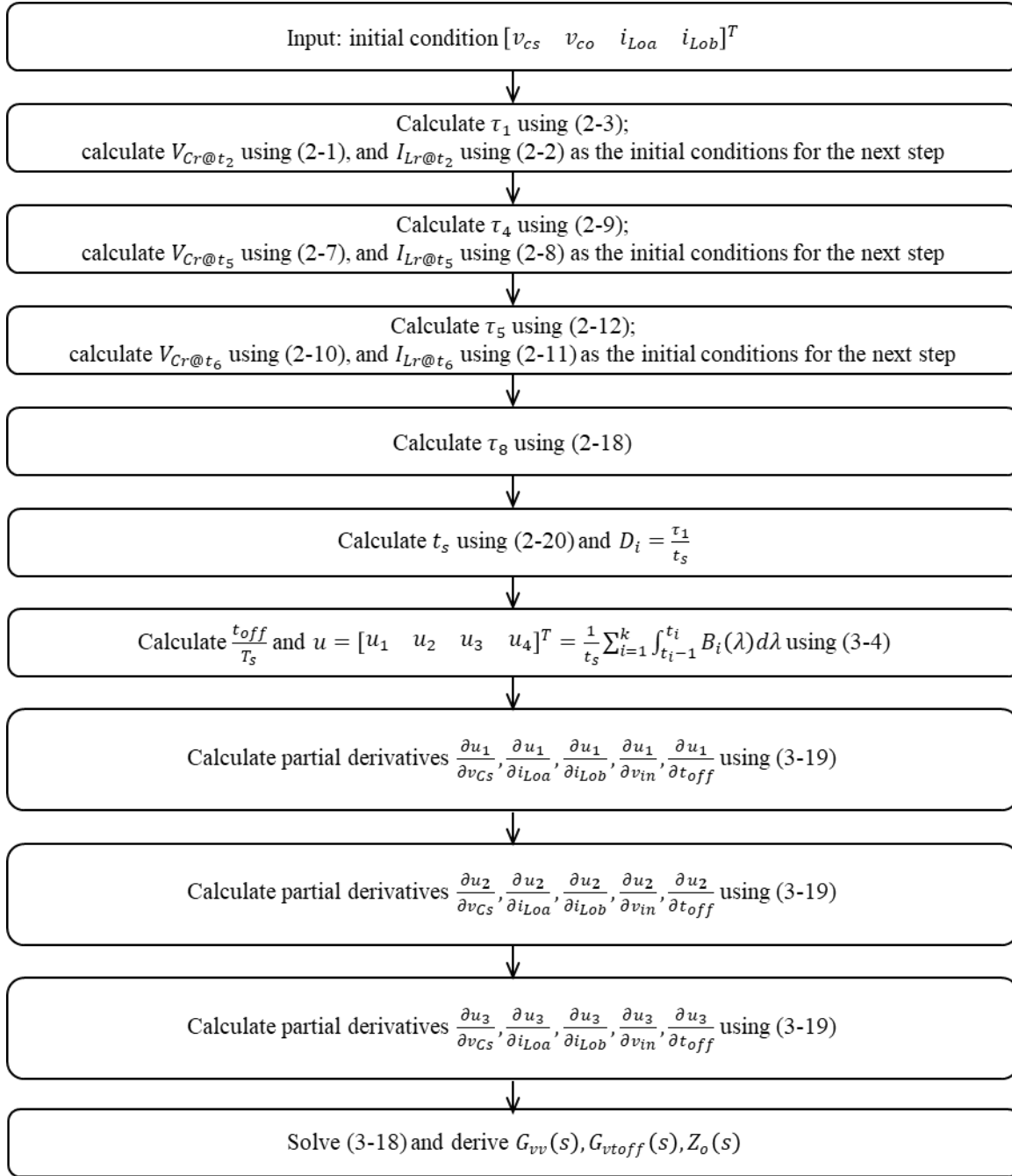
$$= -\frac{2 f_s}{\pi f_r} M Z_r$$

$$\begin{aligned} \frac{\partial u_1}{\partial v_{in}} &= \frac{1}{2} \frac{2t_{\text{off}} - \frac{\pi}{w_r}}{2t_{\text{off}} + 4 \frac{L_r}{v_{in}} \left( i_{L_o} + \frac{v_{in}}{2Z_r} (\pi - w_r t_{\text{off}}) \right)} + \frac{v_{in}}{2} \sigma \\ &= \frac{1}{2} \frac{2t_{\text{off}} - \frac{\pi}{w_r}}{T_s} + \frac{v_{in}}{2} \sigma = \frac{1}{2} \frac{2t_{\text{off}} - \frac{\pi}{w_r}}{T_s} + \frac{v_{in}}{2} \frac{-(2t_{\text{off}} - \frac{\pi}{w_r}) \frac{\partial T_s}{\partial v_{in}}}{T_s^2} \\ &= \frac{1}{2} \frac{2t_{\text{off}} - \frac{\pi}{w_r}}{T_s} + \frac{v_{in}}{2} \frac{\left( 2t_{\text{off}} - \frac{\pi}{w_r} \right) \frac{4L_r i_{L_o}}{v_{in}^2}}{T_s^2} \\ &= \frac{1}{2} \frac{2t_{\text{off}} - \frac{\pi}{w_r}}{T_s} + \frac{1}{2} \frac{\left( 2t_{\text{off}} - \frac{\pi}{w_r} \right) \frac{4L_r i_{L_o}}{v_{in}}}{T_s^2} \\ &= \frac{2t_{\text{off}} - \frac{\pi}{w_r}}{2} \left( \frac{1}{T_s} + \frac{\frac{4L_r i_{L_o}}{v_{in}}}{T_s^2} \right) \\ &= \frac{1}{2} \left( 2t_{\text{off}} - \frac{\pi}{w_r} \right) \left( \frac{1}{T_s} + \frac{\frac{4L_r i_{L_o}}{v_{in}}}{T_s^2} \right) \\ &= \left( \frac{1}{2} \frac{\left( 2t_{\text{off}} - \frac{\pi}{w_r} \right)}{T_s} + \frac{1}{2} \frac{\left( 2t_{\text{off}} - \frac{\pi}{w_r} \right) \frac{4L_r i_{L_o}}{v_{in}}}{T_s} \right) \\ &= M + M \frac{4L_r i_{L_o}}{v_{in} T_s} \end{aligned}$$

Based on the small-signal equivalent circuit in (3-19), the terms associated with  $v_{cs}$  are removed. The derivation of the transfer functions in (3-32), (3-38), and (3-41) using Matlab is

shown.

The flowchart of the code is shown below.



The Matlab code for the flowchart is shown below.

```
% ----- Clear Data _ start -----%
```

```

close all;clc; clear all; tic;

% set(0,'defaultFigureWindowStyle','docked');

% tt1=clock;

format compact

% ----- Clear Data _ END -----%

%% Color

C01=[1.0 0.0 0.0]; % red
C02=[1.0 0.5 0.0]; % dark orange
C03=[0.0 0.5 0.0]; % green
C04=[0.0 0.7 1.0]; % deep sky blue
C05=[0.0 0.0 1.0]; % blue
C06=[0.6 0.0 0.8]; % dark violet
C07=[1.0 0.0 1.0]; % magenta
C08=[0.8 0.4 0.1]; % chocolate
C09=[0.0 0.0 0.0]; % black
C10=[0.4 0.4 0.4]; % dim gray

c=[C01;C02;C03;C04;C05;C06;C07;C08;C09;C10];

%% My model with Req

% normalized variables

```

```
wr=sym('wr');  
Zr=sym('Zr');  
io=sym('io');  
j=sym('j');  
fsfr=sym('fsfr');  
  
% management diff perturbation  
EN_vinhat=1;  
EN_toffhat=0;  
EN_iohat=0;  
  
% component  
Rload=sym('Rload');  
Cs=sym('Cs');  
Lo=sym('Lo');  
RLo=sym('RLo');  
  
% large signal  
vin=sym('vin');  
toff=sym('toff');  
vcs=sym('vcs');  
iLoa=sym('iLoa');  
iLob=sym('iLob');
```

```

% small signal hat

s=sym('s');

vcshat=sym('vcshat');

iLoahat=sym('iLoahat');

iLobhat=sym('iLobhat');

vinhat=sym('vinhat');

% % symbolic combination

%  $w_r=1/\sqrt{L_r*C_r}$ ;

%  $Z_r=\sqrt{L_r/C_r}$ ;

%  $w_{r3}=1/\sqrt{L_r*(C_s+C_r)}$ ;

%  $Z_{r3}=\sqrt{L_r/(C_s+C_r)}$ ;

%% symbolic group

%  $T_s=\text{sym}('T_s')$ ;

%  $p=\text{sym}('p')$ ;

%

%  $\text{dpdvin}=\text{sym}('dpdvin')$ ;

%  $\text{dpdvcs}=\text{sym}('dpdvcs')$ ;

%  $\text{dpdiLoa}=\text{sym}('dpdiLoa')$ ;

%  $\text{dpdiLob}=\text{sym}('dpdiLob')$ ;

%

```

```

% du1dvin=sym('du1dvin');
% du1dvcs=sym('du1dvcs');
% du1diLoa=sym('du1diLoa');
% du1diLob=sym('du1diLob');
%
% du2dvin=sym('du2dvin');
% du2dvcs=sym('du2dvcs');
% du2diLoa=sym('du2diLoa');
% du2diLob=sym('du2diLob');
%
% du3dvin=sym('du3dvin');
% du3dvcs=sym('du3dvcs');
% du3diLoa=sym('du3diLoa');
% du3diLob=sym('du3diLob');

%% some normalized term
Ts=2/wr*(wr*toff+sin(wr*toff)+2*j);

p=toff/Ts;
dpdvin=(fsfr/pi)^2*(wr*toff)*j/vin;
dpdvcs=0;
dpdiLoa=-(fsfr/pi)^2*(wr*toff)*Zr/vin;
dpdiLob=dpdiLoa;

```

du1dvin =fsfr\*sin(wr\*toff)/pi/Zr\*(0.75\*sin(wr\*toff)+j);

du1dvcs =-2\*du1dvin;

du1diLoa=fsfr/2/pi\*(2\*j+sin(wr\*toff));

du1diLob=-du1diLoa;

du2dvin =fsfr/2/pi\*(wr\*toff -sin(wr\*toff)) + (fsfr/2/pi)^2\*(4\*j\*(wr\*toff-1/2\*sin(wr\*toff)));

du2dvcs =sin(toff\*wr)/(Ts\*wr)

du2diLoa=Zr\*(fsfr/pi)^2\*(0.5\*sin(wr\*toff)-wr\*toff);

du2diLob=du2diLoa;

du3dvin =-(fsfr/2/pi)^2\*sin(toff\*wr)\*2\*j;

du3dvcs =-du2dvcs;

du3diLoa=(fsfr/pi)^2\*Zr\*sin(toff\*wr)/2;

du3diLob=du3diLoa;

dp= dpdvcs\*vcshat +dpdiLoa\*iLoahat +dpdiLob\*iLobhat +dpdvin\*vinhat;

du1=du1dvcs\*vcshat+du1diLoa\*iLoahat+du1diLob\*iLobhat+du1dvin\*vinhat;

du2=du2dvcs\*vcshat+du2diLoa\*iLoahat+du2diLob\*iLobhat+du2dvin\*vinhat;

du3=du3dvcs\*vcshat+du3diLoa\*iLoahat+du3diLob\*iLobhat+du3dvin\*vinhat;

%% matrices

K= [

Cs 0 0;

0 Lo 0;

0 0 Lo

];

xhatdot= [

s\*vcshat;

s\*iLoahat;

s\*iLobhat

];

dhatA= [

0 dp -dp;

-dp 0 0;

dp 0 0

];

X0=[vcs;iLoa;iLob];

DA= [

0 p -p;

-p -RLo 0;

p 0 -RLo

];

xhat= [

  vcshat;

  iLoahat;

  iLobhat

];

uhat=[du1;du2;du3];

%% reorganize state space for equivalent circuit

K2= [

  Cs 0 0;

  0 Lo 0;

  0 0 Lo

];

A2= [

  -2\*du1dvin  p+du1diLoa      -(p+du1diLoa);

  -(p-du2dvcs)  -RLo+du2diLoa-dpdiLoa\*vcs  du2diLoa-dpdiLoa\*vcs;

  p-du2dvcs  du3diLoa+dpdiLoa\*vcs      -RLo+du3diLoa+dpdiLoa\*vcs

];

```

uhat2= [
    du1dvin;
    du2dvin-dpdvin*vcs;
    du3dvin+dpdvin*vcs
];

%% equations

% % small signal state equation (origin)
% eq = K*xhatdot==dhatA*X0+DA*xhat+uhat;
% [s1,s2,s3] = solve(eq,xhat); %

% small signal state equation (reorganize for equivalent circuit)
eq2 = K*xhatdot==A2*xhat+uhat2*vinhat;
[s1,s2,s3] = solve(eq2,xhat); %

% % small signal state equation (set s=0 for dc gain)
% eq3 = K*xhatdot*0==A2*xhat+uhat2*vinhat;
% [s1,s2,s3] = solve(eq3,xhat); %

%% transfer function

% Gvin2deliLo

```

Gvin2deliLo=(s2-s3)/vinhat;

%% The end

toc

The solutions provided by the Matlab need to be simplified into a shorter term. The equations are normalized to offer more insights into converter design. The detailed derivation of the quality factor Q in (3-33) is

$$\begin{aligned}
 Q &= \frac{\left(R_{Lo} + 2R_{load} - 2\frac{\partial u_1}{\partial i_{Lo}}\right) \sqrt{\frac{C_o L_o R_{load}}{R_{Lo} + 2R_{load} - 2\frac{\partial u_1}{\partial i_{Lo}}}}}{L_o + C_o R_{Lo} R_{load} - 2C_o R_{load} \frac{\partial u_1}{\partial i_{Lo}}} \\
 &= \frac{\left(R_{Lo} + 2R_{load} + \frac{8L_r M}{T_s}\right) \sqrt{\frac{C_o L_o R_{load}}{R_{Lo} + 2R_{load} + \frac{8L_r M}{T_s}}}}{L_o + C_o R_{Lo} R_{load} + 2C_o R_{load} \frac{8L_r M}{T_s}} \\
 &= \frac{\left(R_{load} + \frac{R_{Lo}}{2} + \frac{4L_r M}{T_s}\right) \sqrt{\frac{C_o \frac{L_o}{2} R_{load}}{R_{load} + \frac{R_{Lo}}{2} + \frac{4L_r M}{T_s}}}}{\frac{L_o}{2} + C_o R_{load} \frac{R_{Lo}}{2} + C_o R_{load} \frac{4L_r M}{T_s}} \tag{xxxiii} \\
 &= \frac{R_{load} \left(1 + \frac{R_{Lo}}{2R_{load}} + \frac{4Z_r I_o V_o}{w_r T_s V_o V_{in}}\right) \sqrt{\frac{C_o \frac{L_o}{2} R_{load}}{R_{load} + \frac{R_{Lo}}{2} + \frac{4L_r M}{T_s}}}}{\frac{L_o}{2} + C_o R_{load} \frac{R_{Lo}}{2} + C_o R_{load} \frac{4L_r M}{T_s}}
 \end{aligned}$$

$$\begin{aligned}
& R_{load} \left( 1 + \frac{R_{Lo}}{2R_{load}} + \frac{2f_s J}{\pi f_r} \right) \sqrt{\frac{C_o \frac{L_o}{2} R_{load}}{R_{load} + \frac{R_{Lo}}{2} + \frac{4L_r M}{T_s}}} \\
= & \frac{R_{load} \left( 1 + \frac{R_{Lo}}{2R_{load}} + \frac{2f_s J}{\pi f_r} \right) \sqrt{\frac{C_o \frac{L_o}{2} R_{load}}{R_{load} + \frac{R_{Lo}}{2} + \frac{4L_r M}{T_s}}}}{\frac{L_o}{2} + C_o R_{load} \frac{R_{Lo}}{2} + C_o R_{load} \frac{4L_r M}{T_s}} \\
& R_{load} \left( 1 + \frac{R_{Lo}}{2R_{load}} + \frac{1}{\frac{\pi}{2J} \frac{1}{\pi} + 1} \right) \sqrt{\frac{C_o \frac{L_o}{2} R_{load}}{R_{load} + \frac{R_{Lo}}{2} + \frac{4L_r M}{T_s}}} \\
= & \frac{R_{load} \left( 1 + \frac{R_{Lo}}{2R_{load}} + \frac{1}{\frac{\pi}{2J} \frac{1}{\pi} + 1} \right) \sqrt{\frac{C_o \frac{L_o}{2} R_{load}}{R_{load} + \frac{R_{Lo}}{2} + \frac{4L_r M}{T_s}}}}{\frac{L_o}{2} + C_o R_{load} \frac{R_{Lo}}{2} + C_o R_{load} \frac{4L_r M}{T_s}} \\
& R_{load} \left( 1 + \frac{R_{Lo}}{2R_{load}} + \frac{1}{1 + \frac{\pi}{2J}} \right) \sqrt{\frac{C_o \frac{L_o}{2} R_{load}}{R_{load} + \frac{R_{Lo}}{2} + \frac{4L_r M}{T_s}}} \\
= & \frac{R_{load} \left( 1 + \frac{R_{Lo}}{2R_{load}} + \frac{1}{1 + \frac{\pi}{2J}} \right) \sqrt{\frac{C_o \frac{L_o}{2} R_{load}}{R_{load} + \frac{R_{Lo}}{2} + \frac{4L_r M}{T_s}}}}{\frac{L_o}{2} + C_o R_{load} \frac{R_{Lo}}{2} + C_o R_{load} \frac{4L_r M}{T_s}} \\
& \sqrt{\frac{C_o \frac{L_o}{2} \left( 1 + \frac{R_{Lo}}{2R_{load}} + \frac{1}{1 + \frac{\pi}{2J}} \right)}{\frac{L_o}{2} + C_o R_{load} \frac{R_{Lo}}{2} + C_o R_{load} \frac{4L_r M}{T_s}}} \\
= & R_{load} \frac{\sqrt{\frac{C_o \frac{L_o}{2} \left( 1 + \frac{R_{Lo}}{2R_{load}} + \frac{1}{1 + \frac{\pi}{2J}} \right)}{\frac{L_o}{2} + C_o R_{load} \frac{R_{Lo}}{2} + C_o R_{load} \frac{4L_r M}{T_s}}}}{\frac{L_o}{2} + C_o R_{load} \frac{R_{Lo}}{2} + C_o R_{load} \frac{4L_r M}{T_s}} \\
& \sqrt{\frac{C_o \frac{L_o}{2} \left( 1 + \frac{R_{Lo}}{2R_{load}} + \frac{1}{1 + \frac{\pi}{2J}} \right)}{\frac{L_o}{2} + C_o R_{load} \frac{R_{Lo}}{2} + C_o R_{load} \frac{4L_r M}{T_s}}} \\
= & R_{load} \frac{\sqrt{\frac{C_o \frac{L_o}{2} \left( 1 + \frac{R_{Lo}}{2R_{load}} + \frac{1}{1 + \frac{\pi}{2J}} \right)}{\frac{L_o}{2} + C_o R_{load} \frac{R_{Lo}}{2} + C_o R_{load} \frac{4L_r M}{T_s}}}}{\frac{L_o}{2} + C_o R_{load} \frac{R_{Lo}}{2} + C_o R_{load} \frac{4L_r M}{T_s}} \\
& \sqrt{\frac{C_o}{\frac{L_o}{2} \left( 1 + \frac{2C_o}{L_o} R_{load} \frac{R_{Lo}}{2} + \frac{2C_o}{L_o} R_{load} \frac{4L_r M}{T_s} \right)}} \sqrt{\frac{1 + \frac{R_{Lo}}{2R_{load}} + \frac{1}{1 + \frac{\pi}{2J}}}{\frac{L_o}{2} + C_o R_{load} \frac{R_{Lo}}{2} + C_o R_{load} \frac{4L_r M}{T_s}}} \\
= & R_{load} \frac{\sqrt{\frac{C_o}{\frac{L_o}{2} \left( 1 + \frac{2C_o}{L_o} R_{load} \frac{R_{Lo}}{2} + \frac{2C_o}{L_o} R_{load} \frac{4L_r M}{T_s} \right)}} \sqrt{\frac{1 + \frac{R_{Lo}}{2R_{load}} + \frac{1}{1 + \frac{\pi}{2J}}}{\frac{L_o}{2} + C_o R_{load} \frac{R_{Lo}}{2} + C_o R_{load} \frac{4L_r M}{T_s}}}}{\frac{L_o}{2} + C_o R_{load} \frac{R_{Lo}}{2} + C_o R_{load} \frac{4L_r M}{T_s}}
\end{aligned}$$

$$= R_{load} \sqrt{\frac{C_o}{\frac{L_o}{2} \left( 1 + \frac{2C_o}{L_o} R_{load} \frac{R_{Lo}}{2} + \frac{2C_o}{L_o} \frac{R_{load}^2}{1 + \frac{\pi}{2} J} \right)}}$$

The detailed derivation of  $w_o$  in (3-33) is

$$\begin{aligned} w_o &= \frac{1}{\sqrt{\frac{\frac{L_o}{2} C_o R_{load}}{R_{load} + \frac{R_{Lo}}{2} - \frac{\partial u_1}{\partial i_{Lo}}}}} = \sqrt{\frac{R_{load} + \frac{R_{Lo}}{2} + \frac{4L_r M}{T_s}}{\frac{L_o}{2} C_o R_{load}}} \\ &= \sqrt{\frac{R_{load} + \frac{R_{Lo}}{2} + \frac{2 f_s}{\pi f_r} M Z_r}{\frac{L_o}{2} C_o R_{load}}} = \sqrt{\frac{1 + \frac{1}{2} \frac{R_{Lo}}{R_{load}} + \frac{2 f_s}{\pi f_r} \frac{L_o}{V_o} \frac{V_o}{V_{in}} Z_r}{\frac{L_o}{2} C_o}} \\ &= \frac{1}{\sqrt{\frac{L_o}{2} C_o}} \sqrt{1 + \frac{1}{2} \frac{R_{Lo}}{R_{load}} + \frac{2 f_s}{\pi f_r} J} \\ &= \frac{1}{\sqrt{\frac{L_o}{2} C_o}} \sqrt{1 + \frac{1}{2} \frac{R_{Lo}}{R_{load}} + \frac{1}{1 + \frac{\pi}{2} J}} \end{aligned} \tag{xxxiv}$$

The detailed derivation of  $G_{vv0}$  in (3-33) is

$$G_{vv0} = \frac{R_{load} \frac{\partial u_1}{\partial v_{in}}}{\frac{R_{Lo}}{2} + R_{load} - \frac{\partial u_1}{\partial i_{Lo}}} = \frac{R_{load} (M + M \frac{4L_r i_{Lo}}{v_{in} T_s})}{R_{load} + \frac{R_{Lo}}{2} + \frac{4L_r M}{T_s}} = M \frac{R_{load} (1 + \frac{4L_r i_{Lo}}{v_{in} T_s})}{R_{load} + \frac{R_{Lo}}{2} + \frac{4L_r M}{T_s}} \tag{xxxv}$$

$$\begin{aligned}
&= M \frac{R_{load} \left(1 + \frac{4Z_r I_o}{V_{in} 2\pi f_r T_s}\right)}{R_{load} + \frac{R_{Lo}}{2} + \frac{R_{load}}{1 + \frac{\pi}{2J}}} = M \frac{1 + J \frac{2f_s}{\pi f_r}}{1 + \frac{R_{Lo}}{2R_{load}} + \frac{1}{1 + \frac{\pi}{2J}}} \\
&= M \frac{1 + J \frac{2f_s}{\pi f_r}}{1 + \frac{R_{Lo}}{2R_{load}} + \frac{1}{1 + \frac{\pi}{2J}}} = M \frac{1 + J \frac{2}{\pi} \frac{1}{\frac{2J}{\pi} + 1}}{1 + \frac{R_{Lo}}{2R_{load}} + \frac{1}{1 + \frac{\pi}{2J}}} \\
&= M \frac{1 + \frac{1}{1 + \frac{\pi}{2J}}}{1 + \frac{R_{Lo}}{2R_{load}} + \frac{1}{1 + \frac{\pi}{2J}}}
\end{aligned}$$

The detailed derivation of the quality factor Q in (3-38) is

$$\begin{aligned}
Q &= \frac{\left(R_{Lo} + 2R_{load} - 2 \frac{\partial u_1}{\partial i_{Lo}}\right) \sqrt{\frac{C_o L_o R_{load}}{R_{Lo} + 2R_{load} - 2 \frac{\partial u_1}{\partial i_{Lo}}}}}{L_o + C_o R_{Lo} R_{load} - 2C_o R_{load} \frac{\partial u_1}{\partial i_{Lo}}} \\
&= \frac{\left(R_{Lo} + 2R_{load} + \frac{8L_r M}{T_s}\right) \sqrt{\frac{C_o L_o R_{load}}{R_{Lo} + 2R_{load} + \frac{8L_r M}{T_s}}}}{L_o + C_o R_{Lo} R_{load} + 2C_o R_{load} \frac{8L_r M}{T_s}} \tag{xxxvi} \\
&= \frac{\left(R_{load} + \frac{R_{Lo}}{2} + \frac{4L_r M}{T_s}\right) \sqrt{\frac{C_o \frac{L_o}{2} R_{load}}{R_{load} + \frac{R_{Lo}}{2} + \frac{4L_r M}{T_s}}}}{\frac{L_o}{2} + C_o R_{load} \frac{R_{Lo}}{2} + C_o R_{load} \frac{4L_r M}{T_s}}
\end{aligned}$$

$$= \frac{R_{load} \left(1 + \frac{R_{Lo}}{2R_{load}} + \frac{4Z_r I_o V_o}{w_r T_s V_o V_{in}}\right) \sqrt{\frac{C_o \frac{L_o}{2} R_{load}}{R_{load} + \frac{R_{Lo}}{2} + \frac{4L_r M}{T_s}}}}{\frac{L_o}{2} + C_o R_{load} \frac{R_{Lo}}{2} + C_o R_{load} \frac{4L_r M}{T_s}}$$

$$= \frac{R_{load} \left(1 + \frac{R_{Lo}}{2R_{load}} + \frac{2f_s J}{\pi f_r}\right) \sqrt{\frac{C_o \frac{L_o}{2} R_{load}}{R_{load} + \frac{R_{Lo}}{2} + \frac{4L_r M}{T_s}}}}{\frac{L_o}{2} + C_o R_{load} \frac{R_{Lo}}{2} + C_o R_{load} \frac{4L_r M}{T_s}}$$

$$= \frac{R_{load} \left(1 + \frac{R_{Lo}}{2R_{load}} + \frac{1}{\pi} \frac{1}{2J} \frac{1}{\pi} + 1\right) \sqrt{\frac{C_o \frac{L_o}{2} R_{load}}{R_{load} + \frac{R_{Lo}}{2} + \frac{4L_r M}{T_s}}}}{\frac{L_o}{2} + C_o R_{load} \frac{R_{Lo}}{2} + C_o R_{load} \frac{4L_r M}{T_s}}$$

$$= \frac{R_{load} \left(1 + \frac{R_{Lo}}{2R_{load}} + \frac{1}{1 + \frac{\pi}{2J}}\right) \sqrt{\frac{C_o \frac{L_o}{2} R_{load}}{R_{load} + \frac{R_{Lo}}{2} + \frac{4L_r M}{T_s}}}}{\frac{L_o}{2} + C_o R_{load} \frac{R_{Lo}}{2} + C_o R_{load} \frac{4L_r M}{T_s}}$$

$$= R_{load} \frac{\sqrt{C_o \frac{L_o}{2} \left(1 + \frac{R_{Lo}}{2R_{load}} + \frac{1}{1 + \frac{\pi}{2J}}\right)}}{\frac{L_o}{2} + C_o R_{load} \frac{R_{Lo}}{2} + C_o R_{load} \frac{4L_r M}{T_s}}$$

$$= R_{load} \frac{\sqrt{C_o \frac{L_o}{2} \left(1 + \frac{R_{Lo}}{2R_{load}} + \frac{1}{1 + \frac{\pi}{2J}}\right)}}{\frac{L_o}{2} + C_o R_{load} \frac{R_{Lo}}{2} + C_o R_{load} \frac{4L_r M}{T_s}}$$

$$\begin{aligned}
&= R_{load} \sqrt{\frac{C_o}{\frac{L_o}{2} \left( 1 + \frac{2C_o}{L_o} R_{load} \frac{R_{Lo}}{2} + \frac{2C_o}{L_o} R_{load} \frac{4L_r M}{T_s} \right)}} \sqrt{1 + \frac{R_{Lo}}{2R_{load}} + \frac{1}{1 + \frac{\pi}{2J}}} \\
&= R_{load} \sqrt{\frac{C_o}{\frac{L_o}{2} \left( 1 + \frac{2C_o}{L_o} R_{load} \frac{R_{Lo}}{2} + \frac{2C_o}{L_o} \frac{R_{load}^2}{1 + \frac{\pi}{2J}} \right)}} \sqrt{1 + \frac{R_{Lo}}{2R_{load}} + \frac{1}{1 + \frac{\pi}{2J}}}
\end{aligned}$$

The detailed derivation of  $w_o$  in (3-38) is

$$\begin{aligned}
w_o &= \frac{1}{\sqrt{\frac{\frac{L_o}{2} C_o R_{load}}{R_{load} + \frac{R_{Lo}}{2} - \frac{\partial u_1}{\partial i_{Lo}}}}} = \sqrt{\frac{R_{load} + \frac{R_{Lo}}{2} + \frac{4L_r M}{T_s}}{\frac{L_o}{2} C_o R_{load}}} \\
&= \sqrt{\frac{R_{load} + \frac{R_{Lo}}{2} + \frac{2 f_s}{\pi f_r} M Z_r}{\frac{L_o}{2} C_o R_{load}}} = \sqrt{\frac{1 + \frac{1}{2} \frac{R_{Lo}}{R_{load}} + \frac{2 f_s}{\pi f_r} \frac{I_o}{V_o} \frac{V_o}{V_{in}} Z_r}{\frac{L_o}{2} C_o}} \quad (\text{xxxvii}) \\
&= \frac{1}{\sqrt{\frac{L_o}{2} C_o}} \sqrt{1 + \frac{1}{2} \frac{R_{Lo}}{R_{load}} + \frac{2 f_s}{\pi f_r} J} \\
&= \frac{1}{\sqrt{\frac{L_o}{2} C_o}} \sqrt{1 + \frac{1}{2} \frac{R_{Lo}}{R_{load}} + \frac{1}{1 + \frac{\pi}{2J}}}
\end{aligned}$$

The detailed derivation of  $G_{d0}$  in (3-38) is

$$\begin{aligned}
G_{do} &= \frac{2R_{load} \frac{\partial u_1}{\partial t_{off}}}{2R_{load} + R_{Lo} - 2 \frac{\partial u_1}{\partial i_{Lo}}} = \frac{R_{load} \frac{v_{in}}{T_s}}{R_{load} + \frac{R_{Lo}}{2} + \frac{4L_r M}{T_s}} \\
&= \frac{\frac{v_{in}}{T_s}}{1 + \frac{R_{Lo}}{2R_{load}} + \frac{1}{R_{load}} \frac{4L_r M}{T_s}} = \frac{\frac{v_{in}}{T_s}}{1 + \frac{R_{Lo}}{2R_{load}} + \frac{1}{1 + \frac{\pi}{2} J}}
\end{aligned} \tag{xxxviii}$$

The detailed derivation of the quality factor Q in (3-41) is

$$\begin{aligned}
Q &= \frac{\left(R_{Lo} + 2R_{load} - 2 \frac{\partial u_1}{\partial i_{Lo}}\right) \sqrt{\frac{C_o L_o R_{load}}{R_{Lo} + 2R_{load} - 2 \frac{\partial u_1}{\partial i_{Lo}}}}}{L_o + C_o R_{Lo} R_{load} - 2C_o R_{load} \frac{\partial u_1}{\partial i_{Lo}}} \\
&= \frac{\left(R_{Lo} + 2R_{load} + \frac{8L_r M}{T_s}\right) \sqrt{\frac{C_o L_o R_{load}}{R_{Lo} + 2R_{load} + \frac{8L_r M}{T_s}}}}{L_o + C_o R_{Lo} R_{load} + 2C_o R_{load} \frac{8L_r M}{T_s}} \\
&= \frac{\left(R_{load} + \frac{R_{Lo}}{2} + \frac{4L_r M}{T_s}\right) \sqrt{\frac{C_o \frac{L_o}{2} R_{load}}{R_{load} + \frac{R_{Lo}}{2} + \frac{4L_r M}{T_s}}}}{\frac{L_o}{2} + C_o R_{load} \frac{R_{Lo}}{2} + C_o R_{load} \frac{4L_r M}{T_s}} \tag{xxxix} \\
&= \frac{R_{load} \left(1 + \frac{R_{Lo}}{2R_{load}} + \frac{4Z_r I_o V_o}{w_r T_s V_o V_{in}}\right) \sqrt{\frac{C_o \frac{L_o}{2} R_{load}}{R_{load} + \frac{R_{Lo}}{2} + \frac{4L_r M}{T_s}}}}{\frac{L_o}{2} + C_o R_{load} \frac{R_{Lo}}{2} + C_o R_{load} \frac{4L_r M}{T_s}} \\
&= \frac{R_{load} \left(1 + \frac{R_{Lo}}{2R_{load}} + \frac{2f_s J}{\pi f_r}\right) \sqrt{\frac{C_o \frac{L_o}{2} R_{load}}{R_{load} + \frac{R_{Lo}}{2} + \frac{4L_r M}{T_s}}}}{\frac{L_o}{2} + C_o R_{load} \frac{R_{Lo}}{2} + C_o R_{load} \frac{4L_r M}{T_s}}
\end{aligned}$$

$$\begin{aligned}
& R_{load} \left( 1 + \frac{R_{Lo}}{2R_{load}} + \frac{1}{\pi} \frac{1}{2J} \frac{1}{\pi} + 1 \right) \sqrt{\frac{C_o \frac{L_o}{2} R_{load}}{R_{load} + \frac{R_{Lo}}{2} + \frac{4L_r M}{T_s}}} \\
= & \frac{R_{load} \left( 1 + \frac{R_{Lo}}{2R_{load}} + \frac{1}{\pi} \frac{1}{2J} \frac{1}{\pi} + 1 \right) \sqrt{\frac{C_o \frac{L_o}{2} R_{load}}{R_{load} + \frac{R_{Lo}}{2} + \frac{4L_r M}{T_s}}}}{\frac{L_o}{2} + C_o R_{load} \frac{R_{Lo}}{2} + C_o R_{load} \frac{4L_r M}{T_s}} \\
& R_{load} \left( 1 + \frac{R_{Lo}}{2R_{load}} + \frac{1}{1 + \frac{\pi}{2J}} \right) \sqrt{\frac{C_o \frac{L_o}{2} R_{load}}{R_{load} + \frac{R_{Lo}}{2} + \frac{4L_r M}{T_s}}} \\
= & \frac{R_{load} \left( 1 + \frac{R_{Lo}}{2R_{load}} + \frac{1}{1 + \frac{\pi}{2J}} \right) \sqrt{\frac{C_o \frac{L_o}{2} R_{load}}{R_{load} + \frac{R_{Lo}}{2} + \frac{4L_r M}{T_s}}}}{\frac{L_o}{2} + C_o R_{load} \frac{R_{Lo}}{2} + C_o R_{load} \frac{4L_r M}{T_s}} \\
& R_{load} \frac{\sqrt{C_o \frac{L_o}{2} \left( 1 + \frac{R_{Lo}}{2R_{load}} + \frac{1}{1 + \frac{\pi}{2J}} \right)}}{\frac{L_o}{2} + C_o R_{load} \frac{R_{Lo}}{2} + C_o R_{load} \frac{4L_r M}{T_s}} \\
& R_{load} \frac{\sqrt{C_o \frac{L_o}{2} \left( 1 + \frac{R_{Lo}}{2R_{load}} + \frac{1}{1 + \frac{\pi}{2J}} \right)}}{\frac{L_o}{2} + C_o R_{load} \frac{R_{Lo}}{2} + C_o R_{load} \frac{4L_r M}{T_s}} \\
= & R_{load} \frac{\sqrt{\frac{C_o}{\frac{L_o}{2}} \frac{\sqrt{1 + \frac{R_{Lo}}{2R_{load}} + \frac{1}{1 + \frac{\pi}{2J}}}}{1 + \frac{2C_o}{L_o} R_{load} \frac{R_{Lo}}{2} + \frac{2C_o}{L_o} R_{load} \frac{4L_r M}{T_s}}}}{\frac{L_o}{2} + C_o R_{load} \frac{R_{Lo}}{2} + C_o R_{load} \frac{4L_r M}{T_s}} \\
= & R_{load} \frac{\sqrt{\frac{C_o}{\frac{L_o}{2}} \frac{\sqrt{1 + \frac{R_{Lo}}{2R_{load}} + \frac{1}{1 + \frac{\pi}{2J}}}}{1 + \frac{2C_o}{L_o} R_{load} \frac{R_{Lo}}{2} + \frac{2C_o}{L_o} R_{load} \frac{4L_r M}{T_s}}}}{\frac{L_o}{2} + C_o R_{load} \frac{R_{Lo}}{2} + C_o R_{load} \frac{4L_r M}{T_s}}
\end{aligned}$$

The detailed derivation of  $w_o$  in (3-41) is

$$\begin{aligned}
w_o &= \frac{1}{\sqrt{\frac{\frac{L_o}{2} C_o R_{load}}{R_{load} + \frac{R_{Lo}}{2} - \frac{\partial u_1}{\partial i_{Lo}}}}} \\
&= \sqrt{\frac{R_{load} + \frac{R_{Lo}}{2} + \frac{4L_r M}{T_s}}{\frac{L_o}{2} C_o R_{load}}} \\
&= \sqrt{\frac{R_{load} + \frac{R_{Lo}}{2} + \frac{2 f_s}{\pi f_r} M Z_r}{\frac{L_o}{2} C_o R_{load}}} \\
&= \sqrt{\frac{1 + \frac{1}{2} \frac{R_{Lo}}{R_{load}} + \frac{2 f_s I_o V_o}{\pi f_r V_o V_{in}} Z_r}{\frac{L_o}{2} C_o}} \\
&= \frac{1}{\sqrt{\frac{L_o}{2} C_o}} \sqrt{1 + \frac{1}{2} \frac{R_{Lo}}{R_{load}} + \frac{2 f_s}{\pi f_r} J} \\
&= \frac{1}{\sqrt{\frac{L_o}{2} C_o}} \sqrt{1 + \frac{1}{2} \frac{R_{Lo}}{R_{load}} + \frac{1}{1 + \frac{\pi}{2} J}}
\end{aligned} \tag{x1}$$

The detailed derivation of  $Z_{odc}$  in (3-41) is

$$\begin{aligned}
Z_{odc} &= \frac{R_{load} R_{Lo} - 2R_{load} \frac{\partial u_1}{\partial i_{Lo}}}{2R_{load} + R_{Lo} - 2 \frac{\partial u_1}{\partial i_{Lo}}} \\
&= \frac{\frac{R_{load} R_{Lo}}{2} - R_{load} \frac{\partial u_1}{\partial i_{Lo}}}{R_{load} + \frac{R_{Lo}}{2} - \frac{\partial u_1}{\partial i_{Lo}}}
\end{aligned} \tag{xli}$$

$$\begin{aligned}
&= \frac{R_{load} \frac{R_{Lo}}{2} + R_{load} \frac{4L_r M}{T_s}}{R_{load} + \frac{R_{Lo}}{2} + \frac{4L_r M}{T_s}} \\
&= \frac{R_{load} \left( \frac{R_{Lo}}{2} + \frac{4L_r M}{T_s} \right)}{R_{load} + \left( \frac{R_{Lo}}{2} + \frac{4L_r M}{T_s} \right)} \\
&= \frac{R_{load} \left( \frac{R_{Lo}}{2} + \frac{R_{load}}{1 + \frac{\pi}{2} J} \right)}{R_{load} + \left( \frac{R_{Lo}}{2} + \frac{R_{load}}{1 + \frac{\pi}{2} J} \right)}
\end{aligned}$$

The detailed derivation of  $w_{zL}$  in (3-41) is

$$\begin{aligned}
w_{zL} &= \frac{R_{load} R_{Lo} - 2R_{load} \frac{\partial u_1}{\partial i_{Lo}}}{L_o R_{load}} \\
&= \frac{R_{load} \frac{R_{Lo}}{2} + R_{load} \frac{4L_r M}{T_s}}{\frac{L_o}{2} R_{load} \frac{R_{Lo}}{2} + \frac{4L_r M}{T_s}} \\
&= \frac{\frac{L_o}{2}}{\frac{R_{Lo}}{2} + \frac{R_{load}}{1 + \frac{\pi}{2} J}} \\
&= \frac{\frac{L_o}{2}}{\frac{L_o}{2}}
\end{aligned} \tag{xlii}$$

The expanding factor  $\sigma_1$  in (3-35) is

$$\sigma_1 = \frac{w_o}{w_{oSCB}} = \frac{\frac{1}{\sqrt{\frac{L_o}{2} C_o}} \sqrt{\frac{R_{load} + \frac{2 f_s}{\pi f_r} M Z_r}{R_{load}}}}{\frac{1}{\sqrt{\frac{L_o}{2} C_o}}} = \sqrt{1 + \frac{1}{R_{load}} \frac{2 f_s}{\pi f_r} M Z_r}$$

(xlili)

$$= \sqrt{1 + \frac{2 f_s I_o V_o}{\pi f_r V_o V_{in}} Z_r} = \sqrt{1 + \frac{2 f_s}{\pi f_r} J}$$

$$\sigma_1 = \sqrt{1 + \frac{2 f_s}{\pi f_r} J} = \sqrt{1 + \frac{2}{\pi} \frac{1}{\frac{2J}{\pi} + 1} J} = \sqrt{1 + \frac{2}{\pi} \frac{1}{\frac{2}{\pi} + \frac{1}{J}}} = \sqrt{1 + \frac{1}{1 + \frac{\pi}{2J}}}$$

The expanding factor  $\sigma_2$  in (3-37) is

$$\sigma_2 = \frac{Q}{Q_{SCB}} = \frac{\sqrt{1 + \frac{R_{Lo}}{2R_{load}} + \frac{1}{1 + \frac{\pi}{2J}}}}{1 + \frac{2C_o}{L_o} R_{load} \frac{R_{Lo}}{2} + \frac{2C_o}{L_o} \frac{R_{load}^2}{1 + \frac{\pi}{2J}}} \approx \frac{\sqrt{1 + \frac{1}{1 + \frac{\pi}{2J}}}}{1 + R_{load}^2 \frac{2C_o}{L_o} \frac{1}{1 + \frac{\pi}{2J}}}$$

(xliv)

## I. Calculation of Circulating Energy

The peak inductor current and peak capacitor voltage calculation is from Chapter 2:

$$I_{LrPkN} = \frac{I_{LrPk}}{I_o} = \frac{\frac{1}{2} \left( \frac{V_{in}}{Z_r} + I_{oMax} \right)}{I_o}$$

$$V_{CrPkN} = \frac{V_{CrPk}}{V_{in}} = \frac{\frac{V_{in}}{2}}{V_{in}} \quad (xlv)$$

$$f_r = \frac{1}{2\pi\sqrt{L_r C_r}}$$

The detailed derivation of normalized resonant tank energy in (4-1) is

$$E_{tank} = \frac{\frac{1}{2} (L_r I_{LrPk}^2 + C_r V_{CrPk}^2)}{\frac{V_o I_{oMax}}{f_r}}$$

$$= f_r \frac{\left( L_r \left( \frac{1}{2} \left( \frac{V_{in}}{Z_r} + I_{oMax} \right) \right)^2 + C_r \left( \frac{V_{in}}{2} \right)^2 \right)}{2V_o I_{oMax}}$$

$$= f_r \frac{L_r \left( \frac{V_{in}}{Z_r} + I_{oMax} \right)^2 + C_r V_{in}^2}{8V_o I_{oMax}} \quad (xlvi)$$

$$= \frac{L_r f_r \left( \frac{V_{in}}{Z_r} + I_{oMax} \right)^2 + C_r f_r V_{in}^2}{8V_o I_{oMax}}$$

$$= \frac{Z_r \left( \frac{V_{in}}{Z_r} + I_{oMax} \right)^2 + \frac{1}{Z_r} V_{in}^2}{16\pi V_o I_{oMax}}$$

The equation above is normalized using

$$I_{oMax} = \frac{J_{max} V_{in}}{Z_r} \quad (xlvii)$$

and further derived as

$$\begin{aligned} E_{tank} &= \frac{Z_r \left( \frac{V_{in}}{Z_r} + \frac{J_{max} V_{in}}{Z_r} \right)^2 + \frac{1}{Z_r} V_{in}^2}{16\pi V_o \frac{J_{max} V_{in}}{Z_r}} \\ &= \frac{Z_r \left( \frac{1}{Z_r} + \frac{J_{max}}{Z_r} \right)^2 + \frac{1}{Z_r}}{16\pi \frac{V_o}{V_{in}} \frac{J_{max}}{Z_r}} \\ &= \frac{(1 + J_{max})^2 + 1}{16\pi M J_{max}} \end{aligned} \tag{xlvi}$$

## J. Calculation of Peak Circulating Energy

The detailed derivation of the peak circulating energy in (4-2) is attached below

```
% ----- Clear Data _ start -----%
close all;clc; clear all; tic;
% set(0,'defaultFigureWindowStyle','docked');
% ttl=clock;
format compact
% ----- Clear Data _ END -----%

%% Color
C01=[1.0 0.0 0.0]; % red
C02=[1.0 0.5 0.0]; % dark orange
C03=[0.0 0.5 0.0]; % green
C04=[0.0 0.7 1.0]; % deep sky blue
C05=[0.0 0.0 1.0]; % blue
C06=[0.6 0.0 0.8]; % dark violet
C07=[1.0 0.0 1.0]; % magenta
C08=[0.8 0.4 0.1]; % chocolate
C09=[0.0 0.0 0.0]; % black
C10=[0.4 0.4 0.4]; % dim gray

c=[C01;C02;C03;C04;C05;C06;C07;C08;C09;C10];
```

```

% component

Rload=sym('Rload');

Cr=sym('Cr');

Lr=sym('Lr');

Cs=sym('Cs');

Co=sym('Co');

Loa=sym('Loa');

Lob=sym('Lob');

RLoa=sym('RLoa');

RLob=sym('RLob');

Lob=Loa;

RLob=RLoa;

% large signal

vin=sym('vin');

toff=sym('toff');

vcs=sym('vcs');

vo=sym('vo');

iLoa=sym('iLoa');

iLob=sym('iLob');

io=sym('io');

% normalized

```

```

j=sym('j');
m=sym('m');

% symbolic combination
wr=1/sqrt(Lr*Cr);
fr=wr/2/pi;
Zr=sqrt(Lr/Cr);
wr3=1/sqrt(Lr*(Cs+Cr));
fr3=wr3/2/pi;
Zr3=sqrt(Lr/(Cs+Cr));

%% Energy density - symbolic

Jmax=io*Zr/vin;

ILrpk=0.5*(vin/Zr+io);
Vcrpk=vin/2;
E_00=0.5*(Lr*ILrpk^2+Cr*Vcrpk^2)/(vo*io/fr);
E_01=(Zr*(1/Zr+Jmax/Zr)^2+1/Zr)/(16*pi*vo*Jmax/vin/Zr);
E_02=((1+Jmax)^2+1)/(16*pi*Jmax*vo/vin);

E_j=((1+j)^2+1)/(16*pi*j*m)

```

```
E_dj=diff(E_j,j)

% check E_j valley point when E_dj=0
eq = E_dj==0
[s1] = solve(eq,j)
toc
```

## K. Calculation of Switching Frequency Curve

The Matlab code for deriving the switching frequency curve in (4-8) is shown below

```
% ----- Clear Data _ start -----%
close all;clc; clear all; tic;
% set(0,'defaultFigureWindowStyle','docked');
% ttl=clock;
format compact
% ----- Clear Data _ END -----%

%% Color
C01=[1.0 0.0 0.0]; % red
C02=[1.0 0.5 0.0]; % dark orange
C03=[0.0 0.5 0.0]; % green
C04=[0.0 0.7 1.0]; % deep sky blue
C05=[0.0 0.0 1.0]; % blue
C06=[0.6 0.0 0.8]; % dark violet
C07=[1.0 0.0 1.0]; % magenta
C08=[0.8 0.4 0.1]; % chocolate
C09=[0.0 0.0 0.0]; % black
C10=[0.4 0.4 0.4]; % dim gray

c=[C01;C02;C03;C04;C05;C06;C07;C08;C09;C10];
```

```

%%

% component
Rload=sym('Rload');
Cr=sym('Cr');
Lr=sym('Lr');
Cs=sym('Cs');
Co=sym('Co');
Loa=sym('Loa');
Lob=sym('Lob');
RLoa=sym('RLoa');
RLob=sym('RLob');
Lob=Loa;
RLob=RLoa;

% large signal
vin=sym('vin');
toff=sym('toff');
vcs=sym('vcs');
vo=sym('vo');
iLoa=sym('iLoa');
iLob=sym('iLob');
io=sym('io');

```

```

% normalized

j=sym('j');
m=sym('m');

% symbolic combination

wr=1/sqrt(Lr*Cr);

fr=wr/2/pi;

Zr=sqrt(Lr/Cr);

wr3=1/sqrt(Lr*(Cs+Cr));

fr3=wr3/2/pi;

Zr3=sqrt(Lr/(Cs+Cr));

%%

Ts_00=2*toff+4*Lr/vin*(io+vin*(pi-wr*toff)/2/Zr)

Ts_01=2*toff+4*J/wr+2*(pi-wr*toff)/wr

Ts_02=(4*J+2*pi)/wr

%% The end

Toc

```

## L. Calculation of Capacitor Voltage Ripple

The detailed derivation of (4-13) from equation (4-12) is listed below

$$\begin{aligned}
C_s \Delta V &= \Delta Q = \left| \int_{t_8}^{t_1} i_{Lr}(\lambda) d\lambda + \int_{t_1}^{t_2} i_{Loa}(\lambda) d\lambda \right| \\
&= -\frac{1}{2} \left( i_{Loa} - \tau_8 \frac{V_{in} - v_{Cs}}{L_r} \right) \frac{\left( i_{Loa} - \tau_8 \frac{V_{in} - v_{Cs}}{L_r} \right)}{-\frac{V_{in} - v_{Cs}}{L_r}} + \frac{1}{2} i_{Loa} \frac{i_{Loa}}{\frac{V_{in} - v_{Cs}}{L_r}} + i_{Loa} t_{off} \\
&= \left( i_{Loa} - \tau_8 \frac{V_{in}}{2L_r} \right) \left( i_{Loa} - \tau_8 \frac{V_{in}}{2L_r} \right) \frac{L_r}{V_{in}} + \frac{L_r}{V_{in}} i_{Loa}^2 + t_{off} i_{Loa} \\
&= \frac{L_r}{V_{in}} \left( i_{Loa} - \tau_8 \frac{V_{in}}{2L_r} \right)^2 + \frac{L_r}{V_{in}} i_{Loa}^2 + t_{off} i_{Loa} \\
&= \frac{L_r}{V_{in}} \left( i_{Loa} - \left( \frac{2L_r I_o}{V_{in}} + \frac{\sin(w_r t_{off})}{w_r} \right) \frac{V_{in}}{2L_r} \right)^2 + \frac{L_r}{V_{in}} i_{Loa}^2 + t_{off} i_{Loa} \\
&= \frac{L_r}{V_{in}} \left( i_{Loa} - I_o + \frac{\sin(w_r t_{off})}{w_r} \frac{V_{in}}{2L_r} \right)^2 + \frac{L_r}{V_{in}} i_{Loa}^2 + t_{off} i_{Loa} \\
&= \frac{L_r}{4V_{in}} \left( \sin(w_r t_{off}) \frac{V_{in}}{Z_r} + I_o \right)^2 + \frac{L_r}{4V_{in}} I_o^2 + t_{off} \frac{I_o}{2} \\
&= \frac{L_r}{4V_{in}} \left( \sin(w_r t_{off}) \frac{V_{in}}{Z_r} + J \frac{V_{in}}{Z_r} \right)^2 + \frac{L_r}{4V_{in}} \left( J \frac{V_{in}}{Z_r} \right)^2 + \frac{1}{2} t_{off} J \frac{V_{in}}{Z_r} \\
&= \frac{V_{in}}{4w_r Z_r} \left( \sin(w_r t_{off}) + J \right)^2 + \frac{V_{in}}{4w_r Z_r} J^2 + \frac{V_{in}}{2w_r Z_r} w_r t_{off} J \\
&= \frac{V_{in}}{4w_r Z_r} \left( \left( \sin(w_r t_{off}) + J \right)^2 + J^2 + 2w_r t_{off} J \right) \\
&= \frac{V_{in} C_r}{4} \left( \left( \sin(w_r t_{off}) + J \right)^2 + J^2 + 2w_r t_{off} J \right)
\end{aligned} \tag{xlix}$$

The charge difference  $\Delta Q$  is replaced with  $\Delta Q = C_s \Delta V$ . The new equation is

$$\frac{\Delta V}{V_{in}} = \frac{1}{4C_n} ( (\sin(w_r t_{off}) + J)^2 + J^2 + 2w_r t_{off} J ) \quad (1)$$
$$\frac{\Delta V}{V_{in}} = \frac{1}{C_n} \frac{ (\sin(w_r t_{off}) + J)^2 + J^2 + 2w_r t_{off} J }{4}$$

## M. Calculation of Inductor Current Ripple

The detailed derivation of (4-17) from equation (4-16) is listed below

$$\begin{aligned}
 L_{ob}\Delta I &= \int_{t_5}^{t_6} v_{Lob}(\lambda)d\lambda \\
 &= \int_{t_5}^{t_6} (v_{Cs} + v_{Cr} - v_{Co})d\lambda \\
 &= \int_{t_5}^{t_6} \left(\frac{V_{in}}{2} + v_{Cr} - \frac{V_o}{2}\right)d\lambda \\
 &= \left(\frac{V_{in}}{2} - V_o\right)T_{off} + \int_{t_5}^{t_6} v_{Cr}d\lambda \\
 &= \left(\frac{V_{in}}{2} - V_o\right)T_{off} - \left(\frac{V_{in}}{2}\right)\frac{\sin(w_r t_{off})}{w_r}
 \end{aligned} \tag{li}$$

The current difference  $\Delta I$  is replaced with  $\Delta I = \Delta J \frac{V_{in}}{Z_r}$ . The new equation is

$$\begin{aligned}
 L_{ob}\Delta J \frac{V_{in}}{Z_r} &= \left(\frac{V_{in}}{2} - V_o\right)T_{off} - \left(\frac{V_{in}}{2}\right)\frac{\sin(w_r t_{off})}{w_r} \\
 L_{ob}\Delta J &= \left(\frac{1}{2} - \frac{V_o}{V_{in}}\right)\frac{Z_r}{w_r}w_r T_{off} - \frac{Z_r}{2}\frac{\sin(w_r t_{off})}{w_r} \\
 L_{ob}\Delta J &= \left(\frac{1}{2} - \frac{V_o}{V_{in}}\right)L_r w_r T_{off} - \frac{L_r}{2}\sin(w_r T_{off}) \\
 \Delta J = \frac{\Delta I}{\frac{V_{in}}{Z_r}} &= \left(\frac{1}{2} - M\right)\frac{L_r}{L_{ob}}w_r T_{off} - \frac{1}{2}\frac{L_r}{L_{ob}}\sin(w_r T_{off}) \\
 \Delta J = \frac{\Delta I}{\frac{V_{in}}{Z_r}} &= \frac{1}{\frac{L_{ob}}{L_r}}\left(\left(\frac{1}{2} - M\right)w_r T_{off} - \frac{1}{2}\sin(w_r T_{off})\right)
 \end{aligned} \tag{lii}$$

$$\Delta J = \frac{\Delta I}{\frac{V_{in}}{Z_r}} = \frac{1}{L_n} \left( \left( \frac{1}{2} - M \right) w_r T_{off} - \frac{1}{2} \sin(w_r T_{off}) \right)$$

## N. Calculation of Component Stresses

The Matlab code for deriving the component stresses from (4-19) to (4-26) is shown below

```
% ----- Clear Data _ start -----%  
close all;clc; clear all; tic;  
  
% set(0,'defaultFigureWindowStyle','docked');  
  
% ttl=clock;  
  
format compact  
  
% ----- Clear Data _ END -----%  
  
%% Color  
  
C01=[1.0 0.0 0.0]; % red  
C02=[1.0 0.5 0.0]; % dark orange  
C03=[0.0 0.5 0.0]; % green  
C04=[0.0 0.7 1.0]; % deep sky blue  
C05=[0.0 0.0 1.0]; % blue  
C06=[0.6 0.0 0.8]; % dark violet  
C07=[1.0 0.0 1.0]; % magenta  
C08=[0.8 0.4 0.1]; % chocolate  
C09=[0.0 0.0 0.0]; % black  
C10=[0.4 0.4 0.4]; % dim gray  
  
c=[C01;C02;C03;C04;C05;C06;C07;C08;C09;C10];
```

```

%%

% component
Rload=sym('Rload');
Cr=sym('Cr');
Lr=sym('Lr');
Cs=sym('Cs');
Co=sym('Co');
Loa=sym('Loa');
Lob=sym('Lob');
RLoa=sym('RLoa');
RLob=sym('RLob');
Lob=Loa;
RLob=RLoa;

% large signal
vin=sym('vin');
toff=sym('toff');
vcs=sym('vcs');
vo=sym('vo');
iLoa=sym('iLoa');
iLob=sym('iLob');
io=sym('io');

```

```

% normalized

j=sym('j');
m=sym('m');

% symbolic combination

wr=1/sqrt(Lr*Cr);
fr=wr/2/pi;
Zr=sqrt(Lr/Cr);
wr3=1/sqrt(Lr*(Cs+Cr));
fr3=wr3/2/pi;
Zr3=sqrt(Lr/(Cs+Cr));

%%

ialrms_99=io/2*sqrt((toff+Lr*io/vin)/Ts)
ialrms_00=sqrt(((toff/Ts)+2*tau6/2/3/Ts)*(io/2)^2)
ialrms_01=io/2*sqrt((toff/Ts)+2*tau6/2/3/Ts)
ialrms_02=io/2*sqrt((toff/Ts)+tau6/Ts/3)
ialrms_11=io/2*sqrt((toff/Ts)+(2*Lr*io/vin)/Ts/3)
ialrms_12=J*vin/2/Zr*sqrt((toff+2*J/3/wr)/Ts)
ialrms_13=0.5*io*sqrt(toff/Ts+J/6/pi)
ialrms_21=0.5*io*sqrt(2*vo/vin+J/6/pi)

```

```
ia2rms_99=io*sqrt((toff+2*Lr*io/vin)/Ts)
```

```
ia2rms_00=io*sqrt((toff+2/3*tau3)/Ts)
```

```
ia2rms_11=io*sqrt(toff/Ts+J/3/pi)
```

```
ia2rms_21=io*sqrt(2*vo/vin+J/3/pi)
```

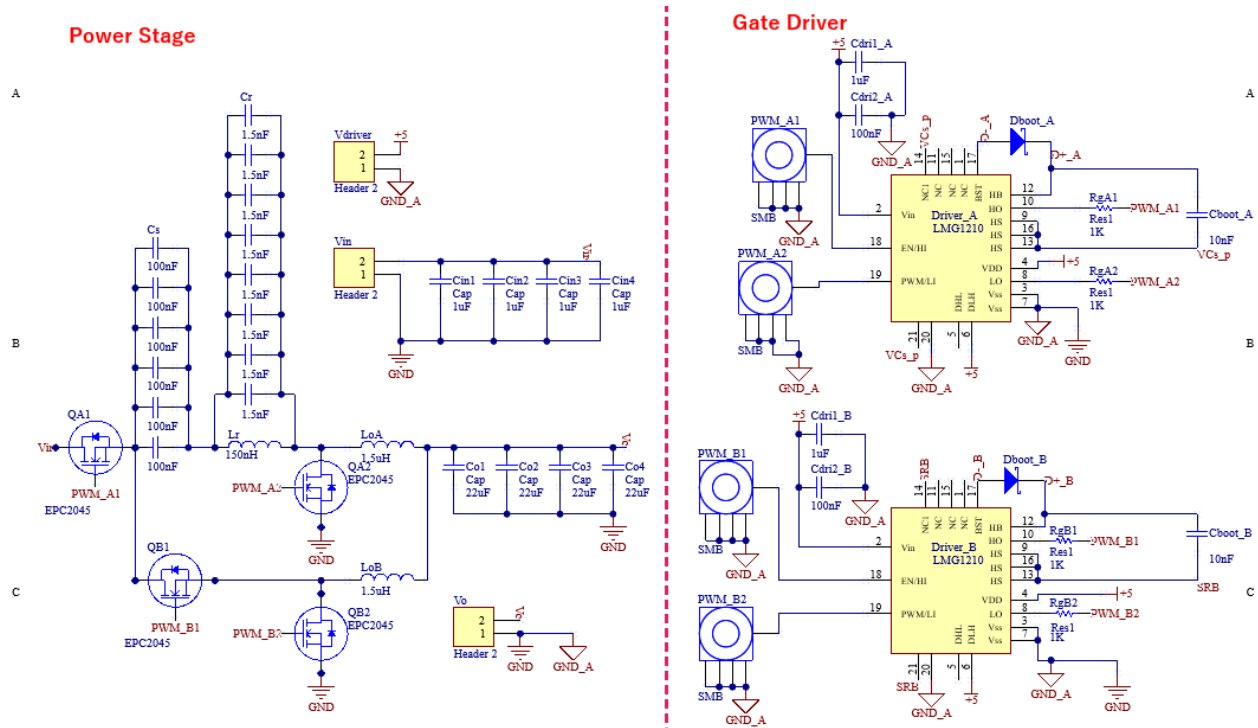
```
ib2rms_21=0.5*io*sqrt(2*vo/vin+7*J/6/pi)
```

```
%% The end
```

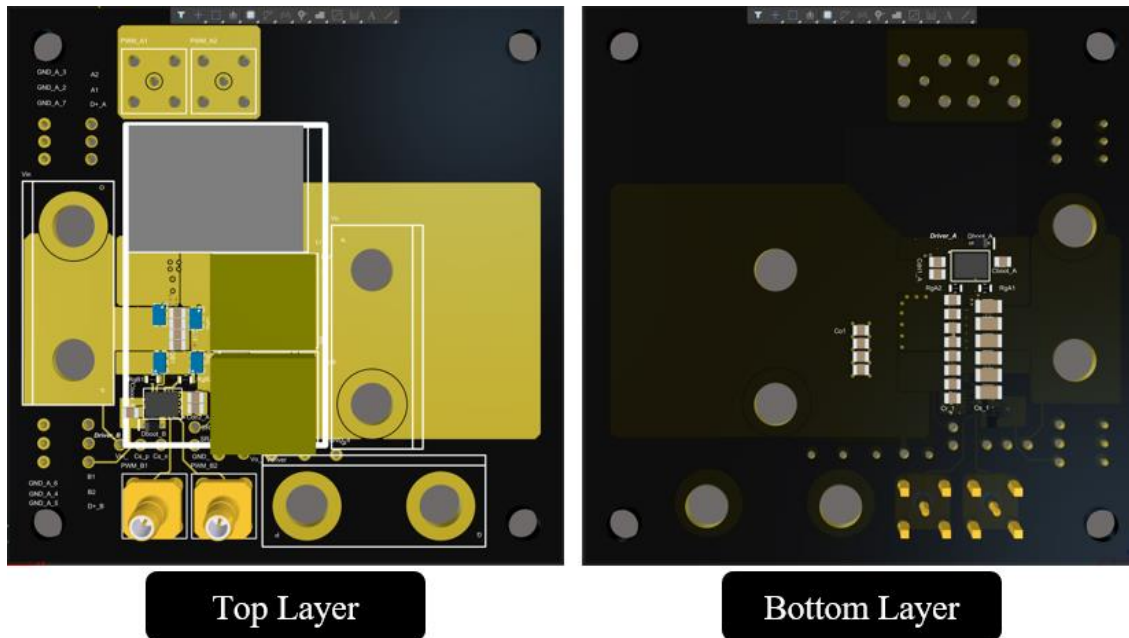
```
toc
```

## O. Schematic

The schematic of the SRB converter is in Fig. 4-10.



The Layout of the SRB converter in Fig. 4-10.



## References

- [1] K. Nishijima, K. Harada, T. Nakano, T. Nabeshima, and T. Sato, "Analysis of Double Step-Down Two-Phase Buck Converter for VRM," *International Telecommunications Conference*, Berlin, 2005, pp. 497-502.
- [2] Yungtaek Jang, M. M. Jovanovic, and Y. Panov, "Multiphase buck converters with extended duty cycle," *IEEE Applied Power Electronics Conference and Exposition (APEC)*, Dallas, TX, 2006, pp. 39-44.
- [3] K. Nishijima, D. Ishida, K. Harada, T. Nabeshima, T. Sato, and T. Nakano, "A novel two-phase buck converter with two cores and four windings," *INTELEC 07 - 29th International Telecommunications Energy Conference*, Rome, Italy, 2007, pp. 861-866
- [4] I. Lee, S. Cho, and G. Moon, "Interleaved Buck Converter Having Low Switching Losses and Improved Step-Down Conversion Ratio," in *IEEE Transactions on Power Electronics*, vol. 27, no. 8, pp. 3664-3675, Aug. 2012.
- [5] P. S. Shenoy et al., "A 5 MHz, 12 V, 10 A, monolithically integrated two-phase series capacitor buck converter," *IEEE Applied Power Electronics Conference and Exposition (APEC)*, Long Beach, CA, 2016, pp. 66-72.
- [6] P. S. Shenoy, M. Amaro, J. Morroni, and D. Freeman, "Comparison of a Buck Converter and a Series Capacitor Buck Converter for High-Frequency, High-Conversion-Ratio Voltage Regulators," in *IEEE Transactions on Power Electronics*, vol. 31, no. 10, pp. 7006-7015, Oct. 2016.
- [7] F. Marvi, E. Adib, and H. Farzanehfard, "Efficient ZVS Synchronous Buck Converter with Extended Duty Cycle and Low-Current Ripple," in *IEEE Transactions on Industrial*

- Electronics*, vol. 63, no. 9, pp. 5403-5409, Sept. 2016.
- [8] L. Zhang and S. Chakraborty, "An Interleaved Series-Capacitor Tapped Buck Converter for High Step-Down DC/DC Application," in *IEEE Transactions on Power Electronics*, vol. 34, no. 7, pp. 6565-6574, July 2019.
- [9] T. Ge, B. Carpenter, and K. D. T. Ngo, "Steady-State Analysis of Resonant Cross-Commutated Buck Converter Under Continuous Voltage Mode," in *IEEE Transactions on Industrial Electronics*, vol. 65, no. 10, pp. 7782-7792, Oct. 2018.
- [10] M. Amiri and H. Farzanehfard, "An Interleaved Nonisolated ZVS Ultrahigh Step-Down DC-DC Converter With Low Voltage Stress," in *IEEE Transactions on Industrial Electronics*, vol. 66, no. 10, pp. 7663-7671, Oct. 2019.
- [11] H. Do, "Zero-Voltage-Switching Synchronous Buck Converter With a Coupled Inductor," in *IEEE Transactions on Industrial Electronics*, vol. 58, no. 8, pp. 3440-3447, Aug. 2011.
- [12] Z. Zhang, W. Eberle, Y. Liu, and P. C. Sen, "A Nonisolated ZVS Asymmetrical Buck Voltage Regulator Module With Direct Energy Transfer," in *IEEE Transactions on Industrial Electronics*, vol. 56, no. 8, pp. 3096-3105, Aug. 2009.
- [13] T. Ge, B. Carpenter, and K. D. T. Ngo, "Resonant Cross-Commutated DC-DC Converter," in *IEEE Transactions on Industrial Electronics*, vol. 64, no. 11, pp. 8782-8785, Nov. 2017.
- [14] C. Tu *et al.*, "Design of Series-Resonator Buck Converter with Minimal Circulating Energy," *2023 IEEE Applied Power Electronics Conference and Exposition (APEC)*.
- [15] P. S. Shenoy *et al.*, "Automatic current sharing mechanism in the series capacitor buck converter," *2015 IEEE Energy Conversion Congress and Exposition (ECCE)*, Montreal, QC, Canada, 2015, pp. 2003-2009.
- [16] P. S. Shenoy, M. Amaro, D. Freeman, and J. Morroni, "Comparison of a 12V, 10A, 3MHz

- buck converter and a series capacitor buck converter," *2015 IEEE Applied Power Electronics Conference and Exposition (APEC)*, Charlotte, NC, USA, 2015, pp. 461-468.
- [17] P. S. Shenoy and M. Amaro, "Improving light load efficiency in a series capacitor buck converter by uneven phase interleaving," *2015 IEEE Applied Power Electronics Conference and Exposition (APEC)*, Charlotte, NC, USA, 2015, pp. 2784-2789.
- [18] Design of Multi-MHz Series Capacitor Buck Converters Used As Voltage Regulators, Presented at *IEEE Applied Power Electronics Conference and Exposition (APEC)*, Tampa, FL, Mar. 2017. [Online]. Available: <http://www.ti.com/lit/ml/slyy129/slyy129.pdf>.
- [19] O. Kirshenboim and M. M. Peretz, "High-Efficiency Non-Isolated Converter with Very High Step-Down Conversion Ratio," in *IEEE Transactions on Power Electronics*, vol. 32, no. 5, pp. 3683-3690, May 2017.
- [20] O. Kirshenboim, T. Vekslender, and M. M. Peretz, "Closed-Loop Design and Transient-Mode Control for a Series-Capacitor Buck Converter," in *IEEE Transactions on Power Electronics*, vol. 34, no. 2, pp. 1823-1837, Feb. 2019.
- [21] O. Kirshenboim and M. M. Peretz, "High-Efficiency Nonisolated Converter With Very High Step-Down Conversion Ratio," in *IEEE Transactions on Power Electronics*, vol. 32, no. 5, pp. 3683-3690, May 2017.
- [22] J. Wei, P. Xu, F. C. Lee, and M. Ye, "Static and dynamic modeling of the active clamp coupled-buck converter", *Proc. IEEE Power Electron. Spec. Conf.*, pp. 260-265, 2001.
- [23] K. Yao, M. Ye, M. Xu, and F. C. Lee, "Tapped-inductor buck converter for high-step-down DC-DC conversion", *IEEE Trans. Power Electron.*, vol. 20, no. 4, pp. 775-780, Jul. 2005.
- [24] M. Chen, P. S. Shenoy, and J. Morroni, "A series-capacitor tapped buck (SC-TaB) converter for regulated high voltage conversion ratio dc-dc applications", *Proc. IEEE Energy Convers.*

- Congr. Expo.*, pp. 3650-3657, 2014.
- [25] X. Zhao, C.-S. Yeh, L. Zhang, J.-S. Lai, and T. Labella, "A 2-MHz wide-input hybrid resonant converter with ultra-compact planar coupled inductor for low power integrated on-chip applications", *IEEE Trans. Ind. Appl.*, vol. 54, no. 1, pp. 376-387, Oct. 2017.
- [26] K. I. Hwu, W. Z. Jiang, and Y. T. Yau, "Ultrahigh step-down converter", *IEEE Trans. Power Electron.*, vol. 30, no. 6, pp. 3262-3274, Jun. 2015.
- [27] K. I. Hwu, W. Z. Jiang, and Y. T. Yau, "Nonisolated Coupled-Inductor-based high step-down converter with zero DC magnetizing inductance current and nonpulsating output current", *IEEE Trans. Power Electron.*, vol. 31, no. 6, pp. 4362-4377, Jun. 2016.
- [28] S. Cuk, "Hybrid-switching step-down converter with a hybrid transformer", Mar. 2011.
- [29] K. Nishijima et al., "A novel tapped-inductor buck converter for divided power distribution system", *Proc. IEEE Power Electron. Spec. Conf.*, pp. 1-6, 2006.
- [30] M. Xu, Y. Ren, J. Zhou, and F. C. Lee, "1-MHz self-driven ZVS fullbridge converter for 48-V power pod and dc/dc brick", *IEEE Trans. Power Electron.*, vol. 20, no. 5, pp. 997-1006, Sep. 2005.
- [31] S. Saggini, O. Zambetti, R. Rizzolatti, A. Zafarana, and P. Saccon, "Isolated resonant full-bridge converter with magnetic integration", *Proc. IEEE Appl. Power Electron. Conf.*, pp. 1733-1740, 2017.
- [32] M. H. Ahmed, C. Fei, F. C. Lee, and Q. Li, "48V voltage regulator module with PCB winding matrix transformer for future data centers", *IEEE Trans. Ind. Electron.*, vol. 64, no. 12, pp. 9302-9310, Dec. 2017.
- [33] C. Fei, M. H. Ahmed, F. C. Lee, and Q. Li, "Two-stage 48V-12V/6V-1.8V voltage regulator module with dynamic bus voltage control for light load efficiency improvement of two-stage

- voltage regulator", *IEEE Trans. Power Electron.*, vol. 32, no. 7, pp. 5628-5636, Jul. 2017.
- [34] M. H. Ahmed, C. Fei, F. C. Lee, and Q. Li, "High-efficiency high-power-density 48/1V sigma converter voltage regulator module", *Proc. IEEE Appl. Power Electron. Conf.*, pp. 2207-2212, 2017.
- [35] J. Sun, M. Xu, D. Reusch, and F. C. Lee, "High efficiency quasi-parallel voltage regulators", *Proc. IEEE App. Power Electron.*, pp. 811-817, 2008.
- [36] D. Reusch and J. Strydom, "Evaluation of Gallium Nitride Transistors in High Frequency Resonant and Soft-Switching DC-DC Converters," in *IEEE Transactions on Power Electronics*, vol. 30, no. 9, pp. 5151-5158, Sept. 2015.
- [37] D. Reusch, S. Biswas, and Y. Zhang, "System Optimization of a High Power Density Non-Isolated Intermediate Bus Converter for 48 V Server Applications," in *IEEE Transactions on Industry Applications*, vol. 55, no. 2, pp. 1619-1627, March-April 2019.
- [38] J. Hu, B. Wen, R. Burgos, and Y. Kang, "Design of a Wide-Input-Voltage PCB-Embedded Transformer Based Active-Clamp Flyback Converter Considering Permeability Degradation," in *IEEE Transactions on Power Electronics*, vol. 36, no. 9, pp. 10355-10365, Sept. 2021.
- [39] J. Hu, B. Wen, R. Burgos, D. Boroyevich, Y. Kang, and H. Dadkhah, "The Optimal Design of A High-Temperature PCB-Embedded Transformer GaN-Based Gate-Drive Power Supply with A Wide-Input Range," *2020 IEEE Applied Power Electronics Conference and Exposition (APEC)*, 2020, pp. 1382-1389.
- [40] T. Ge, Z. Miao, and L. Liu, "Active Cross-Commutated (ACC) Buck Converter," in *IEEE Transactions on Industrial Electronics*, vol. 69, no. 3, pp. 2577-2587, March 2022.
- [41] X. Li and S. Jiang, "Google 48V rack adaptation and onboard power technology

- update", *Proc. Open Compute Project Summit*, 2019.
- [42] M. H. Ahmed, F. C. Lee, Q. Li, M. de Rooij, and D. Reusch, "GaN-based high-density unregulated 48 v to x v LLC converters with 98% efficiency for future data centers", *Proc. Int. Exhib. Conf. Power Electron. Intell. Motion Renewable Energy Energy Manage.*, pp. 1-8, 2019.
- [43] R. A. Abramson, Z. Ye, and R. C. N. Pilawa-Podgurski, "A high performance 48-to-8 v multi-resonant switched-capacitor converter for data center applications", *Proc. 22nd Eur. Conf. Power Electron. Appl.*, pp. 1-10, 2020.
- [44] S. Jiang, C. Nan, X. Li, C. Chung, and M. Yazdani, "Switched tank converters", *Proc. IEEE Appl. Power Electron. Conf. Expo.*, pp. 81-90, 2018.
- [45] Z. Ye, Y. Lei, and R. C. N. Pilawa-Podgurski, "A 48-to-12 v cascaded resonant switched-capacitor converter for data centers with 99% peak efficiency and 2500 W/in<sup>3</sup> power density", *Proc. IEEE Appl. Power Electron. Conf. Expo.*, pp. 13-18, 2019.
- [46] M. Ursino, S. Saggini, S. Jiang, and C. Nan, "High density 48V-to-PoL VRM with hybrid pre-regulator and fixed-ratio buck", *Proc. IEEE Appl. Power Electron. Conf. Expo.*, pp. 498-505, 2020.
- [47] "48 V-12 v regulated intermediate bus converter", 2018.
- [48] "QBVE067A0B41-HZ barracuda datasheet", 2015.
- [49] A. Shehabi et al., *United states data center energy usage report*, Aug 2016, [online] Available: <https://datacenters.lbl.gov/sites/default/files/DCDWebscaleShehabi 072016. pdf>.
- [50] Y. Lei, R. May, and R. C. N. Pilawa-Podgurski, "Split-phase control: Achieving complete soft-charging operation of a dickson switched-capacitor converter", *IEEE Transactions on Power Electronics*, vol. 31, no. 1, pp. 770-782, Jan 2016.

- [51] J. Hu, " Current-Transformer Based Gate-Drive Power Supply With Reinforced Isolation," M.S. thesis, Department of Electrical and Computer Engineering., Virginia Tech, Blacksburg, 2018.
- [52] W. C. Liu and R. C. N. Pilawa-Podgurski, "Bi-lateral energy resonant converter (BERC) with merged two-stage inductor for 48-to-12v applications", *2020 IEEE 21st Workshop on Control and Modeling for Power Electronics (COMPEL)*, pp. 1-6, 2020.
- [53] Z. Ye, Y. Lei, and R. C. N. Pilawa-Podgurski, "The cascaded resonant converter: A hybrid switched-capacitor topology with high power density and efficiency", *IEEE Transactions on Power Electronics*, vol. 35, no. 5, pp. 4946-4958, 2020.
- [54] R. C. N. Pilawa-Podgurski, D. M. Giuliano, and D. J. Perreault, "Merged two-stage power converter architecture with soft charging switched-capacitor energy transfer", *2008 IEEE Power Electronics Specialists Conference*, pp. 4008-4015, June 2008.
- [55] R. C. N. Pilawa-Podgurski and D. J. Perreault, "Merged two-stage power converter with soft charging switched-capacitor stage in 180 nm cmos", *IEEE Journal of Solid-State Circuits*, vol. 47, no. 7, pp. 1557-1567, July 2012.
- [56] Y. Lei and R. C. N. Pilawa-Podgurski, "A general method for analyzing the resonant and soft-charging operation of switched-capacitor converters", *IEEE Transactions on Power Electronics*, vol. 30, no. 10, pp. 5650-5664, Oct 2015.
- [57] Z. Ye, Y. Lei, and R. C. N. Pilawa-Podgurski, "A 48-to-12 v cascaded resonant switched-capacitor converter for data centers with 99% peak efficiency and 2500 w/in<sup>3</sup> power density", *2019 IEEE Applied Power Electronics Conference and Exposition (APEC)*, pp. 13-18, 2019.
- [58] N. Haryani et al, "A Novel ZVS Turn-on Triangular Current Mode Control with Phase

- Synchronization for Three Level Inverters," *2018 IEEE Energy Conversion Congress and Exposition (ECCE)*, Portland, OR, USA, 2018, pp. 2207-2214.
- [59] T. Ge, Z. Ye, R. Abramson, and R. C. N. Pilawa-Podgurski, "A 48-to-12 v cascaded resonant switched-capacitor converter achieving 4068 w/in 3 power density and 99.0% peak efficiency ", *2021 IEEE Applied Power Electronics Conference and Exposition (APEC)*, 2021.
- [60] Z. Ye, R. A. Abramson, and R. C. N. Pilawa-Podgurski, "A 48-to-6 v multi-resonant-doubler switched-capacitor converter for data center applications", *2020 IEEE Applied Power Electronics Conference and Exposition (APEC)*, pp. 475-481, 2020.
- [61] R. A. Abramson, Z. Ye, and R. C. Pilawa-Podgurski, "A high performance 48-to-8 v multi-resonant switched-capacitor converter for data center applications", *2020 22nd European Conference on Power Electronics and Applications (EPE'20 ECCE Europe)*, pp. 1-10, 2020.
- [62] Z. Ye and R. C. N. Pilawa-Podgurski, "A power supply circuit for gate driver of gan-based flying capacitor multi-level converters", *2016 IEEE 4th Workshop on Wide Bandgap Power Devices and Applications (WiPDA)*, pp. 53-58, Nov 2016.
- [63] J. Hu, X. Zhao, L. Ravi, R. Burgos, and D. Dong, "Enhanced Gate Driver Design for SiC-Based Generator Rectifier Unit for Airborne Applications," *2021 IEEE Applied Power Electronics Conference and Exposition (APEC)*, 2021, pp. 2526-2531.
- [64] J. Hu, " Integration Challenges in High Power Density Wide Bandgap Based Circuits for Transportation Applications," Ph.D. dissertation, Department of Electrical and Computer Engineering., Virginia Tech, Blacksburg, 2021.
- [65] Z. Ye, Y. Lei, W. Liu, P. S. Shenoy, and R.. Pilawa-Podgurski, "Improved bootstrap methods for powering floating gate drivers of flying capacitor multilevel converters and hybrid

- switched-capacitor converters", *IEEE Transactions on Power Electronics*, vol. 35, no. 6, pp. 5965-5977, 2020.
- [66] T. Yuan, F. Jin, Z. Li and Q. Li, "High Frequency High Power Integrated Transformer Design for Resonant Converters with SiC Devices," *2022 IEEE 9th Workshop on Wide Bandgap Power Devices & Applications (WiPDA)*, Redondo Beach, CA, USA, 2022, pp. 170-175.
- [67] P.-L. Wong, P. Xu, P. Yang, and F. C. Lee, "Performance improvements of interleaving VRMs with coupling inductors", *IEEE Trans. Power Electron.*, vol. 16, no. 4, pp. 499-507, Jul. 2000.
- [68] J. Li, A. Stratakos, A. Schultz, and C. R. Sullivan, "Using coupled inductors to enhance transient performance of multi-phase buck converters", *Proc. 19th Annu. IEEE Appl. Power Electron. Conf. Expo.*, vol. 2, pp. 1289-1293, 2004.1.
- [69] B. K. Kang, S. K. Chung, and D. S. Oh, "Integrated magnetics for boost PFC and flyback converters with phase-shifted PWM", *Proc. 28 th Annu. IEEE Appl. Power Electron. Conf. Expo.*, pp. 1018-1024, 2013.
- [70] W. Li, P. Li, H. Yang, and X. He, "Three-level forward–flyback phase-shift ZVS converter with integrated series-connected coupled inductors", *IEEE Trans. Power Electron.*, vol. 27, no. 6, pp. 2846-2856, Jun. 2012.
- [71] M. Noah, K. Umetani, J. Imaoka, and M. Yamamoto, "Lagrangian dynamics model and practical implementation of an integrated transformer in multi-phase LLC resonant converter", *IET Power Electron.*, vol. 11, no. 2, pp. 339-347, 2018.
- [72] B. Hesterman, "Analysis and modeling of magnetic coupling", 2007.
- [73] M. Mu, F. C. Lee, Y. Jiao, and S. Lu, "Analysis and design of coupled inductor for

- interleaved multiphase three-level DC-DC converters", *Proc. IEEE Appl. Power Electron. Conf. Expo.*, pp. 2999-3006, 2015.
- [74] Y. Tokad and M. B. Reed, "Criteria and tests for realizability of the inductance matrix", *Trans. AIEE I Commun. Electron.*, vol. 78, pp. 924-926, Jan. 1960.
- [75] Y. Dong, J. Zhou, F. C. Lee, M. Xu, and S. Wang, "Twisted core coupled inductors for microprocessor voltage regulators", *IEEE Trans. Power Electron.*, vol. 23, no. 5, pp. 2536-2545, Sep. 2008.
- [76] L. Ravi et al., "Electrical Insulation Design and Qualification of a SiC-based Generator-Rectifier Unit (GRU) for High-Altitude Operation," *2021 IEEE Energy Conversion Congress and Exposition (ECCE)*, Vancouver, BC, Canada, 2021, pp. 1514-1520.
- [77] J. Hu et al., "Design and Qualification of a 100 kW Three-Phase SiC-Based Generator Rectifier Unit Rated for 50,000 ft Altitude," in *IEEE Journal of Emerging and Selected Topics in Power Electronics*, 2022.
- [78] Y. Dong, Y. Yang, F. C. Lee, and M. Xu, "The short winding path coupled inductor voltage regulators", *Proc. 23rd Annu. IEEE Appl. Power Electron. Conf. Expo.*, pp. 1446-1452, 2008.
- [79] J. Liang, L. Wang, M. Fu, J. Liang, and H. Wang, "Overview of Voltage Regulator Modules in 48 V Bus-Based Data Center Power Systems," in *CPSS Transactions on Power Electronics and Applications*, vol. 7, no. 3, pp. 283-299, September 2022.
- [80] Z. Ye, R. A. Abramson, T. Ge, and R. C. N. Pilawa-Podgurski, "Multi-Resonant Switched-Capacitor Converter: Achieving High Conversion Ratio With Reduced Component Number," in *IEEE Open Journal of Power Electronics*, vol. 3, pp. 492-507, 2022.
- [81] M. Ursino, R. Rizzolatti, G. Deboy, S. Saggini, and K. Zufferli, "High density Hybrid

- Switched-Capacitor Sigma Converter for Data Center Applications," *2022 IEEE Applied Power Electronics Conference and Exposition (APEC)*, 2022, pp. 35-39.
- [82] Y. Zhu, T. Ge, Z. Ye, and R. C. N. Pilawa-Podgurski, "A Dickson-Squared Hybrid Switched-Capacitor Converter for Direct 48 V to Point-of-Load Conversion," *2022 IEEE Applied Power Electronics Conference and Exposition (APEC)*, 2022, pp. 1272-1278.
- [83] Y. Zhu, Z. Ye, T. Ge, R. Abramson, and R. C. N. Pilawa-Podgurski, "A Multi-Phase Cascaded Series-Parallel (CaSP) Hybrid Converter for Direct 48 V to Point-of-Load Applications," *2021 IEEE Energy Conversion Congress and Exposition (ECCE)*, 2021, pp. 1973-1980.
- [84] X. Lou and Q. Li, "300A Single-stage 48V Voltage Regulator with Multiphase Current Doubler Rectifier and Integrated Transformer," *2022 IEEE Applied Power Electronics Conference and Exposition (APEC)*, 2022, pp. 1004-1010.
- [85] X. Lou, Q. Li, and M. H. Ahmed, "Adaptive Voltage Positioning Design of Single Stage 48/1V Sigma Converter for Fast Transient Response," *2021 IEEE Energy Conversion Congress and Exposition (ECCE)*, 2021, pp. 3530-3536.
- [86] X. Lou, Q. Li, F. C. Lee, and M. H. Ahmed, "Modeling and Analysis of Current Mode and V2 Controls with Adaptive Voltage Positioning (AVP) Design," *2021 IEEE Applied Power Electronics Conference and Exposition (APEC)*, 2021, pp. 2549-2555
- [87] F. Li, L. Wang, and L. Yu, "A Novel Integrated Matrix Magnetics for Isolated Single-Stage DC–DC Converter," in *IEEE Transactions on Power Electronics*, vol. 37, no. 10, pp. 12380-12390, Oct. 2022.
- [88] Y. Chen et al., "Virtual Intermediate Bus CPU Voltage Regulator," in *IEEE Transactions on Power Electronics*, vol. 37, no. 6, pp. 6883-6898, June 2022.

- [89] P. Wang, D. Zhou, D. Giuliano, M. Chen, and Y. Chen, "Multistack Switched-Capacitor Architecture with Coupled Magnetics for 48V-to-1V VRM," *2022 IEEE 23rd Workshop on Control and Modeling for Power Electronics (COMPEL)*, 2022, pp. 1-7.
- [90] P. Wang, Y. Chen, J. Yuan, R. C. N. Pilawa-Podgurski, and M. Chen, "Differential Power Processing for Ultra-Efficient Data Storage," in *IEEE Transactions on Power Electronics*, vol. 36, no. 4, pp. 4269-4286, April 2021.
- [91] C. Wang, Y. Lu, N. Sun, and R. P. Martins, "A 3-Phase Resonant Switched-Capacitor Converter for Data Center 48-V Rack Power Distribution," in *IEEE Transactions on Circuits and Systems I: Regular Papers*, vol. 68, no. 6, pp. 2714-2724, June 2021.
- [92] C. Tu, K. D. T. Ngo, and R. Chen, "Series-Capacitor Buck Converter with Soft Turn-On," *2020 IEEE Applied Power Electronics Conference and Exposition (APEC)*, New Orleans, LA, USA, 2020, pp. 41-47.
- [93] C. Tu, R. Chen, and K. D. T. Ngo, "Series-Resonator Buck Converter—Viability Demonstration," in *IEEE Transactions on Power Electronics*, vol. 36, no. 9, pp. 9693-9697, Sept. 2021.
- [94] C. Tu, R. Chen, and K. D. T. Ngo, "Steady-State Analysis of Series-Resonator Buck Converter," in *IEEE Transactions on Power Electronics*, vol. 37, no. 10, pp. 12327-12335, Oct. 2022.
- [95] C. Tu, K. D. T. Ngo, and R. Chen, "A Fast Non-Iterative Design Approach of One-Turn Inductor with Significant AC Flux using Commercially Available Components," *2022 IEEE Applied Power Electronics Conference and Exposition (APEC)*, 2022, pp. 1486-1491.
- [96] F. C. Lee, "High-frequency quasi-resonant converter technologies," in *Proceedings of the IEEE*, vol. 76, no. 4, pp. 377-390, April 1988.

- [97] E. E. Buchanan and E. J. Miller, "Resonant switching power conversion technique," *1975 IEEE Power Electronics Specialists Conference*, 1975, pp. 188-193.
- [98] K. Liu, R. Oruganti, and F. C. Lee, "Resonant switches - Topologies and characteristics," *1985 IEEE Power Electronics Specialists Conference*, 1985, pp. 106-116.
- [99] W. A. Tabisz and F. C. Lee, "Zero-voltage-switching multi-resonant technique-a novel approach to improve performance of high frequency quasi-resonant converters," *PESC '88 Record., 19th Annual IEEE Power Electronics Specialists Conference*, 1988, pp. 9-17 vol.1.
- [100] M. M. Jovanovic, K. -H. Liu, R. Oruganti, and F. C. Y. Lee, "State-Plane Analysis of Quasi-Resonant Converters," in *IEEE Transactions on Power Electronics*, vol. PE-2, no. 1, pp. 36-44, Jan. 1987.
- [101] S. Freeland and R. D. Middlebrook, "A unified analysis of converters with resonant switches," *1987 IEEE Power Electronics Specialists Conference*, 1987, pp. 20-30.
- [102] V. Vorperian, R. Tymerski, and F. C. Y. Lee, "Equivalent circuit models for resonant and PWM switches," in *IEEE Transactions on Power Electronics*, vol. 4, no. 2, pp. 205-214, April 1989.
- [103] R. D. Middlebrook and S. Cuk, "A general unified approach to modelling switching-converter power stages," *1976 IEEE Power Electronics Specialists Conference*, 1976, pp. 18-34.
- [104] A. F. Witulski and R. W. Erickson, "Extension of state-space averaging to resonant switches and beyond," in *IEEE Transactions on Power Electronics*, vol. 5, no. 1, pp. 98-109, Jan. 1990.
- [105] T. Ninomiya, M. Nakahara, T. Higashi, and K. Harada, "A unified analysis of resonant converters," in *IEEE Transactions on Power Electronics*, vol. 6, no. 2, pp. 260-270, April 1991.
- [106] Jianping Xu and C. Q. Lee, "A unified averaging technique for the modeling of quasi-resonant converters," in *IEEE Transactions on Power Electronics*, vol. 13, no. 3, pp. 556-563, May 1998.
- [107] T. Ge, B. Carpenter, and K. D. T. Ngo, "Steady-State Analysis of Resonant Cross-Commutated Buck Converter Under Continuous Voltage Mode," in *IEEE Transactions on Industrial Electronics*, vol. 65, no. 10, pp. 7782-7792, Oct. 2018.

- [108] S. Xu, Q. Qian, T. Tao, S. Lu, and W. Sun, "Small Signal Modeling and Control Loop Design of Critical Conduction Mode Active Clamp Flyback Converter," in *IEEE Transactions on Power Electronics*, vol. 36, no. 6, pp. 7250-7263, June 2021.
- [109] K. D. T. Ngo, "Generalization of resonant switches and quasi-resonant DC-DC converters," *1987 IEEE Power Electronics Specialists Conference*, 1987, pp. 395-403.
- [110] V. Vorperian, "Quasi-square-wave converters: Topologies and analysis", *IEEE Trans. Power Electron.*, vol. 3, no. 2, pp. 183-191, Mar. 1998.
- [111] Z. Zhang, S. Tian, and K. D. T. Ngo, "Small-Signal Equivalent Circuit Model of Quasi-Square-Wave Flyback Converter," in *IEEE Transactions on Power Electronics*, vol. 32, no. 8, pp. 5885-5888, Aug. 2017.
- [112] W. A. Tabisz and F. C. Lee, "Zero-voltage-switching multi-resonant technique-a novel approach to improve performance of high frequency quasi-resonant converters," PESC '88 Record., *19th Annual IEEE Power Electronics Specialists Conference*, 1988, pp. 9-17 vol.1.
- [113] A. Szabo, M. Kamsara, and E. S. Ward, "A unified method for the small-signal modelling of multi-resonant and quasi-resonant converters," *1998 IEEE International Symposium on Circuits and Systems (ISCAS)*, 1998, pp. 522-525 vol.3.
- [114] F. C. Lee and Q. Li, "High-frequency integrated point-of-load converters: Overview", *IEEE Trans. Power Electron.*, vol. 28, no. 9, pp. 4127-4136, Sep. 2013.
- [115] Q. Li, Y. Dong, F. C. Lee, and D. J. Gilham, "High-density low-profile coupled inductor design for integrated point-of-load converters", *IEEE Trans. Power Electron.*, vol. 28, no. 1, pp. 547-554, Jan. 2013.
- [116] W. Huang and B. Lehman, "A compact coupled inductor for interleaved multiphase DC-DC converters", *IEEE Trans. Power Electron.*, vol. 31, no. 10, pp. 6770-6775, Oct. 2016.
- [117] Y. Su, Q. Li, and F. C. Lee, "Design and evaluation of a high-frequency LTCC inductor

- substrate for a three-dimensional integrated DC/DC converter", *IEEE Trans. Power Electron.*, vol. 28, no. 9, pp. 4354-4364, Sep. 2013.
- [118] J. Wang et al., "Design and Testing of 6 kV H-bridge Power Electronics Building Block Based on 10 kV SiC MOSFET Module," *2018 International Power Electronics Conference (IPEC-Niigata 2018 -ECCE Asia)*, Niigata, Japan, 2018, pp. 3985-3992,
- [119] M. H. F. Lim, J. D. van Wyk, and Z. Liang, "Internal geometry variation of LTCC inductors to improve light-load efficiency of DC–DC converters", *IEEE Trans. Compon. Packag. Technol.*, vol. 32, no. 1, pp. 3-11, Mar. 2009.
- [120] J. Hu, B. Wen, and R. Burgos, "Effect of Mechanical Stress Induced by PCB-Embedding Fabrication on Ferrite Magnetics," *2021 IEEE Applied Power Electronics Conference and Exposition (APEC)*, 2021, pp. 2331-2337.
- [121] S. Kelly, C. Collins, M. Duffy, F. M. F. Rhen, and S. Roy, "Core materials for high frequency VRM inductors", *Proc. 2007 IEEE Power Electron. Spec. Conf.*, pp. 1767-1772, 2007.
- [122] T. Ge, B. Carpenter, and K. D. T. Ngo, "Design Methodology of a One-Turn Inductor With Significant DC and AC Fluxes—Demonstration in a Resonant Cross-Commutated Buck Converter," in *IEEE Transactions on Industrial Electronics*, vol. 66, no. 11, pp. 8424-8433, Nov. 2019.
- [123] T. Ge and K. D. T. Ngo, "Omnico coupled Inductors (OCI) Applied in a Resonant Cross-Commutated Buck Converter," in *IEEE Transactions on Industrial Electronics*, vol. 68, no. 6, pp. 4894-4902, June 2021.
- [124] K. D. T. Ngo and M. H. Kuo, "Effects of air gaps on winding loss in high-frequency planar magnetics," *PESC '88 Record., 19th Annual IEEE Power Electronics Specialists Conference*, 1988, pp. 1112-1119 vol.2.

- [125] Z. Zhang, K. D. T. Ngo, and J. L. Nilles, "Design of Inductors With Significant AC Flux," in *IEEE Transactions on Power Electronics*, vol. 32, no. 1, pp. 529-539, Jan. 2017.
- [126] X. Zhao *et al.*, "Planar Common-Mode EMI Filter Design and optimization in a 100-kW SiC-based Generator-Rectifier System for High-Altitude Operation," *2021 IEEE Energy Conversion Congress and Exposition (ECCE)*, Vancouver, BC, Canada, 2021, pp. 3555-3562
- [127] T. Ge, B. Carpenter, and K. D. T. Ngo, "Design Methodology of a One-Turn Inductor With Significant DC and AC Fluxes—Demonstration in a Resonant Cross-Commutated Buck Converter," in *IEEE Transactions on Industrial Electronics*, vol. 66, no. 11, pp. 8424-8433, Nov. 2019.
- [128] X. Zhao *et al.*, "Planar Common-Mode EMI Filter Design and Optimization for High-Altitude 100-kW SiC Inverter/Rectifier System," in *IEEE Journal of Emerging and Selected Topics in Power Electronics*, vol. 10, no. 5, pp. 5290-5303, Oct. 2022
- [129] Y. Yan, L. Geng, L. Zhang, C. Tu, R. Sriramdas *et al.*, "High-Power Magnetoelectric Voltage Tunable Inductors," in *IEEE Transactions on Industrial Electronics*, vol. 68, no. 6, pp. 5355-5365, June 2021.
- [130] Jiankun Hu and C. R. Sullivan, "AC resistance of planar power inductors and the quasidistributed gap technique," in *IEEE Transactions on Power Electronics*, vol. 16, no. 4, pp. 558-567, July 2001
- [131] T. Ge, K. D. T. Ngo, and J. Moss, "Two-Dimensional Gapping to Reduce Light-Load Loss of Point-of-Load Inductor," in *IEEE Transactions on Power Electronics*, vol. 32, no. 1, pp. 540-550, Jan. 2017.

- [132] S. Mukherjee, Y. Gao, and D. Maksimović, "Reduction of AC Winding Losses Due to Fringing-Field Effects in High-Frequency Inductors With Orthogonal Air Gaps," in *IEEE Transactions on Power Electronics*, vol. 36, no. 1, pp. 815-828, Jan. 2021.
- [133] R. S. Yang, A. J. Hanson, C. R. Sullivan, and D. J. Perreault, "Design Flexibility of a Modular Low-Loss High-Frequency Inductor Structure," in *IEEE Transactions on Power Electronics*, vol. 36, no. 11, pp. 13013-13024, Nov. 2021.
- [134] N. Yan, J. Hu, J. Wang, D. Dong, and R. Burgos, "Design Analysis for Current-transformer Based High-frequency Auxiliary Power Supply for SiC-based Medium Voltage Converter Systems," *2020 IEEE Applied Power Electronics Conference and Exposition (APEC)*, New Orleans, LA, USA, 2020, pp. 1390-1397.
- [135] L. Wang, Z. Hu, Y. -F. Liu, Y. Pei, and X. Yang, "Multipermeability Inductors for Increasing the Inductance and Improving the Efficiency of High-Frequency DC/DC Converters," in *IEEE Transactions on Power Electronics*, vol. 28, no. 9, pp. 4402-4413, Sept. 2013.
- [136] J. Schäfer, D. Bortis, and J. W. Kolar, "Novel Highly Efficient/Compact Automotive PCB Winding Inductors Based on the Compensating Air-Gap Fringing Field Concept," in *IEEE Transactions on Power Electronics*, vol. 35, no. 9, pp. 9617-9631, Sept. 2020.
- [137] J. Hu and C. R. Sullivan, "Analytical method for generalization of numerically optimized inductor winding shapes," *30th Annual IEEE Power Electronics Specialists Conference*. Record. (Cat. No.99CH36321), 1999, pp. 568-573 vol.1.
- [138] F. Zhu and Q. Li, "Coupled Inductors With an Adaptive Coupling Coefficient for Multiphase Voltage Regulators," in *IEEE Transactions on Power Electronics*, vol. 38, no. 1, pp. 739-749, Jan. 2023

- [139] F. Zhu and Q. Li, "A Novel PCB-Embedded Coupled Inductor Structure for a 20MHz Integrated Voltage Regulator," in *IEEE Journal of Emerging and Selected Topics in Power Electronics*, 2022
- [140] Z. Yu *et al.*, "A Novel Pyramid Winding for PCB Planar Inductors With Fewer Copper Layers and Lower AC Copper Loss," in *IEEE Transactions on Power Electronics*, vol. 37, no. 10, pp. 11461-11468, Oct. 2022.
- [141] J. Hu, J. Wang, R. Burgos, B. Wen, and D. Boroyevich, "High-Density Current-Transformer-Based Gate-Drive Power Supply With Reinforced Isolation for 10-kV SiC MOSFET Modules," in *IEEE Journal of Emerging and Selected Topics in Power Electronics*, vol. 8, no. 3, pp. 2217-2226, Sept. 2020.
- [142] J. Hu, J. Wang, R. Burgos, and D. Boroyevich, "Current-Transformer Based Gate-Drive Power Supply with Reinforced Isolation," *2018 IEEE Energy Conversion Congress and Exposition (ECCE)*, 2018, pp. 6328-6335.
- [143] Ferroxcube, "3F4 Material Specification," 3F4 datasheet, Sep. 2008.
- [144] Hitachi Metals, "ML95S, ML91S Technical Data," ML91s datasheet, Jan. 2019.
- [145] DMEGC, "DMR51W Material Characteristics," DMR51W datasheet, Jul. 2014.
- [146] ACME Electronics Corporation, "P61 Material Characteristics," P61 datasheet, Jun. 2018.
- [147] C. Tu *et al.*, "Rhombus-Window Resonant Inductor with Significant AC Flux," *2023 IEEE Applied Power Electronics Conference and Exposition (APEC)*.
- [148] R. W. Erickson and D. Maksimović, *Fundamentals of Power Electronics*, Norwell, MA, USA: Kluwer, 2001.
- [149] A. Balakrishnan, W. T. Joines, and T. G. Wilson, "Air-gap reluctance and inductance calculations for magnetic circuits using a Schwarz-Christoffel transformation," in *IEEE*

*Transactions on Power Electronics*, vol. 12, no. 4, pp. 654-663, July 1997.